Z. Kowalik
Institute of Marine Science
University of Alaska, Fairbanks

Introduction to Numerical Modeling of Tsunami Waves

Fairbanks, January, 2012

Table of Contents

CHAPTER I

GENERAL EQUATIONS

1. Equations of motion and continuity

Numerical models describing the fields of velocity and density in the ocean are based on the system of hydrodynamical–thermodynamical equations which incorporate the law of conservation of momentum, mass and energy. These equations will be derived in the Cartesian coordinate system although at times a spherical coordinate system will be used. A right-handed rectangular coordinate system with the origin located at the undisturbed level of the free surface is introduced.

The coordinate system is such that the x axis points towards east, the y axis points towards north, and the z axis points upwards, towards zenith. The components of velocity along these three axes will be respectively denoted by u, v, and w. For convenience and brevity we will use also a tensor summation notation, in which the axes are denoted by x_1, x_2, and x_3 and the velocity components by u_1, u_2, and u_3. In this notation, an index appearing twice in a term implies summation over all three index values.

The equation expressing the conservation of momentum is written in tensor notation as

$$\rho\frac{\partial u_i}{\partial t} + \rho u_j\frac{\partial u_i}{\partial x_j} + 2\rho\epsilon_{ijk}\Omega_j u_k = -\frac{\partial p}{\partial x_i} - g\rho\delta_{3i} + \frac{\partial \sigma_{ij}}{\partial x_j} \tag{I.1}$$

where ρ is the density of water, t time, p pressure, Ω_j is the component of the Earth's angular velocity, and σ_{ij} are the components of stress due to molecular viscosity. Also note that $\epsilon_{ijk} = +1$ if i, j, k are in cyclic order, $\epsilon_{ijk} = -1$ if i, j, k are in anticyclic order, and $\epsilon_{ijk} = 0$ if any pair or all three indices have the same value; $\delta_{3i} = 1$ for $i = 3$ and $\delta_{3i} = 0$ for otherwise.

If μ is the molecular viscosity, then the stress tensor, σ_{ij}, can be expressed in terms of the rate of deformation of a fluid element by the motion

$$\sigma_{ij} = \mu(\frac{\partial u_i}{\partial x_j} + \frac{\partial u_j}{\partial x_i}) \tag{I.2}$$

The conservation of mass can be expressed through the continuity equation

$$\frac{\partial \rho}{\partial t} + \frac{\partial \rho u_i}{\partial x_i} = 0, \tag{I.3}$$

which for an incompressible fluid is

$$\frac{\partial u_i}{\partial x_i} = 0 \tag{I.3a}$$

For any other property of the fluid (e.g., salinity, temperature, etc.), the general form of the conservation equation holds,

$$\frac{\partial \rho\Phi}{\partial t} + \frac{\partial \rho\Phi u_i}{\partial x_i} = -\frac{\partial F_i}{\partial x_i} + q \tag{I.4}$$

Here, F_i are the components of the flux of the property Φ due to internal forces or pressures and q is the total internal source of the property Φ. Note that eq.(I.1) and (I.3) are special forms of eq.(I.4). In the above system the water density is considered as constant. If the density is variable the equations of motion and continuity need to be augmented by thermodynamics (**Cap, 2006**).

2. Energy equations

The conservation of energy of a mechanical system makes energy one of the best parameters to study the time history of the motion, both from the analytical and numerical points of view. Behavior of the various numerical schemes can be easily observed by invoking the energy of the system. We shall define here two types of energy, i.e., kinetic and potential;

$$E_k = \frac{1}{2}\rho u_i^2 = \frac{1}{2}\rho(u^2 + v^2 + w^2); \qquad E_p = \rho g z \tag{I.5}$$

The above expressions define the energy in a unit volume of the fluid (**Gill, 1982**).

Multiplying eq.(I.3) by u_i and adding to eq.(I.1) and using eq.(I.2) after ignoring compressibility of the water, we obtain

$$\frac{\partial \rho u_i}{\partial t} + \frac{\partial \rho u_j u_i}{\partial x_j} + 2\rho\epsilon_{ijk}\Omega_j u_k = -\frac{\partial p}{\partial x_i} - g\rho\delta_{3i} + \mu\frac{\partial^2 u_i}{\partial x_j \partial x_j} \tag{I.6}$$

We shall start by constructing the kinetic energy equation. Multiplying eq.(I.6) by u_i and taking into account equation of continuity for incompressible fluid (I.3a), we arrive at

$$\frac{\partial \rho {u_i}^2/2}{\partial t} + \frac{\partial u_j(p + \rho {u_i}^2/2)}{\partial x_j} + 2\epsilon_{ijk}\Omega_j \rho u_i u_k = -g\rho w + u_i \mu\frac{\partial^2 u_i}{\partial x_j \partial x_j} \tag{I.7}$$

Here $u_3 = w$ is the vertical component of velocity. This equation expresses the balance of the kinetic energy in a unit volume of fluid. The first term on the left-hand-side (LHS) describes the change in time of the kinetic energy; the second term expresses a transport of kinetic energy and pressure by flow and the third term defines the kinetic energy related to the Coriolis force. The term related to the Coriolis force is also rather small and can neglected in the energy balance. The first term on the right-hand-side (RHS) containing vertical component of velocity (w) describes the change of the potential energy in time. The second term on the RHS specifies the work done by the viscous stresses and defines the total dissipation caused by the molecular forces. We shall not consider the last term in detail because, usually in an oceanic flow the molecular friction is negligible. The role of dissipation in eq.(I.7) in a turbulent oceanic flow is usually formulated in terms of the Reynolds stresses (**Hinze, 1975 ; Launder and Spalding, 1972**). Applying the notion

of the eddy viscosity to the Reynolds stresses it is possible to introduce an eddy viscosity coefficient similar to the molecular friction coefficient (μ). Therefore, the simplest approach for the turbulent motion to be inserted in the above equations is to consider (μ) as an eddy viscosity coefficient. However to avoid confusion we shall name this new coefficient as N.

3. Rectangular system of coordinates

The effects of the Earth's curvature on the motion of a fluid at the relatively small distances of the order of 1000 km may be neglected. To describe this motion a rectangular system of coordinates will be employed, thus making the equations and discussion much simpler.

$$\frac{Du}{Dt} - fv = -\frac{1}{\rho}\frac{\partial p}{\partial x} + \frac{\partial}{\partial z}N_z\frac{\partial u}{\partial z} + N_h\Delta u \tag{I.8}$$

$$\frac{Dv}{Dt} + fu = -\frac{1}{\rho}\frac{\partial p}{\partial y} + \frac{\partial}{\partial z}N_z\frac{\partial v}{\partial z} + N_h\Delta v \tag{I.9}$$

$$\frac{Dw}{Dt} = -\frac{1}{\rho}\frac{\partial p}{\partial z} - g + \frac{\partial}{\partial z}N_z\frac{\partial w}{\partial z} + N_h\Delta w \tag{I.10}$$

Here the operator $\dfrac{D}{Dt}$ is

$$\frac{D}{Dt} = \frac{\partial}{\partial t} + u\frac{\partial}{\partial x} + v\frac{\partial}{\partial y} + w\frac{\partial}{\partial z} \tag{I.11}$$

In these equations Coriolis parameter $f = 2\Omega\sin\phi$ is a function of the Earth's angular velocity $\Omega = 7.29\times10^{-5}s^{-1}$ and the latitude ϕ. Two-dimensional Laplace operator Δ is defined as $\Delta = \dfrac{\partial^2}{\partial x^2} + \dfrac{\partial^2}{\partial y^2}$. The eddy viscosity coefficient (N) has been expressed by two coefficients; for the horizontal motion N_h is used and for the vertical motion serves N_z.

Above, for the four unknown variables (u, v, w, p) only three equations have been introduced, therefore one additional equations is required — this will be the equation of continuity. For the problems we intend to solve the sea water can be regarded as an incompressible fluid, and in this case the equation of continuity expresses the conservation of volume (eq.(I.3a)),

$$\frac{\partial u}{\partial x} + \frac{\partial v}{\partial y} + \frac{\partial w}{\partial z} = 0 \tag{I.12; I.3a}$$

We have to notice that the density is assumed as known, so the equation of state is not the part of the above system.

4. Spherical system of coordinates

Whenever fluid motion is considered along large distances on the globe the equation of motion and continuity can be written in the spherical polar coordinates λ, ϕ and R, defined as longitude, latitude and distance from the Earth's center. If the origin of the system

is located on the ocean surface, it is more suitable to introduce a vertical coordinate $z = R - R_0$. Here R_0 is the radius of Earth and is equal 6370 km.

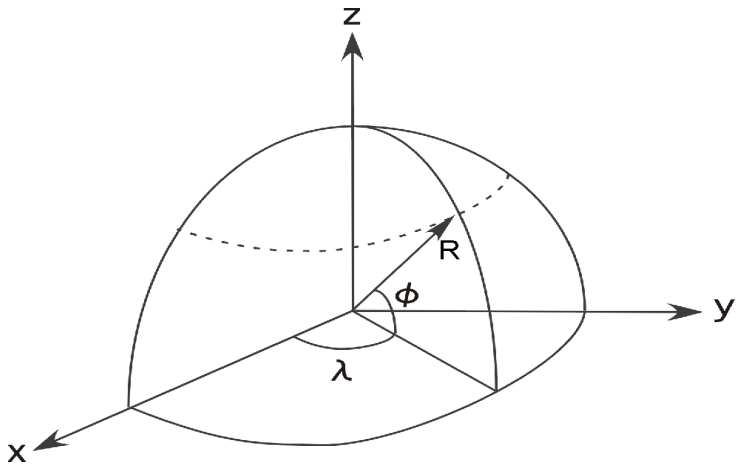

Figure I.1 Spherical and Rectangular System of Coordinate.

Because Earth does not exactly has a spherical shape, the equation given below will better describe the large scale motion relative to the geopotential and not to the spherical surfaces. For further discussion of this problem see Gill (1982).

The equations of motion in the spherical system are

$$\frac{Du}{Dt} - (2\Omega + \frac{u}{R\cos\phi})(v\sin\phi - w\cos\phi) = -\frac{1}{\rho R\cos\phi}\frac{\partial p}{\partial\lambda} + A_\lambda \tag{I.13}$$

$$\frac{Dv}{Dt} + \frac{wv}{R} + (2\Omega + \frac{u}{R\cos\phi})u\sin\phi = -\frac{1}{\rho R}\frac{\partial p}{\partial\phi} + A_\phi \tag{I.14}$$

$$\frac{Dw}{Dt} - \frac{v^2}{R} - (2\Omega + \frac{u}{R\cos\phi})u\cos\phi = -\frac{1}{\rho}\frac{\partial p}{\partial z} - g + A_z \tag{I.15}$$

where A_λ, A_ϕ, and A_z are the components of the viscous force, and the time operator is expressed as

$$\frac{D}{Dt} = \frac{\partial}{\partial t} + \frac{u}{R\cos\phi}\frac{\partial}{\partial\lambda} + \frac{v}{R}\frac{\partial}{\partial\phi} + w\frac{\partial}{\partial z} \tag{I.16}$$

The frictional forces are written in a somewhat complicated form:

$$A_\lambda = A_1 u - \frac{N_h}{R^2\cos^2\phi}(u + 2\frac{\partial}{\partial\lambda}(v\sin\phi - w\cos\phi)) \tag{I.17}$$

$$A_\phi = A_1 v + N_h(-\frac{v}{R^2\cos^2\phi} + \frac{2\sin\phi}{R^2\cos^2\phi}\frac{\partial u}{\partial\lambda} + \frac{2}{R^2}\frac{\partial w}{\partial\phi}) \tag{I.18}$$

$$A_z = A_1 w + N_h(-\frac{2w}{R^2} - \frac{2}{R^2\cos^2\phi}\frac{\partial u}{\partial\lambda} - \frac{2}{R^2\cos\phi}\frac{\partial}{\partial\lambda}(v\cos\phi)) \tag{I.19}$$

where the operator A_1 has the following form,

$$A_1 = N_h\left(\frac{1}{R^2\cos^2\phi}\frac{\partial^2}{\partial\lambda^2} + \frac{1}{R^2\cos\phi}\frac{\partial}{\partial\phi}\left(\cos\phi\frac{\partial}{\partial\phi}\right)\right) + \frac{\partial}{\partial z}\left(N_z\frac{\partial}{\partial z}\right) \tag{I.20}$$

The equation of continuity in the spherical system is

$$\frac{1}{R\cos\phi}\frac{\partial u}{\partial\lambda} + \frac{1}{R\cos\phi}\frac{\partial}{\partial\phi}(v\cos\phi) + \frac{\partial w}{\partial z} = 0 \tag{I.21}$$

5. Hydrostatic approximations

The above derived equations of motion describe a complete spectrum of the vertical and horizontal motion, but we shall study the larger scale motion such as long waves, where motion is mainly horizontal. To obtain from a general set of equations the specific set which will describe only a certain class of motion, traditionally the so-called dimensional analysis has been applied, see, e.g., **Pedlosky (1982)**. This approach assumes that certain information related to the temporal and spatial scale of motion is known *a priori*.

The hydrostatic approximation is only related to the vertical component of equation of motion. Because the horizontal extent of the ocean is much larger than the vertical extent, the vertical component of the motion is much weaker than the horizontal velocity. Typical vertical velocities in the oceans are of the order 10^{-2} cm/s, whereas the horizontal velocities are 1000 times greater. If the flow is predominantly horizontal, and the vertical acceleration is small compared to the gravity acceleration, the equation of vertical motion can be reduced to the simple hydrostatic law (**Proudman, 1953**). Rigorous justification of this approximation has never been given, and it is possible that locally (where the depth changes abruptly) large vertical currents may occur. The hydrostatic assumption simplifies equations (I.10) and (I.15) to

$$-\frac{1}{\rho}\frac{\partial p}{\partial z} - g = 0 \tag{I.22}$$

and can now be integrated from any depth z to the free surface $z = \zeta(x, y, t)$,

$$\int_z^\zeta dp = -\int_z^\zeta g\rho dz$$

Noting that the pressure at the free surface $p(\zeta)$ is equal to the atmospheric pressure (p_a) and the denoting pressure at depth z as $p(z)$ we write the final result as

$$p(z) = p_a + g\rho(\zeta - z) \tag{I.23}$$

Thus we were able, by integrating the equation of motion along the vertical coordinate, to express unknown pressure variations as a sum of terms related to the atmospheric pressure p_a and the sea level changes (ζ).

Introducing pressure variation into the equation of motion (1.8), and applying similar considerations to the equation of motion along the y coordinate, the system of equations with the hydrostatic approximation is obtained:

$$\frac{Du}{Dt} - fv = -\frac{1}{\rho_o}\frac{\partial p_a}{\partial x} - g\frac{\partial \zeta}{\partial x} + \frac{\partial}{\partial z}N_z\frac{\partial u}{\partial z} + N_h\Delta u \tag{I.24}$$

$$\frac{Dv}{Dt} + fu = -\frac{1}{\rho_o}\frac{\partial p_a}{\partial y} - g\frac{\partial \zeta}{\partial y} + \frac{\partial}{\partial z}N_z\frac{\partial v}{\partial z} + N_h\Delta v \tag{I.25}$$

In the above equations the horizontal components of acceleration have been related to the atmospheric pressure (p_a) and the sea level (ζ). The motion is modified by the Coriolis force and the friction. A similar approach can be taken to derive equations in the spherical system of coordinates.

Although the vertical acceleration was assumed to be negligible and the vertical equation has been reduced to the equation of hydrostatic state the vertical velocity still can be calculated from the equation of continuity (I.12) or (I.21).

6. Vertically integrated equations

The pressure due to the sea level slope is constant throughout the water depth, it is therefore feasible to derive a new set of equations from (I.24) and (I.25) by vertical integration. The new set may be used to find the unknown sea slope components or it can be applied to solve problems which do not depend on the vertical distribution. The vertically averaged equations have been applied to predict the sea surface variations in time or the averaged current in tides, storm surges and tsunamis (**Murty, 1984**).

Integration over the vertical coordinate will take place from the bottom $z = -H(x, y)$ to the free surface $z = \zeta(x, y, t)$. Let's first consider two important components of velocity:

at the free surface,

$$w_{z=\zeta} = \frac{\partial \zeta}{\partial t} + u\frac{\partial \zeta}{\partial x} + v\frac{\partial \zeta}{\partial y} \tag{I.26}$$

and at the bottom

$$w_{z=H} = -u\frac{\partial H}{\partial x} - v\frac{\partial H}{\partial y} \tag{I.27}$$

We start by the vertical integration of the frictional force,

$$\rho\int_{-H}^{\zeta}\frac{\partial}{\partial z}N_z\frac{\partial u}{\partial z}dz = \tau_x^s - \tau_x^b \tag{I.28}$$

and

$$\rho\int_{-H}^{\zeta}\frac{\partial}{\partial z}N_z\frac{\partial v}{\partial z}dz = \tau_y^s - \tau_y^b \tag{I.29}$$

Surface (τ^s) and bottom (τ^b) stresses are introduced based on the stress definition

$$\tau_x = \rho N_z\frac{\partial u}{\partial z} \quad \text{and} \quad \tau_y = \rho N_z\frac{\partial v}{\partial z} \tag{I.30}$$

Generally, stress is defined as a tangential force acting on a unit surface and it has the dimension of pressure.

To proceed further the vertically averaged velocity is defined:

$$\tilde{u} = \frac{1}{D}\int_{-H}^{\zeta} u dz \qquad \text{and} \qquad \tilde{v} = \frac{1}{D}\int_{-H}^{\zeta} v dz \tag{I.31}$$

Here $D = H + \zeta$ denotes a total depth.

The horizontal acceleration term in eq.(I.24) is transformed as

$$\int_{-H}^{\zeta} \frac{\partial u}{\partial t} dz = \frac{\partial}{\partial t}\int_{-H}^{\zeta} u dz - \big[u\frac{\partial \zeta}{\partial t}\big]_{z=\zeta}$$

$$\int_{-H}^{\zeta} u\frac{\partial u}{\partial x} dz = \frac{\partial}{\partial x}\int_{-H}^{\zeta} u^2 dz - \int_{-H}^{\zeta} u\frac{\partial u}{\partial x} dz - \big[u^2\frac{\partial \zeta}{\partial x}\big]_{z=\zeta} - \big[u^2\frac{\partial H}{\partial x}\big]_{z=-H}$$

$$\int_{-H}^{\zeta} v\frac{\partial u}{\partial y} dz = \frac{\partial}{\partial y}\int_{-H}^{\zeta} uv dz - \int_{-H}^{\zeta} u\frac{\partial v}{\partial y} dz - \big[uv\frac{\partial \zeta}{\partial y}\big]_{z=\zeta} - \big[uv\frac{\partial H}{\partial y}\big]_{z=-H}$$

$$\int_{-H}^{\zeta} w\frac{\partial u}{\partial z} dz = \big[uw\big]_{z=\zeta} - \big[uw\big]_{z=-H} - \int_{-H}^{\zeta} u\frac{\partial w}{\partial z} dz \tag{I.32}$$

Now let us combine the terms whose sum is equal to zero,

$$-\big[u(\frac{\partial \zeta}{\partial t} + u\frac{\partial \zeta}{\partial x} + v\frac{\partial \zeta}{\partial y})\big]_{z=\zeta} -$$

$$\int_{-H}^{\zeta} u(\frac{\partial u}{\partial x} + \frac{\partial v}{\partial y} + \frac{\partial w}{\partial z})dz + \big[uw\big]_{z=\zeta} - \big[uw\big]_{z=-H}$$

The first term is equal to the third term, the second term is equal to zero because it comprises equation of continuity (I.12). Finally, the last term vanishes assuming that the vertical velocity is equal to zero along the horizontal bottom plane.

The integration of Coriolis term and pressure terms in (I.24 I.25) is straightforward, but the derivation of the horizontal friction term is rather cumbersome. The final result is

$$\frac{\partial}{\partial t}\int_{-H}^{\zeta} u dz + \frac{\partial}{\partial x}\int_{-H}^{\zeta} u^2 dz + \frac{\partial}{\partial y}\int_{-H}^{\zeta} uv dz - f\int_{-H}^{\zeta} v dz$$

$$= -\frac{H+\zeta}{\rho}\frac{\partial p_a}{\partial x} - g(H+\zeta)\frac{\partial \zeta}{\partial x} - \frac{g}{\rho}\int_{-H}^{\zeta}\int_{z}^{\zeta} \frac{\partial \rho'}{\partial x} dz dz + (\tau_x^s - \tau_x^b)/\rho + \text{Hor.Fric.} \tag{I.33}$$

A similar equation can be written along the y direction. These equations will serve as a starting point for a few different approximations.

Shallow water approximation, probably was applied for the first time by **Hansen (1949)** to study numerically propagation of tides. It assumes that the horizontal velocities are constant along the vertical direction, also the motion is usually considered to be barotropic i.e., density stratification is neglected. The nonlinear and horizontal terms in (I.32) can be written as

$$\frac{\partial}{\partial x}\int_{-H}^{\zeta} u^2 dz + \frac{\partial}{\partial y}\int_{-H}^{\zeta} uv dz \approx \frac{\partial}{\partial x}\tilde{u}\tilde{u}D + \frac{\partial}{\partial y}\tilde{u}\tilde{v}D$$

$$\int_{-H}^{\zeta} (N_h \Delta u) dz \approx D N_h \Delta \tilde{u} \tag{I.34}$$

With the above simplifications taken into consideration, the shallow water equations along E-W and N-S directions become

$$\rho(\frac{\partial \tilde{u}}{\partial t} + \tilde{u}\frac{\partial \tilde{u}}{\partial x} + \tilde{v}\frac{\partial \tilde{u}}{\partial y} - f\tilde{v}) = -\frac{\partial p_a}{\partial x} - g\rho\frac{\partial \zeta}{\partial x} + \tau_x^s/D - \tau_x^b/D + \rho N_h \Delta \tilde{u} \tag{I.35}$$

$$\rho(\frac{\partial \tilde{v}}{\partial t} + \tilde{u}\frac{\partial \tilde{v}}{\partial x} + \tilde{v}\frac{\partial \tilde{v}}{\partial y} + f\tilde{u}) = -\frac{\partial p_a}{\partial y} - g\rho\frac{\partial \zeta}{\partial y} + \tau_y^s/D - \tau_y^b/D + \rho N_h \Delta \tilde{v} \tag{I.36}$$

One observation is important; the exchange of momentum in the vertical direction in eq.(I.24) and (I.25) has been described by means of the eddy viscosity coefficient, in eq.(I.35) and (I.36) only stresses at the surface and at the bottom ought to be defined. This makes the shallow water problem much simpler, because the eddy viscosity coefficients are often difficult to define.

Equation of continuity. Integrating the equation of continuity (I.12) along the vertical direction and applying the relations

$$\int_{-H}^{\zeta} \frac{\partial u}{\partial x} dz = \frac{\partial}{\partial z}\int_{-H}^{\zeta} u dz - \left[u\frac{\partial \zeta}{\partial x}\right]_{z=\zeta} - \left[u\frac{\partial H}{\partial x}\right]_{z=-H}$$

$$\int_{-H}^{\zeta} \frac{\partial v}{\partial x} dz = \frac{\partial}{\partial z}\int_{-H}^{\zeta} v dz - \left[v\frac{\partial \zeta}{\partial x}\right]_{z=\zeta} - \left[v\frac{\partial H}{\partial x}\right]_{z=-H}$$

and also taking into account the boundary conditions (I.26) and (I.27), the equation of continuity for the vertically averaged flow is obtained:

$$\frac{\partial}{\partial x}\tilde{u}D + \frac{\partial}{\partial y}\tilde{v}D + \frac{\partial \zeta}{\partial t} = 0 \tag{I.37}$$

Transport equations. Vertical integration defined by (I.31) admits possibility of introducing a different set of variables. We define here the components of the horizontal transport as

$$M_x = D\tilde{u} = \int_{-H}^{\zeta} u dz \qquad \text{and} \qquad M_y = D\tilde{v} = \int_{-H}^{\zeta} v dz \tag{I.38}$$

Using this definition we proceed to eq.(I.24) to rewrite equation of motion in the transport variables. However simple it may seem the nonlinear terms and frictional terms defined by eq.(I.24) ought to be redefined with the proper approximation. Thus starting from eq.(I.24)

$$\frac{\partial}{\partial x}\int_{-H}^{\zeta} u^2 dz + \frac{\partial}{\partial y}\int_{-H}^{\zeta} uv dz \approx \frac{\partial}{\partial x}\tilde{u}\tilde{u}D + \frac{\partial}{\partial y}\tilde{u}\tilde{v}D = \frac{\partial}{\partial x}(\frac{M_x}{D}M_x) + \frac{\partial}{\partial y}(\frac{M_x}{D}M_y)$$

$$\int_{-H}^{\zeta}(N_h\Delta u)dz \approx DN_h\Delta\tilde{u} \approx N_h\Delta M_x \tag{I.39}$$

With these simplifications the equation of motion (I.24) under the shallow water approximation is written as

$$\rho[\frac{\partial M_x}{\partial t} + \frac{\partial}{\partial x}(\frac{M_x}{D}M_x) + \frac{\partial}{\partial y}(\frac{M_x}{D}M_y) - fM_y]$$

$$= -D\frac{\partial p_a}{\partial x} - gD\rho\frac{\partial \zeta}{\partial x} + \tau_x^s - \tau_x^b + \rho N_h\Delta M_x \tag{I.40}$$

Similarly, the motion along the y coordinate is described by the equation

$$\rho[\frac{\partial M_y}{\partial t} + \frac{\partial}{\partial x}(\frac{M_y}{D}M_x) + \frac{\partial}{\partial y}(\frac{M_y}{D}M_y) + fM_x]$$

$$= -D\frac{\partial p_a}{\partial y} - gD\rho_o\frac{\partial \zeta}{\partial y} + \tau_y^s - \tau_y^b + \rho N_h\Delta M_y \tag{I.41}$$

Notice that in the above equations the density stratification is neglected.
Equation of continuity (I.37) for the transport variables is

$$\frac{\partial M_x}{\partial x} + \frac{\partial M_y}{\partial y} + \frac{\partial \zeta}{\partial t} = 0 \tag{I.42}$$

7. Energy equation

We shall continue by constructing energy equation because it is closely related to the physics of tsunami generation, propagation and dissipation. In order to derive this equation let us multiply (I.35) by $D\tilde{u}$, (I.36) by $D\tilde{v}$, and (I.37) by $\rho g\zeta$. Adding the resulting equation on either side, we arrive at

$$\frac{1}{2}\frac{\partial}{\partial t}\big[\rho D(\tilde{u}^2+\tilde{v}^2) + \rho g\zeta^2\big] + \frac{\partial}{\partial x}\{\rho\tilde{u}D\big[(\tilde{u}^2+\tilde{v}^2)/2 + g\zeta\big]\} + \frac{\partial}{\partial y}\{\rho\tilde{v}D\big[(\tilde{u}^2+\tilde{v}^2)/2 + g\zeta\big]\}$$

$$= (\tau_x^s\tilde{u} + \tau_y^s\tilde{v} - \tau_x^b\tilde{u} - \tau_y^b\tilde{v}) + \rho\tilde{u}DN_h\Delta\tilde{u} + \rho\tilde{v}DN_h\Delta\tilde{v} - \frac{\partial p_a}{\partial x}\tilde{u}D - \frac{\partial p_a}{\partial y}\tilde{v}D \tag{I.43}$$

This equation describes the change of the kinetic and potential energy in time so it expresses the power, i.e., the rate at which work is done in the volume of fluid extended from the bottom to the surface and of unit surface area in the horizontal plane.

The various terms in the above equation can be defined as follows:

1. $e_k = \rho D(\tilde{u}^2 + \tilde{v}^2)/2$ denotes surface density of the **kinetic energy**; it is defined by velocity of the tsunami wave and the total depth.

2. $e_p = \rho g \zeta^2/2$ denotes surface density of the **potential energy**; it is defined by the sea level oscillations around mean sea level (MSL).

3. The second and the third terms in (I.43) represent the components of an **energy flux vector**. This vector characterizes the flux of energy through a unit width surface extended from the ocean surface to the bottom. The components of the vector along latitude and longitude are

$$\mathbf{E_h} = \{\rho \tilde{u} D\big[(\tilde{u}^2 + \tilde{v}^2)/2 + g\zeta\big], \rho \tilde{v} D\big[(\tilde{u}^2 + \tilde{v}^2)/2 + g\zeta\big]\} \tag{I.44}$$

The first order approximation (not valid in very shallow water)

$$\mathbf{E_{h1}} = \{\rho g H \tilde{u}\zeta, \rho g H \tilde{v}\zeta\} \tag{I.45}$$

serves often to describe the energy transfer from the source to various locations.

4. Two terms in the eq. I.43 define the energy sources; the energy input is caused by the wind stress $\tau_x^s \tilde{u} + \tau_y^s \tilde{v}$ and by the surface (atmospheric) pressure $-\frac{\partial p_a}{\partial x}\tilde{u}D - \frac{\partial p_a}{\partial y}\tilde{v}D$. These terms are not related to the tsunami motion, therefore they will be neglected in the tsunami energy considerations.

5. The tsunami **energy dissipation** takes place through the bottom stress: $-\tau_x^b \tilde{u} - \tau_y^b \tilde{v}$ and the horizontal friction $\rho \tilde{u} D N_h \Delta \tilde{u} + \rho \tilde{v} D N_h \Delta \tilde{v}$.

6. For the complete description of the tsunami energy balance the sources of tsunami energy ought to be defined as well. The moving bottom is usual source of such energy. This term will be defined later when the bottom motion will be introduced into equations of motion and continuity.

To make energy estimates we need a system of units to measure forces, work and energy. The force defined by equations of motion for the fluid is the water density multiplied by acceleration. This is due to the fact that we consider the mass of the unit volume. Thus, assuming force as mass times acceleration,

$$F = m\frac{Du}{Dt}; \quad \text{units in CGS are} \qquad 1g \times 1\frac{cm}{s^2} \tag{I.46}$$

This unit is called dyne. Since 1 kg=10^3g and 1m/s^2 =10^2 cm/s^2 the larger unit is introduced called newton. 1 N=1 kg $\times$ 1m/s^2 =10^5 dyne. The unit of work is defined as the work done by a unit force moving a water particle a unit distance. In CGS the unit of work is 1dyne $\times$ cm, which is called erg. It is important to notice since the fluid equation of motion is multiplied by the density to properly define the units of force one needs to multiply $\rho\frac{\partial u}{\partial t}$ by the volume of the fluid. In case of the energy eq. (I.43) the fluid considered is vertically average therefore one needs only to multiply the above expression

by the surface. This is why we called $e_k = \rho D(\tilde{u}^2 + \tilde{v}^2)/2$ as the surface density of the kinetic energy.

Finally, the notion of power is defined as the time rate at which work is done,

$$P = \frac{dW}{dt} = Fu = \frac{m}{2}\frac{du^2}{dt}; \quad \text{units in CGS are} \qquad 1\text{J/s} = 10^7\text{erg/s} = 10^7\text{g} \times \frac{cm^2}{s^3} \quad \text{(I.47)}$$

Since 1N is equal 10^5 dyne, therefore 1J=1N·1m=10^7 erg. From above, the power can be also expressed as force multiplied by velocity or the change of the energy in time. The 1j/s is called watt (W). Often much larger units are needed to estimate power like 1 Terawatt=10^{12} W. To estimate the total available tsunami energy, the kinetic and potential energy of the tsunami needs to be known. The magnitude of the potential energy can be evaluated if the bottom displacement (due to earthquake) is known and an assumption can be made that sea level mirrors the bottom displacement. The potential energy in (I.43) is:

$$\frac{1}{2}\int\int \rho g\zeta^2 dxdy = const \quad \text{(I.48)}$$

This energy is expressed in g $\times \frac{cm^2}{s^2}$, therefore to change it into power the above ought to be divided by the time required to establish the bottom displacement. An estimate of the bottom displacement for the 2004 Indian Ocean Tsunami made by **Kowalik et al., (2005)** sets the potential energy to 5.39×10^3TJ (terra joule). The number seems to be impressive but it is close to the potential energy generated in the Cook Inlet, during one tidal period.

The tsunami energy dissipation takes place through bottom friction.

$$E_{dx} = \rho u\tau_x^b \qquad \text{and} \qquad E_{dy} = \rho v\tau_y^b \quad \text{(II.49)}$$

Here τ_x^b and τ_y^b are components of the bottom stress. The bottom stress depends on the current velocity and is expressed as

$$\tau_x^b = \rho c_d u\sqrt{u^2+v^2} \quad \text{and} \quad \tau_y^b = \rho c_d v\sqrt{u^2+v^2} \quad \text{(I.50)}$$

A dimensionless bottom drag coefficient c_d, equals approximately to 3×10^{-3}. The total dissipated energy

$$E_d = E_{dx} + E_{dy} = \rho c_d u^2\sqrt{u^2+v^2} + \rho c_d v^2\sqrt{u^2+v^2} = \rho c_d(u^2+v^2)^{3/2} \quad \text{(I.51)}$$

is proportional to velocity cubed. This term ought to be integrated over the surface of the entire domain.

8. Vertically integrated equations on the sphere

Whenever an integration domain stretches over 1000 km the use of a spherical system is advisable. For the shallow water equations of motion the assumptions made in the previous section namely the absence of the vertical motion and the hydrostatic and Boussinesq

approximations are valid here as well. The technique used to derive a set of vertically integrated equations in the previous section can be repeated here for the spherical coordinates. Equations of motions (I.13) and (I.14) can be written as

$$\frac{Du}{Dt} - (2\Omega + \frac{u}{R\cos\phi})v\sin\phi = -\frac{1}{\rho R\cos\phi}\frac{\partial p_a}{\partial\lambda} - \frac{g}{R\cos\phi}\frac{\partial\zeta}{\partial\lambda} + A'_\lambda \tag{I.52}$$

$$\frac{Dv}{Dt} + (2\Omega + \frac{u}{R\cos\phi})u\sin\phi = -\frac{1}{\rho R}\frac{\partial p_a}{\partial\phi} - \frac{g}{R}\frac{\partial\zeta}{\partial\phi} + A'_\phi \tag{I.53}$$

Here

$$\frac{D}{Dt} = \frac{\partial}{\partial t} + \frac{u}{R\cos\phi}\frac{\partial}{\partial\lambda} + \frac{v}{R}\frac{\partial}{\partial\phi} \tag{I.54}$$

$$A'_\lambda = A_1 u - \frac{N_h}{R^2\cos^2\phi}(u + 2\frac{\partial}{\partial\lambda}(v\sin\phi)) \tag{I.55}$$

$$A'_\phi = A_1 v + N_h(-\frac{v}{R^2\cos^2\phi} + \frac{2\sin\phi}{R^2\cos^2\phi}\frac{\partial u}{\partial\lambda}) \tag{I.56}$$

where operator A_1 has the following form

$$A_1 = N_h(\frac{1}{R^2\cos^2\phi}\frac{\partial^2}{\partial\lambda^2} + \frac{1}{R^2\cos\phi}\frac{\partial}{\partial\phi}(\cos\phi\frac{\partial}{\partial\phi})) + \frac{\partial}{\partial z}(N_z\frac{\partial}{\partial z}) \tag{I.57}$$

Now, integrating eqs.(I.52) and (I.53) along the vertical direction and taking into account the discussion from the Sec. 6 we arrive at

$$\frac{D\tilde{u}}{Dt} - (2\Omega + \frac{\tilde{u}}{R\cos\phi})\tilde{v}\sin\phi = -\frac{1}{\rho_o R\cos\phi}\frac{\partial p_a}{\partial\lambda} - \frac{g}{R\cos\phi}\frac{\partial\zeta}{\partial\lambda} + \frac{\tau^s_\lambda - \tau^b_\lambda}{\rho D} + A'_1\tilde{u} \tag{I.58}$$

$$\frac{D\tilde{v}}{Dt} + (2\Omega + \frac{\tilde{u}}{R\cos\phi})\tilde{u}\sin\phi = -\frac{1}{\rho_o R}\frac{\partial p_a}{\partial\phi} - \frac{g}{R}\frac{\partial\zeta}{\partial\phi} + \frac{\tau^s_\phi - \tau^b_\phi}{\rho D} + A'_1\tilde{v} \tag{I.59}$$

Here tilde above the variables denotes vertical averaging the way it is defined in formulas (I.31). The horizontal friction term has been simplified in (1.58) and (1.59) so that the operator A'_1 is

$$A'_1 = N_h(\frac{1}{R^2\cos^2\phi}\frac{\partial^2}{\partial\lambda^2} + \frac{1}{R^2\cos\phi}\frac{\partial}{\partial\phi}(\cos\phi\frac{\partial}{\partial\phi})) \tag{I.60}$$

Finally integrating equation of continuity (I.21) along the vertical direction we arrive at equation (which is very similar to eq.(I.37))

$$\frac{\partial\zeta}{\partial t} + \frac{1}{R\cos\phi}\frac{\partial\tilde{u}D}{\partial\lambda} + \frac{1}{R\cos\phi}\frac{\partial}{\partial\phi}(D\tilde{v}\cos\phi) = 0 \tag{I.61}$$

9. Dynamics of the two-layer fluid

Tsunami often is originated by the bottom displacement, therefore along with the free surface changes the variable bottom depth ought to be included into equations of motion and continuity. If tsunami is generated by an underwater landslide then the accounting of an water/landslide interaction may be approached through the different avenues: either the landslide is considered as a bottom motion which is variable in time and space, or the landslide is taken as a second layer of fluid of different density from the water density. We introduce basic equations of motion and continuity to study of a two-layers flow in which both layers interact and establish flow with quite different pattern from the single layer flow.

To understand connection of the internal motion to the surface motion a simple model of two layers shown in the FigI.2 is considered. The following notation has been introduced: ζ_1 and ζ_2 denote wave amplitude at the free surface and at the discontinuity between two layers, ρ_1 and ρ_2 denote density of the upper and lower layer. Vertically integrated motion for the homogeneous ocean was considered in Sec.5. As we intend to write separately equation of motion and continuity for the upper and lower layers, the hydrostatic pressure for both layers will be considered.

The equation of motion along the vertical direction given by (I.22)

$$\frac{\partial p}{\partial z} = -g\rho \tag{I.62}$$

can now be integrated from any depth z to the free surface $z = \zeta_1(x, y, t)$,

$$\int_z^{\zeta_1} dp = -\int_z^{\zeta_1} g\rho dz$$

Noting that the pressure at the free surface $p(\zeta_1)$ is equal to the atmospheric pressure (p_a) and pressure at any depth $p(z)$ is equal p_z, we write the final result as

$$p_z = p_a + \rho g(\zeta_1 - z) \tag{I.63}$$

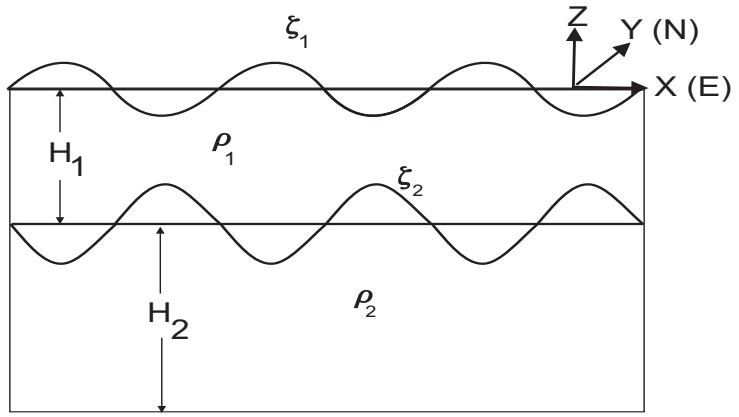

Figure I.2. Waves in two layers of fluid

Now accordingly to the above integral and FigI.2 the pressure in the upper layer is

$$p_1 = p_a + \rho_1 g(\zeta_1 - z) \tag{I.64a}$$

and in the lower layer

$$p_1 = p_a + \rho_1 g(\zeta_1 + H_1 - \zeta_2) + \rho_2 g(\zeta_2 - z) \tag{I.64b}$$

The vertically integrated equation of continuity derived in Sec.6 takes the following form in the upper layer,

$$\frac{\partial(\zeta_1 - \zeta_2)}{\partial t} = -\frac{\partial}{\partial x}(D_1 u_1) - \frac{\partial}{\partial y}(D_1 v_1) \tag{I.65}$$

Here $D_1 = H_1 + \zeta_1 - \zeta_2$ is the total depth for the upper layer. In the lower layer the continuity equation is expressed as,

$$\frac{\partial \zeta_2}{\partial t} = -\frac{\partial}{\partial x}(D_2 u_2) - \frac{\partial}{\partial y}(D_2 v_2) \tag{I.66}$$

Here $D_2 = H_2 + \zeta_2$.

In the upper layer of fluid the equations of momentum can be written in the following way (**Gill, 1982; Proudman, 1953**), along the x direction

$$\frac{\partial u_1}{\partial t} + u_1\frac{\partial u_1}{\partial x} + v_1\frac{\partial u_1}{\partial y} - f v_1 =$$

$$-g\frac{\partial \zeta_1}{\partial x} - \frac{1}{\rho_1}\frac{\partial p_a}{\partial x} + N_h\Big(\frac{\partial^2 u_1}{\partial x^2} + \frac{\partial^2 u_1}{\partial y^2}\Big) + \frac{1}{\rho_1 D_1}[\tau_{s,x} - r_1 u'\sqrt{(u'^2 + v'^2)}] \tag{I.67a}$$

and along the y direction

$$\frac{\partial v_1}{\partial t} + u_1\frac{\partial v_1}{\partial x} + v_1\frac{\partial v_1}{\partial y} + f u_1 =$$

$$-g\frac{\partial \zeta_1}{\partial y} - \frac{1}{\rho_1}\frac{\partial p_a}{\partial y} + N_h\Big(\frac{\partial^2 v_1}{\partial x^2} + \frac{\partial^2 v_1}{\partial y^2}\Big) + \frac{1}{\rho_1 D_1}[\tau_{s,y} - r_1 v'\sqrt{(u'^2 + v'^2)}] \tag{I.67b}$$

Equation of motion in the lower layer along the x direction reads,

$$\frac{\partial u_2}{\partial t} + u_2\frac{\partial u_2}{\partial x} + v_2\frac{\partial u_2}{\partial y} - f v_2 = -\frac{\rho_1}{\rho_2}g\frac{\partial \zeta_1}{\partial x} - \frac{\Delta\rho}{\rho_2}g\frac{\partial \zeta_2}{\partial x}$$

$$-\frac{1}{\rho_2}\frac{\partial p_a}{\partial x} + N_h\Big(\frac{\partial^2 u_2}{\partial x^2} + \frac{\partial^2 u_2}{\partial y^2}\Big) + \frac{1}{\rho_2 D_2}[r_1 u'\sqrt{(u'^2 + v'^2)} - r u_2\sqrt{(u_2^2 + v_2^2)}] \tag{I.68a}$$

and along the y direction,

$$\frac{\partial v_2}{\partial t} + u_2\frac{\partial v_2}{\partial x} + v_2\frac{\partial v_2}{\partial y} + f u_2 = -\frac{\rho_1}{\rho_2}g\frac{\partial \zeta_1}{\partial y} - \frac{\Delta\rho}{\rho_2}g\frac{\partial \zeta_2}{\partial y}$$

$$-\frac{1}{\rho_2}\frac{\partial p_a}{\partial y}+N_h\Big(\frac{\partial^2 v_2}{\partial x^2}+\frac{\partial^2 v_2}{\partial y^2}\Big)+\frac{1}{\rho_2 D_2}[r_1 v'\sqrt{(}u'^2+v'^2)-rv_2\sqrt{(}u_2^2+v_2^2)] \qquad \text{(I.68b)}$$

The following notation is used: u_1 and u_2 velocity in the upper and lower layers, H_1 and H_2 thickness of the upper and lower layers, ζ_1 oscillations of the free surface, ζ_2 oscillations of the internal surface, $\tau_{s,x}$ and $\tau_{s,y}$ are the component of the surface stress, $r_1 u'\sqrt{(}u'^2+v'^2)$ and $r_1 v'\sqrt{(}u'^2+v'^2)$ denote components of **the interface stress**, $ru_2\sqrt{(}u_2^2+v_2^2)$ and $rv_2\sqrt{(}u_2^2+v_2^2)$ denote components of the bottom stress. The f is Coriolis parameter, g is the gravity acceleration, the $\Delta\rho=\rho_2-\rho_1$, $r_1=1.3\times10^{-3}$, $r=3\times10^{-3}$, N_h is the coefficient of the horizontal friction, $u'=u_1-u_2$ and $v'=v_1-v_2$.

In ensuing calculations the sea level terms will be changed in the following way,

$$-\frac{\rho_1}{\rho_2}g\frac{\partial\zeta_1}{\partial x}-\frac{\Delta\rho}{\rho_2}g\frac{\partial\zeta_2}{\partial x}=\frac{\Delta\rho}{\rho_2}g\frac{\partial\zeta_1}{\partial x}-g\frac{\partial\zeta_1}{\partial x}-\frac{\Delta\rho}{\rho_2}g\frac{\partial\zeta_2}{\partial x}=\frac{\Delta\rho}{\rho_2}g\frac{\partial(\zeta_1-\zeta_2)}{\partial x}-g\frac{\partial\zeta_1}{\partial x}$$

and in the similar way the derivatives along the y direction will be transformed.

Tsunami in a single layer fluid: generation due to the bottom displacement

Out of the above set of general equations we single out specific equations of motion and continuity for the tsunami generated by the bottom displacement. For this purpose in FigI.2 we consider only the first layer of fluid. Equation of continuity (I.65) does not change and is rewritten as:

$$\frac{\partial(\zeta_1-\zeta_2)}{\partial t}=\frac{\partial(\zeta-\eta)}{\partial t}=-\frac{\partial}{\partial x}(D_1u_1)-\frac{\partial}{\partial y}(D_1v_1)=-\frac{\partial}{\partial x}(Du)-\frac{\partial}{\partial y}(Dv) \qquad \text{(I.69)}$$

Here $D_1=H_1+\zeta_1-\zeta_2=D=H+\zeta-\eta$ is the total depth which includes both the water and the bottom displacement . Equations of motion in the upper layer of fluid (I.67a and I.67b) now will serve for the entire fluid depth

$$\frac{\partial u}{\partial t}+u\frac{\partial u}{\partial x}+v\frac{\partial u}{\partial y}-fv=$$
$$-g\frac{\partial\zeta}{\partial x}-\frac{1}{\rho D}ru\sqrt{(}u^2+v^2) \qquad \text{(I.70a)}$$

and along the y direction

$$\frac{\partial v}{\partial t}+u\frac{\partial v}{\partial x}+v\frac{\partial v}{\partial y}+fu=$$
$$-g\frac{\partial\zeta}{\partial y}-\frac{1}{\rho D}rv\sqrt{(}u^2+v^2) \qquad \text{(I.70b)}$$

In the above equations of motion for tsunami we have neglected the processes related to the atmospheric pressure, to stresses at the free surface (wind stress) and the dissipation due to the horizontal friction is also neglected. The role of the horizontal friction in the tsunami propagation and dissipation was never researched and remains a moot question. The long tidal waves are always considered with the horizontal friction while the short (wind generated) waves are always studied without horizontal friction.

Tsunami in a two-layer fluid: generation due to the bottom displacement

In this case the motion in the two-layer fluid is going to be generated by the bottom vertical motion. Again referring to FigI.2 we can see that the two-layer needs to be augmented by the moving bottom geometry. The bottom displacement we denote as above by η. Out of the entire set of equations for the two-layer motion (I.65-I.68) only equation of continuity for the second layer (I.66) will be changed to take into consideration the moving bottom

$$\frac{\partial \zeta_2}{\partial t} - \frac{\partial \eta}{\partial t} = -\frac{\partial}{\partial x}(D_2 u_2) - \frac{\partial}{\partial y}(D_2 v_2) \tag{I.71}$$

In (I.71) the definition of the total depth from(I.66) $D_2 = H_2 + \zeta_2$ is changed to $D_2 = H_2 + \zeta_2 - \eta$.

10. The role of the vertical acceleration in the tsunami wave motion

We have introduced the hydrostatic approximation assuming that the vertical motion is small comparing to the horizontal motion. In some regions during tsunami generation, propagation and runup the large vertical acceleration may occur. Such acceleration may be generated by the bottom motion during an earthquake or in the near-shore region where the large amplitude tsunami wave often occur. The strait forward solution to this problem is to apply the full set of equation describing 3-D motion (eqs.I8-I.12). It is useful, to consider the derivation process of such approximation assuming that there is some a priori information related to the scale of phenomena (in our particular case tsunami waves). Thus we wish to answer the basic question: whether tsunami waves (ranging from 5min to 30min periods) can be considered as predominantly horizontal motion which is constant along the vertical direction or the vertical variability needs to be considered as well. Non-dimensional variables and coordinates (x', y', z') are effective tool for comparison of the different terms in the equations of motion and continuity. The new (scaled) variables are defined as follows:

$$(x', y') = (x, y)/L_0 \qquad \text{and} \qquad z' = z/H_0$$

Where; L_0 is typical scale along the horizontal direction (e.g. wavelength) and H_0 defines typical scale along the vertical direction (e.g. depth).

The sea level change resulted from the wave motion is scaled against the wave amplitude ζ_a

$$\zeta' = \zeta/\zeta_a$$

A dimensionless time is defined as

$$t' = t(g/H_0)^{1/2}$$

Non-dimensional components of velocity are:

$$(u', v', w') = (u, v, w)/(gH_0)^{1/2}$$

and are scaled against the phase velocity of the gravity waves in the ocean $(gH_0)^{1/2}$. Pressure is scaled against the dynamical pressure caused by the wave amplitude ζ_a (see eq. I.23)

$$p' = p/(\rho g \zeta_a)$$

Rewriting equations of motion and continuity in the nondimensional variables and coordinates will permit an evaluation of importance of different terms in tsunami waves. The continuity equation (I.12) in the non-dimensional form

$$\frac{(gH_0)^{1/2}}{L_0}(\frac{\partial u'}{\partial x'} + \frac{\partial v'}{\partial y'}) + \frac{(gH_0)^{1/2}}{H_0}(\frac{\partial w'}{\partial z'}) = 0 \tag{I.72}$$

or

$$\frac{1}{L_0}(\frac{\partial u'}{\partial x'} + \frac{\partial v'}{\partial y'}) + \frac{1}{H_0}(\frac{\partial w'}{\partial z'}) = 0 \tag{I.72a}$$

allows to draw conclusion on the relative role of the vertical and horizontal velocities as a function of their scales. If H_0/L_0 is small the horizontal motion will dominate over the vertical motion. This statement for the wave motion means that if the typical wavelength (L_0) is much larger than the typical depth (H_0), the motion is uniform along the vertical direction and the wave propagates along horizontal direction only.

We have introduced previously the hydrostatic approximation based on the assumption of small vertical acceleration as compared to the gravity acceleration g. Considering the free surface motion given by eq.(I.26)

$$w_{z=\zeta} = \frac{\partial \zeta}{\partial t} + u\frac{\partial \zeta}{\partial x} + v\frac{\partial \zeta}{\partial y} \tag{I.73}$$

it can be simplified when ζ_a/L_0 is small, or the wave amplitude is small in comparison to the wavelength

$$w_{z=\zeta} \simeq \frac{\partial \zeta}{\partial t} \tag{I.73a}$$

By time differentiation the acceleration is expressed as

$$\frac{\partial w}{\partial t}_{z=\zeta} = \frac{\partial^2 \zeta}{\partial t^2} \tag{I.74}$$

Assuming that the temporal sea level oscillations can be expressed by a periodical sinusoidal function with an amplitude ζ_0:

$$\zeta(t) = \zeta_0 \sin(\frac{2\pi t}{T_p})$$

From observations the typical tsunami amplitude in the open ocean can be evaluated at $\zeta_0 = 0.1$m, and typical period $T_p = 5$min to 30min. Taking the second derivative from the sea level, the acceleration along the vertical direction reads,

$$\frac{\partial w}{\partial t}_{z=\zeta} = \frac{\partial^2 \zeta}{\partial t^2} = -\frac{4\pi^2 \zeta_0}{T_p^2} \sin(\frac{2\pi t}{T_p}) \tag{I.75}$$

An estimate of the acceleration is an absolute value of $4\pi^2\zeta_0/T_p^2$

$$|\frac{\partial w}{\partial t}| = 7 \times 10^{-5} - 4.2 \times 10^{-4} \mathrm{ms}^{-2}$$

As the gravity acceleration g=9.81 ms^{-2} the acceleration of the surface tsunami wave is indeed very small. Nonetheless eq.(I.75) clearly states that for the shorter period waves the vertical acceleration is increasing.

11. Small amplitude waves

Let's consider a wave motion in a channel along a x and z direction, defined by equations I.8, I.10 and I.12. Neglecting the Coriolis force and the viscous dissipation these equations are:

$$\frac{Du}{Dt} = \frac{\partial u}{\partial t} + u\frac{\partial u}{\partial x} + v\frac{\partial u}{\partial y} + w\frac{\partial u}{\partial z} = -\frac{1}{\rho}\frac{\partial p}{\partial x} \tag{I.76}$$

$$\frac{Dw}{Dt} = \frac{\partial w}{\partial t} + u\frac{\partial w}{\partial x} + v\frac{\partial w}{\partial y} + w\frac{\partial w}{\partial z} = -\frac{1}{\rho}\frac{\partial p}{\partial z} - g \tag{I.77}$$

$$\frac{\partial u}{\partial x} + \frac{\partial v}{\partial y} + \frac{\partial w}{\partial z} = 0 \tag{I.78}$$

Using the non-dimensional variables we can see that the role of the nonlinear terms (related to the horizontal derivative) in the above equation is connected to the dimensionless parameter H_0/L_0. The role of $w\frac{\partial w}{\partial z}$ can be better understood if the vertical velocity is calculated from the sea level. The resulting dimensionless parameter is the ratio of the wave amplitude (ζ_0) and depth H_0. When these parameters are small the nonlinear terms are small as well and linearized equations of motion read,

$$\frac{\partial u}{\partial t} = -\frac{1}{\rho}\frac{\partial p}{\partial x} \tag{I.79}$$

$$\frac{\partial w}{\partial t} = -\frac{1}{\rho}\frac{\partial p}{\partial z} - g \tag{I.80}$$

The boundary conditions for the linearized set of equations are:

at the free surface ($z = 0$) eq. (I.73a) is valid

$$w_{z=0} \simeq \frac{\partial \zeta}{\partial t} \tag{I.81}$$

and the bottom ($z = -H$)

$$w = 0 \tag{I.82}$$

For a progressive wave

$$\zeta = \zeta_0 \cos(\omega t - \kappa x)$$

propagating in the endless channel without any boundaries, the solutions for the velocity and pressure are,

$$u = \zeta_0 \omega \frac{\cosh[\kappa(z+H)]}{\sinh(\kappa H)} \cos(\omega t - \kappa x) \tag{I.83}$$

$$w = -\zeta_0 \omega \frac{\sinh[\kappa(z+H)]}{\sinh(\kappa H)} \sin(\omega t - \kappa x) \tag{I.84}$$

$$p = -\rho g z + \rho g \zeta_0 \frac{\cosh[\kappa(z+H)]}{\cosh(\kappa H)} \cos(\omega t - \kappa x) \tag{I.85}$$

Introducing the above solutions into eq.(I.79) a **dispersion relation** connecting the frequency (ω) and the wave number (κ) follows

$$c^2 = (\omega/\kappa)^2 = \frac{g}{\kappa} \tanh(\kappa H) \tag{I.86}$$

This general dispersive form depends on the relation between the wavelength and the water depth. It is best to consider two cases: very short waves when the wavelength is of the same order as depth and very long waves when the wavelength is much larger than the water depth. For the short waves

$$\tanh(\kappa H) = \frac{\exp(\kappa H) - \exp(-\kappa H)}{\exp(\kappa H) + \exp(-\kappa H)} \simeq 1$$

and

$$c_s^2 = (\frac{\omega}{\kappa})^2 = \frac{g}{\kappa} = \frac{gL}{2\pi} \tag{I.87}$$

from the above the **phase velocity** is defined as

$$c_s = \pm \frac{g}{\omega} \tag{I.87a}$$

For the long waves ($\kappa H << 1$)

$$\tanh(\kappa H) = \frac{\exp(\kappa H) - \exp(-\kappa H)}{\exp(\kappa H) + \exp(-\kappa H)} \simeq \kappa H$$

and

$$c_l^2 = (\omega/\kappa)^2 = gH \tag{I.88}$$

The long and the short waves display a different speed of energy propagation, called **group velocity**:

$$c_g = \frac{d\omega}{d\kappa} \tag{I.89}$$

For the general dispersion form I.86 the group velocity is

$$c_g = \frac{\omega}{2\kappa} \Big[1 + \frac{2\kappa H}{\sinh(2kH)} \Big] \tag{I.90}$$

The short and the long wave cases reduce to simpler forms

$$c_g = \frac{g}{2\omega} \quad \text{for the short waves;} \quad c_g = \sqrt{gH} \quad \text{for the long waves} \tag{I.91}$$

The group velocity for the long waves is equal the phase velocity, therefore these are nondispersive waves. On the other hand the group velocity for the short waves is half of the phase velocity and these are dispersive waves.

The tsunami wave period ranges from 5 min to 30 min. For the given period (T_p) and the water depth (H) the wavelength (L) can be calculated from eq.I.86. For this purpose an iteration method can be used since this dispersive equation is implicit in relation to the wavelength. In below tables the calculations are shown for the shortest period of 5 min and the longest period of 30 min. The wavelength given by the complete formula is compared to the long wave formula. The important parameter showing the influence of the dispersion on the wave propagation is a ratio of the depth to the wavelength.

Table I.1 Wavelength as a function of depth for the 5min wave period.

Depth (meters)→	10m	100m	1000m	5000m	10000m
wavelength (I.86), km	2.971	9.389	29.494	63.962	86.935
wavelength (I.88), km	2.971	9.397	29.715	66.445	93.965
H/L	$3.4\ 10^{-3}$	$1.6\ 10^{-2}$	$3.4\ 10^{-2}$	$7.8\ 10^{-2}$	0.11

Table I.2 Wavelength as a function of depth for the 30min wave period.

Depth (meters)→	10m	100m	1000m	5000m	10000m
wavelength (I.86), km	17.829	56.379	178.254	398.258	562.638
wavelength (I.88), km	17.829	56.380	178.290	398.670	563.805
H/L	$5.6\ 10^{-4}$	$1.8\ 10^{-3}$	$5.6\ 10^{-3}$	$1.3\ 10^{-2}$	$1.8\ 10^{-2}$

From above tables the following can be deduced: 1) For the same period the wavelength calculated from the exact formula (I.86) and the long wave formula (I.88) begin to differer when the water depth increases; 2) The ratio H/L increases when the water depth increases; 3) For the 5 min period the above changes are much stronger than for the 30 min period. In conclusion the dispersive effects over tsunami wave period range are small and they are strongest in the deep water for the short wave periods. While all the above conclusions are true it is important to remember that in the very shallow water the small amplitude approximation cease to hold.

12. A simple approach to dispersion processes: Boussinesq-type equation

Solutions for the particle velocities and pressure (I.83, I.84 and I.85) for the small amplitude long waves take simple form,

$$u = \zeta_0 \sqrt{\frac{g}{H}} \cos(\omega t - \kappa x) \tag{I.92}$$

$$w = -\zeta_0 \sqrt{\frac{g}{H}} \kappa (z + H) \sin(\omega t - \kappa x) \tag{I.93}$$

$$p = -\rho g z + \rho g \zeta_0 \cos(\omega t - \kappa x) \tag{I.94}$$

According to (I.93) the vertical velocity changes linearly from $w_{z=0} = -\zeta_0 \sqrt{gH}\kappa \sin(\omega t - \kappa x)$ to zero at z=-H. Actually the free surface is not located at z=0 but at z=ζ, therefore we can use (I.81) to calculate the vertical velocity at the free surface, as

$$w_s = w_{z=0} \simeq \frac{\partial \zeta}{\partial t} \tag{I.81}$$

If the bottom is flat, the bottom vertical velocity is zero and therefore the vertical velocity at any depth is located by inequality $0 < w(z) < \frac{\partial \zeta}{\partial t}$. On a sloping bottom the vertical velocity is defined by eq. I.27

$$w_b = w_{z=-H} = -u\frac{\partial H}{\partial x} \tag{I.27; I.95}$$

To search solution to eq. (I.80) we assume that the vertical velocity changes linearly along the vertical direction as

$$w(z) = az + b \tag{I.96}$$

Here coefficients a and b are defined from the boundary conditions at the surface (I.81) and at the bottom (I.95) resulting in the following formulae

$$w(z) = \frac{w_s - w_b}{H + \zeta} z + \frac{w_s H + w_b \zeta}{H + \zeta} \tag{I.96a}$$

In addition to the linear approximation it is feasible to assume a parabolic profile for the vertical velocity,

$$w(z) = az^2 + b \tag{I.97}$$

Again applying the boundary conditions at the surface and the bottom we arrive at

$$w(z) = \frac{w_s - w_b}{\zeta^2 - H^2} z^2 + \frac{w_b \zeta^2 - w_s H^2}{\zeta^2 - H^2} \tag{I.97a}$$

Upon time differentiation of I.96a the vertical acceleration reads

$$\frac{\partial w}{\partial t} = \frac{a_s - a_b}{H + \zeta} z + \frac{a_s H + a_b \zeta}{H + \zeta} \tag{I.98}$$

Here a_s and a_b denote the vertical accelerations at the surface and the bottom

$$a_s = \frac{\partial^2 \zeta}{\partial t^2} \qquad \text{and} \qquad a_b = -\frac{\partial u}{\partial t}\frac{\partial H}{\partial x} \tag{I.99}$$

The acceleration expressed by I.98 can be introduced to the eq. (I.80) to obtain the pressure by integrating along the vertical direction from depth z to the free surface at $z = \zeta$

$$p(z) = \rho g(\zeta - z) + \rho \frac{a_s - a_b}{H + \zeta} \frac{(\zeta^2 - z^2)}{2} + \rho \frac{a_s H + a_b \zeta}{H + \zeta}(\zeta - z) \tag{I.100}$$

The new addition to the pressure we shall name as non-hydrostatic or dynamic pressure (p_d). Its value is zero at the free surface and at the bottom ($z = -H$) is

$$p_d \simeq \rho H \frac{(a_s + a_b)}{2} \tag{I.101}$$

In arriving at this formula an assumption is made that $\zeta < H$. Above results are obtained for the linear profile of the vertical velocity suggested by eq.I.96a. Let's investigate consequences of the parabolic profile given by eq.I.97a. Differentiating I.97a in time the vertical acceleration reads,

$$\frac{\partial w}{\partial t} \simeq \frac{a_s - a_b}{\zeta^2 - H^2} z^2 + \frac{a_b \zeta^2 - a_s H^2}{\zeta^2 - H^2} \tag{I.102}$$

This acceleration is again somewhat simplified as we did not differentiate ζ in time which produces smaller terms. The acceleration expressed by I.102 can be again introduced to the eq. (I.80) to obtain the pressure by integrating along the vertical direction from depth z to the free surface at $z = \zeta$

$$p(z) = \rho g(\zeta - z) + \rho \frac{a_s - a_b}{\zeta^2 - H^2} \frac{(\zeta^3 - z^3)}{3} + \rho \frac{a_b \zeta^2 - a_s H^2}{\zeta^2 - H^2} (\zeta - z) \tag{I.103}$$

The non-hydrostatic or dynamic pressure (p_d) for the parabolic profile of the vertical velocity again has zero value at the free surface but at the bottom ($z = -H$) the role of the surface and the bottom acceleration terms is different from the linear profile as now the surface terms is dominating over the bottom term.

$$p_d \simeq \rho H \frac{(2a_s + a_b)}{3} \tag{I.104}$$

The next step is to use the explicit expressions for the pressure in the equations of the horizontal motion so the equations of motions can account for both hydrostatic and non-hydrostatic pressures. To explain the consequences of such approach we take from the linear profile (eq.I.100) only nonhydrostatic pressure due to the surface acceleration. Thus assuming $\zeta < z$ it follows

$$p(z) = \rho g(\zeta - z) + \rho \frac{\partial^2 \zeta}{\partial t^2} (-z - \frac{z^2}{2H}) \tag{I.104}$$

This correction to the pressure term resulted from the vertical velocity taken (to the first order of approximation) as a linear function of the depth. Again considering I.8 and neglecting dissipation, Coriolis and v velocity terms

$$\frac{Du}{Dt} = -g \frac{\partial \zeta}{\partial x} - \frac{\partial^3 \zeta}{\partial t^2 \partial x} (-z - \frac{z^2}{2H}) \tag{I.105}$$

Vertical integration of I.105 results in equation similar to eq.I.35

$$\rho(\frac{\partial \tilde{u}}{\partial t} + \tilde{u} \frac{\partial \tilde{u}}{\partial x}) = -\frac{\partial p_a}{\partial x} - g\rho \frac{\partial \zeta}{\partial x} - \frac{1}{3} H \frac{\partial^3 \zeta}{\partial t^2 \partial x} \tag{I.99}$$

In conclusion the influence of the vertical velocity on the wave propagation is given by an additional pressure term expressed by the sea level changes. The presence of the third derivative is typical for the so-called Boussinesq-type equations (**Fujima et. al., 1985**).

References

Cap F. 2006. *Tsunamis and Hurricanes (A mathematical approach)* , Springer, 197 pp.

Fujima, K., Ch., Goto and Shuto N. 1985. Accuracy of nonlinear dispersive waves equations. *Coastal Engineering in Japan*, 28, 15-30.

Gill, A.L. 1982. *Atmosphere–Ocean Dynamics*. Academic Press, Intl. Geophysical Series, Vol.30, 662 pp.

Hansen, W. 1949. Die halbtägigen Gezeiten im Nordatlantisepen Ozean. *Dtsch. Hydr. Zeit.*, **2**, 44–61.

Hinze, J.O. 1975. *Turbulence*. McGraw–Hill Book Co. 790pp.

Kowalik Z., W. Knight, T. Logan, and P. Whitmore. 2005. Numerical Modeling of the Global Tsunami: Indonesian Tsunami of 26 December 2004. *Science of Tsunami Hazards*, Vol. 23, No. 1, 40- 56.

Launder, B.E and Spalding D.B. 1972. *Mathematical Models of Turbulence.* Academic Press, London, 170 pp.

Murty, T.S. 1984. *Storm Surges – Meteorological Ocean Tides*, Bull. No.212, Dept. Fish. Oceans, Ottawa, 897 pp.

Pedlosky, J. 1982. *Geophysical Fluid Dynamics*. Springer-Verlag, New York. 624 pp.

Proudman, J. 1953. *Dynamical Oceanography*,Methuen, 409 pp.

CHAPTER II

ONE-DIMENSIONAL MOTION

1. Introduction to the long waves propagation

To illustrate processes in the wave propagation the notion of characteristic path of propagation needs to be introduced. A simple propagation of properties through the space in time is expressed by one dimensional advection equation obtained from eq.(I.4)

$$\frac{\partial \Phi}{\partial t} + u\frac{\partial \Phi}{\partial x} = 0 \tag{II.1}$$

Here, the property Φ stands for any scalar such as density, momentum, temperature or salinity and u is advective velocity. If initial distribution of the property Φ is given as $\Phi(x, 0) = \Phi_0$, then the solution to II.1 is,

$$\Phi = \Phi_0(x - ut) \qquad \text{if} \qquad u > 0 \tag{II.2a}$$

and

$$\Phi = \Phi_0(x + ut) \qquad \text{if} \qquad u < 0 \tag{II.2b}$$

The property is transferred along the positive x direction with the speed $u > 0$ and along the negative direction with speed $u < 0$. Along the lines $x - ut$ =const and $x + ut$ =const, called **characteristics**, the properties remain constant in time. To demonstrate the pathline properties let's introduce new independent variables for the propagation towards positive x direction; $\eta = t$ and $\xi = x - ut$. Then dη =dt and dξ= dx -ud$t$, and introducing the differentials into II.1 we arrive at

$$\frac{\partial \Phi}{\partial \eta} = 0 \tag{II.3}$$

This shows that Φ remains constant in time along characteristics pathline. The velocity of the fluid particle which is transferring property Φ is given by

$$u = \frac{dx}{dt} \tag{II.4}$$

Therefore the particle location at any given time is

$$x = x_0 + \int_0^t u dt \tag{II.5}$$

The above two solutions are constructed in separation, let's now consider a general solution as a sum of the two waves

$$\Phi(x,t) = \Phi_1(x-ut) + \Phi_2(x+ut) \tag{II.6}$$

Introducing the initial condition for the property Φ

$$\Phi(x,0) = \Phi_0 = \Phi_1(x) + \Phi_2(x)$$

and assuming that initial velocity $\frac{\partial\Phi(x,0)}{\partial t} = 0$ we arrive at

$$\Phi(x,t) = \frac{\Phi_0(x-ut) + \Phi_0(x+ut)}{2} \tag{II.7}$$

In conclusion, the initial distribution of the amplitude Φ_0 is convected towards the positive and negative directions with the amplitude equal to $\Phi_0/2$. To illustrate the pathlines of property propagation towards positive and negative directions the propagation of an initial signal located along x axis at x_1 at the moment $t = 0$ is shown in Fig.II.1. Velocity u is the slope of the characteristic (**Abbot and Minns, 1998, Durran, 1999**).

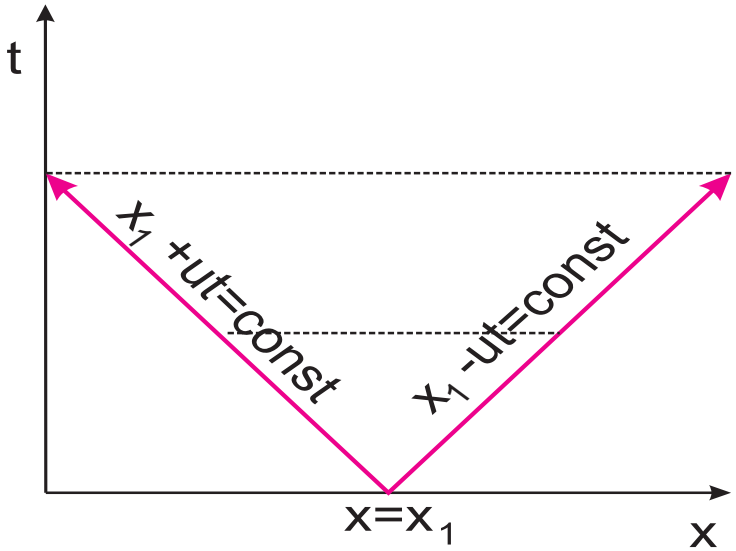

Figure II.1 Signal propagating from the point $\mathbf{x = x_1, t = 0}$ along the characteristics $\mathbf{x_1 - ut}$=const and $\mathbf{x_1 + ut}$ =const.

Let's consider general approach to construction of characteristics. For this purpose along with eq.II.1 the total derivative of u is introduced

$$du = \frac{\partial u}{\partial t}dt + \frac{\partial u}{\partial x}dx \tag{II.8}$$

Equations (II.1) and (II.8) can be written in matrix form

$$\begin{pmatrix} 1 & u \\ dt & dx \end{pmatrix} \begin{pmatrix} \frac{\partial u}{\partial t} \\ \frac{\partial u}{\partial x} \end{pmatrix} = \begin{pmatrix} 0 \\ du \end{pmatrix} \tag{II.9}$$

Setting the determinant of coefficients to zero yields the characteristic equation

$$dx = udt \tag{II.10}$$

2. Free long waves in a channel

In the previous chapter we have formulated the general equations for the wave generation and propagation. These can be solved over world ocean and its local water bodies by application of the numerical solutions. Let's first consider a simplified problem of the free tsunami wave propagation in a simplified geometry. To understand main features important for propagation of a tsunami wave we consider a simplified set of equation of frictionless motion in a narrow channel of the constant depth born by the full equations formulated in Ch.I namely, eq. I.35 and I.37. These are vertically integrated equations to describe the long enough waves when the wavelength is greater then the ocean depth ($L >> H$).

$$\frac{\partial u}{\partial t} = -g\frac{\partial \zeta}{\partial x} \tag{II.11}$$

$$\frac{\partial \zeta}{\partial t} + \frac{\partial uD}{\partial x} = 0 \tag{II.12}$$

Here $D = H$ and H is constant. We have also deleted tilde over velocity u.

Introducing solution in the form $(u, \zeta) = (u_0, \zeta_0)\Phi(x - ct)$ into these equations gives rise to a simple set

$$-cu_0 + g\zeta_0 = 0 \tag{II.13}$$

$$Hu_0 - c\zeta_0 = 0, \tag{II.14}$$

whose solution defines the well known dispersion relation $c = \pm\sqrt{gH}$.

Solutions to eqs.(II.11) and (II.12) can be written now as superposition of two waves traveling into positive and negative directions along the x axis,

$$\zeta = \zeta_0^+\Phi(x - ct) + \zeta_0^-\Phi(x + ct) \tag{II.15}$$

$$u = u_0^+\Phi(x - ct) + u_0^-\Phi(x + ct) \tag{II.16}$$

Through eq.(II.11) and (II.12) the velocity amplitudes are related in the following way to the sea level amplitudes

$$u_0^+ = \sqrt{\frac{g}{H}}\zeta_0^+ \qquad \text{and} \qquad u_0^- = -\sqrt{\frac{g}{H}}\zeta_0^- \tag{II.17}$$

One important observation related to this linear system without external force is that the sea level defines velocity through II.17, and vice versa. The conclusion is that it is sufficient in such system to prescribe only one dependent variable, i.e., velocity or sea level.

Two waves described by II.15 are called **progressive waves** since they propagate in the endless channel without any boundaries. From the point of view of an observer moving with the wave, the phase of the wave remain constant. Consider oscillations described by the first term in (II.15). Introducing the phase velocity as $c = \omega/\kappa$; the constant argument $x - ct$ is expressed as

$$(\omega t - \kappa x) = Const \tag{II.18}$$

In order to keep II.18 as constant while the wave is moving (and assuming that both frequency ω, and wave number κ do not change) we arrive at

$$\frac{\partial}{\partial t} Constant = 0 = \omega - \kappa \frac{\partial x}{\partial t} \tag{II.19}$$

This relations defines the wave propagating towards the positive x direction with the **phase velocity**

$$c = \frac{\partial x}{\partial t} = \frac{\omega}{\kappa} = \sqrt{gH} \tag{II.20}$$

Since $\omega = 2\pi/T_p$ and $\kappa = 2\pi/L$ the phase velocity can be expressed by the **wavelength** L and the wave period T_p,

$$c = \frac{L}{T_p} = \sqrt{gH} \tag{II.21}$$

In Figure II.2 a wavelength is given as a function of depth. It was computed by the II.21 for the typical tsunami range of periods from 5min to 30min. Tsunami displays a relatively long wavelength at the average oceanic depth of 6 km; from 73 km at 5min period, 146 km at 10min period, 291 km at 20min period to 437 km at 30min period. Only at the shallow water, less than 100 m, the wavelength becomes less than 10 km.

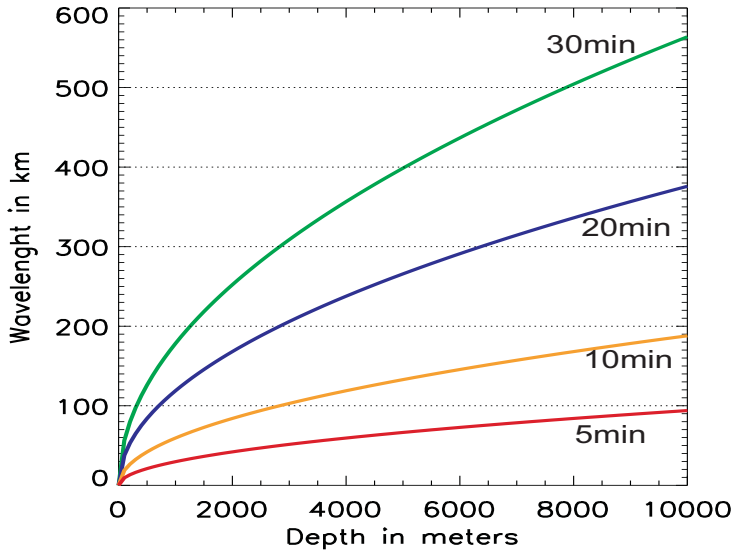

Figure II.2 Wavelength of tsunami waves in the depth varying ocean.

The propagation of these long waves is defined by the characteristics. Therefore we shall write equation to define the characteristic pathlines for two variables ζ and u in one dimensional space x at the given time t. Along with eqs.(II.11) and (II.12), two equations for the total derivatives of u and ζ are constructed

$$du = \frac{\partial u}{\partial t} dt + \frac{\partial u}{\partial x} dx \tag{II.22}$$

$$d\zeta = \frac{\partial \zeta}{\partial t} dt + \frac{\partial \zeta}{\partial x} dx \tag{II.23}$$

Equations (II.11), (II.12) , (II.22) and (II.23) can be written in matrix form

$$\begin{pmatrix} 1 & 0 & 0 & g \\ 0 & H & 1 & dx \\ dt & dx & 0 & 0 \\ 0 & 0 & dt & dx \end{pmatrix} \begin{pmatrix} \frac{\partial u}{\partial t} \\ \frac{\partial u}{\partial x} \\ \frac{\partial \zeta}{\partial t} \\ \frac{\partial \zeta}{\partial x} \end{pmatrix} = \begin{pmatrix} 0 \\ 0 \\ du \\ d\zeta \end{pmatrix} \tag{II.24}$$

Setting the determinant of coefficients to zero yields the characteristic equation

$$dx^2 = gH dt^2 \tag{II.25}$$

Thus the signal propagates along characteristics as in Fig.II.1 but the phase velocity is defined by $c = \pm\sqrt{(gH)}$. As in Fig.II.1 the phase velocity c defines the slope of the characteristic. For the signal propagating towards x positive the slope is c and for the signal propagating towards negative x, the slope is $-c$. General equation for the the sea level propagation (or velocity) can be obtained from eqs.(II.11) and (II.12) by differentiating the first equation in space and the second in time and afterwards eliminating velocity u we arrive at

$$\frac{\partial^2 \zeta}{\partial t^2} - gH \frac{\partial^2 \zeta}{\partial x^2} = 0 \tag{II.26}$$

This partial differential equation(PDE) requires initial and boundary conditions. If the channel along the x direction is infinite the initial conditions can be set as

$$\zeta(x, t = 0) = \phi(x) \qquad \text{and} \qquad \frac{\partial \zeta(x, t = 0)}{\partial t} = \psi(x) \tag{II.27}$$

One solution (when initial velocity is equal to zero) can be set similar to II.6 and II.7 as

$$\zeta(x, t) = \frac{\phi_0(x - ct) + \phi_0(x + ct)}{2} \tag{II.28}$$

3. Application of characteristics for the boundary conditions

Combining eqs.(II.15, II.16) and (II.17) we can express u and ζ by the two disturbances of the sea level $\zeta_0^+ \Phi(x - ct)$ and $\zeta_0^- \Phi(x + ct)$. For clarity we shall rewrite eq.(II.15) as

$$\zeta = \zeta_0^+ \Phi(x - ct) + \zeta_0^- \Phi(x + ct) = \zeta_1(x - ct) + \zeta_2(x + ct) \tag{II.29}$$

and eq.(II.16) reads

$$u = \sqrt{\frac{g}{H}} \zeta_0^+ \Phi(x - ct) - \sqrt{\frac{g}{H}} \zeta_0^- \Phi(x + ct) = \sqrt{\frac{g}{H}} \zeta_1(x - ct) - \sqrt{\frac{g}{H}} \zeta_2(x + ct) \tag{II.30}$$

Using eqs.(II.29) and (II.30) the ζ_1 and ζ_2 are expressed as

$$\zeta_1 = \frac{\zeta + u\sqrt{H/g}}{2} \tag{II.31a}$$

$$\zeta_2 = \frac{\zeta - u\sqrt{H/g}}{2} \tag{II.31b}$$

The ζ_1 is a function of $x - ct$, therefore it must be constant along a characteristic $x - ct$=constant. This pathline describes propagation of a signal which is located at the initial time $t = 0$ at $x = 0$. Therefore, knowing the characteristic pathline allows to predict propagation of a signal in time. Similar approach can taken in the finite difference domain a characteristic located between two spatial grid points at the old time step can be followed to predict the value of ζ_1 at the new time step. The variables ζ_1 and ζ_2 can be also used to construct two new equations based on eqs. (II.11) and (II.12),

$$\frac{\partial \zeta_1}{\partial t} + c\frac{\partial \zeta_1}{\partial x} = 0 \tag{II.32}$$

$$\frac{\partial \zeta_2}{\partial t} - c\frac{\partial \zeta_2}{\partial x} = 0 \tag{II.33}$$

Variables of ζ_1 is preserved along the characteristic which propagates signal towards positive direction and ζ_2 is preserved along characteristics which points to the negative direction. The new variables ζ_1 and ζ_2 are combination of old variables u and ζ, therefore they will better serve to describe propagation which involve both u and ζ. One application is construction of the boundary conditions for the domain of a limited size.

Consider, the wave propagation in a channel with the left end located at $x = 0$ and the right end at the $x = l$. Let's assume that from the left end of this channel enters a wave denoted as ζ_1 and it propagates towards the right end. If we want the right boundary to be transparent to this wave then the condition needs to be established that there will be no reflection from the right boundary. This can be defined as , $\zeta_2(x = l, t) = 0$.

As the characteristic which describes propagation towards negative x is described by eq.(II.33) and ζ_2 is given by (II.31b); it follows that the sea level at the right end of the channel is

$$\zeta_2(t, x = l) = \zeta - u\sqrt{H/g} = 0 \qquad \text{or} \qquad \zeta(x = l, t) = u(x = l, t)\sqrt{H(x = l)/g} \tag{II.34}$$

Similarly, if the left end of channel ought to be transparent for an incoming wave from the right end, eq. (II.31a) will prescribe the sea level under condition that $\zeta_1 = 0$

$$\zeta(x = 0, t) = -u(x = 0, t)\sqrt{H(x = 0)/g} \tag{II.35}$$

Above equations are called the **radiations conditions** and were the first time used for the storm surge computations by **Reid and Bodine (1968)**.

In many applications, while a signal is passed from the one domain (L in Fig.II.3) to the next domain (R in Fig.II.3), the open boundary condition is known either from computations or from measurements. Suppose that in the left hand domain the signal is known and therefore at the boundary the sea level (ζ_b) and the velocity (u_b) are given either from measurements or computations.

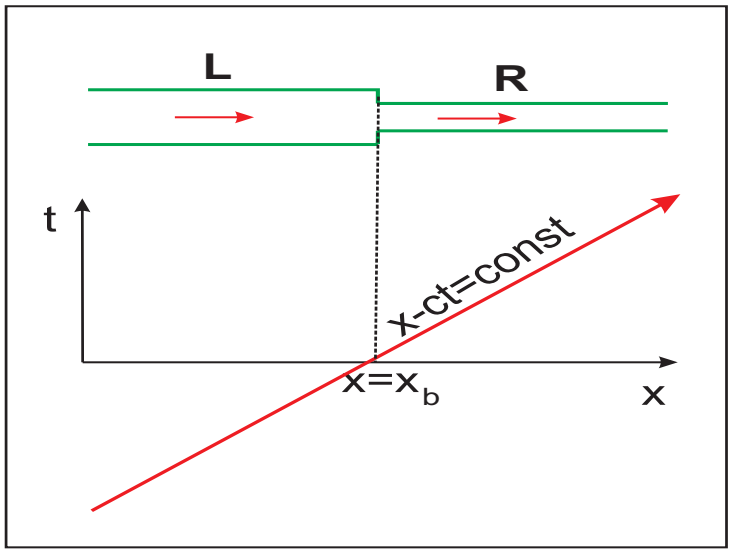

Figure II.3 Signal across the boundary $\mathbf{x = x_b}$ is propagating from the left domain (L) to the right domain (R) along the characteristic preserving function $\zeta_1 = \frac{\zeta + \mathbf{u}\sqrt{\mathbf{H/g}}}{\mathbf{2}}$.

The incoming value of the ζ_1 from L to R is defined as

$$\zeta_1(x = x_b) = \frac{\zeta_b + u_b\sqrt{H/g}}{2} \tag{II.36}$$

and for the smooth propagation into the right domain this value ought to be equal to the invariant specified inside the right (R) computational domain in the close proximity to the boundary

$$\zeta_1(x = x_b + dx) = \frac{\zeta + u\sqrt{H/g}}{2} \tag{II.37}$$

or equating (II.36) and (II.37)

$$\zeta = \zeta_b + (u_b - u)\sqrt{H/g} \tag{II.38}$$

Some understanding of the above condition can be gleaned by recalling the radiation conditions given by eqs. (II.34) and (II.35). Generally eq.(II.38) requires that at the boundary the sea level and velocity in the right domain be equal to the velocity and sea level given at the left domain. One cannot expect this condition to be fulfilled at the initial stage of a computation, since the left domain variables are known and the right domain

distribution will be computed. The two sides of the boundary are especially in disagreement when the computation in the right-hand domain will start from zero velocity and sea level. The second term at the right-hand-side of eq.(II.38) is actually a radiation condition, which radiates difference between prescribed and computed velocity. When adjustment is achieved between two sides of the boundary the difference of velocity will be close to zero. Condition (II.38) is frequently used to establish the open boundary condition for the stationary long wave processes, like tides (**Flather, 1976**). The usefulness of eq.(II.38) for the transient tsunami processes requires further testing.

4. Numerical approximations for the spatial and temporal derivatives.

Consider a simple equation for the wave propagation described by (II.32). The same equation holds for the sea level and velocity as well.

$$\frac{\partial \zeta_1}{\partial t} + c\frac{\partial \zeta_1}{\partial x} = 0 \qquad \text{(II.32; II.39)}$$

To find distribution of ζ_1 in space and time by a numerical solution we change the differential equation into the difference equation. For construction of the space derivatives in the eq.(II.39) the space staggered grid (Fig.II.4) is usually used (Arakawa C grid).

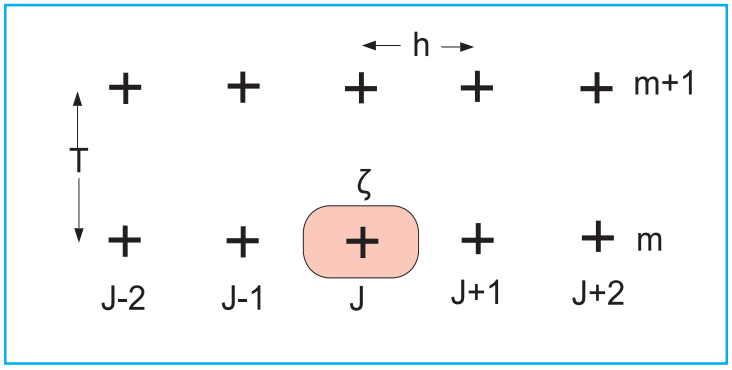

Figure II.4 Space-time grid for the tsunami propagation. j is the space index, h is the space step, m is the time index and T is the time step.

The space step along the x direction is h. Index $j = 1, 2, 3, \ldots$ denotes space stepping and $x = jh$. Index $m = 1, 2, 3, \ldots$ stands for the time stepping. The time step T is connected to the time as $t = mT$. The following notation will be used to express variables in the discrete space-time domain.

$$\zeta_1(x,t) = \zeta_1(jh, mT) = \zeta_{1,j}^m \qquad \text{(II.40)}$$

Discretization of the above equation requires the approximation of the first order partial derivatives $\partial\zeta_1/\partial t$ and $\partial\zeta_1/\partial x$ by their numerical forms. For this purpose we will use Taylor series along the x direction in proximity to the point j in Fig.II.4.

$$\zeta_1(x) = \zeta_1(jh) + (x - jh)(\frac{\partial \zeta_1}{\partial x})_j + \frac{(x-jh)^2}{2!}(\frac{\partial^2 \zeta_1}{\partial x^2})_j + \cdots + \frac{(x-jh)^n}{n!}(\frac{\partial^n \zeta_1}{\partial x^n})_j \qquad \text{(II.41)}$$

The Taylor expansion expresses continuous function ζ_1 by discrete values at point j and derivatives. The x in the Taylor series can be set at any jh. If we consider the closest grid-points to j i.e. $j-1$ and $j+1$ the Taylor series reads,

$$\zeta_1((j-1)h) = \zeta_1(jh) - h(\frac{\partial \zeta_1}{\partial x})_j + \frac{h^2}{2!}(\frac{\partial^2 \zeta_1}{\partial x^2})_j + O \tag{II.41a}$$

$$\zeta_1((j+1)h) = \zeta_1(jh) + h(\frac{\partial \zeta_1}{\partial x})_j + \frac{h^2}{2!}(\frac{\partial^2 \zeta_1}{\partial x^2})_j + O \tag{II.41b}$$

Here O denotes the higher order terms in relation to the space step h. It is possible to write down many numerical forms for the first derivative. From II.41a we define

$$(\frac{\partial \zeta_1}{\partial x})_j = \frac{\zeta_1(jh) - \zeta_1((j-1)h)}{h} - \frac{h}{2!}(\frac{\partial^2 \zeta_1}{\partial x^2})_j + O$$

or

$$(\frac{\partial \zeta_1}{\partial x})_j = \frac{\zeta_1(jh) - \zeta_1((j-1)h)}{h} = \frac{\zeta_{1,j} - \zeta_{1,j-1}}{h} + O(h) \tag{II.42a}$$

The above form is called the backward derivative and $O(h)$ shows that this numerical form is of the first order of approximation.

From eq.(II.41b) the forward derivative is defined as

$$(\frac{\partial \zeta_1}{\partial x})_j = \frac{\zeta_1((j+1)h) - \zeta_1(jh)}{h} = \frac{\zeta_{1,j+1} - \zeta_{1,j}}{h} + O(h) \tag{II.42b}$$

which is also of the first order of approximation. Subtraction of eq.(II.41a) from (II.41b) gives

$$\zeta_1((j+1)h) - \zeta_1((j-1)h) = h(\frac{\partial \zeta_1}{\partial x})_j + \frac{2h^3}{3!}\frac{\partial^3 \zeta_1}{\partial x^3} + O(h^5)$$

From the above the first derivative of the second order of approximation follows as

$$(\frac{\partial \zeta_1}{\partial x})_j = \frac{\zeta_{1,j+1} - \zeta_{1,j-1}}{2h} + O(h^2) \tag{II.42c}$$

This is called the cental derivative. The definition of the first derivative and its approximations are explained in Fig.II.5

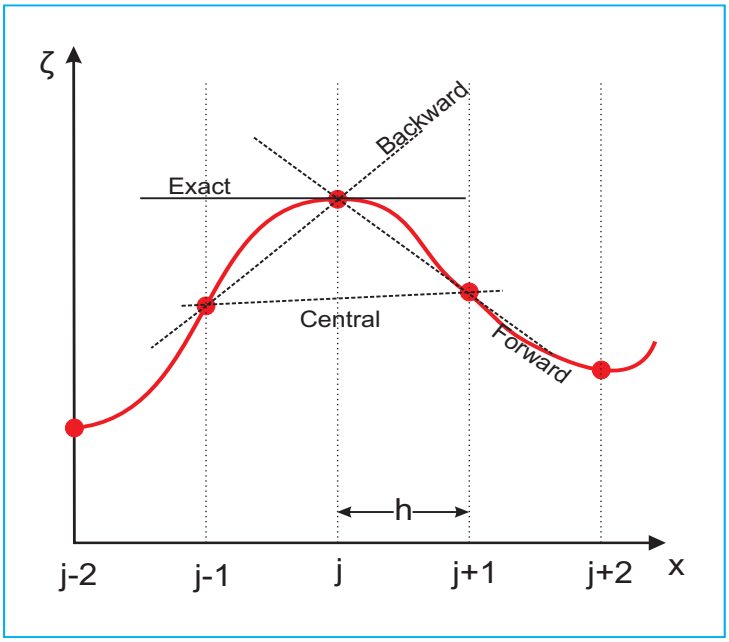

Figure II.5 Definition of the forward, backward and central approximations to the first derivative. j is the space index, h is the space step.

Consider the numerical solution of the eq.(II.40). The following form is suggested for stepping forward in time and backward in space.

$$\frac{\zeta_{1,j}^{m+1} - \zeta_{1,j}^{m}}{T} = -c\frac{\zeta_{1,j}^{m} - \zeta_{1,j-1}^{m}}{h} \tag{II.43}$$

The are quite a few basic questions related to the above numerical formula. We might ask weather this formula going to reproduce physical phenomena in the same way as analytical solution? Or perhaps the finite stepping in time and space is going to distort the physical processes expressed by the original equations? The first problem we are going to tackle is to test whether the numerical solution given by (II.43) is stable in time. Which simply means that solution is either converging in time (stable solution) or is diverging in time (unstable solution). To test stability we shall test how the amplitude of an oscillatory signal is changed by the numerical equations. For this purpose (ζ_1) is presented as the Fourier component:

$$\zeta_1 = \zeta_1^{\star} \exp(i\omega t) \exp(i\kappa x) \tag{II.44}$$

The above expression in discrete form is:

$$\zeta_1 = \zeta_1^{\star} \exp(i\omega T m) \exp(i\kappa j h) \tag{II.45}$$

or

$$\zeta_1 = \zeta_1^{\star} \lambda^m \exp(i\kappa j h) \tag{II.45a}$$

The parameter $\lambda = \exp(i\omega T)$ is called stability parameter or amplification factor. Substituting the above into II.43 an equation for λ is derived. Its behavior as a function of space

and time steps and the physical parameter (c) will determine stability of the numerical equation,

$$\frac{(\lambda^{m+1}-\lambda^m)}{T}\exp(i\kappa jh) = -c\lambda^m\frac{\exp(i\kappa jh)-\exp(i\kappa(j-1)h)}{h}$$

dividing by common terms we arrive at

$$\lambda = 1 - \frac{cT}{h}(1-\exp(-i\kappa h)) \tag{II.46}$$

The condition established by von Neuman requires $|\lambda| \leq 1$ for the stability of a numerical scheme. It is usefully to notice that the stability parameter is a complex number and therefore it can be represented by two real numbers i.e., amplitude and phase. Denoting $a = \cos\kappa h$ and $q = cT/h$, we obtain for the stability parameter

$$|\lambda|^2 = 1 + 2q(q-1)(1-a) \leq 1 \tag{II.47}$$

It follows that $|\lambda| \leq 1$ if

$$\frac{cT}{h} \leq 1 \tag{II.48}$$

Inequality (II.48) is called Courant condition and $q = cT/h$ is called Courant number. The Courant number is the ratio of the two distances: the distance traveled by the long waves during one time step $l_c = cT$ and the grid size h. For stability, the distance l_c must be smaller than grid size h.

The numerical solution given above is dependent on the two dimensionless parameters κh and q. The first parameter involves the wavelength L

$$\kappa h = \frac{2\pi}{L}h$$

and it shows how well is the wavelength resolved by the space step h. Let's consider how the solution will depend on the spatial resolution. To be specific the Courant number is taken as $q = 0.5$. The shortest wavelength in the numerical grid is $2h$, therefore $\kappa h = \pi$, $a = \cos\kappa h = -1$ and $\lambda = 0$. The longer waves will set $\kappa \to 0$ and $|\lambda| \to 1$. We can, therefore, conclude that the long waves (as compared to the space step) for which high resolution is assured are not changed by the numerical solution, but the shorter wave amplitude is diminished ($\lambda < 1$).

The numerical form for the first derivative (eq.II.42) was constructed using the forward, backward and central expression. We have applied for the numerical solution of eq.(II.39) only backward derivative in space. Let's construct solutions using the forward and central derivatives.

$$\frac{\zeta_{1,j}^{m+1}-\zeta_{1,j}^m}{T} = -c\frac{\zeta_{1,j+1}^m-\zeta_{1,j}^m}{h} \tag{II.49}$$

$$\frac{\zeta_{1,j}^{m+1}-\zeta_{1,j}^m}{T} = -c\frac{\zeta_{1,j+1}^m-\zeta_{1,j-1}^m}{2h} \tag{II.50}$$

Searching for stability of eq.(II.49) the λ is defined as

$$|\lambda|^2 = 1 + 2q(1-q)(1-a) \tag{II.51}$$

since $q \leq 1$ and $a \leq 1$ the parameter $|\lambda| > 1$ and consequently the numerical scheme is unstable. For the symmetrical spatial derivative the stability parameter is given by

$$|\lambda|^2 = 1 + (\frac{cT}{h})^2 \sin^2 \kappa h \tag{II.52}$$

and the numerical solution is also unstable.

Changing the partial derivative by the difference is only the first step towards constructing the numerical scheme. From the above results it is obvious that all numerical schemes are approximation to analytical solutions but some of the numerical schemes seem to be failing completely the necessary stability conditions. Why only certain numerical schemes properly emulate the wave propagation can be gleaned from eq.(II.39). This equation describes an initial disturbance propagating in time towards the positive x. The propagation process is expressed by the characteristic $x - ct = const$. Numerical solution given by eq.(II.43)

$$\zeta_{1,j}^{m+1} = \zeta_{1,j}^{m} - \frac{cT}{h}(\zeta_{1,j}^{m} - \zeta_{1,j-1}^{m}) \tag{II.53}$$

ought to describe the similar process. The distance traveled along the characteristic is $dx - cdt = 0$ or setting dt as the time step T, the distance traveled is $dx = cT = l_c$. In the above notations eq.(II.53) reads,

$$\zeta_{1,j}^{m+1} = \zeta_{1,j}^{m} - \frac{l_c}{h}(\zeta_{1,j}^{m} - \zeta_{1,j-1}^{m}) \tag{II.53a}$$

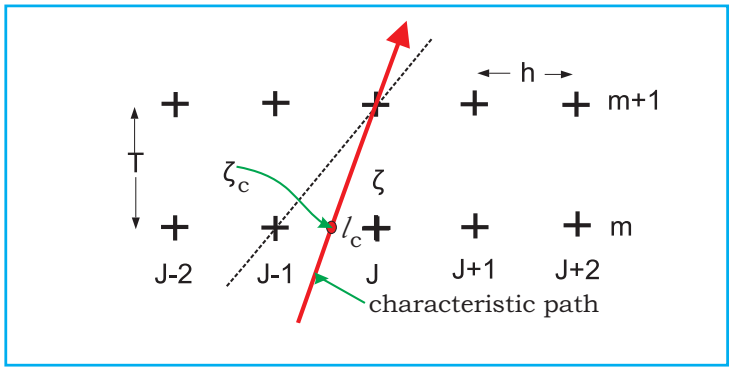

Figure II.6 Characteristic path in the space-time domain. j is the space index, h is the space step, m is the time index and T is the time step.

Fig.II.6 is depicts characteristic which at the time $(m+1)T$ passes through the grid point j. The value of ζ_1 along the characteristic pathline is always constant and equals to ζ_c. If eq.(II.53a) describes the characteristic path for the signal which travels from time

step m to time step $m+1$ and hits the point j at the time $m+1$ then $\zeta_{1,j}^{m+1}$ should be equal ζ_c. To prove this we can notice from Fig.II.6 that

$$\zeta_c = \frac{l_c\zeta_{1,j-1} + (h-l_c)\zeta_{1,j}}{h} = \zeta_{1,j} - \frac{l_c}{h}(\zeta_{1,j} - \zeta_{1,j-1}) \tag{II.54}$$

Therefore, we can conclude that eq.(II.53a) to the first order of approximation describes the signal propagating along the characteristic.

5. The long waves in the channel.

Consider the numerical solution of the equations of motion and continuity (II.11) and (II.12). Solution of this system is searched by the two-time-level numerical schemes (**Kowalik and Murty, 1993, Imamura, 1996**). For construction of the space derivatives a space staggered grid (Fig.II.7) is usually used (Arakawa C grid).

$$\frac{(u_j^{m+1} - u_j^m)}{T} = -g\frac{\zeta_j^m - \zeta_{j-1}^m}{h} \tag{II.55}$$

$$\frac{\zeta_j^{m+1} - \zeta_j^m}{T} = -\frac{(u_{j+1}^{m+1}H_{j+1} - u_j^{m+1}H_j)}{h} \tag{II.56}$$

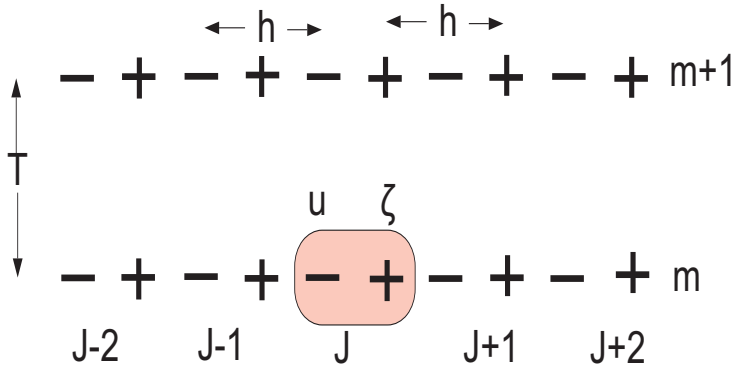

Figure II.7 Staggered numerical grid for calculation of the sea level (ζ) and velocity (u). j is the space index, h is the space step, m is the time index and T is the time step.

The space-staggered grid given in Fig.II.7 is used to construct space derivatives in the above equations. In such grid the variables denoted with the same index j are separated by the distance $h/2$. Variables u located at dashes and ζ located at crosses are positioned in such a way that the second order of approximation in space is achieved. The depth (H) is taken in the sea level points. To test stability we shall test how the amplitude oscillatory signal is changed by numerical equations. For this purpose the sea level (ζ) and velocity u in II.55 and II.56 are presented as the Fourier component:

$$\zeta = \zeta^\star \exp(i\omega t)\exp(i\kappa x) \quad \text{and} \quad u = u^\star \exp(i\omega t)\exp(i\kappa x) \tag{II.57}$$

The above expressions in the discrete form reads:

$$\zeta = \zeta^\star \exp(i\omega T m) \exp(i\kappa j h) \quad \text{and} \quad u = u^\star \exp(i\omega T m) \exp(i\kappa j h) \tag{II.58}$$

or

$$\zeta = \zeta^\star \lambda^m \exp(i\kappa j h) \quad \text{and} \quad u = u^\star \lambda^m \exp(i\kappa j h) \tag{II.58a}$$

Substituting II.58a into II.55 and II.56 a set of equations for λ will be derived.

$$(\lambda - 1)u^\star + g\frac{T}{h}(1 - e^{-\kappa h})\zeta^\star = 0$$

$$H\lambda\frac{T}{h}(e^{\kappa h} - 1)u^\star + (\lambda - 1)\zeta^\star = 0$$

The above system has a nontrivial solution if the coefficient determinant is equal to zero

$$\lambda^2 + (Q - 2)\lambda + 1 = 0 \tag{II.59}$$

Here

$$Q = 4gH(\frac{T}{h}\sin\frac{\kappa h}{2})^2 \tag{II.60}$$

$$\lambda_{1,2} = \frac{2 - Q \pm \sqrt{Q^2 - 4Q}}{2}$$

For stability the absolute value of $|\lambda| \leq 1$. It follows from the above expression that $|\lambda| = 1$ if

$$4gH(\frac{T}{h}\sin\frac{\kappa h}{2})^2 \leq 4 \tag{II.61}$$

Therefore the above expression for λ is

$$\lambda_{1,2} = \frac{2 - Q \pm i\sqrt{4Q - Q^2}}{2} = a + ib$$

Simplifying II.61 we can write

$$\sqrt{gH} \leq \frac{h}{T} \tag{II.62}$$

This is so called Courant-Friedrichs-Levy (CFL) stability condition. As in eq.(II.48) the above inequality can be written as the ratio of the two distances: the distance traveled by the long waves during the one time step $l_c = cT$ and the grid size h.

$$\frac{T\sqrt{gH}}{h} = \frac{l_c}{h} \leq 1 \tag{II.62a}$$

For stability, the distance l_c must be smaller than the grid size h. Unfortunately this condition does not guaranty a proper reproduction of the wave. A signal reproduced by

the eqs. (II.55) and (II.56) will be altered mainly in phase. Since $\lambda = exp(i\omega T) = a + ib$ The phase change (Φ) of the signal over one time step is

$$\tan\Phi = \tan\omega T = \frac{\sqrt{4Q - Q^2}}{(2 - Q)} \tag{II.63}$$

Where: $\omega = 2\pi/T_p$, and T_p denotes the wave period. The nondimensional number L/h defines a spatial resolution and is connected with the wave number $\kappa = 2\pi/L$. For the well resolved processes the wave length is covered by many space steps ($\kappa h \to 0$). In such a case $Q \to 0$, and from eq. (II.63) follows that this numerical scheme will not change phase ($\Phi = 0$) of the signal. Taking into account both the stability and spatial resolution leads to difficult choice: while the shorter time step diminishes parameter Q and makes stability stronger, the smaller space step introduces better spatial resolution but may cause, accordingly to formula (II.62), instability of the numerical scheme. It is important to observe that the errors increase over the longer time of integration and over the longer propagation distance. The choice proposed here is to test both stability and resolution through the application of the proposed numerical schemes to the tsunami wave propagation in a channel. Let us consider a simple problem of a sinusoidal wave propagating over the long distance in the channel of the constant depth. At the left end of the channel a sinusoidal wave is given as

$$\zeta = \zeta_0 \sin(\frac{2\pi t}{T_p}) \tag{II.64}$$

Here the amplitude is ζ_0=100 cm, and the period T_p will be taken from 5 min to 0.5 hour range. The space index runs from $j = js$ at the left–hand boundary (LHB) to the $j = je$ at the right–hand boundary (RHB). As we have seen in Fig.II.7 the one index j is used for the two points. Therefore, if at the LHB the sea level is given, the velocity computation starts at $j = js + 1$, i.e. one grid point away from the left boundary, and proceeds up to the point $j = je$ (the last point is actually computed by the radiation condition). The sea level computation starts at the left boundary ($j = js$) but it runs only to the $j = je - 1$ point. The sea level at the left boundary will be given by eq.(II.64) and velocity at the right boundary is specified by the radiation condition (II.34)

$$u^m_{je} = \zeta^m_{je-1}\sqrt{\frac{g}{H}} \tag{II.65}$$

At the left end of the channel eq(II.64) is applied for one period only; after that, the radiating condition (II.35) is used as

$$\zeta^m_{js} = -u^m_{js+1}\sqrt{\frac{H}{g}} \tag{II.66}$$

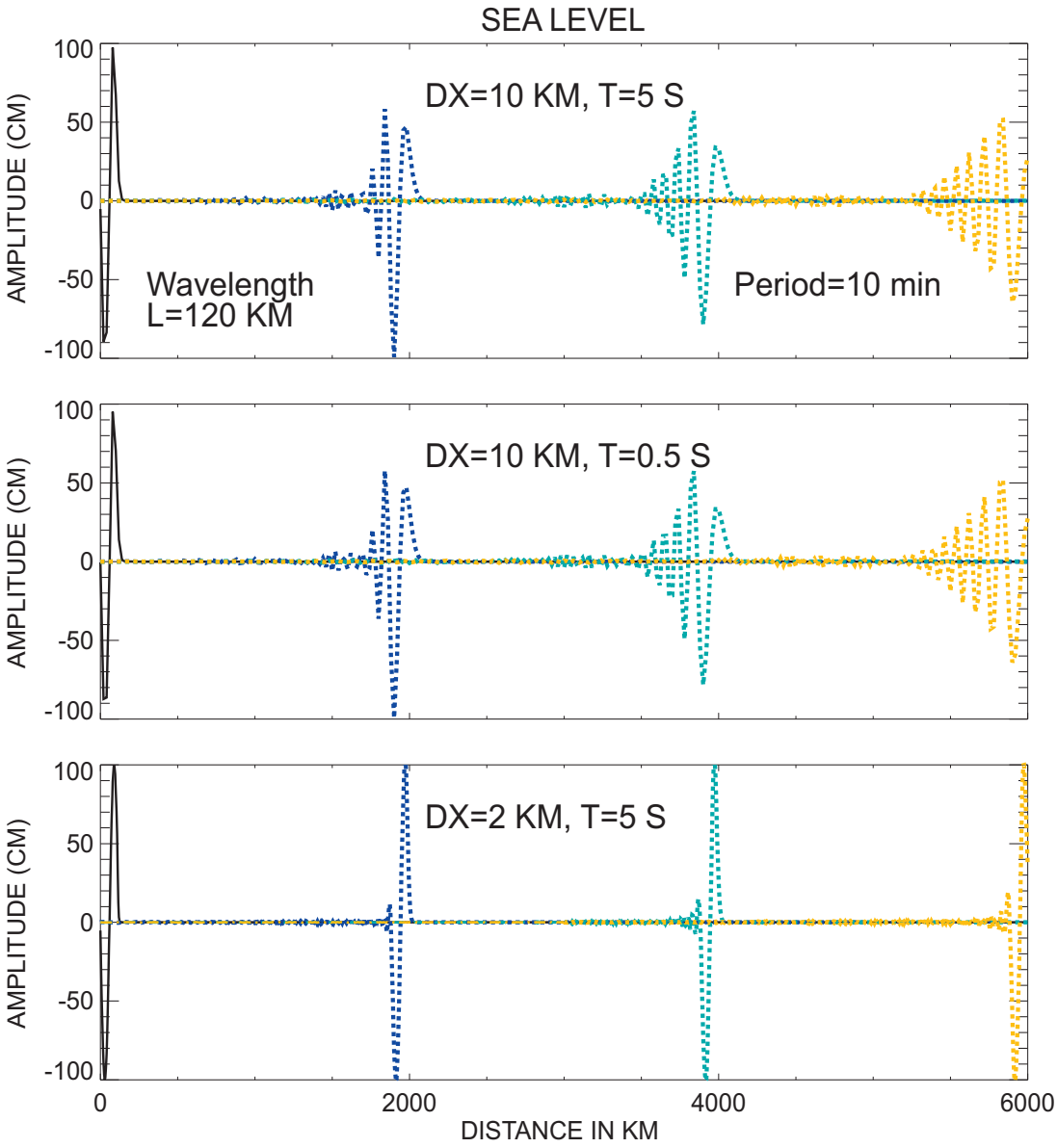

Figure II.8 Propagation of the monochromatic wave of 10 min period along the channel of constant 4077 m depth. DX denotes the spatial step (h) and T is the time step.

The channel is 6000 km long and 4077 m deep. The wave period under consideration is 10 min, which results in a 120-km wavelength. The time step of numerical integration will be taken in experiments equal to 5 s or 0.5 s. The initial space step is chosen equal to 10 km (close to 5′ represented by PDP5 gridded topography). The FORTRAN program for computation **fisher.f90** is given in Appendix to Chapter II. The 10-km space grid sets 12 steps per wavelength (SPW). Such a resolution will slowly introduce numerical errors into reproduced waves. In Fig.II.8 results of computation are given for the space step of 10 km (SPW=12) and the time step 5 s (upper panel), for the space step of 10 km and the time step 0.5 s (middle panel), and for the space step of 2 km (SPW= 60) and the time step 5 s (bottom panel). The wave propagation from the left end has been depicted

at distances of 2000 km, 4000 km, and 6000 km. The relatively poor space resolution in the upper and middle panels results in a diminishing amplitude of the wave along the channel. At approximately 3000 km the amplitude of the first wave became smaller than the amplitude of the second wave. Traveling wave train has a tail of secondary waves following the main wave. The shorter time step does not correct dispersive behavior (see the middle panel), only shorter space step which increases the number of SPW allows nondispersive propagation. It is also important to remember that the dispersive numerical error is cumulative, i.e. for the longer distances it will become large enough to generate dispersive waves again. Therefore, the choice of the SPEW index will depend on the propagation distance as well. Numerical dispersion depends on an error of approximation of the numerical scheme, and it can be defined through the Taylor series (**Kowalik and Murty, 1993**).

6. Higher approximations for the long waves computation.

While computing an open-ocean propagation at the finite resolution the numerical dispersion slowly changes tsunami wave parameters by changing amplitude and generating the short dissipative waves. This is especially important for the long-distance deep-ocean propagation of the short-period waves (5min-15min period). To alleviate these numerical effects we suggest using of the higher order of approximations especially for the spatial derivative. The time step is aimed at resolving the tsunami wave period and the space step at resolving wavelength. The above discussion shows that the encountered problems are related to the space resolution. This is because we are able to control time resolution but the spatial resolution depends on the resolution of the available bathymetric data. We start by constructing the space derivative for the sea level in the equation of motion. The central point (u point) located in the j grid point is surrounded by the two sea level grid points at the distance $h/2$ from the velocity point (see Fig.II.7). Consider Taylor series in these points,

$$\zeta_{j+1/2} = \zeta_j = \zeta_j^u + \frac{\partial \zeta_j^u}{\partial x}\frac{h}{2} + \frac{1}{2}\frac{\partial^2 \zeta_j^u}{\partial x^2}(\frac{h}{2})^2 + \frac{1}{3!}\frac{\partial^3 \zeta_j^u}{\partial x^3}(\frac{h}{2})^3 + \frac{1}{4!}\frac{\partial^2 \zeta_j^u}{\partial x^2}(\frac{h}{2})^4 + O(h^5) \quad \text{(II.67)}$$

$$\zeta_{j-1/2} = \zeta_{j-1} = \zeta_j^u - \frac{\partial \zeta_j^u}{\partial x}\frac{h}{2} + \frac{1}{2}\frac{\partial^2 \zeta_j^u}{\partial x^2}(\frac{h}{2})^2 - \frac{1}{3!}\frac{\partial^3 \zeta_j^u}{\partial x^3}(\frac{h}{2})^3 + \frac{1}{4!}\frac{\partial^2 \zeta_j^u}{\partial x^2}(\frac{h}{2})^4 - O(h^5) \quad \text{(II.68)}$$

The above expressions allows us first to estimate the error of approximations in the spatial derivative eq.(II.55)

$$\frac{\zeta_j^m - \zeta_{j-1}^m}{h} = \frac{\partial \zeta_j^u}{\partial x} + \frac{1}{3!}\frac{\partial^3 \zeta_j^u}{\partial x^3}(\frac{h}{2})^2 + O(h^5) \quad \text{(II.69)}$$

All derivatives are taken at the u point as it is the central point between the two sea level points. The order approximation is second (h^2) and the third derivatives is responsible for this error as well. To understand better the influence of this error on the computational process let's consider the simplest model for the wave propagation given by eq.(II.32)

$$\frac{\partial \zeta}{\partial t} + c\frac{\partial \zeta}{\partial x} = 0 \quad \text{(II.70)}$$

Its numerical solution defined by eq.(II.43) and written in the geometry depicted in Fig.II.7 reads,

$$\frac{\zeta_j^{m+1}-\zeta_j^m}{T}=-c\frac{\zeta_j^m-\zeta_{j-1}^m}{h}=-c\frac{\partial\zeta_j^u}{\partial x}-\frac{c}{3!}\frac{\partial^3\zeta_j^u}{\partial x^3}(\frac{h}{2})^2 \tag{II.71}$$

We can say that instead of the original eq.(II.70) a new equation was generated through the numerical approximation as

$$\frac{\partial\zeta_j^u}{\partial t}+c\frac{\partial\zeta_j^u}{\partial x}+\frac{c}{3!}\frac{\partial^3\zeta_j^u}{\partial x^3}(\frac{h}{2})^2=0 \tag{II.72}$$

While original eq.(II.70) defines the phase velocity $c=\frac{\omega}{\kappa}=\sqrt{gH}$ as independent of the wavelength, eq.(II.72) gives phase velocity as

$$c=\frac{\omega}{\kappa}+\alpha\kappa^2 \tag{II.73}$$

Here $\alpha=\frac{c}{3!}(\frac{h}{2})^2$. These are dispersive waves since the different waves (with different wavelength) propagate with the different phase velocity.

To alleviate such errors we consider the higher order of approximation to the space derivative. For this purpose along with (II.67) and (II.68) the Taylor series at the distance $h3/2$ is introduced

$$\zeta_{j+3/2}=\zeta_{j+1}=\zeta_j^u+\frac{\partial\zeta_j^u}{\partial x}\frac{3h}{2}+\frac{1}{2}\frac{\partial^2\zeta_j^u}{\partial x^2}(\frac{3h}{2})^2+\frac{1}{3!}\frac{\partial^3\zeta_j^u}{\partial x^3}(\frac{3h}{2})^3+\frac{1}{4!}\frac{\partial^2\zeta_j^u}{\partial x^2}(\frac{3h}{2})^4+O(h^5) \tag{II.74}$$

$$\zeta_{j-3/2}=\zeta_{j-2}=\zeta_j^u-\frac{\partial\zeta_j^u}{\partial x}\frac{3h}{2}+\frac{1}{2}\frac{\partial^2\zeta_j^u}{\partial x^2}(\frac{3h}{2})^2-\frac{1}{3!}\frac{\partial^3\zeta_j^u}{\partial x^3}(\frac{3h}{2})^3+\frac{1}{4!}\frac{\partial^2\zeta_j^u}{\partial x^2}(\frac{3h}{2})^4-O(h^5) \tag{II.75}$$

Here ζ_j^u denotes the sea level in the u point. Space derivative for the sea level in (II.55) is obtained by subtracting (II.68) from (II.67). Similar formula follows from (II.74) and (II.75), but with the longer space step of $3h$. The errors (the order of approximation) in both formulas, for the first derivative are proportional to the third derivatives. Thus by combining the two formulas the higher order formula can be constructed. The new formula for the first derivative of the sea level in the u point reads,

$$\frac{\partial\zeta}{\partial x}=[27(\zeta_j-\zeta_{j-1})-(\zeta_{j+1}-\zeta_{j-2})]/24h+O(h^4) \tag{II.76}$$

Space derivative for the velocity in the continuity equation (II.12) can be constructed in the similar way by noticing that the central point for such derivative is the sea level and the space index should be moved to the right so that j ought to be substituted by $j+1$. Thus the derivative for the velocity in the ζ point reads

$$\frac{\partial}{\partial x}(Hu)=\{27[u_{j+1}(H_j+H_{j+1})/2-u_j(H_j+H_{j-1})/2]-$$

$$[u_{j+2}(H_{j+2}+H_{j+1})/2 - u_{j-1}(H_{j-2}+H_{j-1})/2]\}/24h + O(h^4) \qquad \text{(II.77)}$$

The propagation of the monochromatic wave described with the new derivatives is given in Fig.II.9. In this computation program **fisher_high.f90** (see appendix) is used. This is repetition of the Fig. II.8 with the middle panel resulting from application the new formulas. It shows essential improvement when compared against the results obtained with the second order derivatives (upper panel).

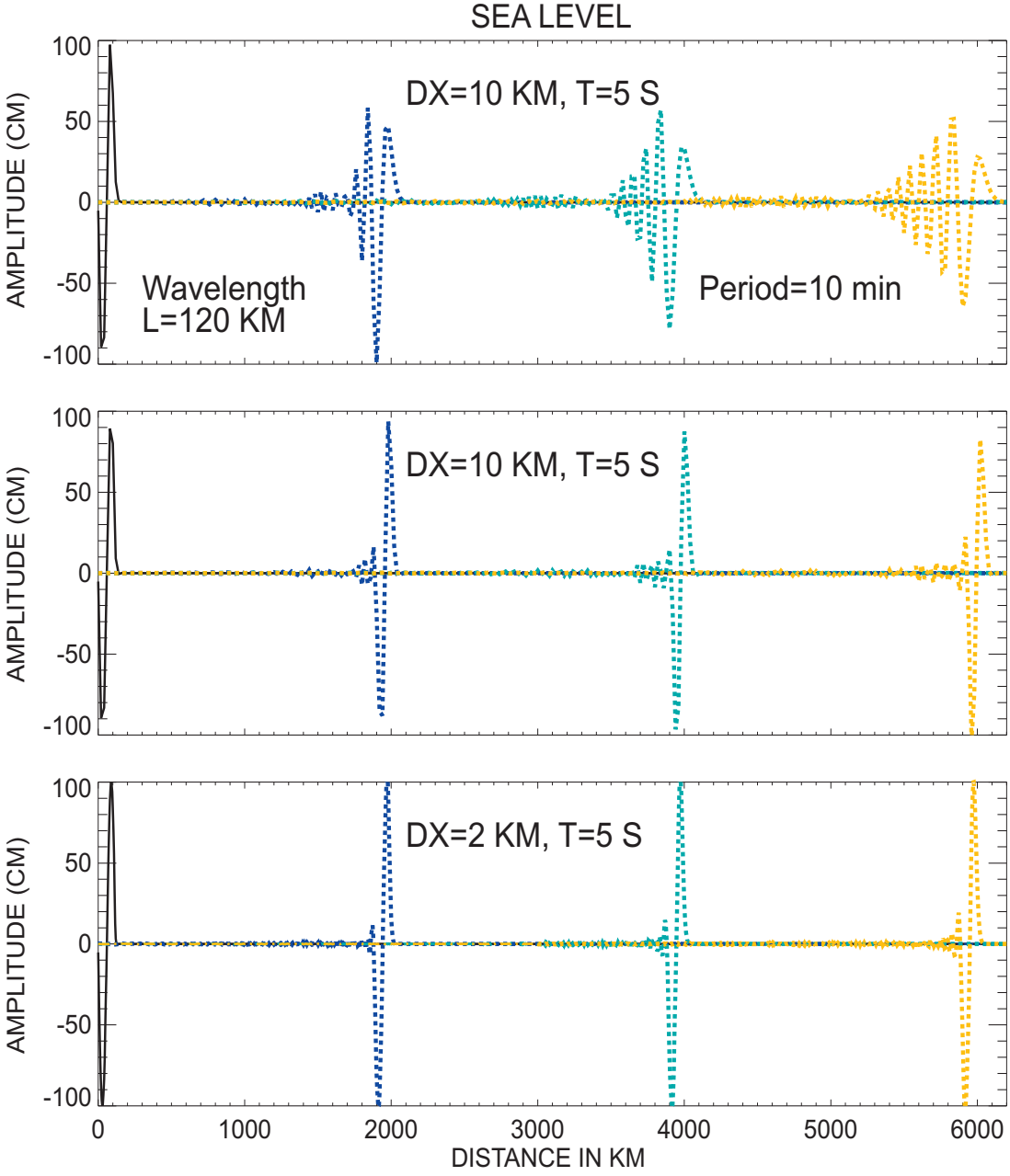

Figure II.9 Propagation of the monochromatic wave of 10 min period along the channel of constant 4077 m depth. DX denotes the spatial step h and T is the time step. Fourth order approximation is applied in the middle panel computation.

7. Own (resonance) oscillations and radiating boundary conditions.

The situation becomes more complicated if channel is closed by one wall or two walls. The waves reflected from the wall start to interact with the progressive waves resulting in the complicated field of standing and progressive waves. The channel closed on both ends is characterized by the **own (natural) oscillations**, often called eigenoscillations. We shall investigate these oscillations in a channel of length l, closed at $x = 0$ and $x = l$. At the both ends, velocity of the water particles is zero,

$$u(x = 0) = 0 \qquad \text{and} \qquad u(x = l) = 0 \tag{II.78}$$

Boundary conditions for the sea level can be formulated through equation of motion as

$$\left.\frac{\partial \zeta}{\partial x}\right|_{x=0} = 0 \qquad \text{and} \qquad \left.\frac{\partial \zeta}{\partial x}\right|_{x=l} = 0 \tag{II.79}$$

Solution to the general equation for the the sea level propagation (eq.II.26)

$$\frac{\partial^2 \zeta}{\partial t^2} - gH\frac{\partial^2 \zeta}{\partial x^2} = 0 \tag{II.80}$$

can be written down as superposition of two waves: running towards positive and negative x directions $\zeta = (A \exp -i\kappa x + B \exp i\kappa x) \exp i(\omega t)$.

This solution with the above boundary conditions define the oscillations in the closed channel. Consider first the sea level, the condition at $x = 0$, sets A=B, thus

$$\zeta = A(\exp -i\kappa x + \exp i\kappa x) \exp i(\omega t) = 2A \cos \kappa x \exp i(\omega t) \tag{II.81a}$$

Boundary condition at $x = l$ requires that

$$\left.\frac{\partial \zeta}{\partial x}\right|_{x=l} = 0 = \sin \kappa l \tag{II.81b}$$

Above is fulfilled if $\kappa l = n\pi$; or introducing period through the dispersion equation II.21 we arrive at the expressions for the own period of oscillations (often called seiche) in the closed (narrow) channel

$$T_{p,n} = \frac{2l}{n\sqrt{gH}} \tag{II.82}$$

Here $n = 1, 2, ...$ are nodes of oscillations. First node (n=1) denotes the longest period oscillations. The seiche is uninodal for $l = \lambda/2$, binodal for $l = \lambda$, trinodal for $l = 3\lambda/2, \ldots$, n-nodal for $l = n\lambda/2$.

For a channel of a length l open at the left end and of the uniform depth H, the boundary condition requires $\zeta(x = 0) = 0$ and the seiche period is given by (**Kowalik and Murty, 1993, p.344**)

$$T_{p,n} = \frac{4l}{n\sqrt{gH}} \tag{II.83}$$

Here $n = 1, 3, 5, \ldots$

One possible way to search for the resonance oscillations is to construct numerical form for the eigenvalues from the equation of motion and continuity neglecting the dissipation and nonlinear terms (see Kowalik and Murty, 1993). A different approach is to apply the oscillatory forcing to our system of equations and to search for resonance response. Oscillatory forcing can be applied to the limited domain at the open boundary, the way external waves enter the local domain. This approach can easily incorporate the friction and nonlinear effects. It also allows us to consider some practical aspects related to the numerical solutions when the periodical forcing occurs. To an open ended channel of 20m depth and 4200 m length (see insert in Fig.II.10) a sinusoidal signal is applied in the continuous way. The solution is searched through the eq.II.55 and II.56 (see program **Resonance.f90** in Appendix). After a signal traveled from the left open end to the right closed end and have been reflected back the energy inside domain grows and the entire computation becomes unstable. This experiment opens important question whether this behavior is due to the sinusoidal signal at the open boundary condition. What will happen when the open boundary will have oscillatory signal, let's say from the tidal observations, will the computation be again unstable? The major problem is that the oscillatory signal at the open boundary includes only the signal propagating into the domain, there is no signal out of the domain. In natural observations these signal are mixed. Therefore, to make computation stable we need to introduce signal propagating out of the domain. The following boundary is used at the left end of the channel:

$$\zeta(j=1) = \zeta_0 \sin(\frac{2\pi t}{T_p}) - u(j=2)\sqrt{H(j=2)/g} \tag{II.84}$$

which is a combination of the sinusoidal signal and the wave radiating to the left towards the open boundary according to eq. (II.35). With this new boundary condition the oscillatory signal of the various periods is applied to find the distribution of the amplitude and velocity in the proximity to the resonance period. According the formula (II.83) the resonance periods for the open-ended channel are: $T_1 \simeq 1200$s=20 min, $T_2 = 400$s=6.6 min, $T_3 = 240$s=4 min. The computed amplitude and the velocity for the longest period of the natural (eigen) oscillations is shown in Fig.II.10. The open boundary sea level amplitude in (II.84) is $\zeta_0 = 100$ cm. The sea level amplitude (upper panel in Fig.II.10) depicts the theoretical distribution with the amplitude close to zero at the open end. The velocity (lower panel in Fig.II.10), on the other hand has the maximum at the open end of the channel. The computed distributions for the second and third modes, again confirm theoretical distributions. In Fig.II.11 we have plotted the amplitude in the proximity of the open end for the periods in the range from 1min to 40 min. The major amplitude minima are at the 4min, 6.6min and 20 min periods. Thus again confirming the theoretical values for the resonance periods. This response function of the sea level amplitude at $j = 3$ grid point for the different periods of the forcing function is given for the ideal case of no bottom friction and the nonlinear terms are neglected as well. The resonance conditions under dissipitation and the nonlinear processes behave differently, therefore they cannot be investigated through the own frequency only, the response functions, similar to the one given in Fig.II.11 are better to describe resonance conditions for the incoming waves into semiclosed domains.

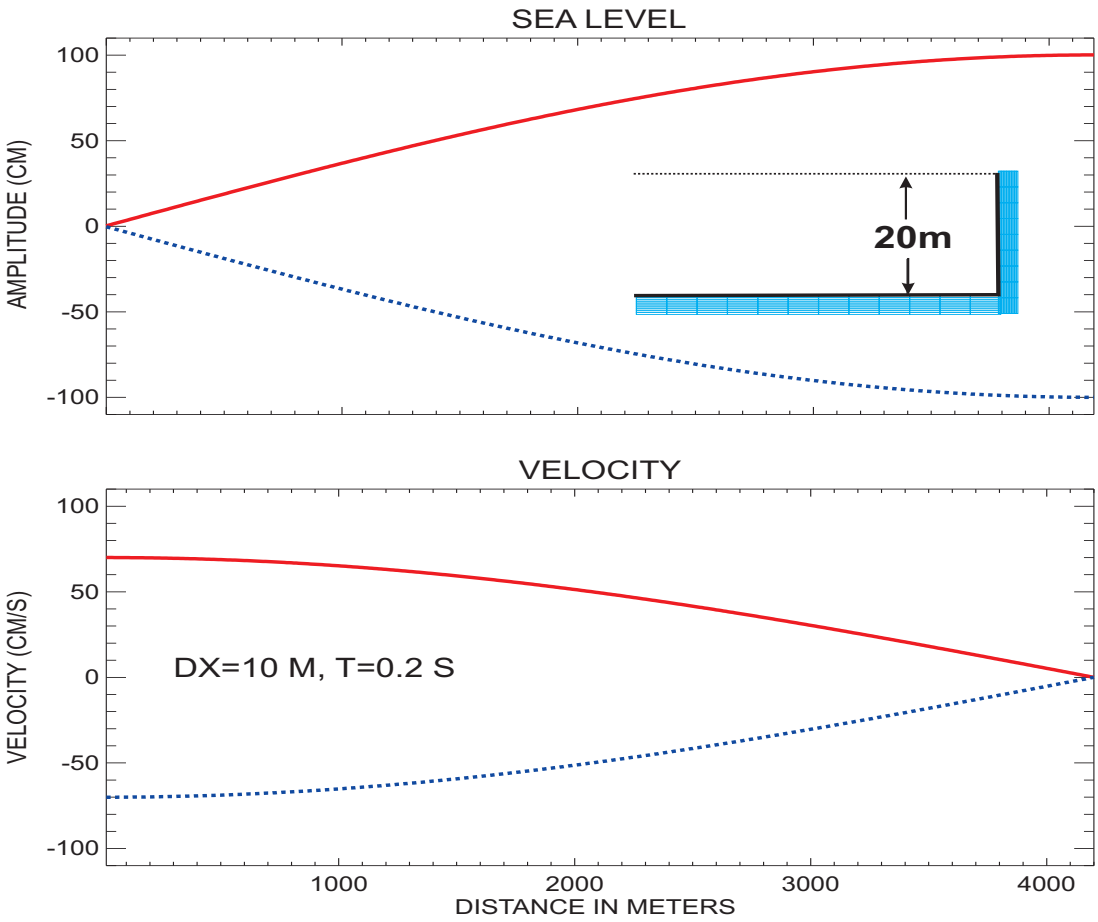

Figure II.10 The sea level amplitude (upper panel) and the velocity amplitude (lower panel) along the channel for the first resonance mode. The channel's geometry is shown in the inset.

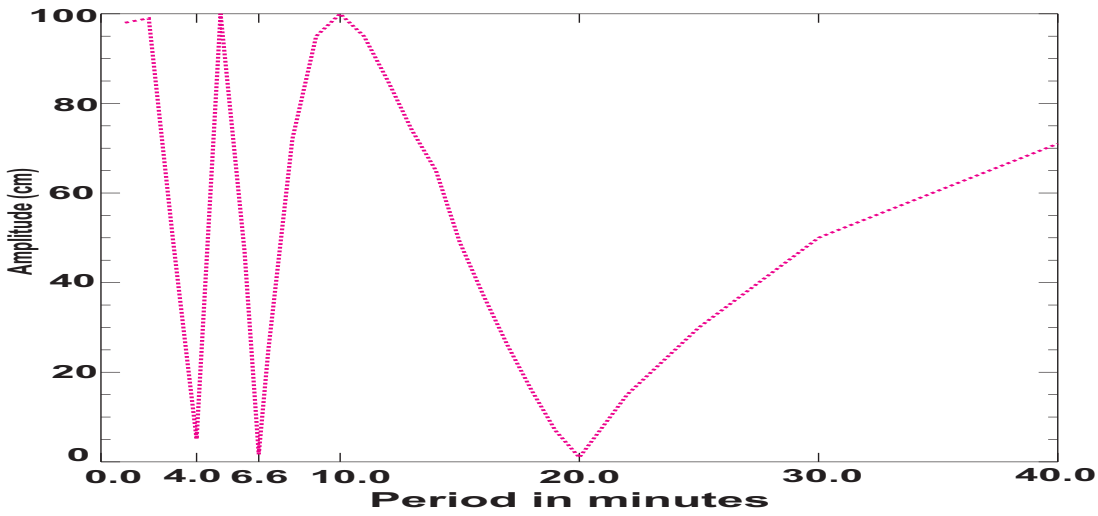

Figure II.11 The sea level amplitude at the open end of the channel as a function of the wave period. The resonance period display the minimum amplitude.

8. The nonlinear advective terms.

In shallow-water areas and in the computation of the horizontal motion, at times the nonlinear advective terms might have to be included. Through dimensional analysis it is possible to show that the nonlinear advective terms become important when the free surface height is of the same order of magnitude as the water depth.

Let us first consider a simple advection equation in the shallow water problem defined by eq. (I.35)

$$\frac{\partial u}{\partial t} + u\frac{\partial u}{\partial x} = 0 \tag{II.85}$$

The general solution can be written as

$$u = f(x - ut) \tag{II.86}$$

where f is an arbitrary function. It will be shown that the finite-difference form of eq.(II.85) will give rise to errors due to the inability of a discrete scheme to resolve wavelengths shorter that $2h$ (or wave number greater than $\kappa_{max} = 2\pi/L = \pi/h$).

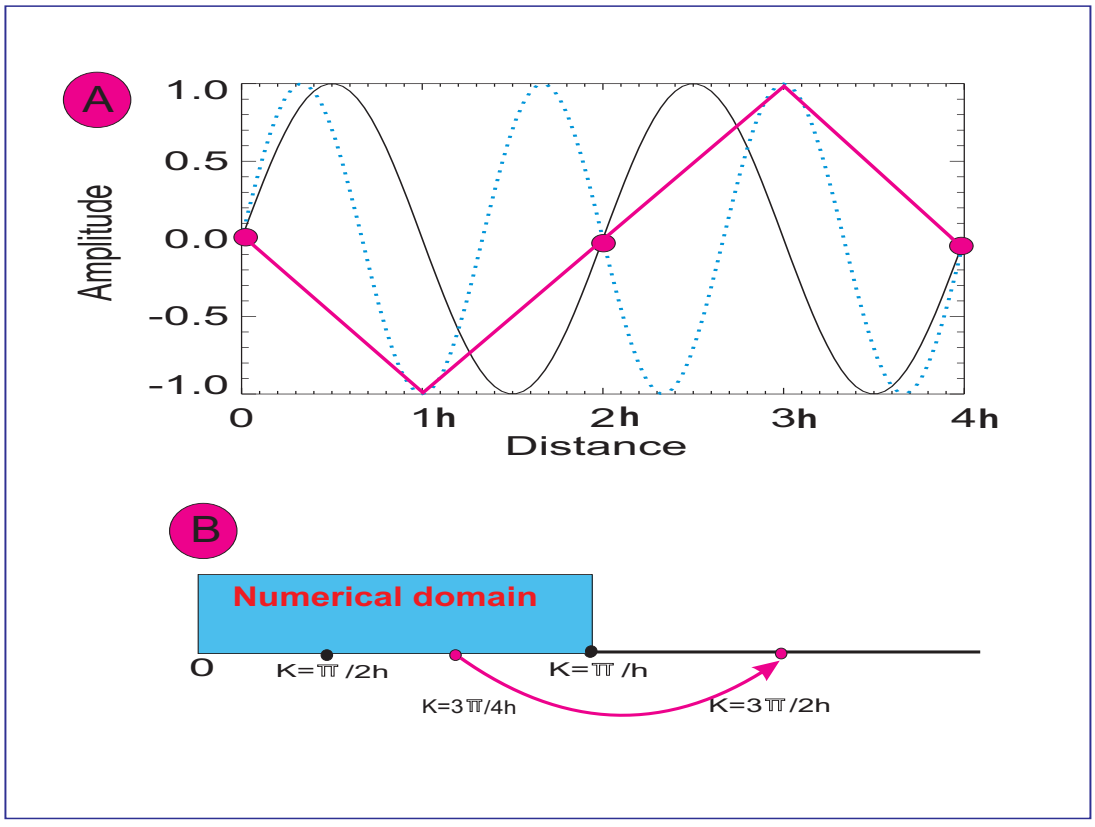

Figure II.12 (A) Blue dotted line represents the wave of length 4h/3 (wave number $3\pi/2h$) misrepresented by the finite-difference grid as a wave of length 4h (red line). The wave of length 2h is given by black line ; (B) misrepresentation of a wave number: $\kappa = 3\pi/4h$ inside computational domain generates $\kappa = 3\pi/2h$ located outside of this domain.

Consider a function $u(x)$ given by

$$u = \sin(\kappa x) \tag{II.87}$$

for $\kappa < \kappa_{max}$. From eq.(II.85)

$$u\frac{\partial u}{\partial x} = \kappa \sin(\kappa x)\cos(\kappa x) = \frac{1}{2}\kappa \sin(2\kappa x) \tag{II.88}$$

For the wave numbers in the range $\pi/2h < \kappa \leq \kappa_{max}$, (wavelength $2h$ to $4h$), the nonlinear term $u(\partial u/\partial x)$ will give rise to a wave number that lies in a range that cannot be resolved by the grid.

With reference to Fig.II.12,upper panel, let wavelength $L = h\,8/3$ interact according to the above equation and the new wave is generated $L = h\,4/3$. The latter is located outside our computational domain, but when plotted in Fig.II.12 as dotted blue line its value at the grid points $(0, h, 2h, 3h$ and $4h)$ generate a new curve given as a red line with the period of $4h$. Thus, all wavelengths that cannot be resolved by the grid will be misrepresented (or aliased) as long wavelengths. The same process is explained in the wave-number representation in Fig.II.12, lower panel. Computational domain extends from the very small wave number to the maximum related to distance $2h$. In the range from $\kappa = 2\pi/2h$ to $\kappa = 2\pi/4h$ the wave number $\kappa = 3\pi/4h$ through the simple nonlinear interaction of the same wavelength generates wave number $\kappa = 3\pi/2h$ located outside of the computational domain.

The above results for the single wave can be generalized to the case when u consists of a number of harmonic components:

$$u = \sum_n u_n \tag{II.89}$$

The term $u(\partial u/\partial x)$ will contain products of harmonics of different wavelengths, such as $\sin(\kappa_1 x)\sin(\kappa_2 x)$. The following trigonometric identity can be easily obtained:

$$\sin(\kappa_1 x)\sin(\kappa_2 x) = \frac{1}{2}[\cos(\kappa_1 - \kappa_2)x - \cos(\kappa_1 + \kappa_2)x] \tag{II.90}$$

Hence, even if initially all wave numbers, κ, are less than or equal to κ_{max}, through nonlinear interaction, wave with $\kappa > \kappa_{max}$ will develop, and aliasing will occur. One can also write

$$\sin(\kappa x) = sin[2\kappa_{max} - (2\kappa_{max} - \kappa)]x \tag{II.91}$$

It can be seen from Fig.II.12 that the wave number κ will be misinterpreted as a wave number $2\kappa_{max} - \kappa$.

Next, visualization of the consequences of aliasing is attempted. To do this, it can be assumed that the dependent variables of concern here are made up of a series of harmonic components. The energy spectrum of these various components determines the relative contributions of different scales to the dependent variable. Aliasing errors will create a spurious inflow of energy at wave numbers that are not much less than κ_{max} and, with the progress of time, the energy of these components grows in a rapid manner. **Phillips (1959)** referred to this as nonlinear instability.

9. Numerical approximations for the nonlinear terms.

Starting from the shallow water equations given in Ch.I (eq. I.35 and I.37), the motion in a channel can be described by

$$\frac{\partial u}{\partial t} + u\frac{\partial u}{\partial x} = -g\frac{\partial \zeta}{\partial x} + \tau_x^s/D\rho - \tau_x^b/D\rho \tag{II.92}$$

$$\frac{\partial}{\partial x}uD + \frac{\partial \zeta}{\partial t} = 0 \tag{II.93}$$

In the above equations the standard notation is used. D is the total depth $D = H + \zeta$. The bottom friction force is nonlinear functions of velocity:

$$\tau_x^b = ru|u| \tag{II.94}$$

The dimensionless bottom friction coefficient r is taken in the range $(2-4)\times 10^{-3}$.

The following numerical scheme is used to march in time:

$$\begin{aligned}\frac{(u_j^{m+1} - u_j^m)}{T} + up\frac{(u_j^m - u_{j-1}^m)}{h} + un\frac{(u_{j+1}^m - u_j^m)}{h} \\ = -g\frac{(\zeta_j^m - \zeta_{j-1}^m)}{h} + \frac{ru_j^m|u_j^m|}{0.5(D_j^m + D_{j-1}^m)}\end{aligned} \tag{II.95}$$

Here: $up = 0.5(u_j^m + |u_j^m|)$, and $un = 0.5(u_j^m - |u_j^m|)$

$$\frac{\zeta_j^{m+1} - \zeta_j^m}{T} = -[(u_{j+1}^{m+1}0.5(D_j^m + D_{j+1}^m) - u_j^{m+1}0.5(D_{j-1}^m + D_j^m)]/h \tag{II.96}$$

As in every numerical approach we aim to construct the stable numerical scheme and of the high order of approximation. Let's analyze the above numerical formulas so the approach taken will be better understood. The nonlinear advective term reads

$$up\frac{(u_j^m - u_{j-1}^m)}{h} + un\frac{(u_{j+1}^m - u_j^m)}{h} =$$

$$0.5(u_j^m + |u_j^m|)\frac{(u_j^m - u_{j-1}^m)}{h} + 0.5(u_j^m - |u_j^m|)\frac{(u_{j+1}^m - u_j^m)}{h} \tag{II.97}$$

This so called upstream derivative.

In the previous section we have seen that analytical solution to the advective equation (II.85) is $u = f(x - ut)$. This signal propagates along the characteristic $x - ut$ if u is positive and along the characteristic $x + ut$ if u is negative. According in the above numerical approach the positive and negative velocity call for different derivatives. As we have seen in eq.(II.54) these derivatives define the slope of characteristics. The signal propagating along the positive characteristic has been depicted in Fig.II.13. On the other hand the velocity up and un is estimated in the grid-point j which is at the distance l_c from the characteristic path (see Fig.II.13).

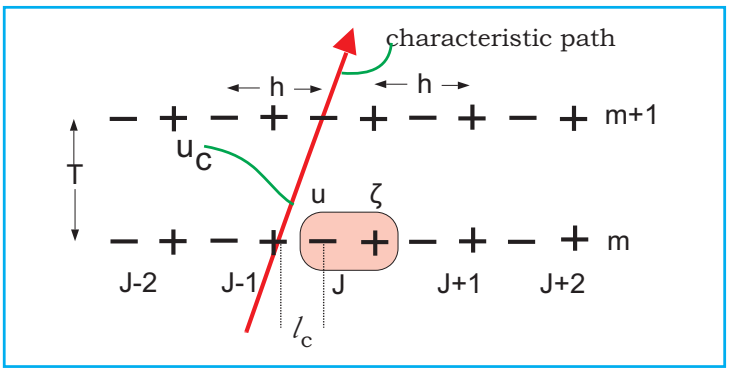

Figure II.13 Staggered numerical grid for calculation of the sea level (ζ) and velocity (u). The characteristic path for the velocity at the j point and the $m+1$ time step is given by the red vector.

To define the velocity along the characteristic path at the time step m we can use a linear approximation between points j and $j-1$

$$u_c^+ = \frac{l_c^+ u_{j-1}^m + (h - l_c^+) u_j^m}{h} = u_j^m - \frac{l_c^+}{h}(u_j^m - u_{j-1}^m) \tag{II.98}$$

In this equation the l_c^+ is the distance related to the positive characteristic as plotted in Fig.II.13. This distance is equal $l_c^+ = 0.5(u_j^m + |u_j^m|)T$. Using u_c^+ instead of up in the advective equation gives the higher order of approximation. On the other hand when the velocity is negative at the grid point j we can repeat the above construction for the negative characteristic and arrive at expression for the negative velocity

$$u_c^- = \frac{l_c^- u_{j+1}^m + (h - l_c^-) u_j^m}{h} = u_j^m + \frac{l_c^-}{h}(u_{j+1}^m - u_j^m) \tag{II.99}$$

To the advective term in eq. (II.95) the upstream method of the first order approximation in space is applied. The upstream approach is used for the stability reason. To deal with stability problems in the higher order of approximation for the first derivatives (see **Kowalik and Bang, 1987, Kowalik and Murty, 1993**) the upstream approach is needed as well. Construction of the first derivative can be carried out on the three-point or four-point stencil. For the three-point stencil the following construction can be used for the advective term,

$$u\frac{\partial u}{\partial x} \simeq up\frac{(3u_j^m - 4u_{j-1}^m + u_{j-2}^m)}{2h} + un\frac{(-u_{j+2}^m + 4u_{j+1}^m - 3u_j^m)}{2h} + O(h^3) \tag{II.100}$$

Somewhat differently the space derivative can be constructed for the equation of continuity (II.12) when the total depth $D = H + \zeta$

$$\frac{\partial \zeta}{\partial t} = -\frac{\partial uD}{\partial x} = -\frac{\partial u\zeta}{\partial x} - \frac{\partial uH}{\partial x} \tag{II.101}$$

The temporal change of the sea level is caused by two terms: the advective transport of the sea level due to velocity and change of the volume transport. The latter term is related to the depth H which is constant in time but the former term variability is related to the sea level itself. The sea level change at the j grid point is caused by the fluxes through the walls depicted at the velocity grid points j and $j+1$ (see Fig.II.14).

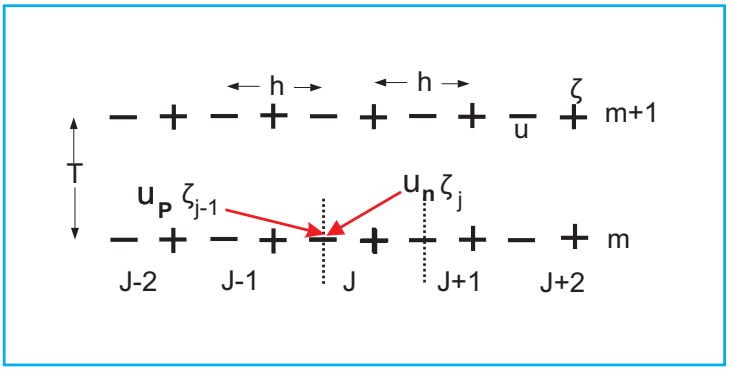

Figure II.14 Staggered numerical grid for calculation of the sea level flux in the cell shown by the vertical walls at the j and $j+1$ velocity grid points.

Let's consider the fluxes through the left-hand wall. The influx into the cell is due to the positive velocity $u_p = 0.5(u_j^{m+1} + |u_j^{m+1}|)$. This velocity is transporting the sea level from the cell $j-1$, therefore the flux is $u_p^{m+1}\zeta_{j-1}^m$. On the other hand, if the velocity is negative $u_n = 0.5(u_j^{m+1} - |u_j^{m+1}|)$, the flux $u_n^{m+1}\zeta_j^m$ is directed out of the domain. The total flux through the left-hand wall is

$$flux_j = u_p^{m+1}\zeta_{j-1}^m + u_n^{m+1}\zeta_j^m + u_{j,k}^{m+1}\frac{(H_{j,k} + H_{j-1,k})}{2} \tag{II.102}$$

The reason for taking the velocity at the $m+1$ time step is related to stability preservation. The explicit velocity results in the unstable scheme. The total flux through the right-hand wall located at the $j+1$ velocity grid-point can be easily obtained by noticing that it is enough to change all the j indeces in the above formula to $j+1$. The finite difference form for the continuity equation takes the following form in the flux notation

$$\zeta_j^{m+1} = \zeta_j^m - \frac{T}{h}(flux_{j+1} - flux_j) \tag{II.103}$$

The improvement of approximation in the above numerical formula can be constructed based on the characteristics related to the equation of continuity. As we have seen the positive velocity at the left wall transports into the cell the sea level located at the $j-1$ grid point. The positive characteristics passing though the j velocity point transports into this point the value of the sea level from the distance $l_c^+ = uT$. Thus instead of ζ_{j-1} we may take for the positive inflowing flux and average value between two grid points $j-1$ and j as

$$\zeta_p = \frac{(l_c^+ + h/2)\zeta_{j-1} + (h/2 - l_c^+)\zeta_j}{h} = (0.5 + u_p^{m+1}\frac{T}{h})\zeta_{j-1}^m + (0.5 - u_p^{m+1}\frac{T}{h})\zeta_j^m \tag{II.104a}$$

For the negative flux the sea level reads,

$$\zeta_n = (0.5 + u_n^{m+1}\frac{T}{h})\zeta_{j-1}^m + (0.5 - u_n^{m+1}\frac{T}{h})\zeta_j^m \tag{II.104b}$$

Rewriting the above formulas as

$$\zeta_p = \zeta_{j-1}^m + 0.5(1 - 2u_p^{m+1}\frac{T}{h})(\zeta_j^m - \zeta_{j-1}^m) \tag{II.105a}$$

$$\zeta_n = \zeta_j^m - 0.5(1 + 2u_n^{m+1}\frac{T}{h})(\zeta_j^m - \zeta_{j-1}^m) \tag{II.105b}$$

the relation to the simple formulas given by eq.(II.102) can be seen. The higher order of approximation is achieved by the additional differences, which accounts for the slope of the sea level. It is interesting to find the condition when the new and the old expressions are identical. For the positive velocity from eq.(II.105a)

$$\zeta_p = \zeta_{j-1}^m \qquad \text{if} \qquad u_p^{m+1}T = \frac{h}{2} \tag{II.106}$$

Thus when signal travels during one time step the distance of half of the grid step (i.e. from the $j-1$ grid point for the sea level to the j grid point for the velocity) the old and the new approximations are expressed by the same formulas.

10. A simple resource – an old analytical solution.

We shall proceed to investigate the long waves like tsunami, tides or surges traveling across the shelf. To delineate the influence of friction and nonlinear terms on the process of propagation and dissipation the up-sloping channel is considered.

An analytical solution for the wave traveling upsloping channel was developed long time ago (see **H. Lamb, Hydrodynamics, p.276**). In our experiment depth is changing linearly from 5m to 50m over the distance of 100km. Expressing depth and distance in cm the analytical expression for this change is $H = 500. + 4.5 \times 10^{-4}x = a + bx$. Taking for simplicity a rectangular system of coordinate with x axis directed along the channel the linear equations of motion and continuity (eqs.II.11, II.12) for the frictionless fluid can be written as

$$\frac{\partial u}{\partial t} = -g\frac{\partial \zeta}{\partial x} \tag{II.107}$$

$$\frac{\partial \zeta}{\partial t} + \frac{\partial uH}{\partial x} = 0 \tag{II.108}$$

By eliminating the velocity we arrive at one equation for the sea level change

$$\frac{\partial^2 \zeta}{\partial t^2} - g\frac{\partial}{\partial x}H\frac{\partial \zeta}{\partial x} = 0 \tag{II.109}$$

Searching solution in time as $\zeta \sim \cos(\omega t)$ from the above we derive

$$-\omega^2\zeta - g\frac{\partial}{\partial x}H\frac{\partial \zeta}{\partial x} = 0 \tag{II.110}$$

Now to rewrite this equation in the form fitting for application of the Bessel function we introduce a new variable x_1 where $x_1 = a+bx$. The derivative in eq.(II.109) is reformulated as $bdx = dx_1$ and eq.(II.110) is rewritten as

$$-\omega^2\zeta - gb^2\frac{\partial}{\partial x_1}x_1\frac{\partial\zeta}{\partial x_1} = 0 \qquad \text{(II.111)}$$

or

$$\frac{\partial}{\partial x_1}x_1\frac{\partial\zeta}{\partial x_1} + \frac{\omega^2}{gb^2}\zeta = 0 \qquad \text{(II.112)}$$

Solution to this equation is determined as

$$\zeta = AJ_o(2\sqrt{\kappa}\sqrt{x_1}) \qquad \text{(II.113)}$$

Here: $\omega^2/gb^2 = \kappa$ and A is an amplitude. For the wave of the 5 min period and 100 cm amplitude which enters channel at the 50 m depth the analytical solution in the channel is plotted in the lower panel of Fig.II.15. A numerical solution (eqs.II.95 and II.96 with nonlinear and friction terms neglected) obtained with time step 0.1s and space step 25 m is given in the upper panel. In the numerical solution the wave is generated at the open boundary for the time span of one period and afterwards it propagates into channel while at the boundary a radiation boundary condition is established.

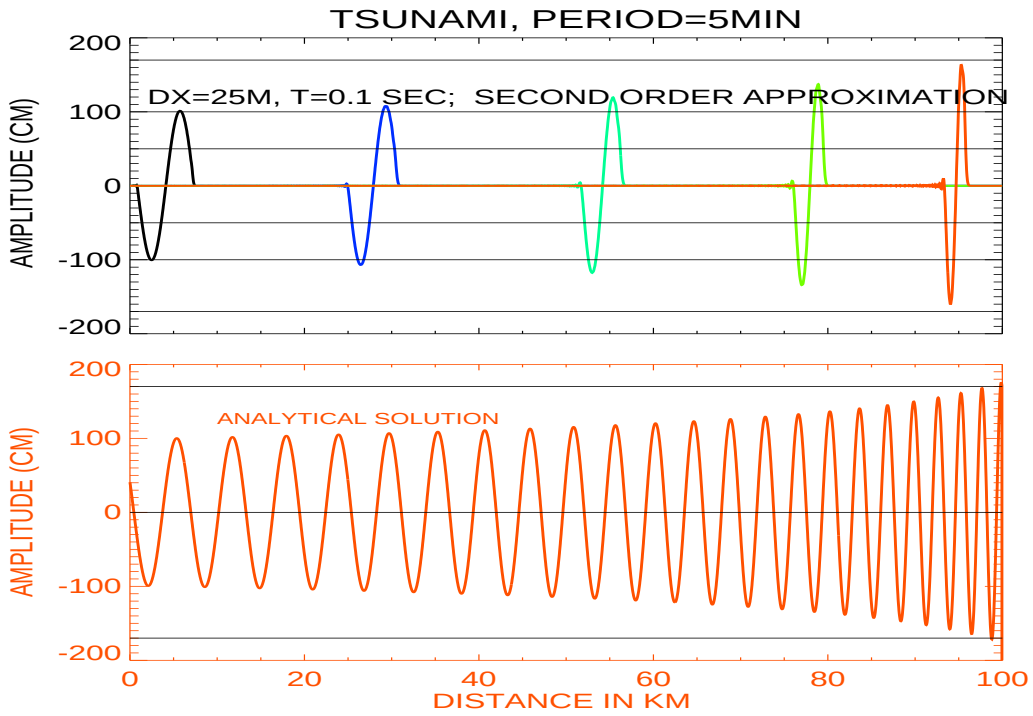

Figure II.15
Numerical (upper panel) and analytical (lower panel) solutions for the wave traveling up the sloping channel.

The figure shows how accordingly to eq.(II.113) in the periodic wave traveling up the channel the amplitude continuously increases and the wave-length diminishes.

The comparison between numerical and analytical solution made after wave traveled 94km (Fig.II.16) shows that numerical solution simulates well both the amplitude and the period of the wave. The figure also depicts a small distortion in the wave front of the regular sinusoidal shape produced by the numerical solution. A small tail of a short period dispersive numerical waves has been also generated. These distortion can be alleviated by using a finer spatial grid step, e.g. 5m.

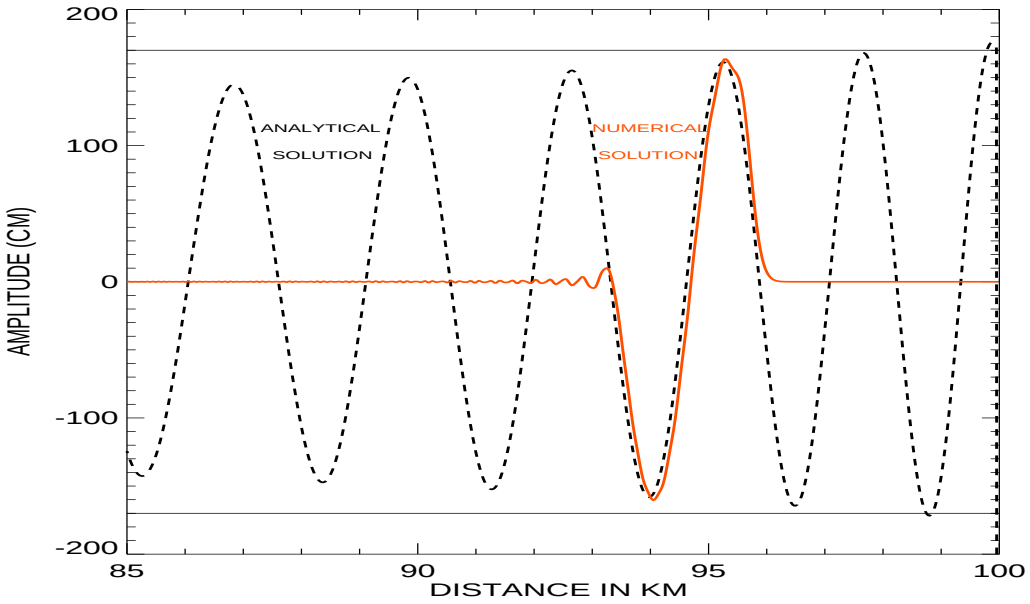

Figure II.16
Comparison of the analytical and numerical solutions after wave traveled 94km up the channel.

11. The role of various terms nonlinear terms and their numerical approximations.

To the above problem we add first the bottom friction term. The result of computation is given in Fig.II.17 (upper panel) and compared to the numerical computation of the frictionless propagation (lower panel); already depicted in Fig.II.16. The results from these two panels are compared again in Fig.II.18. Here the two waves are shown after they traveled about 95 km in the channel. The friction damps amplitude, it generates a slight distortion but it does not generate the new short dispersive waves. The amplitude distortion is probably related to the nonlinearity of the bottom friction term.

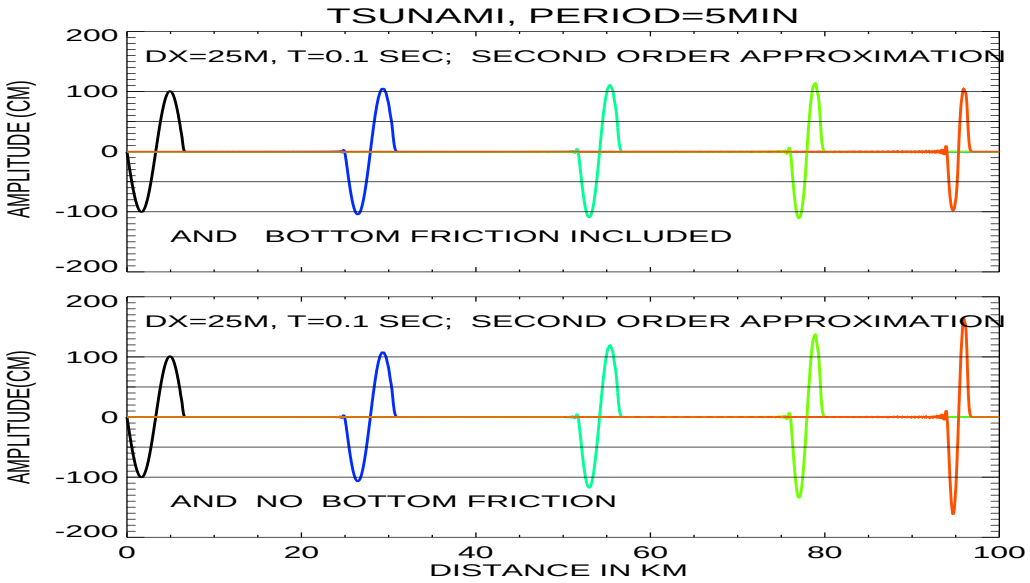

Figure II.17
Wave travels up the sloping channel.
Bottom friction included (upper panel), no bottom friction (lower panel).

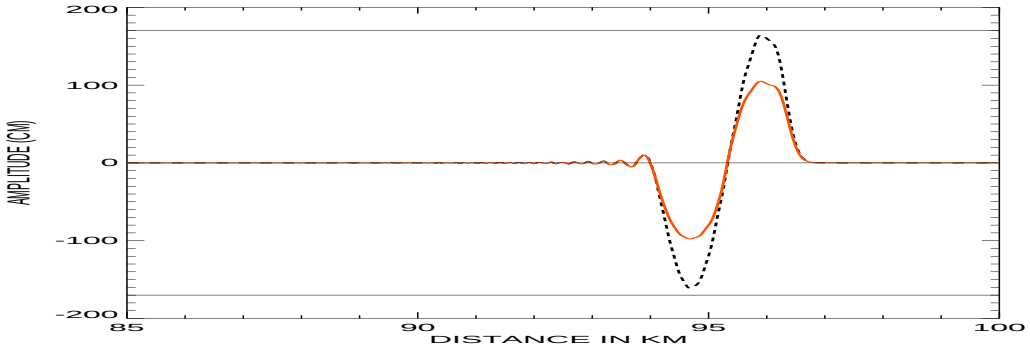

Figure II.18
Comparison of the numerical solutions for friction (red line) and frictionless (dotted line) cases after wave traveled 94 km up the channel.

Further complication to the propagation in the channel is added by including the nonlinear (advective) term into the equation of motion while keeping the continuity equation in the linear form (D=H). The overall change to the wave amplitude and period is depicted in FigII.19.

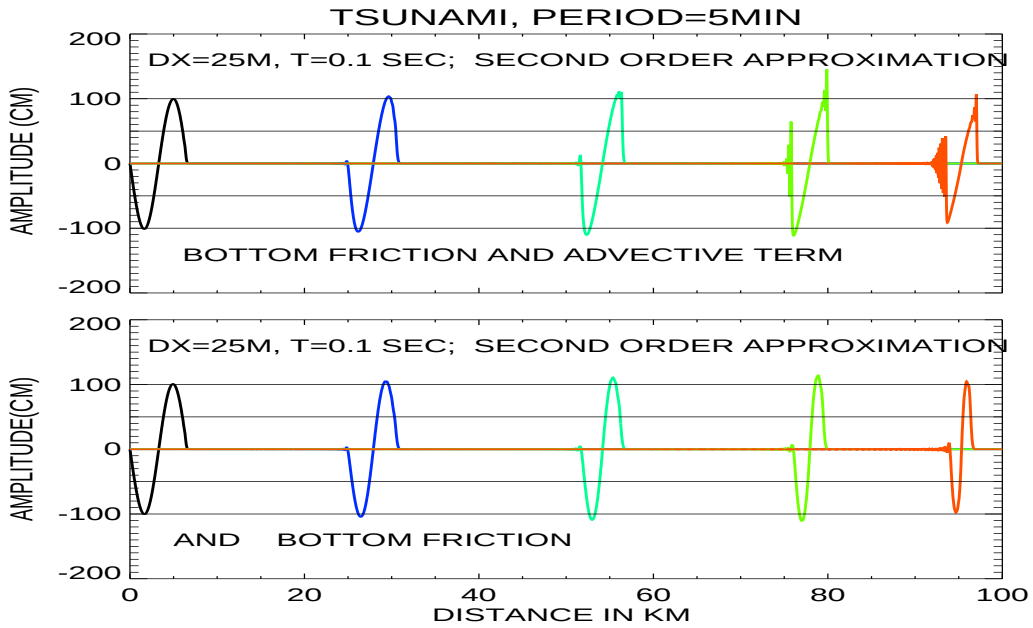

Figure II.19

Wave travels up the sloping channel. Bottom friction and advective term (upper panel), and bottom friction (lower panel).

The lower panel contains the previous result (friction only) and the upper panel contains results for both friction and nonlinear advective terms. The numerical solution for the advective term is based on formulas (II.97). The addition of nonlinearity diminishes the wave amplitude, generates the short wave and changes the wave shape to the triangular.

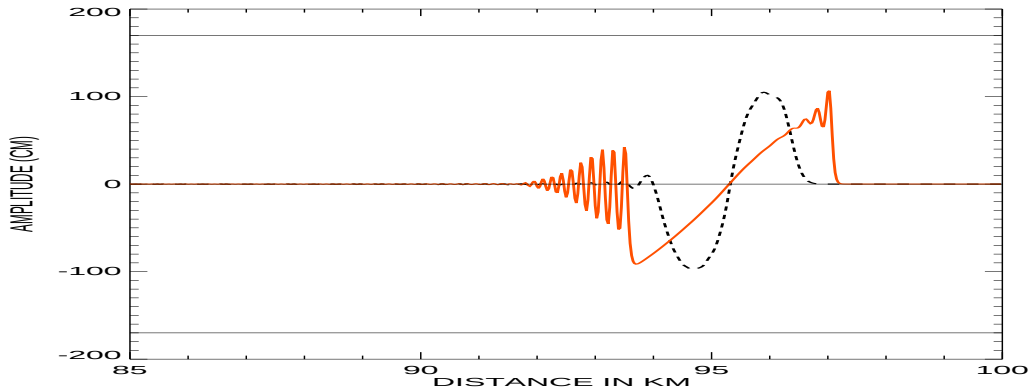

Figure II.20

Comparison of the numerical solutions after wave traveled 94 km up the channel. Dashed line -friction only; continuous line friction and advection.

The process of the short wave generation recollect the soliton fission observed in the laboratory experiments. It is well described in FigII.20.

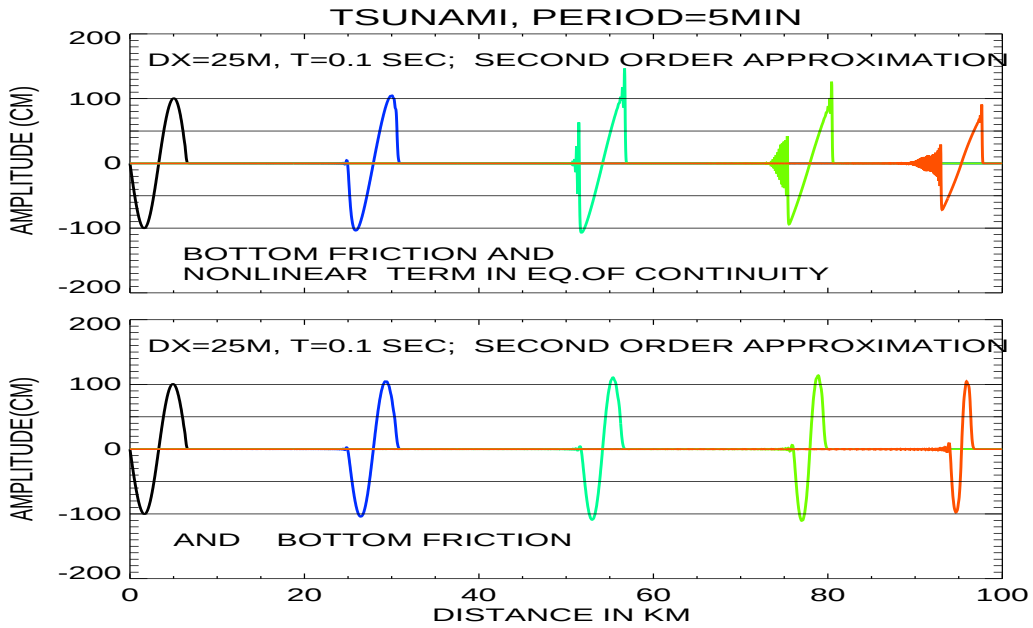

Figure II.21
Wave travels up the sloping channel. Bottom friction in eq. of motion and nonlinearity in eq. of continuity (upper panel), and bottom friction (lower panel).

In the next numerical experiment we study the nonlinearity related only to continuity equation but in the equation of motion advective term is set to zero. Results are given in Figs II.21 and II.22.

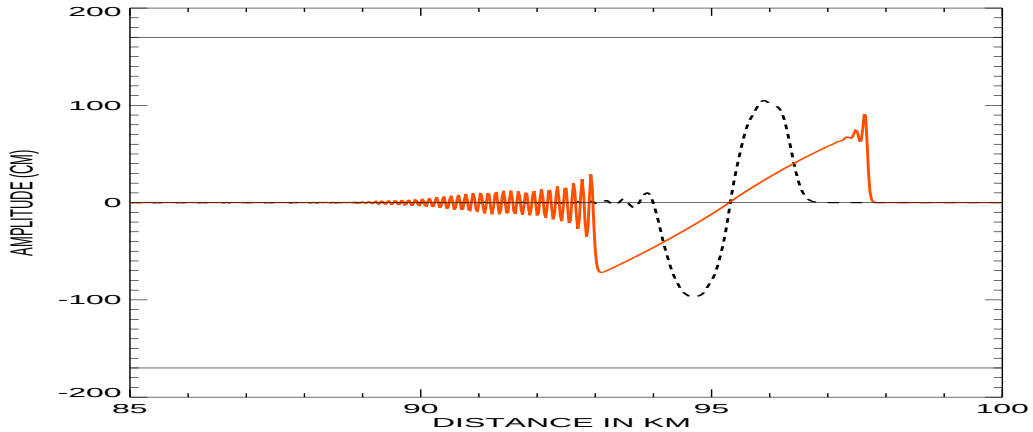

Figure II.22
Magnified results from FigII.21 after the wave traveled 94 km up the channel. Dashed line: friction only; continuous line: friction in eq. of motion and nonlinearity in eq. of continuity.

Conclusions are obvious: the nonlinearity occuring in continuity equation behaves similarly to the advective term but is much stronger as the processes of generating the

shorter dispersive waves are much stronger and the main wave amplitude diminishes much faster along the channel.

We compare (FigII.23) two different methods to compute the nonlinear advective term in equation of motion. The first order upwind/downwind computation is plotted together with the higher order of approximation as given by eqs.II.98 and II.99.

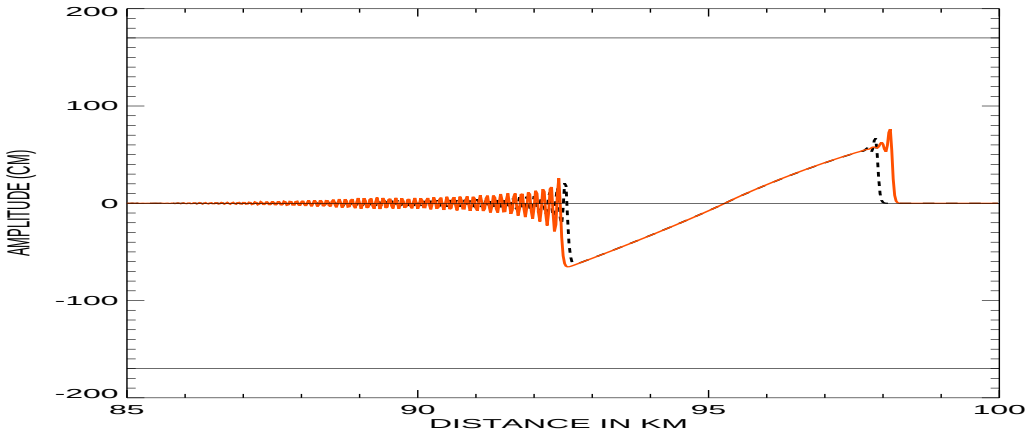

Figure II.23
Computations using two different approximation of the advective term. Dashed line -first order approximation; continuous line- higher order.

The higher order seems to generate stronger short wave tail and the main wave seems to posses a bit higher amplitude. The stronger parasitic short oscillations, if they would grow in time may cause instabilities.

12. Energy balance and numerical dissipation.

As we have seen in the previous section the processes of destruction of the tsunami waves due to the short wave numerical dissipation/dispersion are well observed when the wave travels in the upsloping channel. To investigate the role of numerical friction the wave propagation in the 3000 km long channel closed at both ends is considered. The shape of the channel is given in FigII.24. Computations are done by the forward time stepping numerical code based on the eqs (II.95 and II.96).

Tsunami wave is generated by the bottom displacement in the center of the channel. The high spatial resolution is achieved by the 10 m space step. The time step of 10^{-2} s is used. In the first experiment, a rectangular bottom displacement of 100 km length and 2 m height generates the sea level bulge of the same shape in the center of the channel. This displacement propagates both to the left and the right shores as shown in FigII.25. As the waves propagate towards the shores, even in the deep water the rectangular signal starts to change by generating short numerical dispersive waves in the front and in the tail of the sea level displacement. Such behavior demonstrates that the numerical scheme with the finite resolution is not able to reproduce the square wave without loosing an energy either through the dissipative or dispersive numerical processes. The time-history of a trapezoidal bottom displacement is shown in FigII.26.

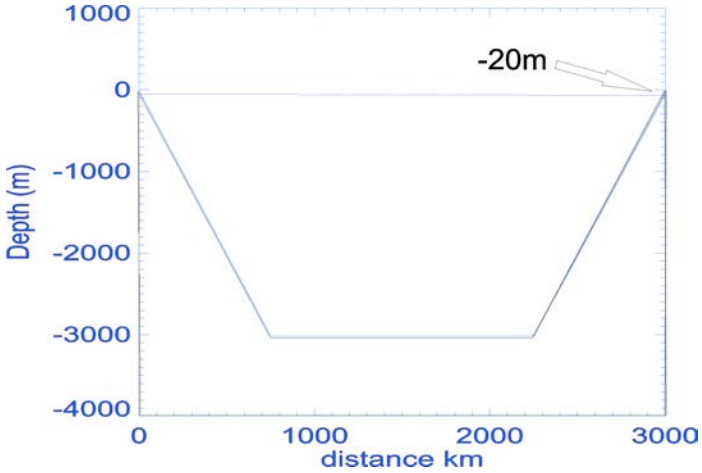

Figure II.24

Bathymetry of a channel. Constant depth of 3 km at the distance of 750 km from the shores changes linearly to achieve 20 m depth at the shores.

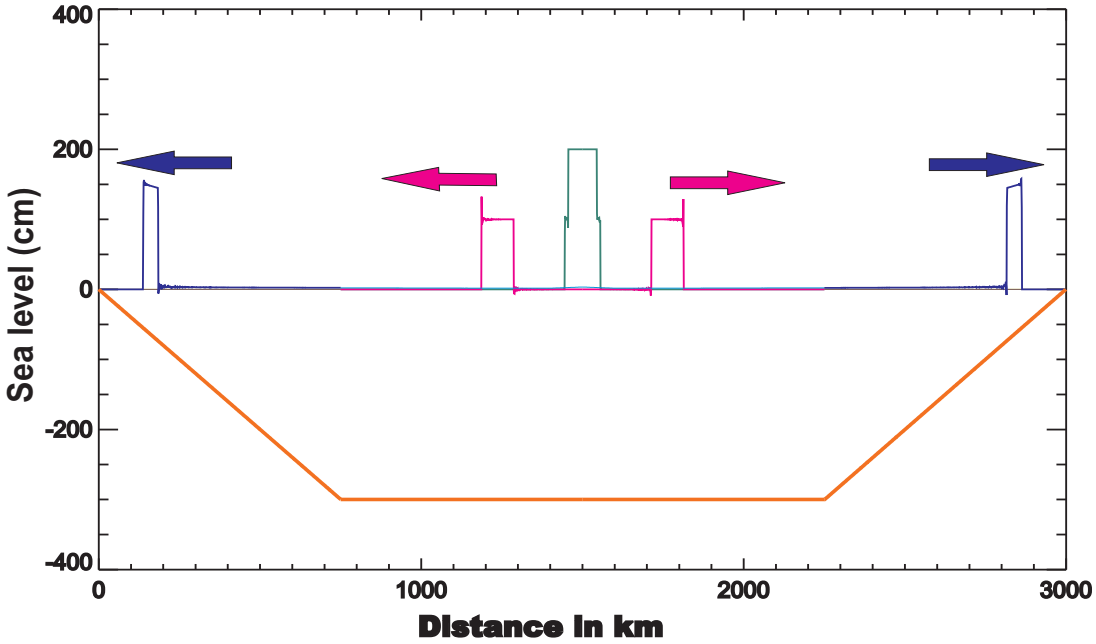

Figure II.25

A rectangular bottom displacement of 100 km long generates two waves propagating towards the left and the right shores. Notice dispersive waves in the front and the tail of the main displacement.

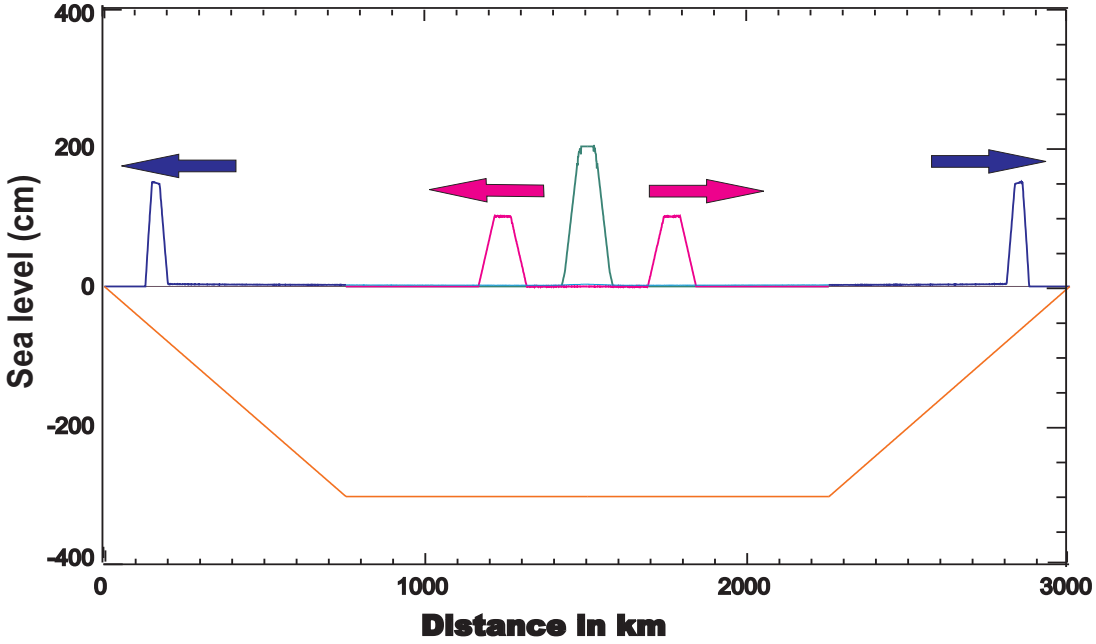

Figure II.26

A trapezoidal bottom displacement of 100 km long generates two waves propagating towards the left and the right shores. Notice the lack of numerical dispersive waves in the front and the tail of the main displacement.

Next we investigate the energy balance equation according to Sec. 7, ChI

$$\frac{1}{2}\frac{\partial}{\partial t}(\rho D u^2 + \rho g \zeta^2) + \frac{\partial}{\partial x}[\rho u D(u^2/2 + g\zeta)] = -\tau_x^b u \qquad \text{(II.114)}$$

If this equation is integrated over the entire length of channel we arrive at:

$$\int_0^l \frac{1}{2}\frac{\partial}{\partial t}(\rho D u^2 + \rho g \zeta^2)dx + \int_0^l \frac{\partial}{\partial x}[\rho u D(u^2/2 + g\zeta)]dx = -\int_0^l \tau_x^b u dx \qquad \text{(II.115)}$$

The second term on the LHS describes the energy flux, in the entire channel it yields

$$\int_0^l \frac{\partial}{\partial x}[\rho u D(u^2/2 + g\zeta)]dx = [\rho u D(u^2/2 + g\zeta)]_0^l = 0$$

since the velocity at the ends of the channel is equal to zero. We can further conclude that the change of the total energy in the channel is due only to the bottom dissipation, and if the bottom friction is neglected the total energy is constant in time

$$\int_0^l \frac{1}{2}\frac{\partial}{\partial t}(\rho D u^2 + \rho g \zeta^2)dx = 0 \qquad \text{or} \qquad \int_0^l \frac{1}{2}(\rho D u^2 + \rho g \zeta^2)dx = \text{const} \qquad \text{(II.116)}$$

Unfortunately computation made in the channel do not confirm this law of energy conservation. During the initial propagation in the deep water domain (FigII.27, time from 0 to 150 min) the energy averaged over channel is conserved well. As signal enters the shallow

water domain it starts to loose the energy both in case when the bottom friction term is included (dotted lines) and when the bottom friction term is set to zero (continuous lines). The propagation in the deep domain from 250 to 550 min again is conserving the total energy. The second encounter of the shallow water region bring even stronger dissipation. Thus the energy dissipation is due both to the physics and spatial and temporal resolution by numerical schemes. It is useful to notice that in the shallow water region, a small maximum of the energy occurs, thus the energy instead of being dissipated is growing in this region. These are effects of nonlinear interactions which mix numerical and physical dissipative processes. This figure also points out that numerical dissipation associated with the rectangular signal is much stronger than the dissipation of the trapezoidal water displacement.

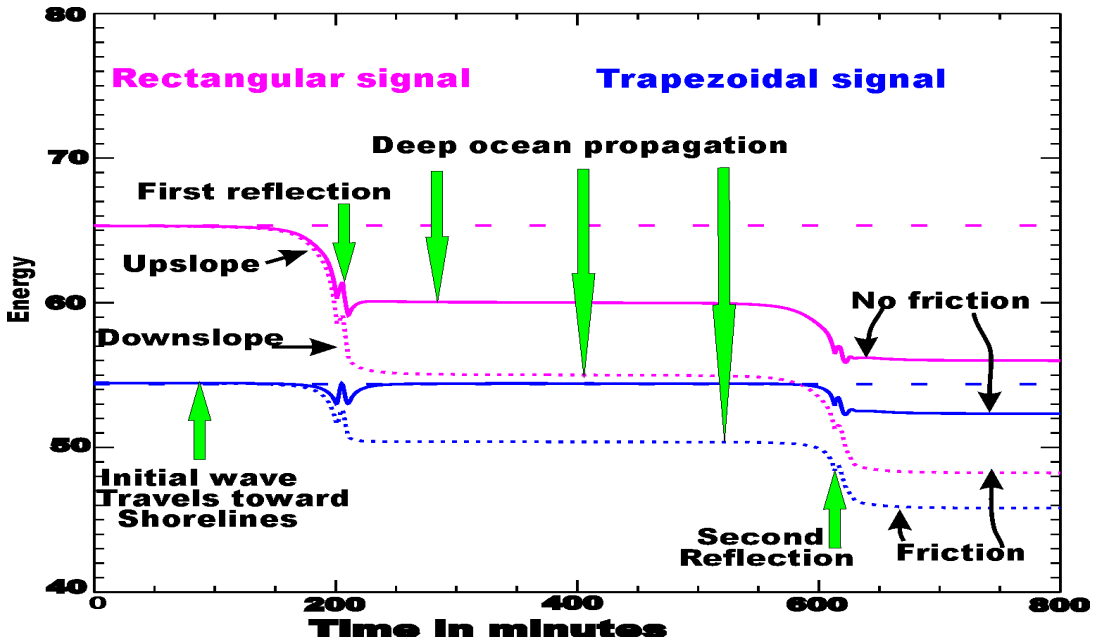

Figure II.27
Total energy (kinetic and potential) averaged over computational domain. Numbers are given in terra joules.

In our computations the nonlinear advective term has been rendered into a numerical form through the upstream/downstream method (eq.II.95), therefore to explain the energy loss we can invoke numerical friction due to the first order of approximation. For this purpose in eq. (II.95) only advection with the positive velocity is considered

$$\frac{(u_j^{m+1} - u_j^m)}{T} + u_p \frac{(u_j^m - u_{j-1}^m)}{h} = 0 \qquad \text{(II.117)}$$

The numerical error introduced by spatial and temporal approximations in (II.117) can be evaluated by the Taylor series

$$u_{j-1}^m = u_j^m - \frac{\partial u_j^m}{\partial x} h + \frac{1}{2} \frac{\partial^2 u_j^m}{\partial x^2} h^2 - \frac{1}{3!} \frac{\partial^3 u_j^m}{\partial x^3} h^3 + \frac{1}{4!} \frac{\partial^2 u_j^m}{\partial x^2} h^4 + O(h^5) \qquad \text{(II.118a)}$$

$$u_j^{m+1} = u_j^m + \frac{\partial u_j^m}{\partial t}T + \frac{1}{2}\frac{\partial^2 u_j^m}{\partial t^2}T^2 + \frac{1}{3!}\frac{\partial^3 u_j^m}{\partial t^3}T^3 + \frac{1}{4!}\frac{\partial^2 u_j^m}{\partial t^2}T^4 + O(T^5) \qquad \text{(II.118b)}$$

Introducing temporal and spatial derivatives from the Taylor series into II.117 we obtain

$$\frac{\partial u_j^m}{\partial t} + \frac{1}{2}\frac{\partial^2 u_j^m}{\partial t^2}T + O(T^2) + u_p(\frac{\partial u_j^m}{\partial x} - \frac{1}{2}\frac{\partial^2 u_j^m}{\partial x^2}h + O(h^2) = 0 \qquad \text{(II.119)}$$

This numerical error is of the first order of approximation in space and time. The spatial term

$$-u_p h\frac{1}{2}\frac{\partial^2 u_j^m}{\partial x^2}$$

is actually similar to the horizontal friction with viscosity coefficient being a function of the space step and velocity $(u_p h/2)$. Such numerical viscosity coefficient, because of its dependence on the velocity, produces the strongest dissipation in the shallow water region. Unfortunately, this numerical viscosity coefficient does not explain the deep-water dissipative processes, as the deep-water velocity is very small. Spectral properties of the numerical dissipation can be further elucidated by considering an amplification factor. As the advective equation (II.117) is similar to eq.(II.43) we can use amplification factor II.47, just by changing velocity c by u_p

Denoting $a = \cos\kappa h$ and $q = u_p T/h$, we obtain for the stability parameter (amplification factor)

$$|\lambda|^2 = 1 + 2q(q-1)(1-a) \leq 1 \qquad \text{(II.120)}$$

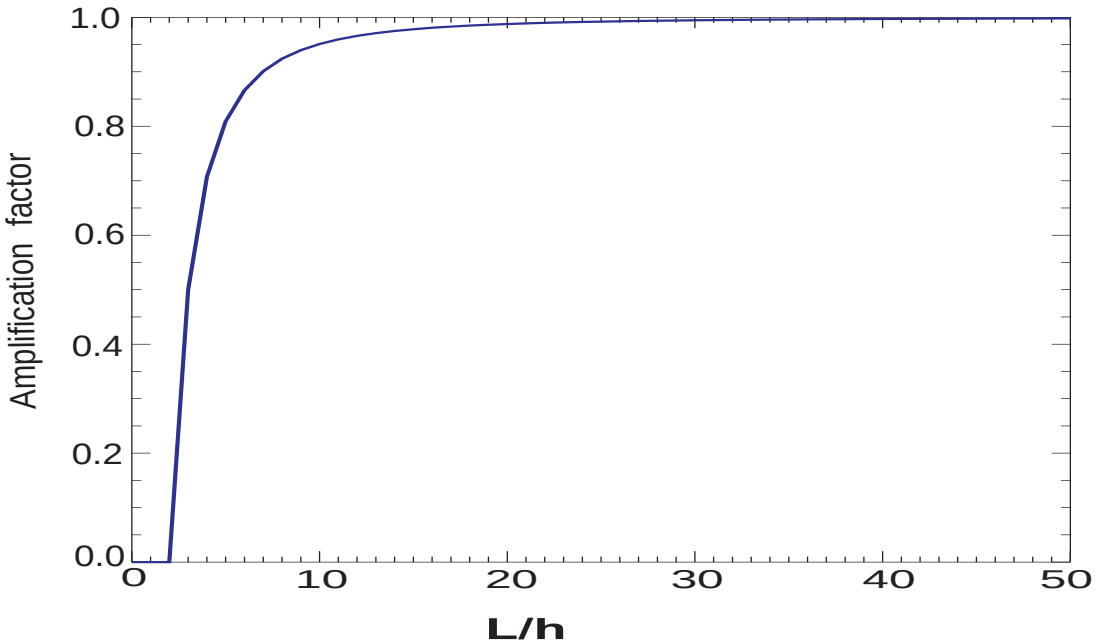

Figure II.28
Amplification factor (λ) for the eq.(II.117) as a function of wavelength resolution (L/h), Courant number $q = 0.5$

Amplification factor in Fig.II.28 is depicted for the Courant number $q = 0.5$ and for the variable resolution of the wavelength by the space step h. In the numerical scheme given by eq.(II.117) the amplification factor suppresses short waves, thus the dissipation of energy takes place in the short wave range. For the longer waves when $\kappa \to 0$ the damping will be negligible. FigII.28 shows λ as a function of the wave number. In this figure, the Courant number $q = 0.5$. Argument of the cosine function $\kappa h = 2\pi\frac{h}{L} = 2\pi\frac{1}{(L/h)}$ defines how well is the wavelength resolved by the spatial step. It changes as a function of the wavelength, starting from the shortest wave $L = 2h$, $\kappa h = 2\pi\frac{h}{2h} = \pi$ and continues increasing towards the longer waves as shown in Fig.II.28. The amplitude of the shortest wave $L = 2h$ is completely suppressed in this numerical system. Even if the wavelength is resolved ten times $\frac{L}{h} = 10$, the amplification factor is equal $\lambda = 0.95$. The wave described by the rectangular sea level change (Fig.II.25) if analyzed by the Fourier series consists of multiple short waves; therefore the numerical scheme will quickly dissipate the short wave energy. Somewhat differently dissipation proceeds in the trapezoidal wave as it can be represented by the smaller number of the short waves.

The total energy in the near shore region in Fig.II.27 depicts a small kink as the wave reflects from the shore. The wave energy instead of being dissipated is growing in this region, thus pointing towards instabilities of the numerical scheme (**Phillips, 1959**). The source of this energy is not related to physics but to numerics. As eq.(II.117) is not completely linear, the nonlinear effects will grow in the shallow water due to the sea level and velocity enhancement. A numerical nonlinear instability usually starts at the shortest wavelength in the system since a cascade of motion which arrives from the large scales to the small scales is blocked by the lack of finer resolution. The result is the build up of energy at the short wavelengths which induces instability. Often this type of instability is referred to as aliasing, which points out to the fact that the finite numerical grid cannot discern certain wavelength (see **Roache, 1976, p. 81**). An example how the new wavelength can be generated through the nonlinear interaction has been given in see Sec.8, Ch.II.

13. A solution to the runup problem.

We shall proceed to construct a simple algorithm for the run-up in the channel by using eqs. (II.11) and (II.12). Solution of this system will be searched through the two-time-level numerical scheme. The numerical form for the equation of motion is expressed by eq. (II.95) and for equation of continuity by (II.103). The major problem arises when wave starts to move in and out of the dry domain. Obviously none of the second order symmetrical space schemes can not be used, because the movement is defined only in the wet domain. Strong nonlinearity and discontinuity are often sources of computational instabilities (**Lewis and Adams, 1983; Imamura, 1996**). One of the major new assumptions is that equation of continuity can be approximated by the upwind/downwind approach as well. This approach introduced by **Mader (1986)** makes equation of continuity quite stable at the boundary between wet and dry domains. To simulate run-up and run-down, the variable domain of integration is established after every time step by checking whether total depth is positive. The following numerical scheme is used to march in time for the equations of motion:

$$\frac{(u_j^{m+1}-u_j^m)}{T}+u_p^m\frac{(u_j^m-u_{j-1}^m)}{h}+u_n^m\frac{(u_{j+1}^m-u_j^m)}{h}$$
$$=-g\frac{(\zeta_j^m-\zeta_{j-1}^m)}{h}+\frac{ru_j^m|u_j^m|}{0.5(D_j^m+D_{j-1}^m)} \tag{II.121}$$

Here: $u_p^m=0.5(u_j^m+|u_j^m|)$, and $u_n^m=0.5(u_j^m-|u_j^m|)$

The flux form of equation of continuity is important for successful computation in the domain which includes both dry and wet points. The $flux_j$ is located at the u_j point. As velocity is tested in this point to be positive or negative, the associated sea level is taken to form the flux:

$$\zeta_j^{m+1}=\zeta_j^m-\frac{T}{h}(flux_{j+1}-flux_j) \tag{II.122}$$

Usual form of the upstream/downstream flux is given by eq. (II.102) as

$$flux_j=u_p^{m+1}\zeta_{j-1}^m+u_n^{m+1}\zeta_j^m+u_{j,k}^{m+1}\frac{(H_{j,k}+H_{j-1,k})}{2}$$

and $u_p^{m+1}=0.5(u_j^{m+1}+|u_j^{m+1}|)$, and $u_n^{m+1}=0.5(u_j^{m+1}-|u_j^{m+1}|)$

To apply the boundary conditions at the water–land boundary, first, the boundary must be located at each time step. This in our program runup_beach.f90 is done by tracking in the every grid point j the total depth $D_j=h_j+\zeta_j^m$. At the old time step ζ_j^m is named in the program SLO. Thus if the total sea depth is negative the grid point belongs to the land, SLO(j)=-H(j) and the cell number CELL is set to zero, if on the other hand the total depth is positive the cell number CELL(j)=1 and the grid point belongs to the wet domain. This part of program reads, (here epsilon =0.001 is small positive number)

```
do j=js,je
d(j)=h(j)+SLO(j) ! total depth
IF(D(J).LT.EPSILON)THEN ! land grid points
SLO(J)=-H(J)
CELL(J)=0.
ELSE IF (D(J).GE.EPSILON) THEN ! water grid points
CELL(J)=1.
END IF
END do
```

The location of the dry and wet grid points is only the first step in computing the runup. When the water is moving towards the dry domain, the approach must be taken towards incorporating the dry points into the wet domain. This is usually done by extrapolating the sea level or velocity from the wet domain to the dry domain. The best known, classical extrapolation scheme by **Sielecki and Wurtele's (1970)** gives often unsatisfactory results. The extrapolation scheme which we use can be explained with the help of FigII.29. In the upper panel the boundary between dry and wet domains is located between the j and $j+1$ grid points. The j point is wet, therefore cell number CELL(J)=1 and D(J)>0, but the $j+1$ grid point is dry CELL(J)=0 and D(J)<0.

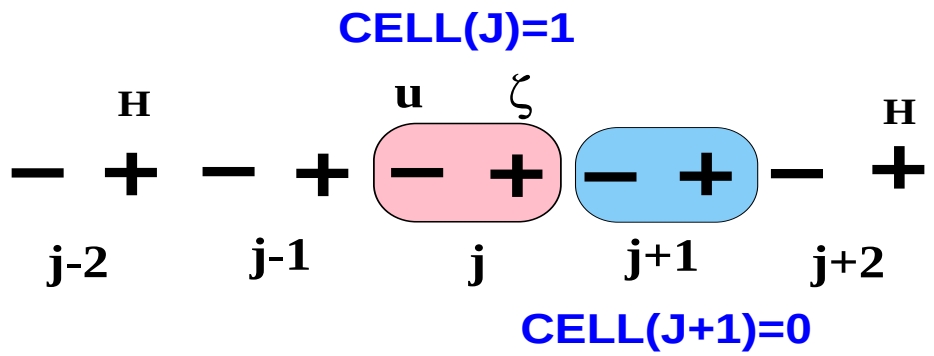

IF(CELL(J)=1.AND. CELL(J+1)=0) THEN

IF(ζ (J)+H(J+1)> 0) THEN

CELL(J+1)=1

U(J+1)=U(J)

ζ (J+1)= ζ (J)
END IF ; END IF

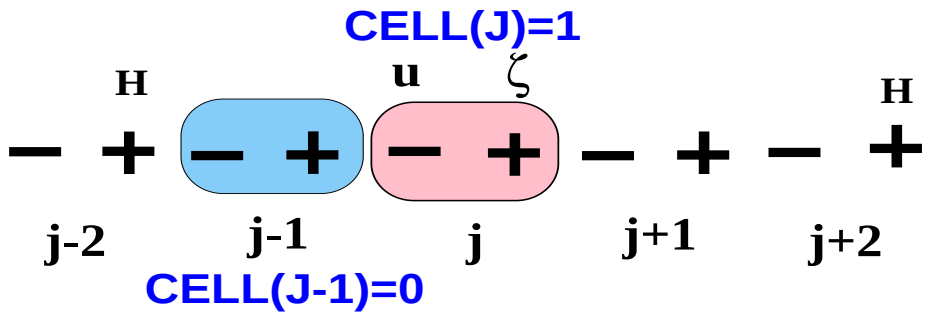

IF(CELL(J)=1.AND. CELL(J-1)=0) THEN

IF(ζ (J)+H(J-1)> 0) THEN

CELL(J-1)=1

U(J)=U(J+1)

ζ (J-1)= ζ (J)
END IF ; END IF

Figure II.29
Grid distribution for the run-up problem. Crosses denote sea level and dashes are velocity grid points. Blue color is for the dry and red color for the wet points.

Two questions ought to be answered: a) Under what condition the dry point will become wet? and b) What kind of extrapolation ought to be used? To solve the first question we apply the following reasoning. Let's assume that the sea level from j grid point travels to the point $j+1$, then with the new sea level the total depth in $j+1$ grid point ought to be checked. If it is negative the point continuous to be dry. If the total depth is positive the new total depth D(J+1)= SLO(J) + H(J+1)=$\zeta(j)$+H(J) is taken in the $j+1$ grid point and the cell number is declared as Cell(j+1) = 1. Since the $j+1$ grid point can be incorporated into the wet domain either the velocity or the sea level ought to be extrapolated from the wet to the dry domain. Our multiple numerical experiments showed that to properly calculate the runup only the velocity should be extrapolated to this new grid point. In the program runup1d.f90 the velocity at $j+1$ grid point is taken as UO(J+1)=UO(J), but in FigII.29 we explain how to extrapolate the sea level as well.

Similar reasoning and extrapolation schemes can be used when $j-1$ grid point is dry and j grid point is wet; this case is detailed in the FigII.29, lower panel.

13a. Runup on the sloping beach

The program runup_beach.f90 is used first in the very simple experiment. The bathymetry of the 2 km-long channel is linearly changing from 10 m in the water to the -10 m on the land. At the open boundary at 10 m depth the sinusoidal wave enters the channel according to radiative boundary condition (II.84)

$$\zeta(j=1) = \zeta_0 \sin(\frac{2\pi t}{T_p}) - u(j=2)\sqrt{H(j=2)/g})$$

Here $\zeta_0 = 200$cm. The time history of this wave traveling up the beach is given in FigII.30 (upper panel). The wave traveling down slope from the highest to the lowest points is plotted in the lower panel. It is of interest to see how the processes of the propagation and reflection from the shore have influenced the wave amplitude at the channel's entrance. In the above boundary condition we have set the amplitude of 2 m, but in the FigII.30 the amplitude is close to 0.5 m. This magnitude was generated by the two processes: propagation from the open boundary to the left (away from the channel) diminished the amplitude by half and subsequently the reflection from the shore in the interaction with the above condition further diminished the amplitude. The most important observation from FigII.30 is the presence, in the initial stage of a wave running up the beach, of the short period parasitic waves. These short waves point towards processes of the wave breaking. The results plotted are calculated for the bottom friction $r = 0.003$. The frictionless parasitic waves are much stronger than those depicted in FigII.30.

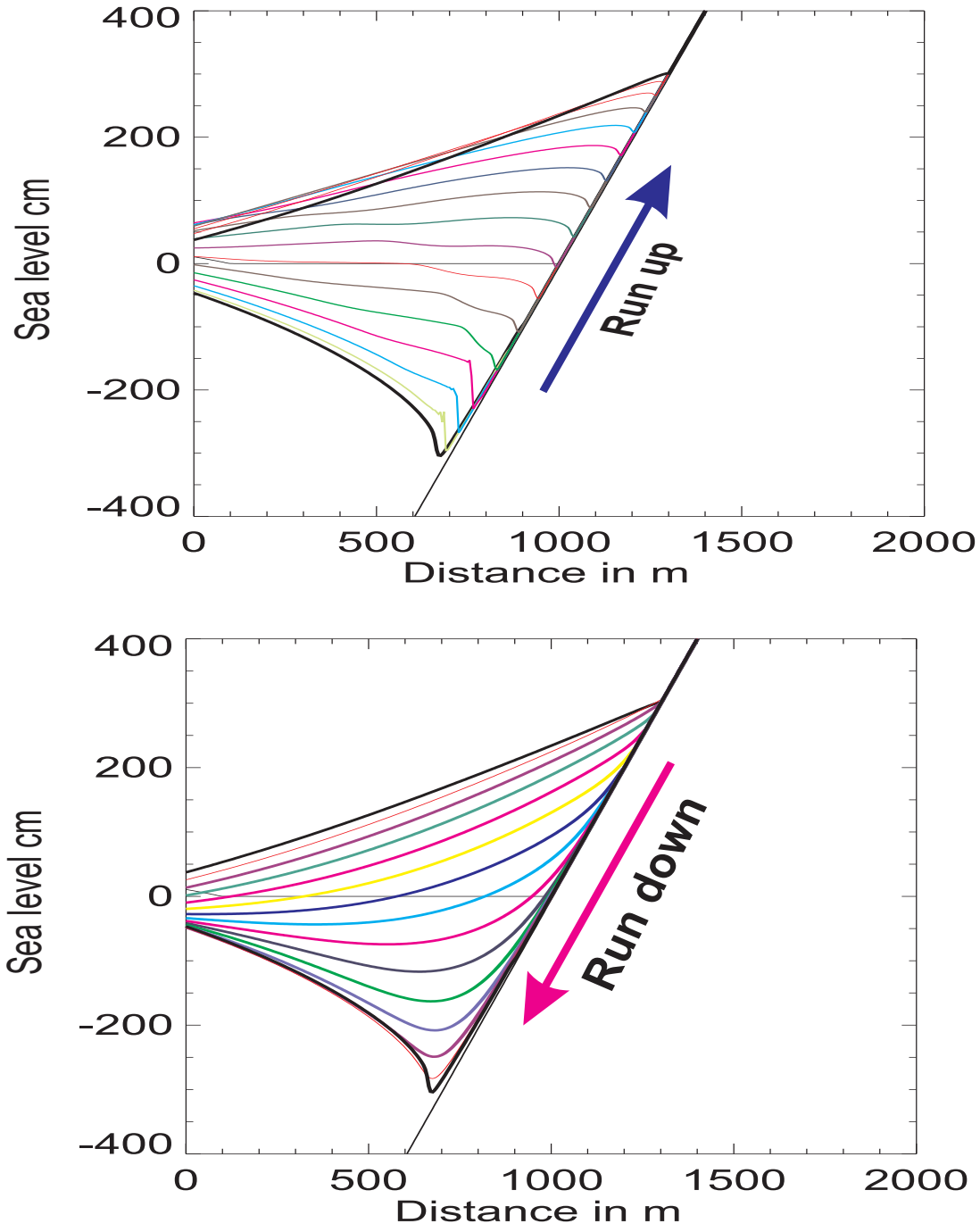

Figure II.30
Sinusoidal wave traveling up the beach (upper panel) and down the beach (lower panel). The length of the channel is 2 km

13b. Oscillations in the parabolic water body.

Ball (1965) and Thacker (1981) described analytically the oscillations of the planar surface in the parabolic basin for the frictionless fluid. This is a problem in which the

depth and sea level variations are of the same order. Therefore, these analytical solutions are very useful in testing numerical solutions of the nonlinear shallow water equations which involve moving shorelines. The geometry of the problem describes FigII.31.

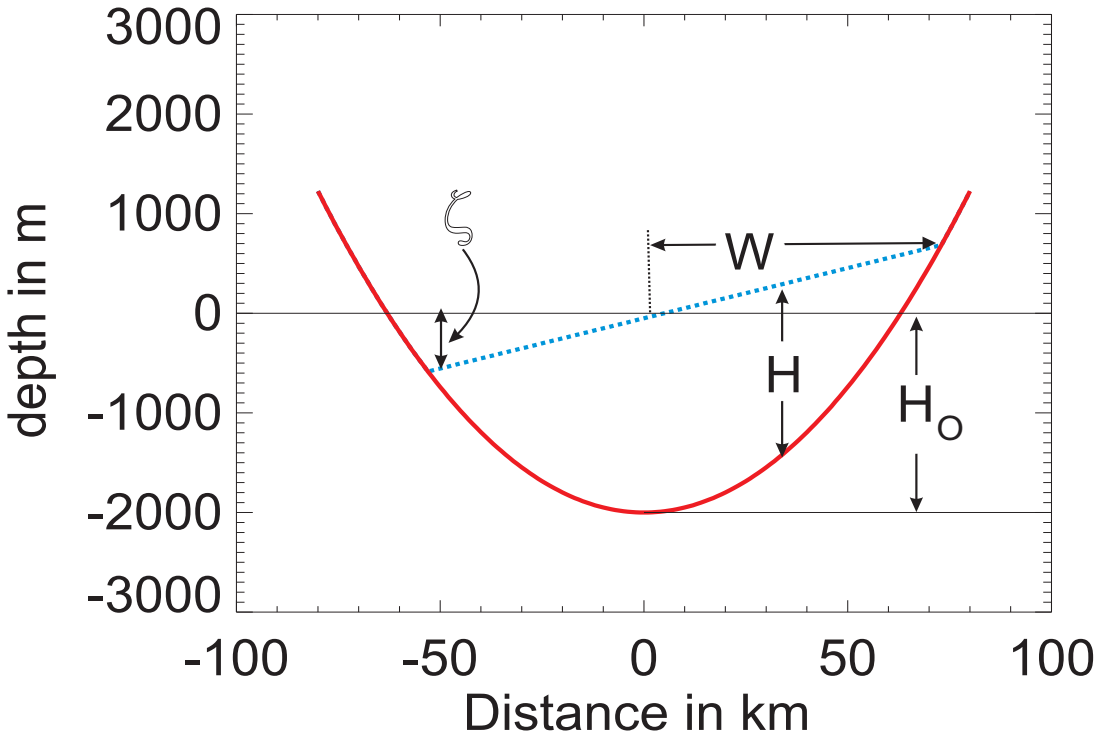

Figure II.31
Geometry of the planar oscillations in the parabolic water body.

The bottom geometry is given by

$$H = H_0(1 - \frac{x^2}{W^2}) \tag{II.123}$$

Here H_0 is the maximum of depth achieved at the distance $x = 0$ and W denotes the width of the water body. Fluid configured with a planar surface as in FigII.31 and initially at rest will undergo harmonic motion, planarity maintained. The analytical solution, given by **Thacker (1981)**, of water motions with an inclined water surface in a parabolic basin is expressed as

$$\zeta(x,t) = \frac{H_0 sl_0}{W^2}(2x\cos\omega t + 2x\sin\omega t - sl_0) \tag{II.124}$$

The frequency of this oscillation is

$$\omega = \frac{\sqrt{2gH_0}}{W} \tag{II.124}$$

In the numerical example the following parameters are taken $H_0 = 2$ km, $W = 63$ km, $sl_0 = 10$ km. The parameter sl_0 sets initial inclination of the free surface. The frequency of oscillations $\omega = 0.00314430$ s^{-1} and the period is $T = 2\pi/\omega = 1998.28$ s. To simulate

numerically the planar oscillation without friction ($r = 0$) the program runup_parab.f90 is used which is very similar to the previous runup program. The data block, the depth subroutine and initial sea level has been changed.

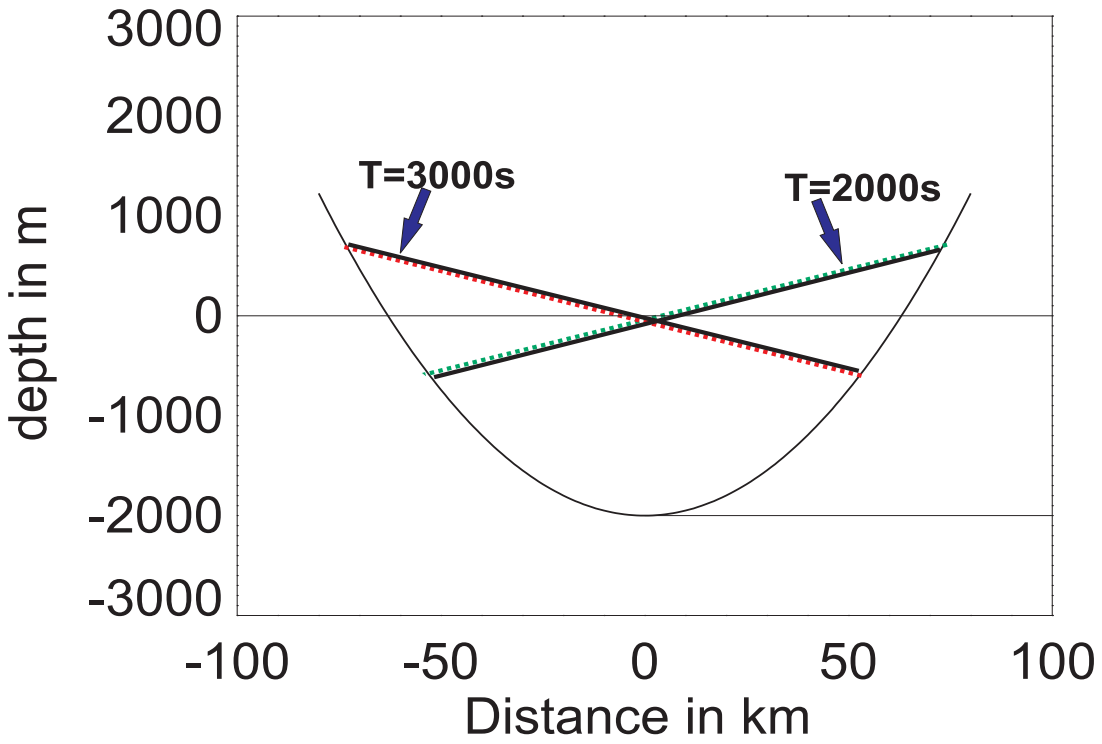

Figure II.32
Planar oscillations in the parabolic water body. Period is approximately 2000 s. Analytical solution: black lines Numerical solution: color lines.

The results depicted in FigII.32 are exactly the same as derived from analytical solution. Even though this simulation seems to be successful, the oscillations of a planar surface in a parabolic basin are a function of the velocity only, the theory predicts no gradients of velocity, which in fact makes the problem linear.

14. Tsunami-bathymetry interaction in the shallow water: shelf mode oscillations.

To investigate tsunami interaction with the shallow water bathymetry along the shelf and shelf break, we start with a simplified case of tsunami propagation up the linear depth profile given in FigII.33. The tsunami is generated due to the bottom uplift of 100 km long. The initial wave height is 200 cm. As the wave propagates towards the open boundary (to the left) and towards the shallow water (to the right) it splits into two waves (according to eq. II.7) of 100 cm height. The period of the rectangular disturbance depends on the horizontal length and on the water depth. It is close to 17 min ($T = 100000/\sqrt{(}9.81*1000)$.

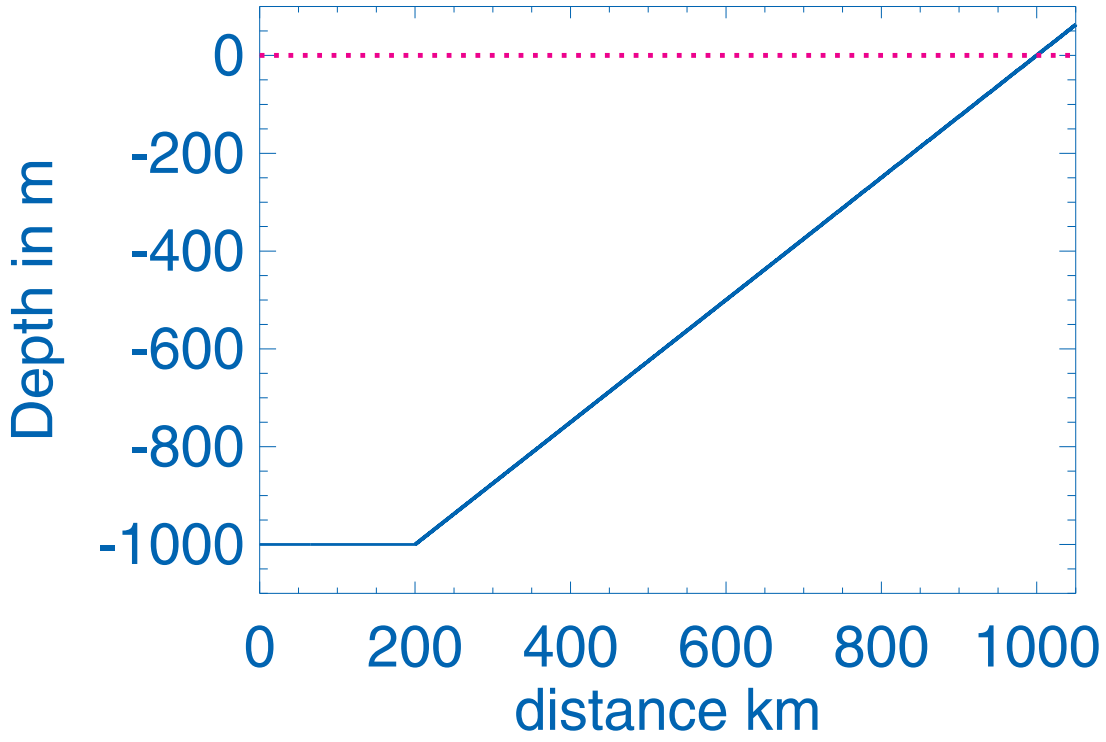

Figure II.33

Linear bottom profile. Tsunami due the bottom uplift is generated between 50 and 150 km from the open boundary.

The time history of the sea level plotted in FigII.34 show the levels at 500 km from the open boundary and at the shoreline.

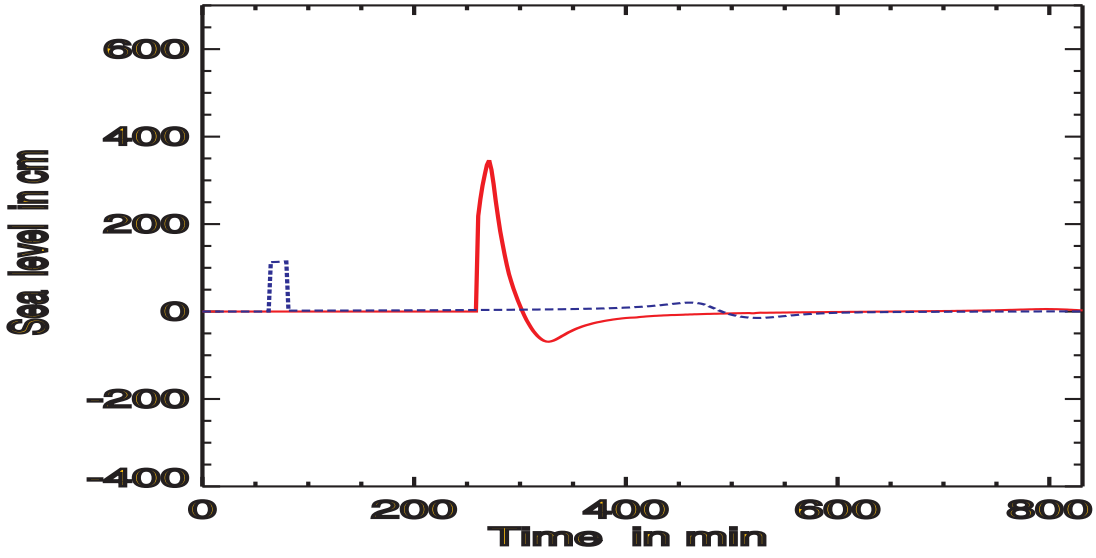

Figure II.34

Time-history of the sea level propagating towards the shore: a) at 500 km from entrance: blue dash line; b) at the shoreline: red continuous line.

The water depth emulating the Gulf of Alaska depth profile is shown in FigII.35

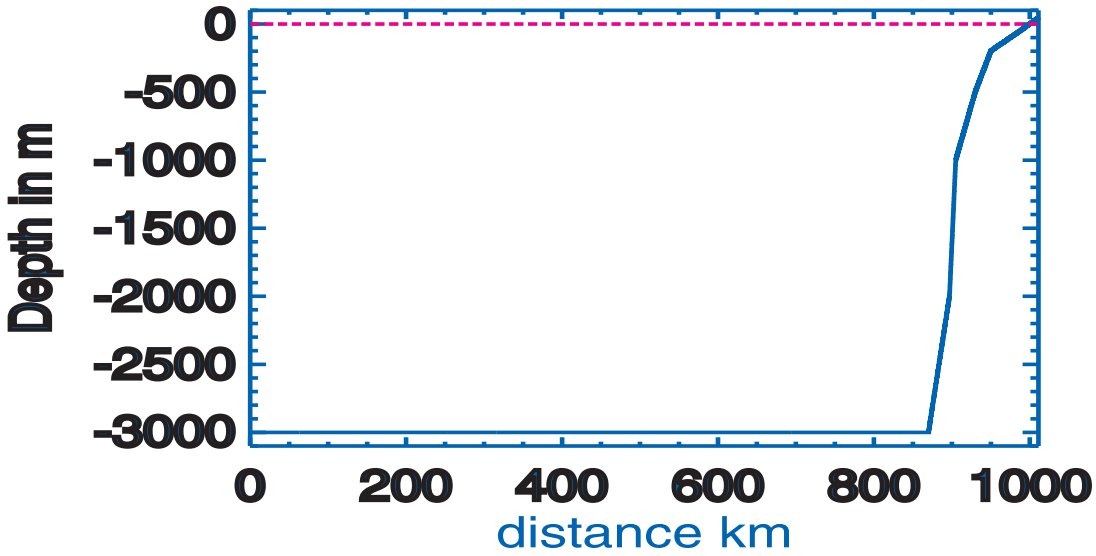

Figure II.35

Typical bathymetry (in meters) profile cutting continental slope and shelf break in the Gulf of Alaska.

Here the deep basin of practically constant depth is changed into the steep shelf break and the narrow shelf. The broken red line in the figure shows the free surface. The time history of the sea level at 500 km and at the shoreline is shown in FigII.36. These sea levels are very different from what is depicted in FigII.34.

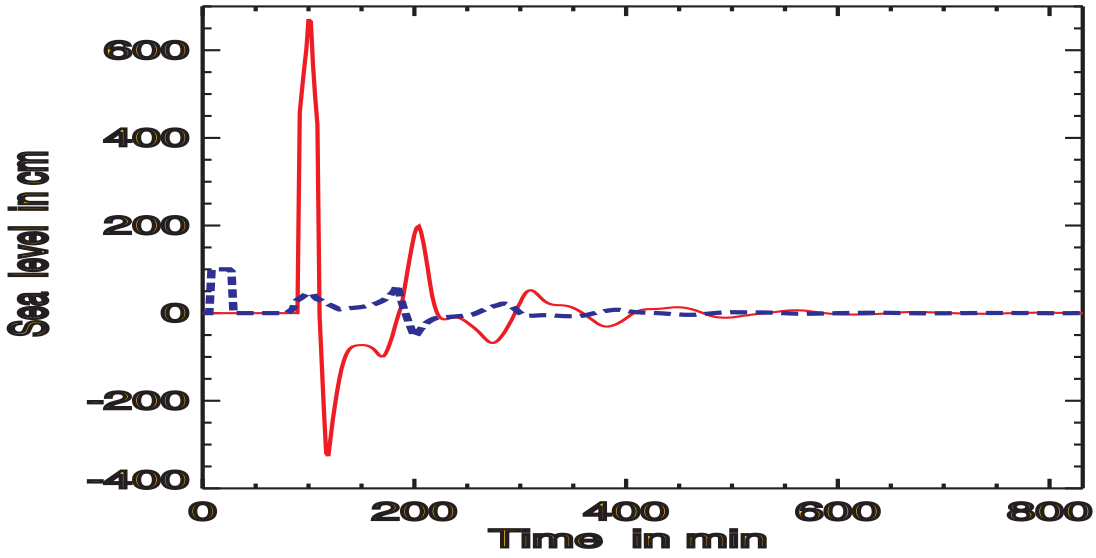

Figure II.36

Time-history of the sea level: a) at 500 km from entrance: blue dash line; b) at the shoreline: red continuous line.

Although the initial SSH at the 500 km is very similar in both cases the time history of the reflected signal (blue-broken line) in FigII.36 shows the complicated interaction with the shelf break and the shelf. The first signal ariving at T=100 min is a reflection from the shelf break with an amplitude of approximately half of the incident wave. The remaining

waves result from the shelf/coast trapping and reflection.

The sea level at the shoreline depicts a stronger amplification than for the linear profile due probably to the shorter interaction with the shallow water (less influence of the bottom friction). It is of importance to notice that the reflection from the shore line and interaction with the shelf and shelf break generated three consecutive waves while for the linear depth distribution only one wave was observed. The tsunami wave energy is trapped in the proximity to the shoreline by the bathymetry and is slowly leaked to the open ocean domain. These trapped and partially leaky oscillations continue for many hours, slowly losing energy due to waves radiating into the open ocean and due to the bottom dissipation. At the open boundary the initial box signal of about 20min period is followed by the wave reflected from the shelf break and the semiperiodic waves radiated back from the shelf/shelf break domain. The open boundary signal which is radiated into open ocean, is therefore superposition of the main wave and secondary waves. The period of the main wave is defined by the size of the bottom deformation and ocean depth (initial wave generated by earthquake) while the periods of the secondary waves are defined by reflection and generation of the new modes of oscillations through an interaction of the tsunami waves with the shelf/shelf break geometry. In numerous publications (e.g. **Munk, 1962; Clarke, 1974, Mei, 1989**), it was shown that the shelf modes of oscillations usually dominate meteorological disturbances observed along coasts. The evidence for tsunamis trapped in a similar manner have been presented both, theoretically (**Abe and Ishii, 1980**) and in observations (**Loomis, 1966; Yanuma and Tsuji, 1998; Mofjeld et. al., 1999**).

15. Surging over land–the dam-break problem

The dam-break problem presents simplified features of a tsunami wave front or bore running over a relatively flat bed.

An analytical solution for the dam-break problem using the nonlinear shallow water equations is derived based on the method of characteristics. This is one of the oldest hydraulic problems whose solutions goes back to **Saint-Venant (1871) and Ritter (1882)** and its still has important applications (**Chanson, 2005**). Starting from the shallow water equations given in Ch.I (eq. I.35 and I.37), the frictionless motion in a channel can be described by

$$\frac{\partial u}{\partial t} + u\frac{\partial u}{\partial x} = -g\frac{\partial \zeta}{\partial x} \tag{II.125}$$

$$\frac{\partial}{\partial x}uD + \frac{\partial \zeta}{\partial t} = D\frac{\partial u}{\partial x} + u\frac{\partial \zeta}{\partial x} + u\frac{\partial H}{\partial x} + \frac{\partial \zeta}{\partial t} = 0 \tag{II.126}$$

The above equations together with (II.22) and (II.23) can be written in matrix form

$$\begin{pmatrix} 1 & u & 0 & g \\ 0 & D & 1 & u \\ dt & dx & 0 & 0 \\ 0 & 0 & dt & dx \end{pmatrix} \begin{pmatrix} \frac{\partial u}{\partial t} \\ \frac{\partial u}{\partial x} \\ \frac{\partial \zeta}{\partial t} \\ \frac{\partial \zeta}{\partial x} \end{pmatrix} = \begin{pmatrix} 0 \\ -u\frac{\partial H}{\partial x} \\ du \\ d\zeta \end{pmatrix} \tag{II.127}$$

Setting the determinant of coefficients to zero yields the characteristic equation

$$\frac{dx}{dt} = u \pm \sqrt{gD} \tag{II.128}$$

This equation describe the speed of tsunami signal. Along the forward characteristic the speed is $u + c$ while along the backward characteristic the speed is $u - c$. Comparing to the speed over constant depth without the nonlinear terms now the speed depends on the particle velocity u and on the sea level height, since $D = H + \zeta$. The system of equations constructed on the two dependent variables u and ζ can be transformed into so called characteristic system with c and u as the new dependent variables.

$$c = \sqrt{g(H+\zeta)} \qquad \text{therefore} \qquad \zeta = \frac{c^2}{g} - H \tag{II.129}$$

Recasting equations of motion and continuity as

$$\frac{\partial u}{\partial t} + u\frac{\partial u}{\partial x} + 2c\frac{\partial c}{\partial x} = g\frac{\partial H}{\partial x} \tag{II.130}$$

$$2\frac{\partial c}{\partial t} + 2u\frac{\partial c}{\partial x} + c\frac{\partial u}{\partial x} = 0 \tag{II.131}$$

and combining them together by adding and subtracting the two equations are obtained

$$\frac{D(u+2c)}{Dt} = 0 \tag{II.132}$$

$$\frac{D(u-2c)}{Dt} = 0 \tag{II.133}$$

Here $\frac{\partial H}{\partial x} = 0$.

The full derivative reads

$$\frac{D(u+2c)}{Dt} = \frac{\partial(u+2c)}{\partial t} + (u+c)\frac{\partial(u+2c)}{\partial x} \tag{II.134}$$

$$\frac{D(u-2c)}{Dt} = \frac{\partial(u-2c)}{\partial t} + (u-c)\frac{\partial(u-2c)}{\partial x} \tag{II.135}$$

Thus the first equation describes the signal propagating along the forward characteristic and the second the signal along the backward characteristic. The dam breaks instantaneously at $t = 0$ and generates two waves: a negative wave propagating to the left into a fluid and a positive wave propagating over the dry bed. The wave to the left propagates initially into the fluid in the rest ($u = 0$). The tip of the positive wave propagates in the proximity to the bottom, where depth is $D \simeq 0$. The wave front of the nonviscous fluid propagates over the dry-bed with a speed $C_f = 2\sqrt{gD_0}$ which is two times greater than the wave front speed moving in the negative direction. At the dam site, the water depth drops instantaneously to a constant value of $\frac{4}{9}D_o$ with constant horizontal velocity equal to $\frac{2}{3}\sqrt{gD_o}$.

The free surface profile of the water surging over dry bed for an infinite reservoir is defined as parabola:

$$\frac{x}{t} = 2\sqrt{gD_0} - 3\sqrt{gD} \tag{II.136}$$

Here x is the coordinate along the channel as shown in FigII.37, t is the time. The parabolic free-surface profile may be rewritten as (**Chanson, 2005**)

$$\frac{D}{D_0} = \frac{1}{9}\Big(2 - \frac{x}{t\sqrt{gD_o}}\Big)^2 \quad \text{for} \quad -1 \leq \frac{x}{t\sqrt{gD_o}} \leq 2 \tag{II.137}$$

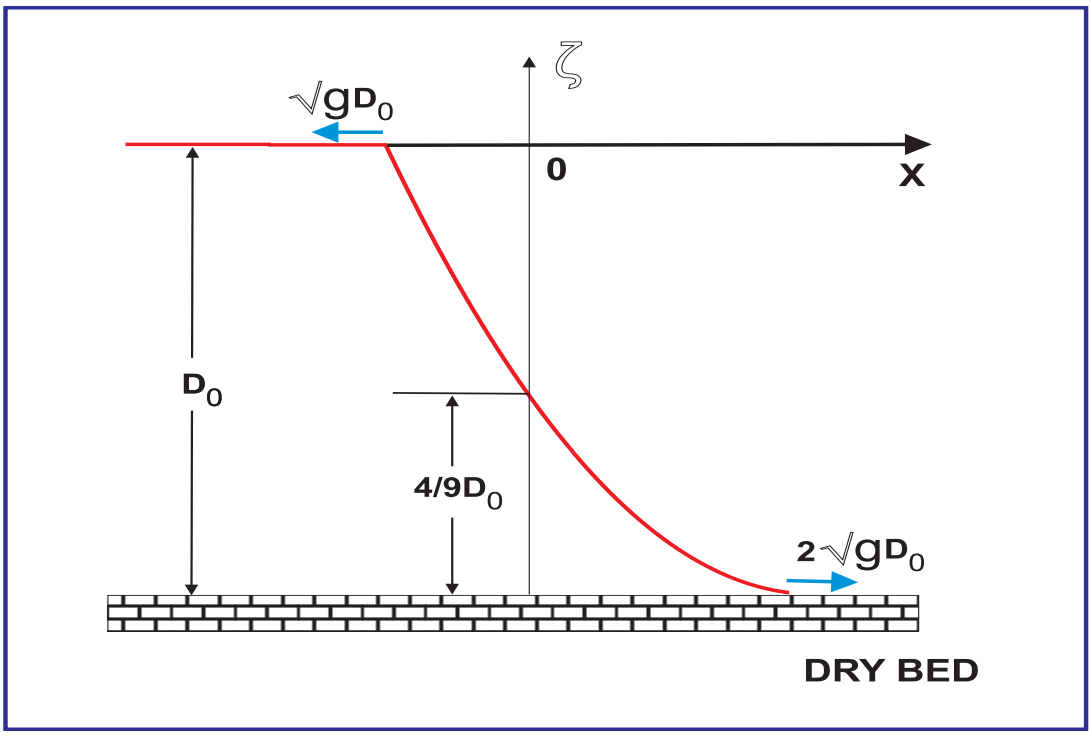

Figure II.37
Definition sketch for the dam-break problem.

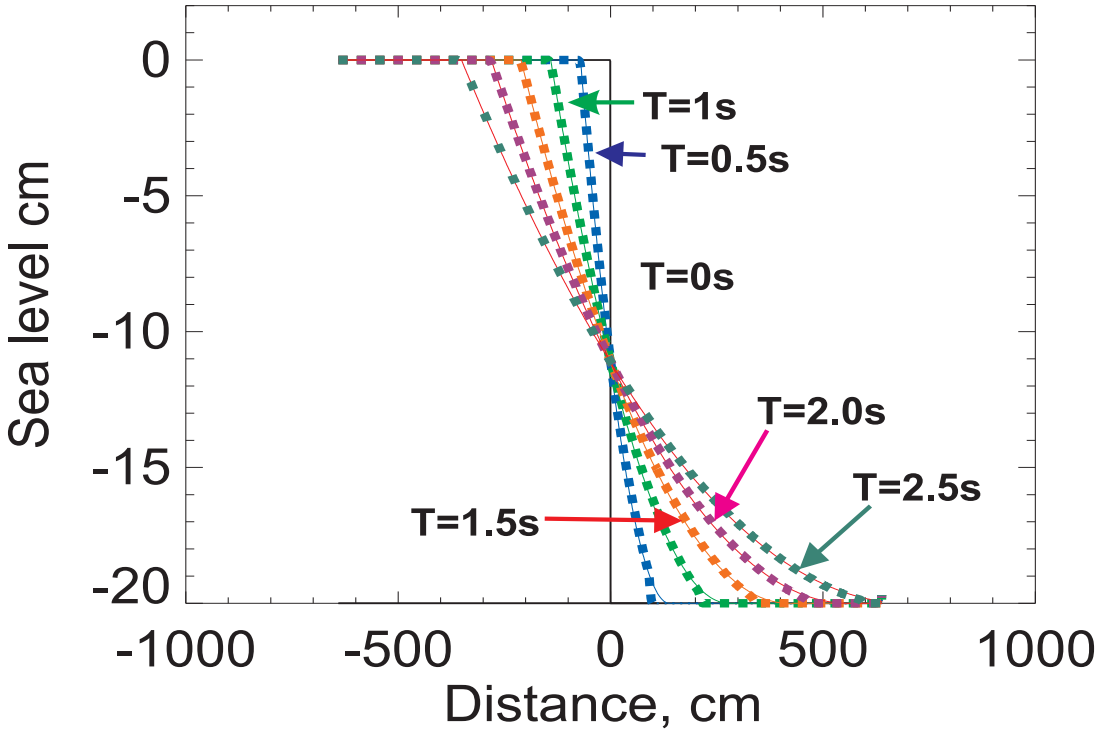

Figure II.38
Dam-break free surface profiles. Continuous lines: analytical solution
Broken lines: numerical solution

Numerical solutions are achieved through eqs. (II.121) and (II.122). Two numerical approximations are used to treat the fluxes in the equation of continuity. The upstream method given by (II.123) and improved upstream as defined by (II.104a and II.104b).

$$\frac{(u_j^{m+1}-u_j^m)}{T}+u_p^m\frac{(u_j^m-u_{j-1}^m)}{h}+u_n^m\frac{(u_{j+1}^m-u_j^m)}{h}$$

$$=-g\frac{(\zeta_j^m-\zeta_{j-1}^m)}{h}+\frac{ru_j^m|u_j^m|}{0.5(D_j^m+D_{j-1}^m)} \qquad \text{(II.121; II.138)}$$

Here: $u_p^m=0.5(u_j^m+|u_j^m|)$, and $u_n^m=0.5(u_j^m-|u_j^m|)$

-

$$\zeta_j^{m+1}=\zeta_j^m-\frac{T}{h}(flux_{j+1}-flux_j) \qquad \text{(II.122; II.139)}$$

Usual form of the upstream/downstream flux for the equation of continuity is given by eq. (II.102) and we call it C1

$$flux_j=u_p^{m+1}\zeta_{j-1}^m+u_n^{m+1}\zeta_j^m+u_{j,k}^{m+1}\frac{(H_{j,k}+H_{j-1,k})}{2} \qquad \text{(C1)}$$

Here $u_p^{m+1}=0.5(u_j^{m+1}+|u_j^{m+1}|)$, and $u_n^{m+1}=0.5(u_j^{m+1}-|u_j^{m+1}|)$.

Afterwards the improved upstream approach will be applied for the continuity equation. It is called C2 and the sea level is defined as (see II.104a and II.104b),

$$\zeta_p=(0.5+u_p^{m+1}\frac{T}{h})\zeta_{j-1}^m+(0.5-u_p^{m+1}\frac{T}{h})\zeta_j^m \qquad (\mathrm{C2_p})$$

$$\zeta_n=(0.5+u_n^{m+1}\frac{T}{h})\zeta_{j-1}^m+(0.5-u_n^{m+1}\frac{T}{h})\zeta_j^m \qquad (\mathrm{C2_n})$$

In the above to simplify notation the sea level at the positive velocity will be called ζ_p and at the negative velocity ζ_n.

In FigII.38 results from the analytical solutions (continuous lines) and numerical solution are shown for the few snapshots. These are computed by eqs.(II.138, II.139) with the fluxes in equation of continuity defined by C2. Although results are quite good, an amplified picture of the free wave profile at the tip given in FigII.39 shows that the numerical solution profiles are slightly lagging behind the analytical profiles. This especially is observed for the approximation given by the C1 upstream/downstream flux approximation (green line in FigII.39). It is noticeable that the best prediction for the wave tip is obtained by the C2 approximation. It is useful to remember that the above results for the different approximations are computed with the same spatial and temporal resolution. Decreasing the time step and space step in the C1 method will result in the much better prediction of the free wave as compared to the results given in FigII.39.

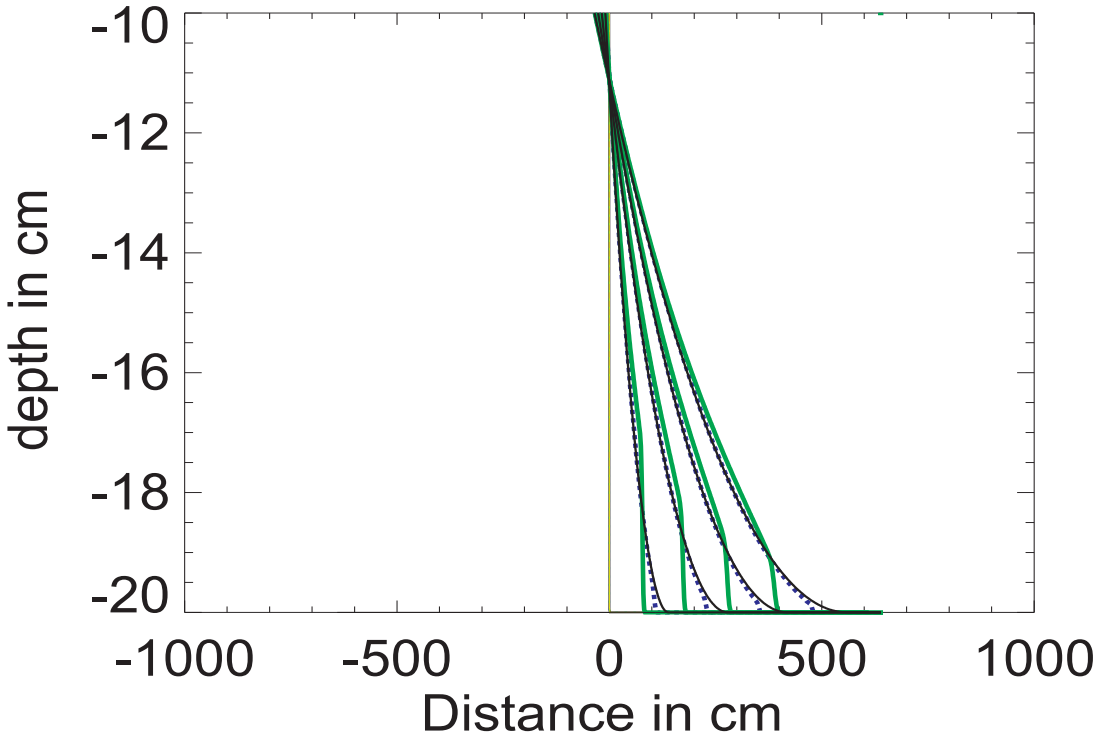

Figure II.39
Dam-break free surface profiles. Continuous : analytical solution-dark line first-order numerical solution-green line. Broken blue line: second-order numerical solution.

References

Abbot, M.B. and A.W. Minns. 1998. *Computational Hydraulics*. Ashgate, Aldershot, 557pp.

Abe, K. and Ishii, H. 1980. Propagation of tsunami on a linear slope between two flat regions. Part II reflection and transmission,*J. Phys. Earth*, 28, 543-552.

Ball, F. K. 1965. Second-class motions of a shallow liquid. . *J. Flid Mech.*, 23, 545-561.

Chanson, H. 2005. Applications of the Saint-Venant equations and method of characteristics to the dam break wave problem. Rep. No. CH 55/05, ISBN 1864997966, Department of Civil Engineering, The University of Queensland, 136 pp.

Clarke, D. J. 1974. Long edge waves over a continental shelf,*Deutsche Hydr. Zeit.*, 27, 1, 1-8.

Durran, D.R. 1999.*Numerical Methods for Wave Equations in Geophysical Fluid Dynamics*. Springer, 465pp.

Flather, R.A. 1976. A tidal model of the north-west European continental shelf. *Mem. Soc. R. Sci. Liege*, 6, 141164.

Imamura F. 1996. Review of tsunami simulation with a finite difference method. In *Long- Wave Runup Models*, H.Yeah, P. Liu and C. Synolakis, Eds, World Scientific, 2542.

Kowalik, Z. and I. Bang. 1987. Numerical computation of tsunami run-up by the upstream derivative method.*Science of Tsunami Hazards*, 5, 2, 7784.

Kowalik, Z. and Murty, T.S. 1993. *Numerical Modeling of Ocean Dynamics*, World Scientific, 481 pp.

Lamb, H. 1945. *Hydrodynamics*, Dover publ., 738 pp.

Lewis, C.H. III and Adams, W.M. 1983. Development of a tsunami-flooding model having versatile formulation of moving boundary conditions. *The Tsunami Society MONOGRAPH SERIES*, No. 1, 128 pp.

Loomis, H. G. 1966. Spectral analysis of tsunami records from stations in the Hawaiian Islands. *Bull. Seis. Soc. Amer.*, 56, 3 697-713.

Mader, C. L. 1986. *Numerical Modeling of Water Waves*, Univ. Calif. Press, Berkeley, Los Angeles, 206 pp.

Mei, C. C. 1989. *The Applied Dynamics of Ocean Surface Waves*, World Scientific, 740 pp.

Mofjeld, H.O., V.V. Titov, F.I. Gonzalez, and J.C. Newman (1999): Tsunami wave scattering in the North Pacific. *IUGG 99 Abstracts, Week B*, July 2630, 1999, B.132.

Munk, W. H. 1962. Long ocean waves, In: *The Sea*, v. 1, Ed. M. N. Hill, InterScience Publ., 647- 663.

Phillips, N.A. 1959. An example of nonlinear computational instability. *The Atmosphere and Sea in Motion*, Rockefeller Ins. Press, New York.

Roache, P.J. 1976. *Computational Fluid Dynamics*, Hermosa Publisher, Albu-

querque, N.M., 446pp.

Reid, R.O. and R.O. Bodine. 1968. Numerical model for storm surges in Galveston Bay. *J. Waterway Harbour Div.,* **94(WWI)**, 33–57.

Ritter, A. 1882. The Propagation of the Water Waves. *V.D.I. Zeitschr.*, Berlin, v.36, pt. 2,no. 33.

Saint-Venant, Barre, A.J.C. 1871a. Thorie et Equations Gnrales du Mouvement Non Permanent des Eaux Courantes. *Comptes Rendus des sances de l'Acadmie des Sciences*, Paris, France, Sance 17 July 1871, Vol. 73, pp. 147-154 (in French).

Sielecki, A. and Wurtele, M.G. 1970. The numerical integration of the nonlinear shallow-water equations with sloping boundaries. *J. Comput. Physics*, **6**, 219–236.

Thacker, W. 1981. Some Exact Solutions to the nonlinear shallow water wave equations. *Journal of Fluid Mechanics*. 107, 499-508.

Yanuma, T. and Tsuji Y. 1998. Observation of Edge Waves Trapped on the Continental Shelf in the Vicinity of Makurazaki Harbor, Kyushu, *Japan. Journal of Oceanography*, 54, 9 -18.

CHAPTER III

INVESTIGATION INTO TSUNAMI GENERATION PROCESSES.

1. Tsunami generation: introduction

Tsunamis are induced by sudden upheaval or subsidence of the sea floor by an earthquake, submarine landslide, or volcanic explosion. Great tsunamis, like 2004 Indian Ocean Tsunami, are caused by massive earthquakes.

Tsunami generation by an earthquake is generally modeled by instantaneous water surface displacement identical to the vertical displacement of the bottom due an abrupt slip at the plate interface. The fault rupture area located between two plates may extend up to 1,000 km. In numerical models to accommodate trench curvature, the fault plane is often broken into a few segments. Seismological observations give indications that the rupture may travel along the plates boundary and its rise time is short but not instantaneous. The recordings made during the Sumatra earthquake of 26 December 2004 by the seismic network showed that the rupture initiated around 3°N near Simeulue Island and propagated northward for about 1250 kilometers up to the Andaman Islands. Starting from the epicenter the rupture along the fault line occurred gradually with a rupture front speed 2-3 km/s and whole process was completed in 500-600 s.

The landslide generated tsunami often are caused by an earthquake-triggered submarine landslide along steep bathymetric features of the continental slopes similar to the Aleutian Trench. During the 1964 Prince William Sound earthquake many local tsunami waves in the steep-sided fjords were caused by landslides from the river deltas consisted of unconsolidated bottom sediments. The most catastrophic tsunami recorded in the recent history was generated by the 1958 earthquake at Lituya Bay (Alaska). This earthquake caused enormous subaerial rock slide which pushed water up to 525m. A massive prehistoric landslides were discovered in many locations of the World Ocean. The best known is the Storegga landslide along the continental slope off the coast of Norway. Submarine slide found in Storegga area depicts the width of approximately 290 km and it extends for more than 800 km. This major submarine sliding coincides with regions of gas hydrates reservoirs suggesting that hydrates play some role in destabilizing bottom sediments. Usually slides propagate with the velocity of the order of 25 m/s but the slide-impact velocity for the Lituya Bay rock slide was estimated as close to 100 m/s. The numerical and laboratory experiments made with subaerial and underwater landslide gave clear indication that the underwater landslides are ineffective at tsunami generation.

Tsunamis of volcanic origin are caused by a variety of phenomena among the most destructive is large-scale gravitational failure of the volcanic edifice. The collapsing material is incorporated in fast-moving debris avalanches which can reach velocities in excess of 100 m/sec. The worst catastrophe due to volcano collapse occurred on 21 May 1792 at the Unzen volcanic complex in Kyushu (Japan). The ensuing tsunami killed 14524 people

and swept 5972 houses. For more recent eruptions, Krakatau, in 1883, is the only large eruption for which good information exists on the timing of explosions and wave arrivals at modern tide gage stations. The tsunamis generated during the course of the eruption reached wave heights of 41 m, and at least 36,417 people living along the shores of the Sunda Straits lost their lives. Casualties were reported from the Sumatra and Java coasts as far as 120 km from Krakatau.

At the present time, many volcanos located at shorelines and volcano islands have oversteepened edifices, therefore the collapse of volcano may trigger tsunami. A significant tsunami hazard exists near many coastal volcanos in the circum- Pacific regions of Alaska, Kamchatka, the Kurile Islands, Japan, the Philippines, Indonesia, and Papua New Guinea, as well as in other areas with volcanos near the coast, for example, the Mediterranean region or the West Indies. For description of the tsunami events generated by massive earthquakes and volcanos the reader is referred to the website (**http://www.drgeorgepc.com/**) maintained by George Pararas-Carayannis, president of the Tsunami Society.

It should be noted that an earthquake, submarine landslide, or volcanic explosion are not always the sole causes for generation, and often times it may be a combination of any number of these conditions (**Murty, 1977**)

2. Simple models of tsunami generation by an earthquake

Let's consider a tsunami generation caused by the bottom displacement. For this purpose we will use equation of continuity (I.69) and equations of motion (I.70a and I.70b) developed in Ch.I.

$$\frac{\partial(\zeta-\eta)}{\partial t} = -\frac{\partial}{\partial x}(Du) - \frac{\partial}{\partial y}(Dv) \tag{I.69}$$

Here $D = H + \zeta - \eta$ is the total depth which includes both the free surface (ζ) and the bottom (η) displacement.

Equation of motion along the x direction reads

$$\frac{\partial u}{\partial t} + u\frac{\partial u}{\partial x} + v\frac{\partial u}{\partial y} - fv =$$

$$-g\frac{\partial \zeta}{\partial x} - \frac{1}{\rho D} ru\sqrt{(u^2+v^2)} \tag{I.70a}$$

and along the y direction reads

$$\frac{\partial v}{\partial t} + u\frac{\partial v}{\partial x} + v\frac{\partial v}{\partial y} + fu =$$

$$-g\frac{\partial \zeta}{\partial y} - \frac{1}{\rho D} rv\sqrt{(u^2+v^2)} \tag{I.70b}$$

The simplest tsunami source is a linear bottom displacement extended along the sole direction only. To investigate tsunami generated by such source we neglect nonlinear terms

and set the constant depth as well. For this case the equations of continuity and motion reduce to the following forms:

$$\frac{\partial(\zeta-\eta)}{\partial t} = -H\frac{\partial}{\partial x}(u) \tag{III.1}$$

$$\frac{\partial u}{\partial t} = -g\frac{\partial \zeta}{\partial x} \tag{III.2}$$

This system can as well be reduced to one equation for the sea level,

$$\frac{\partial^2 \zeta}{\partial t^2} - gH\frac{\partial^2 \zeta}{\partial x^2} = \frac{\partial^2 \eta}{\partial t^2} \tag{III.3}$$

This PDE is similar to the one we investigated in Ch.II (eq.II.26), but the above equation includes an additional term at the right-hand-side which is the forcing function due to the bottom displacement. The forcing is expressed by the vertical acceleration. If we assume an instantaneous bottom displacement and an instantaneous transfer of the bottom displacement to the free surface; the above problem can be reduced to the uniform equation (II.26) whose initial sea level distribution is the bottom displacement. If the channel along the x direction is infinite the initial conditions can be set as

$$\zeta(x, t=0) = \eta_0(x) \qquad \text{and} \qquad \frac{\partial \zeta(x, t=0)}{\partial t} = 0 \tag{II.27; III.4}$$

One solution (when initial velocity is equal to zero) can be written as

$$\zeta(x,t) = \frac{\eta_0(x-ct) + \eta_0(x+ct)}{2} \tag{II.28; III.5}$$

At the initial moment the source area is extended over length L. Which can be written as

$$\eta_0(x, t=0) = C \quad \text{at} \qquad -L/2 < x < L/2$$

and

$$\eta_0(x, t=0) = 0 \qquad \text{at} \qquad L/2 < x < -L/2$$

Eq.III.5 shows that the constant uplift of the length L is propagating as the surface (rectangular) wave towards the right and the left end of the channel, but the initial wave height C will travel towards the channel's ends as the wave of half of the initial height, i.e., $C/2$.

Computations for the above case are done by the forward time stepping numerical code (**source_01s.f90**) based on the eqs (II.95 and II.96). Tsunami wave is generated by the bottom displacement in the center of the 3000 km long and 3000 m deep channel. The high spatial resolution is achieved by the 10 m space step. The time step of 10^{-2} s is used.

In the first experiment, a rectangular bottom displacement of 100 km length and 2 m height generates the sea level bulge of the same shape located in the center of the channel (from 1450 km to 1550 km). This disturbance propagates both to the left and the right end of the channel as shown in FigIII.1. According to solution III.5 the signals propagate

with the phase velocity $\pm\sqrt{(gH)} = \pm 171.5$m/s, therefore the signal separation occurs after each wave travels half of the bottom displacement length, i.e. separation time is defined as

$$t_s = \frac{L}{2\sqrt{(gH)}} = \frac{50000m}{171.5m/s} \simeq 291s$$

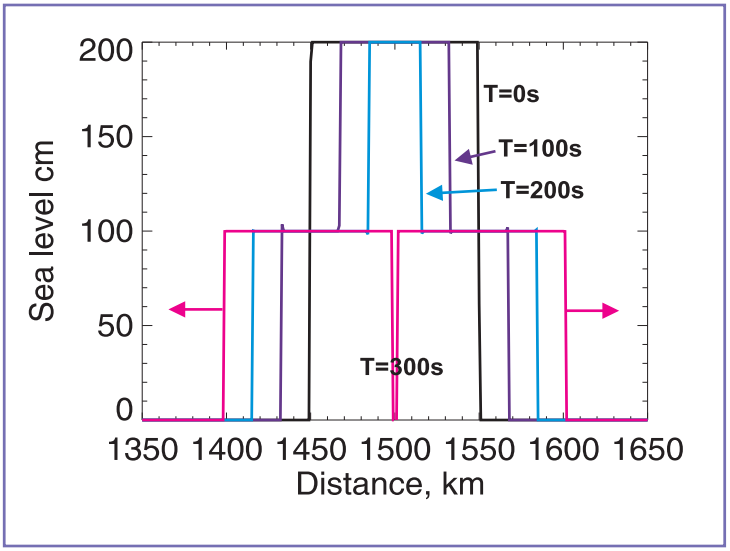

Figure III.1 An instantaneous rectangular bottom displacement of 100 km long generates two waves propagating towards the left and the right ends of the channel. Channel depth is 3 km.

Separated waves display only 100 cm wave height, half of the initial wave height, but the displacement distance remains the same i.e., 100 km. Usually source functions generated by an earthquake have both the positive and the negative bottom displacements, therefore for tsunami waves generated near the source area the typical periods may be assumed to be the travel time over the length of the source $T \simeq L/c$. The main unknown in such estimate is the ocean depth at the source function location. For $L = 200$ km and for the depth $H = 4000$ km we find $T \simeq 17$ min, but for the $H = 500$ m the period will increase to 48 min.

To continue, the second experiment is done with the same rectangular bottom shape but it rises slowly in time from zero to 2 m. The time (t_d) for the bottom deformation is taken as 0.5 h. During this time period the signal will travel along the horizontal direction for distance $\simeq ct_d = 171.5 \times 1800 \simeq 309$km. As the bottom deformation slowly proceeds upward the sea level generated is also drawn into the horizontal motion. The time history of the sea level generated by this source function is given in FigIII.2. Starting from rectangular signal which extends over 100 km at time t=10 s, it grows to the maximum amplitude of 32 cm (t=800 s), while time proceeds and the bottom displacement is still growing the sea level stops growing vertically but it extends horizontally preserving amplitudes (t=1600 s). After approximately 0.5 h of process the sea level starts to separate into two trapezoidal waves (t=2400 s). The amplitudes of these waves are the same as the source function wave, i.e. 32 cm but the area is two time smaller. As one can glean from the FigIII.2 the horizontal dimensions of the sea level change is much larger than the source function length

of 100 km. The approximate height of the sea level generated by the slow moving bottom deformation can be calculated from the simple premise that in the both experiment the volume of displaced water is the same. In the first experiment it extends over 100 km length but in the second experiments due to the horizontal motion it has been spread horizontally.

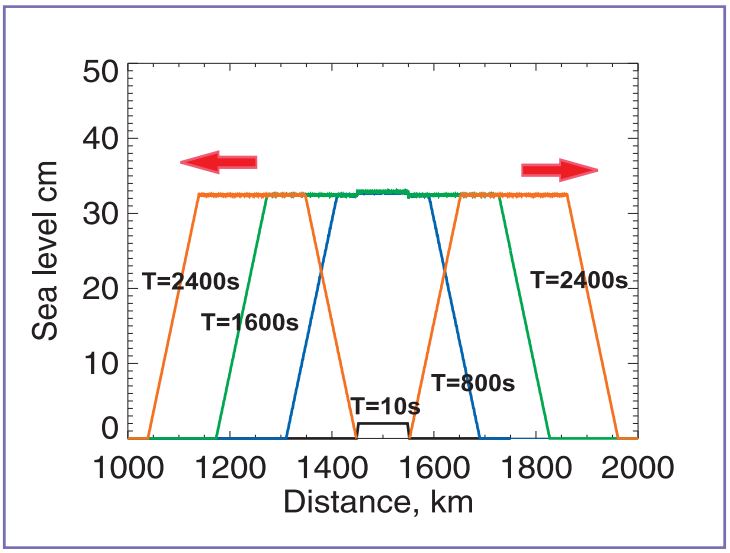

Figure III.2 An initial upward bottom displacement of 100 km long take place during 0.5 h time period and it generates two trapezoidal waves propagating towards the left and the right ends of the channel. Channel depth is 3 km

The spreading of the initial signal depends on the ratio of the initial source area length (L) and the horizontal distance traveled by tsunami during the bottom deformation time (t_d). The horizontal distance approximately equal to ct_d. Therefore, if $ct_d/L < 1$ spreading is small and the initial sea surface deformation follows the bottom deformation, on the other hand if $ct_d/L > 1$ spreading dominates and the initial sea level change is much smaller than the bottom deformation and the wavelength of the sea level change exceeds the initial source length (L).

As the spreading depends strongly on the phase velocity of the signal in the third experiment we consider again the rectangular bottom deformation slowly rising up during 0.5 h time period, but the depth will be changed from 3000 m to 100 m. Due to the smaller phase velocity (31.3 m/s) the spreading ought to be smaller as well since in 0.5 h time span the tsunami will travel horizontally for about 56 km. The sea level over the source function reaches the maximum of about 180 cm at the 28 min (FigIII.3). At this time the sea level signal extends over 200 km distance. The sea level signal separates into two trapezoidal waves after about 1 h. The trapezoidal wave height is 100 cm and each wave extends over 150 km, thus exceeding original source length of 100 km.

From the above experiments we conclude that:

1. If the bottom deformation occurs instantaneously the sea level change is equal to the bottom deformation and this process is independent of the water depth.

2. Slow bottom deformations are less effective at tsunami generation as an initial sea

level disturbance is spread horizontally by the long waves and the sea level rarely reaches the height of the bottom deformation.

3. As the initial sea level disturbance is spread much slower in the shallow water, for the similar bottom deformations and deformation times the shallow water is more effective at tsunami generation than the deep water.

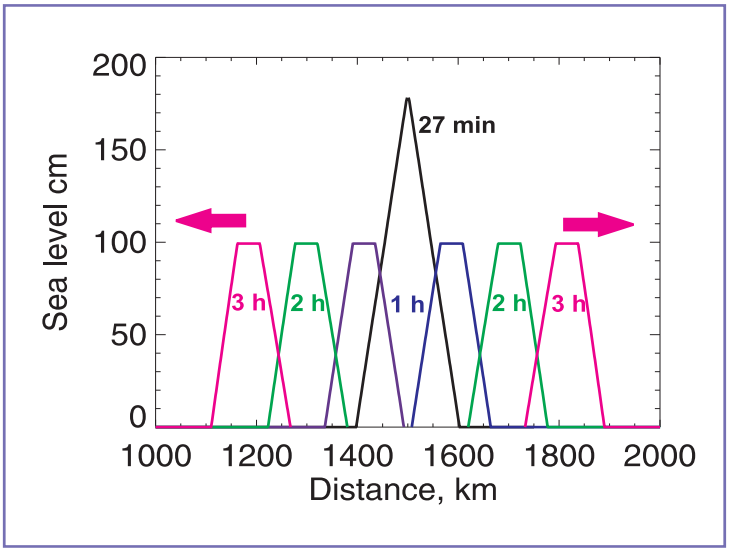

Figure III.3 An upward bottom displacement of 100 km long take place during 0.5 h time period and it generates two trapezoidal waves propagating towards the left and the right ends of the channel. Channel depth is 100 m.

3. Rudiments of seismology.

The earthquakes which generate tsunami occur near continental margins where large plates of the earth crust collide. As tectonic plates interact they fault (bend) along or near plate boundaries and when the stress exceeds the elastic limit of the rock an earthquake occurs. The constitutive law for the material behavior before and during earthquake is approximated by linearly elastic material which expresses relation between stress and strain. The properties of such material describe the elastic moduli. As, in the first approximation, the material properties within the earth do not depend on the direction, the isotropy of material is assumed. The widely used parameters for describing properties are Lame constants λ and ν. The latter (ν) has a simple interpretation as rigidity or shear modulus. Many problems are further simplified by assuming that $\lambda = \nu$. Such an earth material is called a Poisson solid. When an earthquake occurs seismic waves propagate in all directions, causing the ground motion (FigIII.4). Seismic waves are referred to as P waves, S waves, and surface waves (**Stein and Wysession, 2003**). The first wave to arrive from an earthquake is **P (primary) wave**, also called compressional or longitudinal. The second arriving is **S (secondary) wave** or shear wave. The velocity of propagation for the P-wave is defined as

$$V_p = \sqrt{\frac{\lambda + 2\nu}{\rho}} \tag{III.6}$$

Here, $\lambda \simeq \nu \simeq 3 \times 10^{11}$ dyn/cm^2, and $\rho = 3$g/cm^3 is the density of the earth's crust. Hence the P-wave propagates with a velocity of $\simeq 5.5$ km/s.

The velocity for the S-wave is given by the formula

$$V_s = \sqrt{\frac{\nu}{\rho}} \tag{III.7}$$

Thus introducing the above constant ν and the density, the S-wave velocity is $\simeq 3.2$km/s.

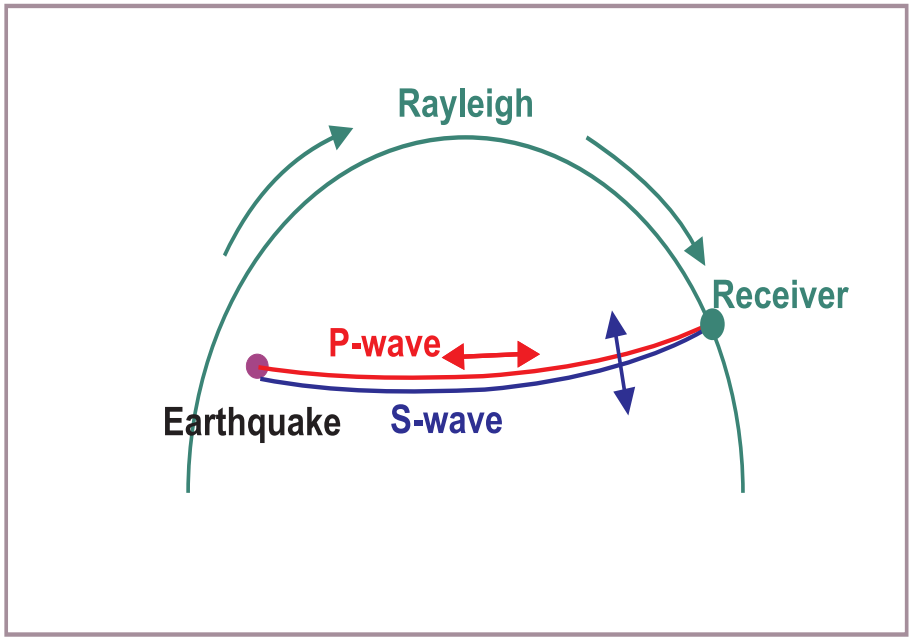

Figure III.4 Seismic waves generated by an earthquake. P-primary wave, S-secondary wave, Rayleigh- surface waves. Double arrows denote particles movement direction.

Both seismic waves are arriving up vertically towards earth's surface. The first arriving to any point is P-wave, it produces a ground motion parallel to the wave direction, i.e. along the vertical direction. The second arriving S-wave produces ground motion perpendicular to wave direction, i.e. along the horizontal direction. As structures, such as buildings, are more easily damaged by the horizontal motion than by the vertical motion, the S-wave arrival is related to the most damages. The last to arrive to a receiver are the large amplitude surface waves (Rayleigh waves and Love waves). These waves propagate along the paths close to the Earth's surface, thus causing ground motion mainly near the surface.

Earthquake usually occurs on fault, i.e. the area around a fracture where two sides of a fracture moves relatively to each other. The slow building of the strain in the rock leads eventually to the breaking of an elastic limit and when the fault slips an earthquake occurs. Faults were detected up to few hundreds km within the Earth but their effects at the surface are strong as well. To describe an input of the slipping fault on the water motion and tsunamis generation we need to know the deformation which results from an earthquake in the fault area. Therefore, we start from describing the fault geometry as a tool to study basic types of faulting and its influence on the ocean bottom deformation.

Usually fault consists of two plates (blocks); their relative motion is described by the slip vector, which is characterized by the slip length and slip angle. Faults are actually defines by the type of the slip. For further considerations we introduce the notion of the hanging wall block (upper part of the fault) and foot wall block (lower part of the fault). FigIII.5 describes the cut through the fault along the normal to the fault line.

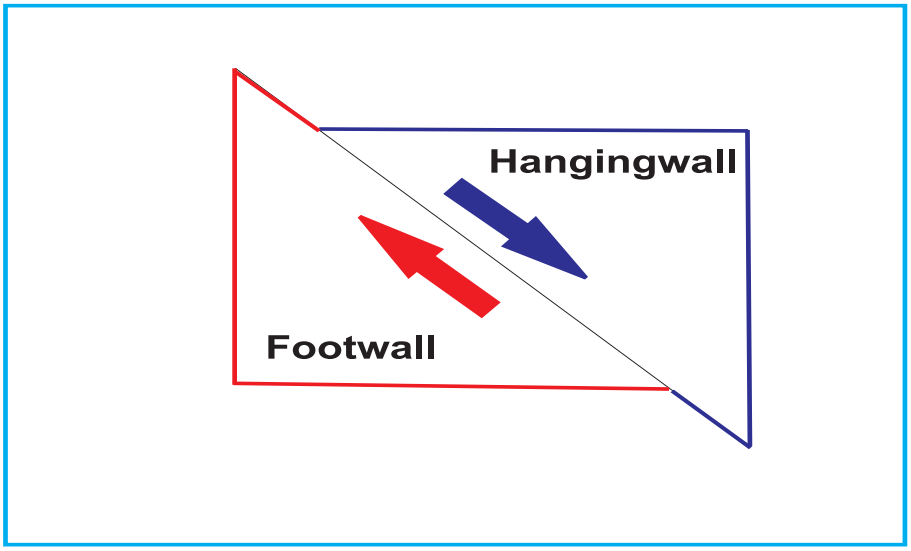

Figure III.5 Basic blocks of the fault. A cut along the normal to the rupture line.

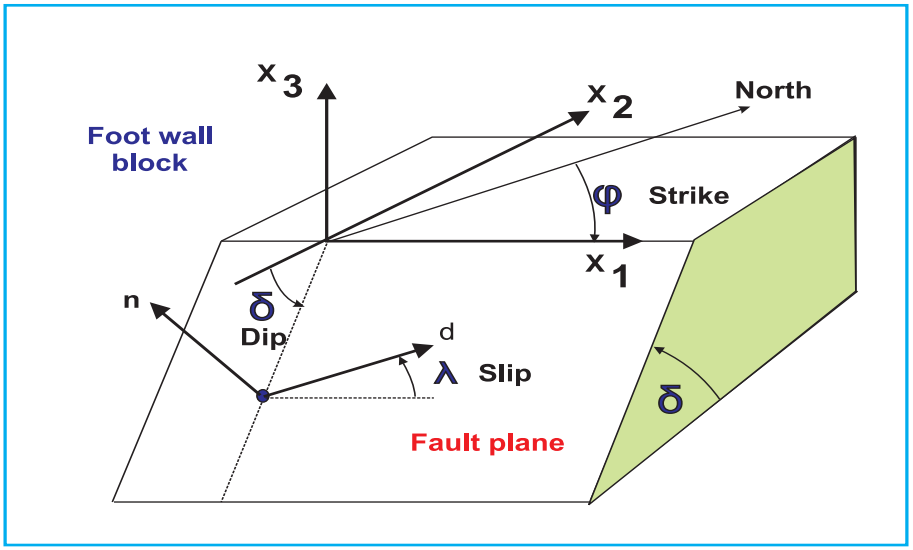

Figure III.6 Local coordinate system x_1, x_2 and x_3 related to the foot wall block. The slip vector d is located at the fault plane and n is normal to this plane.

The main coordinate systems are related to the foot wall block as explained in FigIII.6.

The local coordinate system (x_1, x_2 and x_3) is set in such a way that x_1 is along the fault strike direction (along a rupture). The strike angle ϕ is measured in the horizontal plane from the North to x_1 axis (clockwise). The dip angle (δ) is measured between the horizontal plane and the fault plane. The actual motion of the hanging wall block with respect to the foot wall block describes the slip vector. It is characterized by the slip angle λ (also known as rake) and the slip distance d. The angle is measured from the x_1 axis in the fault plane.

In tsunami wave generation the starting point is the bottom deformation history in the fault area resulting from an earthquake. For this purpose we shall use a solution obtained by **Okada (1985, 1992)**. Okada's formulae produce static displacements. To simulate a moving seafloor one can increase in time a displacement to the final value given by Okada. Another way is to take into account the rupture velocity and to obtain the final displacement dynamically. As experiments in Sec. 2 of this chapter demonstrated the dynamical and static (instantaneous) bottom deformations may result in the different sea surface displacement. To compute the bottom deformation the fault parameters such as length, width, depth, dip, strike, slip as well as seismic moment ought to be introduced into Okada's formulae. The vertical and horizontal slips are calculated from these formulae not at the focal depth (deep in the earth), where actual earthquake occurs but at the earth's surface or the oceanic bottom. The system of coordinates used by Okada is plotted in FigIII.7. The basic parameter needed for computation of the deformation (displacement) due to shear and tensile forces is the slip vector. Faults are categorized into three groups based on the sense of slip vector. In FigIII.7 the three components of the slip vector are given: U_1 strike-slip; U_2 dip-slip and U_3 tensile component. Deformation of the sea bottom is influenced only by the strike and dip components. These can be calculated as

$$U_1 = d_s = d\cos\lambda \qquad \text{and} \qquad U_2 = d_d = d\sin\lambda \tag{III.8}$$

Traditionally the slip angle (λ) is often named as the rake angle r. The slip vector magnitude d is related to the static (scalar) seismic moment (M_0)

$$M_0 = \nu A d \tag{III.9}$$

Where ν is the shear modulus of the rocks involved in the earthquake, d is the slip on the fault with area A. The area is calculated as $A = WL$ and the width W and the length L of the fault are described in FigIII.7.

Seismic moment is a quantity used by earthquake seismologists to measure the size and energy release of an earthquake (**Aki and Richards, 1980**). The earthquake magnitude scale, called the moment magnitude (M_w) is based on the seismic moment (**Stein and Wysession, 2003**),

$$M_w = \frac{\log M_0}{1.5} - 10.73 \tag{III.10}$$

Here M_0 is expressed in dyn·cm.

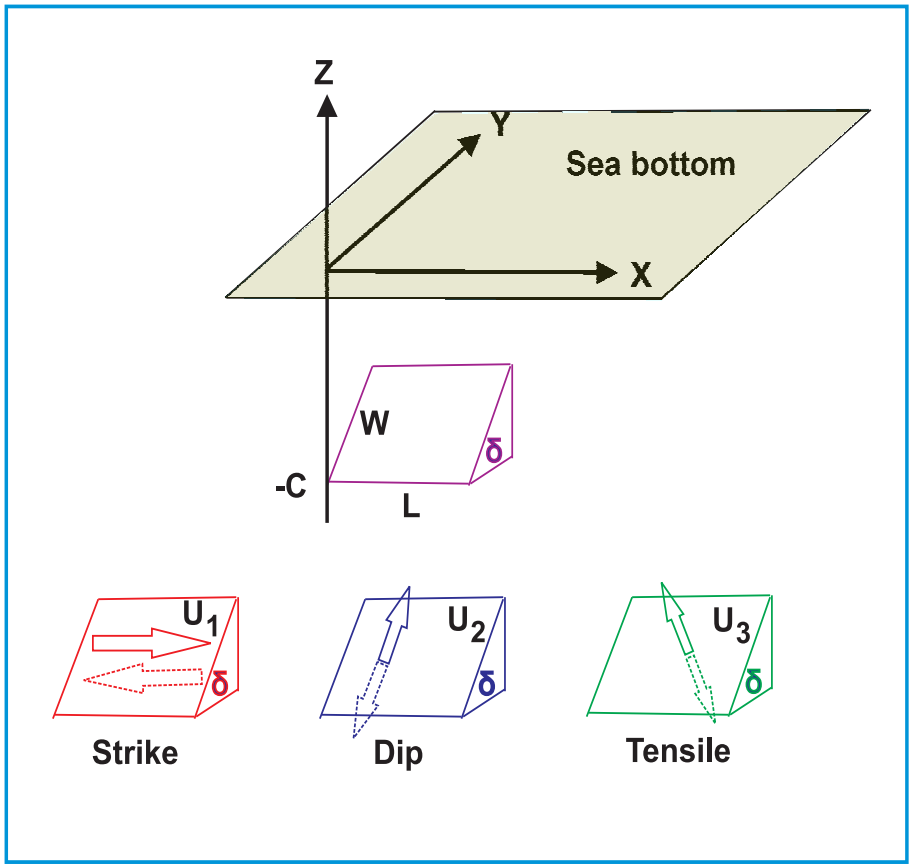

Figure III.7 The system of coordinate used by Okada (1985, 1992) related to the foot wall block. W is the width and L is the length of the fault. Depth of the earthquake is $-c$, U_1, U_2 and U_3 are components of the slip vector.

The large historic earthquake, the 1960 Chile event is described by the seismic moment $M_0 = 2.5 \times 10^{30}$ dyn· cm and the moment magnitude $M_w = 9.5$. Great earthquakes of moment magnitude $M_w > 8.5$ are very important for the tsunami prediction. New methods based on the GPS measurements seem to be very promising in the rapid determination of the earthquake size and tsunami potential (**Blewitt, et al., 2006**). Especially important is tracking ground motion using ocean bottom GPS sensors to estimate the strain behavior before earthquakes (**Lay and Kanamori, 2011**). The semiological methods using the various seismic arrays like the Hi-Net seismic array in Japan can produce detailed data on rupture within 30 min from the earthquake (**Ishii et al., 2005**). The slip responsible for tsunami generation is proportional to the seismic moment (eq.III.9), which in turn is proportional to the long-period radiation from the source. Therefore, novel approaches to a fast and simple diagnostic methods for identifying tsunamigenic earthquakes are based tracking the long period signal recorded by seismograms (**Shapiro et al., 1998**).

4. Source function for the earthquake generated tsunami

a) Indian Ocean Tsunami of December 2004.

As an example of application of the Okada's formulae for the ocean bottom deforma-

tion and the seismological data needed for such computation we consider a source function for the Indian Ocean Tsunami (IOT) of December 26, 2004. The Global Seismographic Network distributed all over the World recorded vibrations caused by this earthquake. The major conclusion was that the Sumatra-Andaman earthquake produced complicated rupture: after the initial rapid rupture subsequent slip between India and Sunda plates traveled to the north for approximately 1,200 km with decreasing speed (**Ishii et al. 2005; Lay et al, 2005**). Although, initially the rupture velocity (v) was estimated at 2 to 3 km/s, recent studies define large range of rupture velocities (**Hirata et al., 2006**, $v = 0.7$ km/s; **Piatanesi and Lorito, 2007**, $v = 2$ km/s). This complex rupture lead to an idea of subdivision the entire rupture area into a few segments. The seismologists subdivided the rupture into three segments according to the rupture processes (**Lay et al., 2005**). The southern most segment (along Sumatra), where rupture began, had very short rise time (about 50 s) and then the slip propagated up north to the Nicobar and Andaman segments with total duration of about 500s. The rapid and large slips up to $20 - 30$ m occurred in the Sumatra segment. In tsunami modeling **Koshimura et al., (2009)** subdivided the rupture area into 6 fault segments. To estimate the tsunami source model **Hirata et al., (2006)** inverted the satellite SSH data and found that as many as 14 subfaults is required to describe the source. **Titov et al., (2005)** in computing global tsunami used four subfaults (with slip from south to north: 21 m, 13 m, 17 m, 2 m). Such slip was chosen to provide best fit for satellite altimetry data and correlate with seismic and geodetic data inversions. To determine the subfaults locations the two sets of data are very useful: Jason 1 altimetry (**Gover, 2007**) and the vertical displacement obtained through the satellite radar (**Tobita et al., 2006**). Further confirmation of the subfaults formations provide the bathymetric maps of the rupture area (**Lobkovsky et al., 2006**).

In ensuing considerations we shall describe the source construction for the first paper on global tsunami modeling of 2004 event by **Kowalik et al., (2005)**. The generation mechanism for the Indian Ocean tsunami is based on the static sea floor uplift caused by abrupt slip at the India/Sunda plate interface. Permanent, vertical sea floor displacement is computed using the static dislocation formulae from **Okada (1985)**. Inputs to these formulae are fault plane location, depth, strike, dip, slip, length, and width as well as seismic moment and rigidity. The earthquake's total rupture extent can be estimated by several approaches. Finite fault seismic data inversion is one method which yield fault lengths on the order of 350 km to 650 km (e.g. **Ji, 2004; Yagi, 2005**). Another traditional method to delineate earthquake fault zones is plotting the aftershocks which occur in the first 24 hours following the main shock. The aftershocks are expected to cluster within the slip zone. This approach leads to an estimate of 1200 km for the fault length (**NEIC, 2004**). In **Kowalik et al., (2005)**, the fault extent is constrained by observed tsunami travel times to the northwest, east, and south of the slip zone. Figure III.8 displays the tsunami arrival time constraints on the fault zone. Tsunami arrival times at Paradip-India (SOI, 2005), Ko Tarutao-Thailand (**Iwasaki, 2005**), and Cocos Island (**Merrifield et al., 2005**) tide gages are plotted in reverse. That is, the observed travel time contour is plotted with the tide gage location as the origin point. This method indicates a fault zone approximately 1000 km by 200 km. The epicenter location lies on the southern end of the fault zone.

To accommodate trench curvature, the fault plane is broken into two segments. Fault parameters for the two segments are listed in Table 1. Strike, dip, and slip are based on the definitions from **Aki and Richards (1980)**. Strike is determined by the trench orientation. Dip is taken from the Harvard CMT solution (**HRV, 2005**). The slip for the southern segment is based on the Harvard CMT solution while slip for the northern segment is set at 90° based on observed tsunami first motions on Indian tide gages (**NIO, 2005**). Depth is based on the finite fault inversion of **Ji (2004)**. The total moment release (derived by assuming an average slip of 13m and rigidity of 4.2×10^{11}dyne·cm^{-2}) in the two segments equals 1.08×10^{30} dyne·cm (Mw $\simeq$9.3) which is in good agreement to 1.3×10^{30} dyne·cm proposed by **Stein and Okal (2005)** based on normal mode analysis.

Table III.1.Fault parameters used to generate the vertical sea floor movement.

Earthquake Parameter	Southern Fault Segment	Northern Fault Segment
Strike	335°	350°
Dip	8°	8°
Slip	110°	90°
Length	300 km	700 km
Depth (SW corner)	8 km	8 km
SW corner Latitude	3.0N	5.6N
SW corner Longitude	94.4E	93.3E
Moment	3.2×10^{29}dyne·cm	7.6×10^{29}dyne·cm
Rigidity	4.2×10^{11}dyne cm^{-2}	4.2×10^{11}dyne cm^{-2}

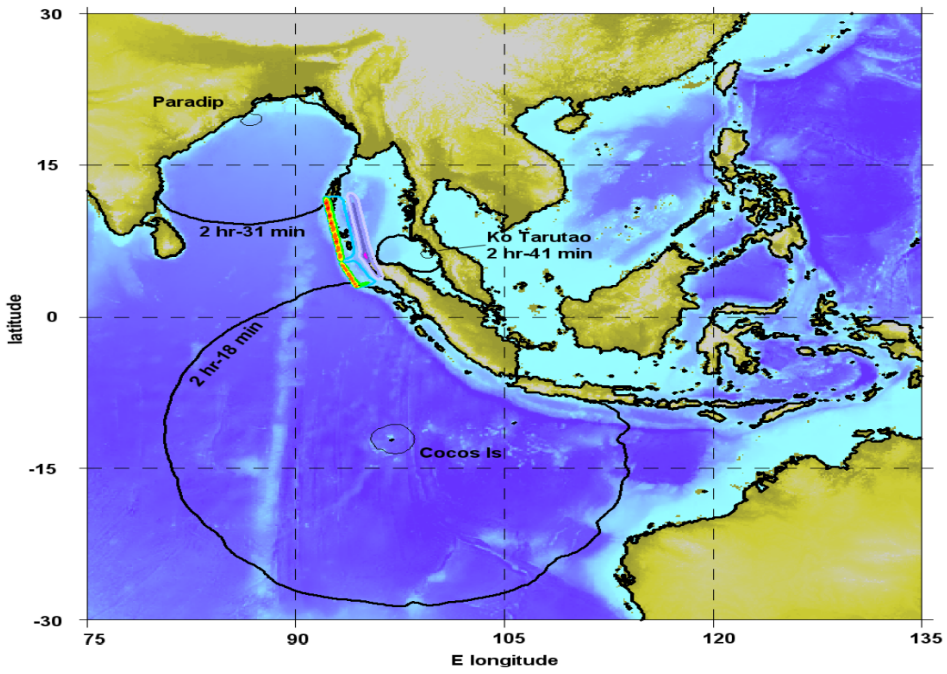

Figure III.8. December 26, 2004 Sumatra earthquake uplift as constrained by tsunami travel times to the tide gauge stations.

The contours of the source functions are given in FigIII.9. The result of introducing two subfaults is clearly depicted. As source acts as an elongated antenna for the tsunami generation, at the boundary of the subfaults the minimum in the directional distribution of the tsunami amplitude is produced.

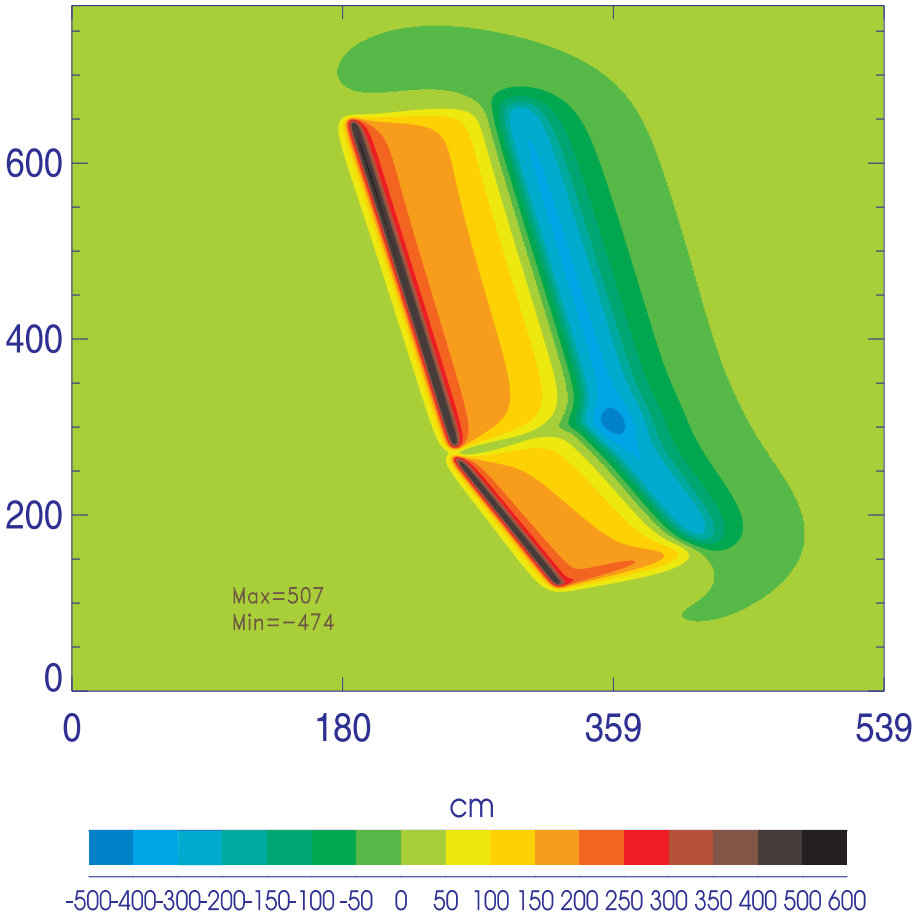

Figure III. 9. The source deformation contours. Maximum uplift is 507 cm and maximum subsidence is approximately 474 cm. Coordinates are given in geographical minutes. Point (0,0) is located at 89°E and 1°N.

The total potential energy related to the bottom deformation given in FigIII.9 which is transferred to the sea level oscillations is calculated as (see eq.I.43 and I.48)

$$E_p = 0.5 \int \int \rho g \zeta^2 R_\circ^2 \cos\phi \delta\phi \delta\lambda \tag{III.11}$$

Calculation over the area of deformation sets the potential energy to 5.39×10^3TJ (terra joule). The energy released by the 2004 Indian Ocean earthquake was estimated at 1.1×10^5TJ (USGS Energy and Broadband Solution). Therefore, only approximately 5% of the total energy is transferred into tsunami generation.

b) Samoa Tsunami of September 2008.

On 29 September 2009 an earthquake of $M_w = 8$ occurred off the Samoa Islands and generated a tsunami with height of 2.7m near the coast of American Samoa Islands in Pago Pago. The earthquake occurred near the Tonga Trench (FigIII.10), located in the Pacific Ocean (the largest depth in the trench is 10.882 m). The high level of seismicity in the region is due to relatively fast motion of the Pacific Plate which dives beneath the Australian Plate. As the Pacific Plate moves westward, sinking beneath the Australian Plate the faults are forming. This earthquake was particularly unusual as it did not occur on the inter-plate thrust fault within the subducting Pacific Plate but further (to the East) out on the outer-rise region. Outer-rise earthquakes are caused by extreme stresses that result in bending within the subducting oceanic plate itself before it enters the subduction zone. The earthquake epicenter was located at lon=172.073 W and lat=15.509 S. The distribution of aftershocks, the quake's magnitude and the focal mechanism analysis suggest that ruptures length was approximately 175 km, along one or more normal faults on the outer-rise of the subducting Pacific Plate.

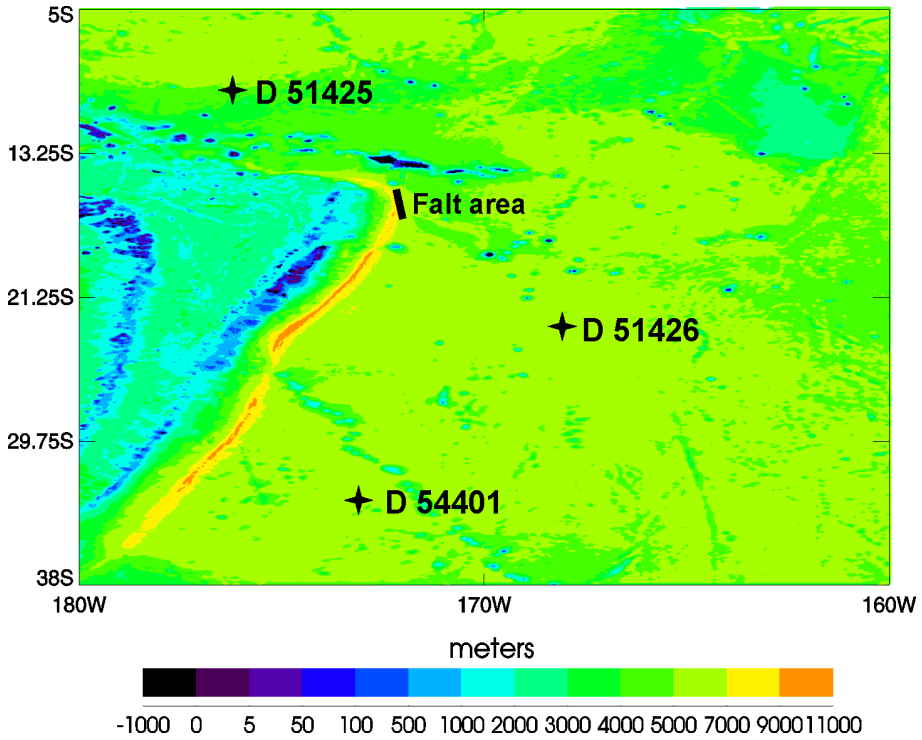

Figure III.10 Bathymetry in the region of Samoa Tsunami. The tsunami was recorded by the three NOAA Dart Buoys.

The generation mechanism for the Samoa tsunami will be based on the static sea floor uplift caused by the event on the outer-rise region of the plate and not by the abrupt slip at the plate interface as was the case of the Indian Ocean tsunami. Permanent, vertical sea floor displacement is computed using the static dislocation formulae from **Okada (1985)**. Inputs to these formulae are fault plane location, depth,

strike, dip, slip, length, and width as well as seismic moment and rigidity. The program to compute the displacement is called okada.f90 and it includes the all_input_okada block. The input file to this program named fault_2009_USGS.txt contains data compiled from the USGS Website: ftp://hazards.cr.usgs.gov/weekly/qedevents.txt. Along with the above data the depth distribution on 0.5' grid near the Tonga Trench is compiled in the file: samoa_30s_G_rec.dat. The more complicated distribution of the bottom deformation is given in the finite fault model constructed by G. Hayes, http://earthquake.usgs.gov/earthquakes/eqinthenews/2009/us2009mdbi/finite_fault.php.

The computed sea bottom displacement using the Okada formulae is given in the FigIII.11.

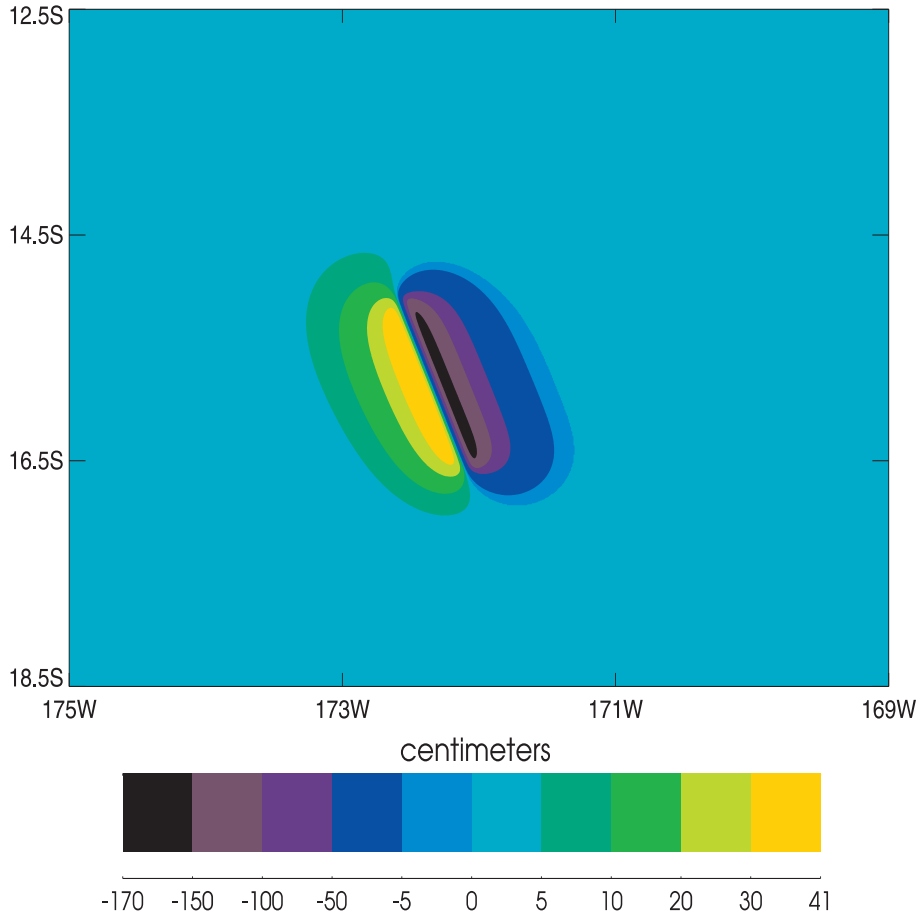

Figure III. 11. The source deformation contours for Samoa 2009 Tsunami. Maximum uplift is 40.4 cm and maximum subsidence is approximately -164.7 cm.

Failure of a normal fault on the outer rise as described in the FigIII.11 is still modeled by the traditional double-couple (DC) source, when positive displacement is associated with the negative bottom displacement. Although such fault differs from the faults at the plate interface since the absolute value of the maximum uplift is smaller than the maximum subsidence.

The bottom deformation served as input data for the tsunami calculations based

on the equations of motion and continuity. Our aim is to compare time series obtained from computations and observations recorded by the Dart Buoys. The purpose is to give preliminary comparison based on the source function from FigIII.11. The buoys against which the computations are compared are located to the north-east (D 51425) to the south (D 54401) and to the south-west (D 51426) from the rapture area (FigIII.10). The maximum energy is radiated toward E, N-E striking Samoa Island Chain and toward W, S-W striking the Island Arc Chain which is parallel to the Tonga Trench. The reflected signals from these island chains sends towards the south the energy flux which is stronger than the initial wave arriving strait from the source (FigIII.12).

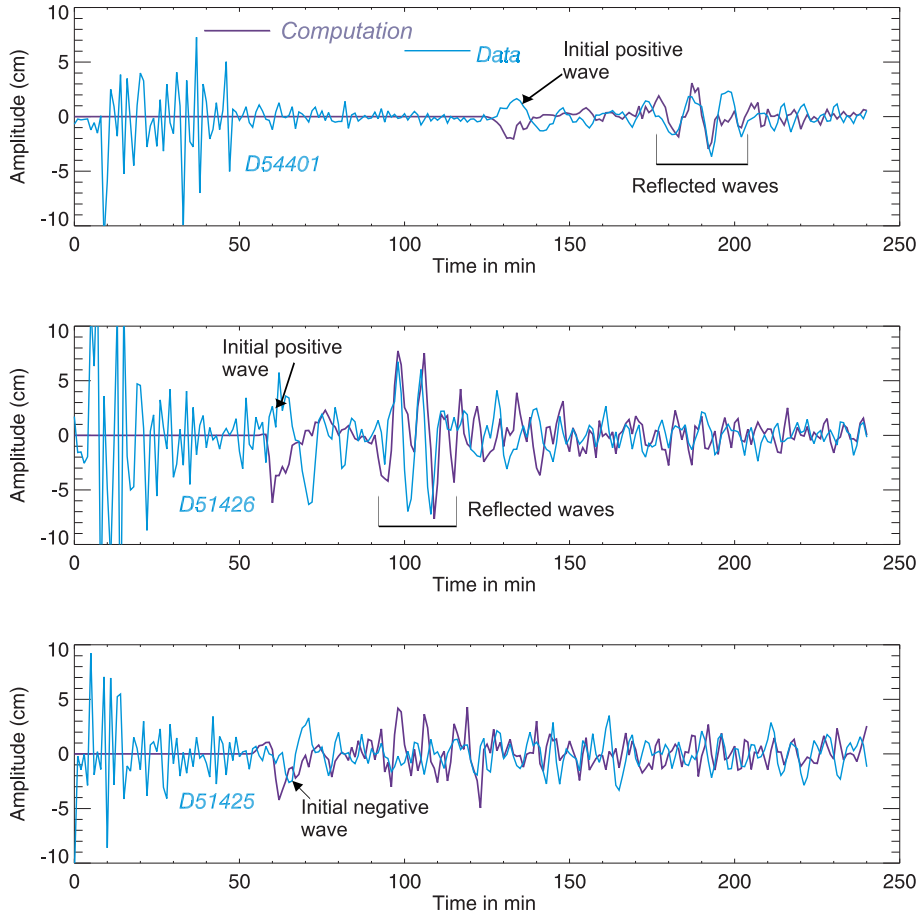

Figure III. 12. Time series of the sea level data recorded by Dart Buoys and computed from the source function given in FigIII.11.

A negative initial wave is recorded by D 51425 (located northward from the fault) and is also given by computations. The buoys toward the South, South-West (D 51426 and D 54401) show an initial positive wave while computations give the negative initial waves. Amazingly the reflected signal in southern buoys is well depicted from the measurements and computations. All this indicate that the double-couple source is too simple and that a stronger positive deformation should be present in the Southern part of the fault. The comprehensive discussion of the possible complications related to the normal faults is given by **G. Pararas-Carayanis**

(http://www.drgeorgepc.com/Tsunami2009Samoa.html). He suggests that the D-C source may not reflect all the complicated processes since "*it is possible that none of the solutions depict all the source characteristics, particularly if there was rotation or a slight extrusion of crustal material along a transform fault at the southeastern end of the designated source. Such source mechanism could account for the abnormal tsunami wave recorded at the DART gauge to the south*".

5. Landslide generated tsunamis

Tsunamis can be generated directly by seismic impact. However, in some seismic events, tsunamis appear to be much larger than expected from their seismic waves. Examples of such earthquakes include the 1896 earthquake in Sanriku, Japan, (M_w=8.0 and runup=38.2 m, Bryant, 2008), the 1946 Aleutian earthquake (M_w=8.2 and runup= 35 m, Tanioka and Seno, 2001; Fryer et al., 2004; López and Okal, 2006). The unusual events the 1963 and 1975 in Kurile Islands, and the 1960 earthquake in Peru (Okal, 1993; Pelayo and Wien, 1992) suggests anomalously long source durations and large seismic moments comparing to the regular earthquake. For some of these earthquakes, it has been proposed (Kanamori, 1985) that the caused tsunamis were triggered by the massive failure of the sea floor in the form of giant submarine landslides. This hypothesis has been supported by direct observations of such tsunami generating or tsunamigenic landslides as those triggered by earthquakes off the Grand Banks of Newfoundland (1929) (Heezen and Ewing, 1952; Fine et al., 2005), Alaska (1958) (Miller, 1960; Mader, 1999, Mader, 2004; Fritz et al., 2001), Alaska (1964) (Coulter and Migliaccio, 1966; Plafker et al., 1969; Lander and Lockridge, 1989). Submarine landslides usually result from slumping of unconsolidated sediments due to earthquakes but the slope failure can be triggered by the erosion and sea level changes as well (Keating et al., 2000). Volcanic tsunamis can occur by submarine explosive activity, but more commonly by the entrance of debris avalanches or debris flows into the sea. Debris avalanches leave sometimes volcano summit with velocity of 100 m/s. The tsunami generation process by the volcanic debris is similar to the landslides.

In general, the following three stages in the evolution of the landslide-generated tsunami can be distinguished: (I) the slope failure; (II) the post failure landslide; and (III) the tsunami generation and propagation. Each of these stages represents a number of consecutive processes. Modeling of the tsunami wave generation (Stage III) is frequently performed in separation from Stage II. Most numerical simulations have to assume the landslide motion as an input rather than modeling the whole generation process. Often, tsunami models implement (Jiang and LeBlond, 1992) a coupling of Stage III with the post failure landslide evolution (Stage II), which in turn is a sequence of the downslope sliding or slumping of the sediments (Lee and Edwards, 1986), possibly followed by the turbidity current (Heezen and Ewing, 1952, Nisbet and Piper, 1998) and a turbidite deposit (Rothwell et al., 1998).

Clearly, we should consider the slope failure (Stage I) also as a dynamic process leading to the moment when the slope reaches the state of limiting equilibrium. Without the significant initial velocity it is difficult to explain high maximum velocities of the observed landslides - an essential parameter defining the tsunami wave height (Pelinovsky and Poplavsky, 1996). Although the new mechanism observed both in laboratory and in

nature, the hydroplaning of sediments in the subaqueous debris flows produces the needed high velocities. The hydroplaning dramatically reduces the bed drag, thus increasing head velocity, this in turn promotes sediment suspension and turbidity-current formation (Mohrig et al.,1998; Elverhøi et al., 2005). The stability of submarine slopes (Stage I) and the landslide movement (Stage II) can be successfully analyzed using the FLAC code (Lobkovsky et al., 2005) applied in geomechanical modeling. The explicit difference scheme enables the modeling of nonlinear behavior of pore-saturated sedimentary masses under the condition of plastic flow above the yield strength.

The various mechanism of transferring energy from landslide to tsunami have been tested through analytical solutions, hydraulic and numerical modeling. The conventional and frequently employed model of tsunami generation, assumes that the rigid bottom motion imparted by the underwater earthquake is transferred to the surface wave. The time period of interaction is defined by the earthquake. Similar approach can be used for investigation of the water waves induced by an underwater landslide. To simulate the complicated motion of a landslide, one ought to take into account the downslope component of the rigid bottom motion. Velocity of that movement should depict the velocity of debris avalanches.

The well known theoretical solution for the landslide movement, was constructed by Kajiura (1963). The submarine landslide was modeled by a rectangular slab which moved with the constant speed at the ocean bottom. The coupling between the landslide and the water was based on the assumption of impermeable rigid bottom interacting with the water over specific time period. Because parameters of the problem i.e., slab length and thickness, and water depth are defined, the Kajiura's (1963) solution often serves for comparison against laboratory and numerical results. Numerical experiments performed by Aida (1969) used above solution to study a progressive deformation of the sea bottom over constant depth. After comparison was made against the Kajiura (1963) solution, the numerical model results were extended to the sloping bottom. Due to possibility of the large waves generated by huge rock falls or landslide this phenomenon plays an important role in designing the water structures by engineers. For such applications Noda (1970) constructed two analytical solutions using assumptions of continuity of velocity between landslide and water, and volume conservation of a landslide. Two types of landslides were considered to produce estimates of water velocities and waveheights.

The first one, the vertical landslide, was modeled by box dropping down on the water surface at one end of a semi-infinite channel. The velocity-time history of the box as it falls through the water is assumed to be known. The second type, the horizontal landslide, was generated by the vertical wall moving in the water. Again the velocity-time history of the moving wall was assumed to be known. Derived analytical solutions were compared with earlier laboratory experiments of Wiegel (1955), in which for generation of the water waves, various bodies were dropped vertically or moved along the inclined bottom. The theory differ from observations when the ratio of slide thickness to bottom depth was finite. The limitations of the theory resulted from linear solutions, the nonlinear interactions were omitted. The rigid bottom deformation, conservation of the landslide volume and continuity of the movement between the landslide and fluid are important assumptions of the above theories. The solid block experiments showed the difference between subaerial

and subaqueous landslide on the wave generation.

The solid block experiments converted between 3 and 7 % of the kinetic block energy into wave energy. The energy conversion increased with decreasing initial submergence, but remained significantly lower than in subaerial landslide impacts with energy conversions up to 50 % (Kamphuis and Bowering, 1970; Fritz et al., 2004; Ataie-Ashtiani and Nik-Khah, 2008).

Our goal in this chapter is to describe an approach to the landslide tsunami generation through the two-dimensional, vertically integrated model. First, based on the previous computation of a rigid block motion along the vertical direction, the investigation will describe tsunami generated by the block moving along the horizontal direction. Subsequently, including friction, the block motion along the inclined surface will be considered. The two-layered motion equations (Imamura and Imteaz, 1995) will aid to formulate a more complicated problem of water/sediment interaction.

Typically landslide is composed of unconsolidated sediments which move downslope and accumulates at new location. The interaction of the unconsolidated sediments is not always the volume preserving process. The actual process of landslide entering into fluid and interaction with fluid is so complicated that whenever the new models which describe the new physics are introduced they ought to be compared with the previous results derived for the rigid bottom deformation. Because many materials such as lava, river sediments or snow behave approximately as Bingham plastic fluid, Jiang and LeBlond (1993) studied underwater plastic mudslide using this constitutive law.

6. Simple models of tsunami generation by a submarine slide

The simplest model of a landslide is a rectangular bottom displacement which is moving along the bottom with the horizontal velocity V (FigIII.13).

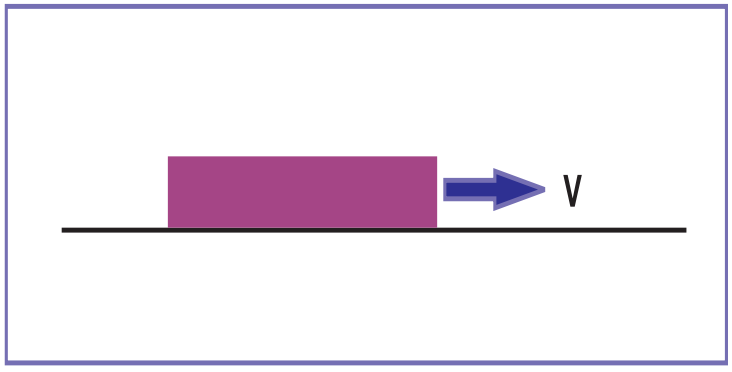

Figure III.13 A simple model of a submarine slide.

Analytical solutions for this problem were found by Pelinovsky (1996, 2003) and by Tinti and Bertolucci (2000a). The solution is given by a superposition of three waves. One of them is forced by the slide and stays above the moving slide. Out of the source region the two free waves are propagating towards the left and the right with the phace speed of the long waves. To be able to identify these three waves let's consider solution of eq. III.3

$$\frac{\partial^2\zeta}{\partial t^2} - gH\frac{\partial^2\zeta}{\partial x^2} = \frac{\partial^2\eta}{\partial t^2} \tag{III.12}$$

for the horizontally moving bottom deformation described by $\eta = \eta_0(x - Vt)$.

Eq. III.3 with this forcing function reads

$$\frac{\partial^2\zeta}{\partial t^2} - gH\frac{\partial^2\zeta}{\partial x^2} = V^2\frac{\partial^2\eta_0}{\partial\tau^2} = V^2F(x - Vt) \tag{III.13}$$

Here $x - Vt = \tau$ The solution to eq.III.13 can be searched as a sum of a free and forced waves

$$\zeta = \zeta_1 + \zeta_2 = \zeta_1(x - ct) + A\eta_0(x - Vt) \tag{III.14}$$

Introducing eq.III.14 into III.13 we obtain two sets of equations. One to define free solutions from which follows that $c^2 = \sqrt{(}gH)$, and therefore the two waves propagates with the phase velocity $\pm\sqrt{(}gH)$. The second set, namely

$$A\big[V^2\frac{\partial^2\eta_0}{\partial\tau^2} - c^2\frac{\partial^2\eta_0}{\partial\tau^2}\big] = V^2\frac{\partial^2\eta_0}{\partial\tau^2}$$

serves to define constant $A = V^2/(V^2 - c^2)$.

The motion of the free surface is described in terms of the three waves as

$$\zeta = \zeta_1(x \pm ct) + \frac{V^2}{V^2 - c^2}\eta_0(x - Vt) \tag{III.14a}$$

For slow ($V < c$) and fast ($V > c$) moving bottom slides the forced solution changes its character. Due to nature of the above solution the important change occurs if $V \simeq c$. When the speed of the forcing function and the phace speed of free waves in the ocean are equal the resonance enhancement of the sea level will follow. The landslide velocity is of the order of 25 m/s and the phase velocity of the free wave in the deep ocean of 4000 m depth is close to 200 m/s. Therefore, while the forced wave travels with velocity V the free waves radiate out from the source region and are separated from the generation area (especially for the longer propagation times). The resonance condition for the slide of 25 m/s speed requires much shallower water bodies.

The construction of this simple source proceeds at the computer in two steps. At computational lattices located to the right from the center of the channel, the bottom is lifted up and then moved horizontally by including the consecutive lattice. Thus if the horizontal spatial grid is 10 m and the time step is 10^{-2} s using the slide speed of 25 m/s requires 40 time steps (0.4 s) to travel 10 m distance. During the same time span the free wave in a 3 km deep ocean ($c \simeq 171.5$ m/s) travels 68.6 m. The Fortran program source_slide.f90 is very similar to the one used previously for the tsunami generation by the vertical bottom displacement, only subroutine bottom_def is a new addition to simulate the slide movement. The data block is called block_slide.f90. In each computational lattice the bottom is lifted up to 200 cm in about 0.02 s and afterwards moved horizontaly. The

sea level deformation after 5000 s from the onset of the motion is given in FigIII.14. At this time moment the slide moved about 125 km to the right from the initial position.

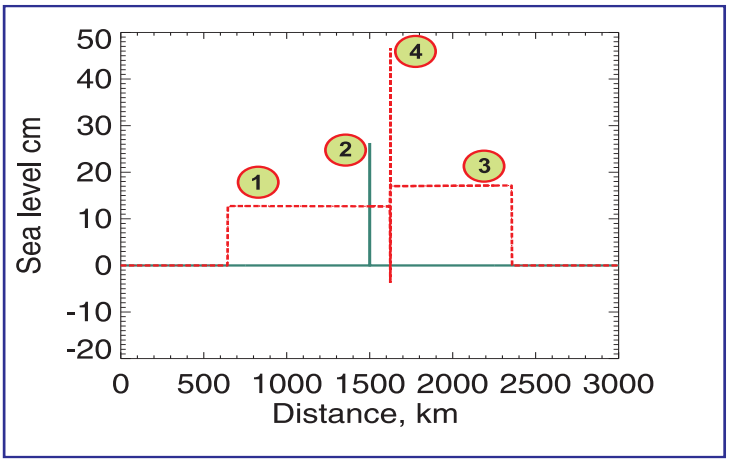

Figure III.14 A free surface responce to a moving submarine slide. Slide moves into positive direction with speed (V < c): 1. negative wave 2. initial wave 3. positive wave 4. forced wave.

It is of interest to see that the forced wave region lags behind the front of the positive wave. The forced wave region consist actually of many short waves of the different amplitude and wavelength.

Second numerical simulation considers waves generated by the landlide when the horizontal speed of the slide and the phase speed of the free wave propagating out of the source region are equal ($V = c$). To fulfill this requirement the depth of the water body has been chosen as 63.775 m. The results are given in FigIII.15 at the time span of 5000 s from the initial disturbance.

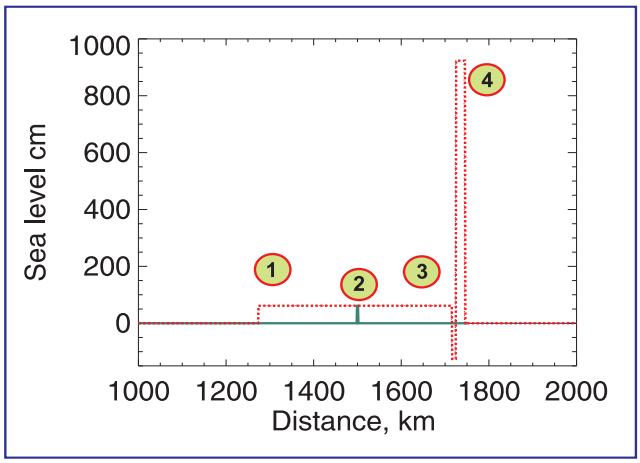

Figure III.15 A free surface disturbance due to the submarine slide traveling into positive direction (V = c): 1. negative wave 2. initial wave 3. positive wave 4. resonance domain.

As before the three waves are generated, i.e., the free waves traveling into positive and

negative directions along the x axis, and the forced wave of enormous positive amplitude close to 10 m (but depicting the negative disturbance as well). It is to be noticed that the resonce amplification occurs only at the front of the sea level disturbance traveling into the positive direction.

The third numerical experiment investigates the free surface disturbance as a responce to fast ($V > c$) moving bottom slides.

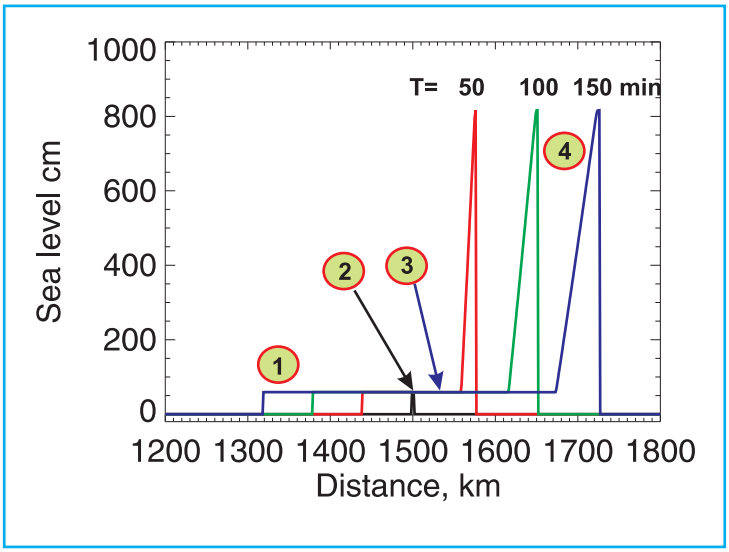

Figure III.16 A free surface disturbance due to the submarine slide traveling into positive direction (V > c): 1. negative wave 2. initial wave 3. positive wave 4. forced wave.

The 40 m depth is chosen, therefore the free wave travels with 19.8 m/s speed. As the forced signal travels faster (25 m/s) than the free wave it runs in front and depicts quite strong sea level change. This signal is quickly magnified from the initial disturbance and in 10 min time span it reaches constant value (approximately 800 cm) which is observed at the different times (see FigIII.16). The forced wave widens in space for the longer propagation times. During propagation it tapers off from the maximum of about 800 cm to the constant magnitude of 70 cm. The free waves travelling to the positive direction (just behind the forced wave) and to the negative direction display this constant height.

In summary, large amplitude responces of the water surface are caused by the fast -moving landslides ($V > c$) and by the by the resonant transfer of energy when slides moving with the same speed as the phase speed of the free wave ($V = c$), (Marchuk et al., 1983; Marchuk, 2008; Kowalik, 1997). These large amplitude waves require some time to grow as initial waves in Figures III.15 and III.16 are quite small. The slow-moving bottom disturbance ($V < c$) does not generate large amplitudes (FigIII.14). In the latter case the stronger signal is associated with the forcing region which is located behind the front of the positive wave.

7. Rigid body slide in the air

In a series of numerical experiments described in the above section we have investigated coupling between the slide and water body. The rigid body slide moved along the horizontal

plane and the properties of this slide were characterized only by its speed. The main conclusion is that coupling depends on the ratio of the slide speed V to the phase speed of the long wave $c = \sqrt{gH}$.

$$Fr = \frac{V}{c} \tag{III.15}$$

Where Fr is Froude number.

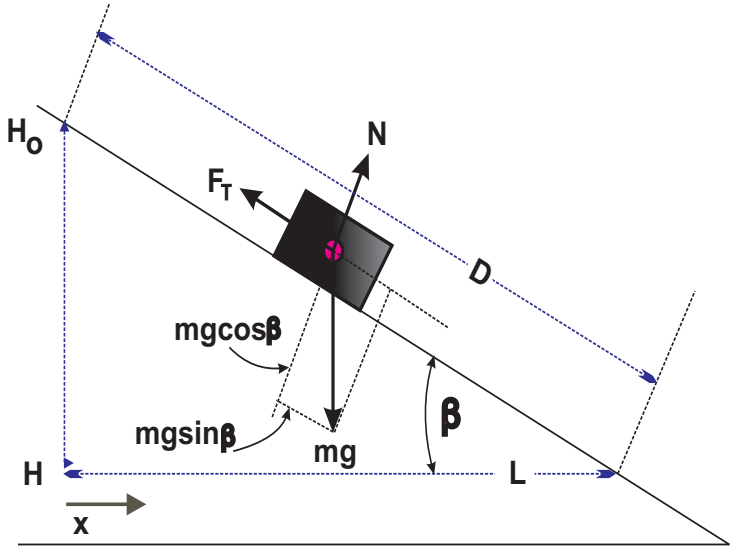

Figure III.17 A body forces for the block on inclined plane

The block will serve as a simple model for the landslide motion. Tsunami generation requires understanding of fundamental problems: the initiation of the landslide motion, the speed and the time of the flow, and the run out distance. The forces acting on the block are shown at the center of mass (FigIII.17). The weight of the block is $W = mg$, N is normal force exerted by the inclined surface, and F_τ is tangential (friction) force (often called Coulomb friction force). If the block is at rest, resolving the forces along the normal and tangential to the plain, the two equations are obtained

$$N - mg\cos\beta = 0 \qquad \text{and} \qquad F_{\tau,s} - mg\sin\beta = 0 \tag{III.16}$$

The driving force which starts the motion depends on the $\sin\beta$.

The ratio of the static friction force $F_{\tau,s}$ to the normal force is called the coefficient of static friction ν_s, therefore

$$F_{\tau,s} = \nu_s N \tag{III.16a}$$

If the angle β is increased the landslide is able to flow only when the driving force reaches a critical value. This angle is called β_c and we can introduce a new friction coefficient for the moving block, called the coefficient of kinetic friction (ν_k). The tangential force of friction is

$$F_{\tau,k} = \nu_k N \tag{III.16b}$$

Substituting eq.III.16a into III.16, yield for the static coefficient of friction, when the angle β is smaller than the critical one

$$\nu_s = \tan\beta_s \tag{III.17a}$$

The kinetic friction coefficient is defined for the angle larger than the critical one

$$\nu_k = \tan\beta_k \tag{III.17b}$$

With the above notation the equation of motion for the moving block along the inclined plane is

$$ma = mg\sin\beta_k - F_{\tau,k} = mg\sin\beta_k - \nu_k N = mg(\sin\beta_k - \nu_k\cos\beta_k) \tag{III.18}$$

The acceleration of the center of mass is

$$a = g(\sin\beta_k - \nu_k\cos\beta_k) = g(\tan\beta_k - \nu_k)\cos\beta_k \tag{III.19}$$

It can be further simplified for the small angles since $\cos\beta_k \simeq 1$

$$a = g(\tan\beta_k - \nu_k) \tag{III.19a}$$

The motion of the block (or the rigid slide) depends on the magnitude of the friction coefficient. Out of this simple model a few answers can be derived. Let's notice that velocity and acceleration are expressed as

$$v = \frac{dx}{dt} \qquad \text{and} \qquad a = \frac{dv}{dt} \tag{III.20}$$

and inserting dt from the velocity into acceleration, yield the following expression $vdv = adx$ and upon integration we arrive at

$$v_1^2 - v_0^2 = 2\int_0^{x_1} a dx \tag{III.21}$$

Here the velocity at the distance x_1 is expressed as the function of acceleration over the traveled distance.

Using a simplified expression (III.19a) for the acceleration of the block, the above can be integrated over the entire runout distance L,

$$v_L^2 - v_0^2 = 2\int_0^L a dx = 2\int_0^L g(\tan\beta_k - \nu_k)dx \tag{III.22}$$

For the inclined plane the slope is (see FigIII.17) $\tan\beta_k = (H_0 - H)/L$, therefore

$$v_L^2 - v_0^2 = 2g(H_0 - H - \nu_k L) \tag{III.23}$$

Assuming that at the end of the runout the block velocity is zero,

$$L = \frac{v_0^2}{2g\nu_k} + \frac{H_0 - H}{\nu_k} \tag{III.24}$$

Further simplification may be introduced when the initial velocity $v_0 = 0$

$$L = \frac{H_0 - H}{\nu_k} \tag{III.24a}$$

The runout distance of the block (or rigid body landslide) is defined only by the two parameters the hight of the fall and kinematic friction coefficient.

For the bulk estimate of the maximum velocity of the rigid landslide, the conservation of the energy of the free fall can be used. This energy is easily derived from eq.III.23 by neglecting friction

$$v_{max} = \sqrt{v_0^2 + 2g(H_0 - H)} \tag{III.25}$$

From the above simple consideration it is important to notice that presence of the initial velocity will influence both the runout distance and the maximum velocity of the landslide. The significant initial velocity is a key parameter in generating high velocities of the observed landslides (Pelinovsky and Poplavsky, 1996).

A more realistic block sliding will include the continuous change of the angle of incline as a function of the distance (Ward and Day, 2003). In such a case the angle β is a function of distance and the general expression for the acceleration reads,

$$a(x) = g[\sin\beta_k(x) - \nu_k \cos\beta_k(x)] = g[\tan\beta_k(x) - \nu_k]\cos\beta_k(x) \tag{III.26}$$

8. Rigid body slide in the water

The above section considers motion in the air (subaerial slide). The rigid slide in the water differs from the subaerial slide in two important aspects: the slide possesses different density from the water, therefore Archimedian force ought to be introduced and the friction coefficient in the water becomes a complex coefficient accounting for the tangential stresses between the block (slide) and the bottom and between block and the water. The slide's body resistance also may introduce additional energy loss.

The general force balance along the inclined plane was considered by Watts (1998)

$$m_s \frac{dv}{dt} = F_a + F_g + F_b + F_\tau + F_d + F_f \tag{III.27}$$

where F_a is the added mass force, F_g is the component of the gravitational force along the slope, F_b is the buoyancy (Archimedian) force along the slope, F_τ is the tangential friction force between block and the bottom sediments, F_d is the water drag force, and F_f is the force associated with the lubrication between the block and the bottom sediments. Out of this complex equation the approximate equation of motion is usually applied to investigate the landslide motion (Harbitz, 1992; Pelinovsky and Poplavsky, 1996).

$$m_s \frac{dv}{dt} = F_g + F_b + F_\tau + F_d \tag{III.28}$$

The mass of the landslide is $m_s = \rho_s W H_s L_s$, ρ_s is the density of the slide, W is the width, H_s is the thickness, and L_s is the length of the landslide.
The gravity force diminished by the buoyancy force along the incline is equal to (see FigIII.17)

$$F_g + F_b = (m_s g - m_w g) \sin \beta_k \tag{III.28a}$$

Here $m_w = \rho W H_s L_s$ is the mass of the water in the landslide volume.

The two components of the frictional forces are the Coulomb friction force associated with coefficient ν_k (see eq.III.18)

$$-g(m_s - m_w)\nu_k \cos \beta_k \tag{III.28b}$$

and the water drag force

$$F_d = \rho C_d S \frac{v^2}{2} \tag{III.28c}$$

Here S is the slide cross-section area, $S = W H_s$.

Introducing the above explicit expressions for the forces acting along the incline into eq.III.28, yields

$$\frac{dv}{dt} = g \frac{\rho_s - \rho}{\rho_s} (\sin \beta_k - \nu_k \cos \beta_k) - \frac{\rho}{\rho_s} C_d \frac{v^2}{2L_s} \tag{III.29}$$

As slide velocity initially is small and at the end of run out it slows to zero we may assume that at certain time it achieve maximum which is called the terminal velocity, therefore setting $dv/dt = 0$ we arrive at,

$$v_{term} = \sqrt{\frac{2L_s}{C_d} g \frac{\rho_s - \rho}{\rho_s} (\sin \beta_k - \nu_k \cos \beta_k)} \tag{III.30}$$

This velocity depends strongly on the drag coefficient C_d, Coulomb friction coefficient ν_k and the slide length L_s.

A somewhat different approach to the dissipation term was used by Harbitz (1992), instead of the drag force (F_d), the shear stresses along the bottom and the upper surface of the slide were considered. In this case the stresses are expressed by the formula similar to eq. I.50.

$$\tau^b = \rho_s c_d^b v^2 \quad \text{and} \quad \tau^u = \rho_s c_d^u v^2 \tag{III.31}$$

and the tangential force integrated over the horizontal surface of the slide reads,

$$F_{\tau,s} = W L_s (\tau^b + \tau^u) = W L_s \rho_s (c_d^b + c_d^u) v^2 \tag{III.32}$$

The slide acceleration (eq.III.29) under the tangential dissipative forces is expressed as,

$$\frac{dv}{dt} = g\frac{\rho_s - \rho}{\rho_s}(\sin\beta_k - \nu_k \cos\beta_k) - (c_d^u + c_d^b)\frac{v^2}{H_s} \tag{III.33}$$

and the terminal velocity is a function of slide thickness

$$v_{term} = \sqrt{\frac{H_s}{(c_d^u + c_d^b)} g\frac{\rho_s - \rho}{\rho_s}(\sin\beta_k - \nu_k \cos\beta_k)} \tag{III.34}$$

Solution to the time-dependent equation eq.III.29 is easily found if assumption is made that all coefficients are constant. Such solution was given by Pelinovsky and Poplavsky, (1996).

$$v(t_n) = v_{term}\tanh t_n \quad \text{and} \quad x(t_n) = x_0 + \frac{H_s}{(c_d^b + c_d^u)}\ln\cosh(t_n) \tag{III.35}$$

Here t_n is dimensionless time

$$t_n = \frac{(c_d^b + c_d^u)v_{term}t}{H_s}$$

Both velocity and coordinate x describe the center of the rigid slide and are very useful to understand kinematic properties of the slide (Watts, 2000; Watts et al., 2000).

There are many uncertainties associated with the frictional parameters in equations for the terminal velocity. We repeat here the rough estimates of the velocity given by Harbitz (1992) for the Massive Storegga Slides. The Storegga submarine slides occurred off the coast of western Norway. There were three slide events: the first slide occurred approximately 30,000-35,000 years B.P., the second and third slides occurred at approximately 7,000 years B.P. The First Storegga Slide (Bugge et al., 1988), probably caused by the seismic impact and/or methane hydrate decomposition, triggered the 150 km landslide, which accelerated to the maximum velocity of 50 m/s and generated a 19 m tsunami. According to Harbitz(1992) the First Slide can be described by the following parameters: $H_s = 114$ m, $\beta_k = 0.5°$, $\rho_s = 1700$ kg/m^3, $\rho = 1100$ kg/m^3, $\nu_k = 5\times10^{-3}$, $c_d^u = 0.95\times10^{-3}$ and $c_d^b = 0$.

The density of the ambient water is assumed to be the density of the turbidity currents, therefore it is slightly higher than the sea water density. The terminal velocity estimated from III.34 is 48.9 m/s. This is the estimated velocity, it will be reduced if the bottom stress and drag force are included. On the other hand the presence of a basal lubricating layer of water underneath hydroplaning slides as shown in the laboratory experiments by Mohrig et al.,(1998) offers a possible explanation for diminishing (or deleting) the bottom stress.

The phase velocity of the long wave propagating out of the Storegga Slide generating region (located approximately at 2000m depth) is 140 m/s. Since the slide velocity v is much smaller than the free wave speed, the signal (see FigIII.14) will quickly leave the generation area.

The simplified slide geometry Harbitz (1992) deduced from the field measurements. To introduce time/space changes of a slide the equation of continuity (I.69) is used

$$\frac{\partial(\zeta-\eta)}{\partial t}=-\frac{\partial}{\partial x}(Du)-\frac{\partial}{\partial y}(Dv) \tag{I.69}$$

Here $D=H+\zeta-\eta$ is the total depth which includes both the water and the bottom displacement. The bottom displacement η is changed according to the time/space history of the slide thickness. The Harbitz's actual model for the landslide was a block 114 m high, 170 km long, and 150 km wide that moved 150 km down slope. A parabolic velocity of landslide was assumed: starting at zero and accelerating to v_{term}, and then slowing down to zero over a distance of 150 km. The above delineated approach is used in the most numerical simulations. The main premise of this method is that the landslide motion is an input to the tsunami model, rather than modeling the whole landslide and tsunami generation as one process.

9. Two-layer, landslide-tsunami model

9.1. Small slopes of the bottom plane

We are going to make a first step towards the modeling the landslide-tsunami interaction as one process by assuming a two-layer geometry. The upper layer is the sea water and the lower water is composed of sediments and water. The purpose is to investigate process of tsunami generation by the landslide which is no more a rigid block but deformable body changing in time and space.

If tsunami is generated by an underwater landslide then the accounting of an water/landslide interaction may be approached through the different avenues: either the landslide is considered as a bottom which is variable in time and space, as it is done in Sec.8 of this chapter, or the landslide is taken as a second layer of fluid of different density from the water density. We introduce basic equations of motion and continuity to study of a two-layers flow in which both layers interact and establish flow with quite different pattern from the single layer flow. This approach allowed to shed some light on the complex mechanism of the landslide tsunami generation (Imamura and Imteaz, 1995; Imamura and Gica 1996; Shigihara et al., 2006).

A deformable landslide of density ρ_2 is outlined in FigIII.18. Comparison of the setting of the two-layer problem given in the Ch.I and the geometry of the flow described by the FigIII.18 shows that the landslide which is going to be modeled as a second layer is located over very limited space and the upper surface of the the second layer is not a horizontal plane as in Ch.I but is inclined to the horizontal plane. The surface of the lower layer fluid from FigIII.18 will plausibly depict some internal oscillations as shown in FigI.2 but due to gravity it will slide down along the inclined plane resembling the rigid slide movement.

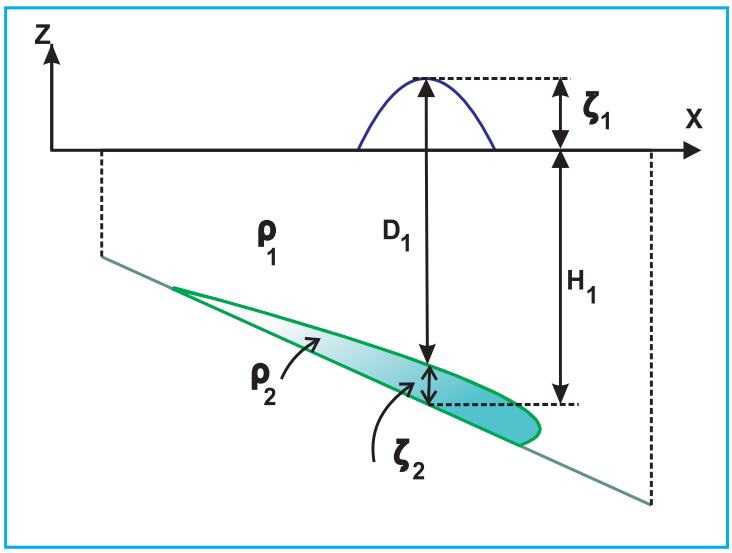

Figure III.18 A slide on the inclined bottom plane

The vertically integrated equation of continuity derived in Ch.I will hold as well for the problem given in FigIII.18. In the upper layer,

$$\frac{\partial(\zeta_1-\zeta_2)}{\partial t}=-\frac{\partial}{\partial x}(D_1u_1)-\frac{\partial}{\partial y}(D_1v_1) \qquad \text{(I.65, III.36)}$$

Here $D_1 = H_1 + \zeta_1 - \zeta_2$ is the total depth of the upper layer. In the lower layer the continuity equation is expressed as,

$$\frac{\partial\zeta_2}{\partial t}=-\frac{\partial}{\partial x}(D_2u_2)-\frac{\partial}{\partial y}(D_2v_2) \qquad \text{(I.66, III.37)}$$

Here $D_2 = \zeta_2$ does not refer to the internal surface oscillations as in Ch.I but it denotes the total depth of the second layer.

In the upper layer of fluid the equation of motion along the x direction is

$$\frac{\partial u_1}{\partial t}+u_1\frac{\partial u_1}{\partial x}+v_1\frac{\partial u_1}{\partial y}-fv_1=$$

$$-g\frac{\partial\zeta_1}{\partial x}-\frac{1}{\rho_1}\frac{\partial p_a}{\partial x}+N_h\Big(\frac{\partial^2u_1}{\partial x^2}+\frac{\partial^2u_1}{\partial y^2}\Big)+\frac{1}{\rho_1D_1}[\tau_{s,x}-r_1u'\sqrt{(u'^2+v'^2)}] \qquad \text{(I.67a, III.38a)}$$

and along the y direction

$$\frac{\partial v_1}{\partial t}+u_1\frac{\partial v_1}{\partial x}+v_1\frac{\partial v_1}{\partial y}+fu_1=$$

$$-g\frac{\partial\zeta_1}{\partial y}-\frac{1}{\rho_1}\frac{\partial p_a}{\partial y}+N_h\Big(\frac{\partial^2v_1}{\partial x^2}+\frac{\partial^2v_1}{\partial y^2}\Big)+\frac{1}{\rho_1D_1}[\tau_{s,y}-r_1v'\sqrt{(u'^2+v'^2)}] \qquad \text{(I.67b, III.38b)}$$

The lower layer is assumed to be a mud behaving as plastic material. We postpone the thorough discussion of the properties of the plastic material to the next section. Presently we assume that the pressure in such fluid is approximately hydrostatic and can be described as

$$p_2 = \rho_1 g(H_1 + \zeta_1 - \zeta_2) - \rho_2 g(z + H_1 - \zeta_2)$$

At the fluid interface $z = -(H_1 - \zeta_2)$ the second term is equal zero. At the bottom $z = -H_1$ the second term is $\rho_2 g \zeta_2$. The horizontal derivative of this pressure

$$-\frac{1}{\rho_2}\frac{\partial p_2}{\partial x} = -\frac{\rho_1}{\rho_2} g \frac{\partial \zeta_1}{\partial x} - \frac{\Delta\rho}{\rho_2} g\left(\frac{\partial \zeta_2}{\partial x} - \frac{\partial H_1}{\partial x}\right)$$

Equation of motion in the lower layer along the x direction now reads,

$$\frac{\partial u_2}{\partial t} + u_2\frac{\partial u_2}{\partial x} + v_2\frac{\partial u_2}{\partial y} - f v_2 = -\frac{\rho_1}{\rho_2} g \frac{\partial \zeta_1}{\partial x} - \frac{\Delta\rho}{\rho_2} g\left(\frac{\partial \zeta_2}{\partial x} - \frac{\partial H_1}{\partial x}\right)$$

$$-\frac{1}{\rho_2}\frac{\partial p_a}{\partial x} + N_h\left(\frac{\partial^2 u_2}{\partial x^2} + \frac{\partial^2 u_2}{\partial y^2}\right) + \frac{1}{\rho_2 D_2}\left[r_1 u' \sqrt{(u'^2 + v'^2)} - r u_2 \sqrt{(u_2^2 + v_2^2)}\right] \quad \text{(I.68a, III.39a)}$$

and along the y direction,

$$\frac{\partial v_2}{\partial t} + u_2\frac{\partial v_2}{\partial x} + v_2\frac{\partial v_2}{\partial y} + f u_2 = -\frac{\rho_1}{\rho_2} g \frac{\partial \zeta_1}{\partial y} - \frac{\Delta\rho}{\rho_2} g\left(\frac{\partial \zeta_2}{\partial y} - \frac{\partial H_1}{\partial y}\right)$$

$$-\frac{1}{\rho_2}\frac{\partial p_a}{\partial y} + N_h\left(\frac{\partial^2 v_2}{\partial x^2} + \frac{\partial^2 v_2}{\partial y^2}\right) + \frac{1}{\rho_2 D_2}\left[r_1 v' \sqrt{(u'^2 + v'^2)} - r v_2 \sqrt{(u_2^2 + v_2^2)}\right] \quad \text{(I.68b, III.39b)}$$

The following notation is used: u_1 and u_2 are the velocity components along the x direction in the upper and lower layers, H_1 is the depth from the undisturbed free surface to the bottom, when slide is absent. $D_1 = H_1 + \zeta_1 - \zeta_2$ is the thickness of the upper layer, ζ_1 denotes the oscillations of the free surface, $D_2 = \zeta_2$ is the thickens of the lower layer, $\tau_{s,x}$ and $\tau_{s,y}$ are the component of the surface stress along the x and y axes, respectively, $r_1 u' \sqrt{(u'^2 + v'^2)}$ and $r_1 v' \sqrt{(u'^2 + v'^2)}$ are components of **the interface stress** and $r u_2 \sqrt{(u_2^2 + v_2^2)}$ and $r v_2 \sqrt{(u_2^2 + v_2^2)}$ are components of the bottom stress along the x and y axes, respectively. The f is Coriolis parameter, g is the gravity acceleration, the $\Delta\rho = \rho_2 - \rho_1$, $r_1 = 1.3 \times 10^{-3}$, $r = 3 \times 10^{-3}$, N_h is the coefficient of the horizontal friction, $u' = u_1 - u_2$ and $v' = v_1 - v_2$.

In ensuing calculations the sea level terms will be changed as,

$$-\frac{\rho_1}{\rho_2} g \frac{\partial \zeta_1}{\partial x} - \frac{\Delta\rho}{\rho_2} g \frac{\partial \zeta_2}{\partial x} = \frac{\Delta\rho}{\rho_2} g \frac{\partial \zeta_1}{\partial x} - g\frac{\partial \zeta_1}{\partial x} - \frac{\Delta\rho}{\rho_2} g \frac{\partial \zeta_2}{\partial x} = \frac{\Delta\rho}{\rho_2} g \frac{\partial(\zeta_1 - \zeta_2)}{\partial x} - g\frac{\partial \zeta_1}{\partial x} \quad \text{(III.40)}$$

and in the similar way the derivatives along the y direction will be transformed.

9.2 Large slopes of the bottom plane

The horizontal derivative of the pressure in the lower layer

$$-\frac{1}{\rho_2}\frac{\partial p_2}{\partial x} = -\frac{\rho_1}{\rho_2}g\frac{\partial \zeta_1}{\partial x} - \frac{\Delta\rho}{\rho_2}g(\frac{\partial \zeta_2}{\partial x} - \frac{\partial H_1}{\partial x})$$

if compared against the pressure term given for the two-layer dynamics in ChI, shows the new term

$$\frac{\Delta\rho}{\rho_2}g\frac{\partial H_1}{\partial x}$$

This expression for the small inclinations when $\sin\beta_s \simeq \tan\beta_s$ is very similar to the gravity/buoyancy force acting on the slide along an inclined surface (III.29)

$$g\frac{\rho_s - \rho}{\rho_s}\sin\beta_s$$

For the larger angles we will change $\frac{\partial H_1}{\partial x}$ to

$$\sin\beta_x = \frac{\frac{\partial H_1}{\partial x}}{\sqrt{1+\frac{\partial H_1}{\partial x}}} \tag{III.41a}$$

and $\frac{\partial H_1}{\partial y}$ to

$$\sin\beta_y = \frac{\frac{\partial H_1}{\partial y}}{\sqrt{1+\frac{\partial H_1}{\partial y}}} \tag{III.41b}$$

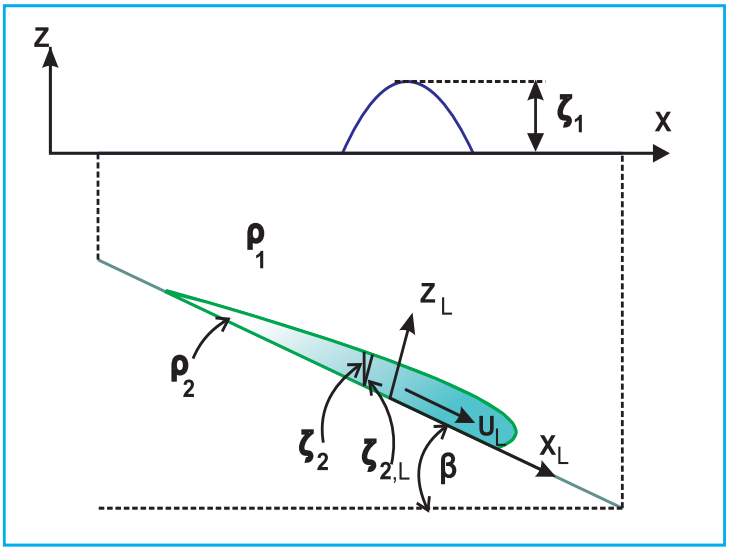

Figure III.19 A local system of coordinate for the slide on the inclined bottom plane

Above equations of motion are derived assuming the small inclination of the bottom slope. For the larger slopes the new equations are introduced to describe the slide motion based on the local system of coordinates attached to the nonerodible bottom, see FigIII.19. Along slope coordinates are x_L and y_L, the normal to the slope coordinate is z_L. The velocity components along the slope are $u_{2,L}$ and $v_{2,L}$. These velocities are averaged over the slide thickness along the normal to the slope coordinate. The equation of continuity in the new coordinates reads (Heinrich et al., 2001; Fernandez-Nieto et al., 2008)

$$\frac{\partial \zeta_{2,L}}{\partial t} = -\frac{\partial}{\partial x_L}(\zeta_{2,L} u_{2,L}) - \frac{\partial}{\partial y_L}(\zeta_{2,L} v_{2,L}) \tag{III.42}$$

The momentum equations are

$$\frac{\partial u_{2,L}}{\partial t} + u_{2,L}\frac{\partial u_{2,L}}{\partial x_L} + v_{2,L}\frac{\partial u_{2,L}}{\partial y_L} = -\frac{\rho_1}{\rho_2} g \frac{\partial \zeta_1}{\partial x_L} - \frac{\Delta\rho}{\rho_2} g\left(\frac{\partial \zeta_{2,L}}{\partial x_L}\cos\beta - \sin\beta_x\right) + FR_x \tag{III.43a}$$

$$\frac{\partial v_{2,L}}{\partial t} + u_{2,L}\frac{\partial v_{2,L}}{\partial x_L} + v_{2,l}\frac{\partial v_{2,L}}{\partial y_L} = -\frac{\rho_1}{\rho_2} g \frac{\partial \zeta_1}{\partial y_L} - \frac{\Delta\rho}{\rho_2} g\left(\frac{\partial \zeta_{2,L}}{\partial y_L}\cos\beta - \sin\beta_y\right) + FR_y \tag{III.43b}$$

The major difference due to the new system of coordinate is the $\cos\beta$ which changes pressure term arising from the landslide thickness ζ_2. The following rules (deduced from FigIII.19) can be applied to transformation from the regular to the local coordinates.

$$dx = \cos\beta dx_L \qquad \zeta_2 = \zeta_{2,L}\cos\beta \qquad u_2 = \cos\beta u_{2,L} \tag{III.44}$$

In the above equations FR denotes all friction forces, β is the local angle measured along the steepest slope, β_x and β_y are slope angles along the x and y directions. Equations for the landslide will be considered together with the water motion described by the regular set of equations (eqs III.36, III.37 and III.38). Two layers are linked by the total depth of the upper layer (eq. III.36) $D_1 = H_1 + \zeta_1 - \zeta_2$. Here $\zeta_2 = \zeta_{2,L}\cos\beta$. The link due to pressure has been already accounted for in eqs. III.43. The tangential stress between two layers will also cause an additional exchange of momentum between the water and landslide.

The force moving a slide along the x direction down a uniform slope is

$$F_\beta = -\frac{\Delta\rho}{\rho_2} g\left(\frac{\partial \zeta_{2,L}}{\partial x_L}\cos\beta - \sin\beta_x\right) \tag{III.45a}$$

To compare this force with the expression given for the small slopes

$$F_x = -\frac{\Delta\rho}{\rho_2} g\left(\frac{\partial \zeta_2}{\partial x} - \frac{\partial H_1}{\partial x}\right) = -\frac{\Delta\rho}{\rho_2} g\left(\frac{\partial \zeta_2}{\partial x} - \tan\beta_x\right) \tag{III.45b}$$

eq.III.45a is transformed to the regular system of coordinate using eq. III.44

$$F_\beta = -\frac{\Delta\rho}{\rho_2} g\left(\frac{\partial \zeta_2}{\partial x}\cos\beta - \sin\beta_x\right) = -\frac{\Delta\rho}{\rho_2} g\cos\beta\left(\frac{\partial \zeta_2}{\partial x} - \tan\beta_x\right) \tag{III.46}$$

The component along the x direction is $F_\beta \cos\beta$

$$F_x = F_\beta \cos\beta = -\frac{\Delta\rho}{\rho_2} g \cos^2\beta (\frac{\partial\zeta_2}{\partial x} - \tan\beta_x) \qquad \text{(III.46a)}$$

and therefore the difference between small and steep slopes is the $\cos^2\beta$ factor. For the 10° slope the factor is 0.97 and for the 20° slope it is 0.88, so the errors between two approaches are 3% and 12% respectively. In conclusion, the application of the small slope equations up to 25° seems to be reasonable.

10. Friction, dissipation and runout distance.

The slide motion, the runout distance and the final geometry when the motion is stopped will strongly depend on the fluid rheology. A critical part of the landslide modeling is the choice of the frictional forces. The slide parameters such as velocity and run-out distance are in the direct dependence on frictional forces. Let's investigate again equations of motion by considering different slide materials with different constitutive law. The differences will be expressed by the frictional forces. To discuss different frictional mechanisms the equation in the lower layer, along the x is written as,

$$\frac{\partial u_2}{\partial t} + u_2\frac{\partial u_2}{\partial x} + v_2\frac{\partial u_2}{\partial y} = -\frac{\rho_1}{\rho_2} g\frac{\partial\zeta_1}{\partial x} - \frac{\Delta\rho}{\rho_2} g(\frac{\partial\zeta_2}{\partial x} - \frac{\partial H_1}{\partial x}) + FR_x \qquad \text{(III.39a, III.47a)}$$

and along the y direction as,

$$\frac{\partial v_2}{\partial t} + u_2\frac{\partial v_2}{\partial x} + v_2\frac{\partial v_2}{\partial y} = -\frac{\rho_1}{\rho_2} g\frac{\partial\zeta_1}{\partial y} - \frac{\Delta\rho}{\rho_2} g(\frac{\partial\zeta_2}{\partial y} - \frac{\partial H_1}{\partial y}) + FR_y \qquad \text{(III.39b, III.47b)}$$

Here collectively all frictional forces are named FR. The right hand sides of equations contain forces which impart the landslide motion: these are the differences between gravitational and frictional forces. Typically the frictional forces are defined by the material of the heavy lower layer.

10.1. Viscous fluid.

The simplest approach to the underwater landslide modeling is to consider the two layer fluid. The heavy incompressible fluid is located along the bottom and it does not mix with the lighter upper layer. Its motion is dissipated by the two stresses a) basal stress along the lower surface of the landslide and b) upper surface stress between the water and the landslide. The tangential stress acting at the water-slide interface is usually much smaller than that of the basal stress and therefore can be neglected. The bottom stresses are expressed as the function of velocity and the bottom drag coefficient

$$\tau_{b,x} = \rho_2 r u_2\sqrt{(u_2^2 + v_2^2)} \qquad \text{and} \qquad \tau_{b,y} = \rho_2 r v_2\sqrt{(u_2^2 + v_2^2)} \qquad \text{(III.48)}$$

The friction forces in eq.III.47a and III.47b are

$$FR_x = -\frac{\tau_{b,x}}{\rho_2 D_2} = -\frac{r u_2 \sqrt{(u_2^2 + v_2^2)}}{D_2} \tag{III.49a}$$

$$FR_y = -\frac{\tau_{b,y}}{\rho_2 D_2} = -\frac{r v_2 \sqrt{(u_2^2 + v_2^2)}}{D_2} \tag{III.49b}$$

When Manning's law is adopted for a friction formula, the bottom stress is expressed as

$$\frac{\tau_b}{\rho_2} = \frac{g n^2}{{D_2}^{1/3}} u|u| \tag{III.50}$$

where n is the roughness coeficient (Fujima et al., 2002). This coefficient has dimension [s/m$^{1/3}$]. The Manning coefficient of 0.01 can be used for the smooth bottom slope and 0.015 for the rough slope. This small change of $5{\times}10^{-3}$ in the coefficient will strongly change velocity and the distance travelled by the landslide, thus pointing to the delicate balance between gravitational and frictional forces.

Together with the bottom stresses the internal stress which imitates the horizontal friction can be introduced (Shigihara et al., 2006). Definition of the horizontal friction given in eqs.I.8 and I.9 is used. The additional terms in the frictional forces related to the horizontal friction are written as

$$FR_x = N_h \Delta u \qquad \text{and} \qquad FR_y = N_h \Delta v \tag{III.51}$$

Here N_h is the horizontal viscosity coefficient. Two-dimensional Laplace operator Δ is defined as $\Delta = \dfrac{\partial^2}{\partial x^2} + \dfrac{\partial^2}{\partial y^2}$. The horizontal viscosity coefficient of the order of 100 cm^2/s was chosen by Shigihara et al., (2006) to influence the slide dynamics.

In the real landslide simulation the main problem to be solved is calculation of the runout distance. Experiments with fluids in a water tank show that the spreding will be continuous until the fluid is stoped by the capillary forces. Therefore, generally the viscous fluid is unable to simulate all stages of a landslide.

The use of the horizontal viscosity allows us to make and additional step by assuming that the heavy fluid is actually a granular flow of sediments mixed with the water. In such flow the small tensile stresses will keep sediment particles from interaction. This motion is similar to the fluid behavior and therefore can be expressed as the heavy fluid motion. On the other hand the compressive stresses will bring the sediment particle closer, hence during this process an additional internal pressure will be generated in the sediments. For simplicity we may express such pressure as

$$p = -A_p\left(\frac{\partial u}{\partial x} + \frac{\partial v}{\partial y}\right) \qquad \text{for converging flow} \quad \frac{\partial u}{\partial x} + \frac{\partial v}{\partial y} < 0 \tag{III.52a}$$

$$p = 0 \qquad \text{for diverging flow} \quad \frac{\partial u}{\partial x} + \frac{\partial v}{\partial y} > 0 \tag{III.52b}$$

The force imparted by the additional pressure along the x axis is expressed as

$$-\frac{\partial p}{\partial x} = A_p(\frac{\partial^2 u}{\partial x^2} + \frac{\partial^2 v}{\partial x \partial y}) \tag{III.53a}$$

and along the y axis as

$$-\frac{\partial p}{\partial y} = A_p(\frac{\partial^2 u}{\partial y \partial x} + \frac{\partial^2 v}{\partial y^2}) \tag{III.53b}$$

By increasing internal pressure coefficient A_p we may bring the granular flow to the rest defined by the runout distance. Although the coefficient A_p is introduced for the limited subdomain of converging flow and it changes rather ubruptly comparing to the horizontal viscosity coefficient, their dimensions and physical meaning are the same.

10.2. Bingham fluid. Submarine sediments are often composed of clay minerals which dispay behavior similar to the Bingham visco-plastic fluid. In this fluid no deformation occurs untill the shear stress exceeds the yield stress. Above the yield stress the deformation is driven by the excess stress and the material behaves like a viscous fluid (Mei and Liu, 1987; Jiang and LeBlond, 1993; Fine et al., 1998). For the one-dimensional Bingham fluid flow, the stress-strain relation is defined as (Mei and Liu, 1987)

$$N\frac{\partial u}{\partial z} = 0 \qquad \text{if} \qquad |\tau| < \tau_y \tag{III.54a}$$

$$N\frac{\partial u}{\partial z} = \tau - \tau_y sgn(\frac{\partial u}{\partial z}) \qquad \text{if} \qquad |\tau| > \tau_y \tag{III.54b}$$

where τ is th shear stress, τ_y is the yield stress (Bingham yield stress) and N is the coefficient of dynamic viscosity. The main assumptions for the viscous landslide and its interaction with the upper fluid layer have been defined by Jiang and LeBlond (1993),

1. Both the water and the mud are homogeneous with distinct densities and there exists a sharp interface between water and mud.

2. The constitutive equation (eqIII.54) is valid only for the laminar flow.

3. The pressure within the landslide is assumed to be hydrostatic (see FigIII.18)

$$p_2 = \rho_1 g(H_1 + \zeta_1 - \zeta_2) - \rho_2 g(z + H_1 - \zeta_2) \tag{III.55}$$

According to Jiang and LeBlond (1993), the constitutive relations (eqIII.54) lead to two distinct flow zones flow. A shear zone in close proximity to the bottom where the shear stress exceeds the yield stress and the velocity varies along the z direction. A plug zone, located above the shear zone, where the stress is smaller than the yield stress, and the horizontal velocity is uniform in z (FigIII.20).

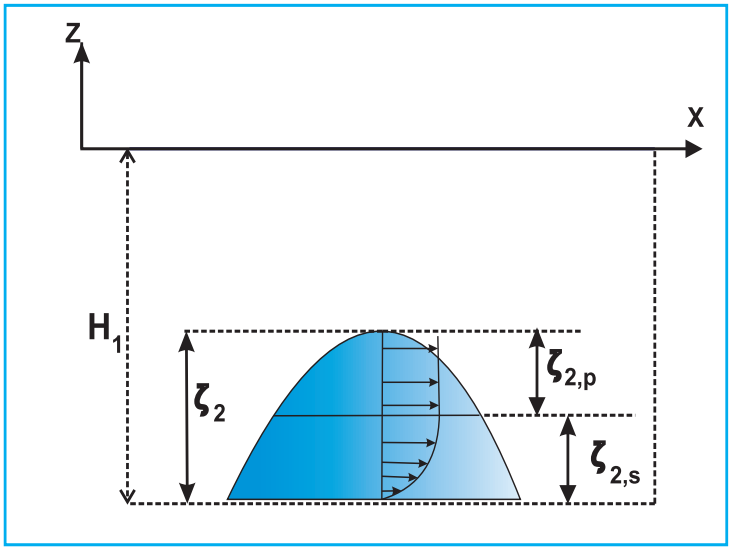

Figure III.20 Velocity distribution in a Bingham fluid. Shear zone at the bottom of $\zeta_{2,s}$ thickness and the plug region $\zeta_{2,p}$ of uniform velocity.

Integrating equations of motion I.8 and I.9 and continuity equation I.12 along the verical direction from $z = -H_1$ to $z = -(H_1 - \zeta_2)$ (Jiang and LeBlond, 1993; Fine et al., 1998) :

the continuty equation yields for the mass conservation

$$\frac{\partial \zeta_2}{\partial t} + \frac{2}{3}\Big[\frac{\partial(\zeta_2 u_2)}{\partial x} + \frac{\partial(\zeta_2 v_2)}{\partial y}\Big] = 0 \tag{III.56}$$

and the equations of motion in the mud layer now read:

$$\frac{2}{3}\frac{\partial u_2}{\partial t} + \frac{8}{15}\Big(u_2\frac{\partial u_2}{\partial x} + v_2\frac{\partial u_2}{\partial y}\Big) - \frac{2}{15}\frac{u_2}{\zeta_2}\frac{\partial \zeta_2}{\partial t} = -\frac{\rho_1}{\rho_2}g\frac{\partial \zeta_1}{\partial x} - \frac{\Delta\rho}{\rho_2}g\Big(\frac{\partial \zeta_2}{\partial x} - \frac{\partial H_1}{\partial x}\Big) - \frac{2Nu_2}{\zeta_2^2} \tag{III.57}$$

$$\frac{2}{3}\frac{\partial v_2}{\partial t} + \frac{8}{15}\Big(u_2\frac{\partial v_2}{\partial x} + v_2\frac{\partial v_2}{\partial y}\Big) - \frac{2}{15}\frac{v_2}{\zeta_2}\frac{\partial \zeta_2}{\partial t} = -\frac{\rho_1}{\rho_2}g\frac{\partial \zeta_1}{\partial y} - \frac{\Delta\rho}{\rho_2}g\Big(\frac{\partial \zeta_2}{\partial y} - \frac{\partial H_1}{\partial y}\Big) - \frac{2Nv_2}{\zeta_2^2} \tag{III.58}$$

While the left hand-sides of these equations got numerical coefficients, due to the parabololic velocity profile in the shear flow layer, the right hand-sides contain the same forces as in the viscous flow. The momentum dissipation is taken place by the bottom stress between the slide and nonerrodible bottom. According to eqsIII.49 the frictional forces are expressed as

$$FR_x = -\frac{\tau_{b,x}}{\rho_2\zeta_2} = -\frac{ru_2\sqrt{(u_2^2 + v_2^2)}}{\zeta_2} = -\frac{2Nu_2}{\zeta_2^2} \tag{III.59a}$$

$$FR_y = -\frac{\tau_{b,y}}{\rho_2\zeta_2} = -\frac{rv_2\sqrt{(u_2^2 + v_2^2)}}{\zeta_2} = -\frac{2Nv_2}{\zeta_2^2} \tag{III.59b}$$

Therefore, the bottom stresses in eqIII.57 and III.58 are

$$\tau_{b,x} = \frac{2\rho_2 N u_2}{\zeta_2} \quad \text{and} \quad \tau_{b,y} = \frac{2\rho_2 N v_2}{\zeta_2} \tag{III.60}$$

Presence of the viscosity coefficient allows to express the bottom drag coefficient as a function of the flow parameters

$$r = \frac{2N}{\zeta_2 \sqrt{(u_2^2 + v_2^2)}} \tag{III.61}$$

Numerical experiments which we have performed (program is not given here) for typical range of coefficients (Mei and Liu, 1987) $N = 20 - 2000$ cm^{2}s^{-1}, show that the behavior of the mud layer (runout and speed) very strongly depends on the value of the viscosity coefficient.

10.3. Granular flow.

Again to study landslide/tsunami generation and interaction a two-layer fluid is considered. The upper layer, is composed of a homogeneous fluid. The lower layer is fluidized granular material. The pores in the granular material are filled with the fluid of the upper layer. Dissipation in granular materials is generally described by a Coulomb-type friction law when the bottom stress is expressed as (cf eq.III.18)

$$\vec{\tau_b} = -\frac{\Delta\rho}{\rho_2} g \zeta_2 \cos\beta \tan\delta \frac{\vec{u}}{|\vec{u}|} \tag{III.62}$$

Here $\frac{\vec{u}}{|\vec{u}|}$ is a unit vector which defines the bottom stress direction.

The above Coulomb-type behavior we have ascribed before to the rigid body in the air and in the water. Under the name of granular flow one can understand many different media like a rock slide or sand slide. Those will be difficult to study by the same Coulomb type dissipation. While the rock slide behavior is akin to the rigid body slide, the sand slide will tend to move if the bottom slope is larger than the angle of repose and the slide will deaccelerate and stop if the bottom slope is smaller than the angle of repose. The angles of repose for the fluidized granular material can be quite smaller than the dry material displays in the air.

In the above formula δ is the dynamic friction angle. For debris avalanches it is in the range from 20° to 40°. When the bottom slope $\tan\beta$ is greater than the dynamic friction angle the granular flow will never stop. On the other hand if the dynamic friction angle is greater than the slope the granular flow may stop, but the rigid body will definitely stop. To understand the difference between rigid body and granular flow let's recall the momentum equation for the sliding rigid body in the water:

$$\frac{du_2}{dt} = g\frac{\rho_s - \rho}{\rho_s}(\sin\beta_s - \nu\cos\beta_s) \tag{III.63; III.29}$$

In this equation the drag force due to the lanslide form has been neglected, angles $\beta_s = \beta$ and $\nu = \tan\delta$. Therefore, when the bottom slope is equal the dynamic friction angle $\delta = \beta$, the above simplifies to

$$\frac{du_2}{dt} = 0 \tag{III.63a}$$

and if $\beta < \delta$ the rigid slide motion will dissipate. The force moving a deformable slide down a uniform slope is (see eqIII.43a and 46)

$$\frac{\partial u_2}{\partial t} = -\frac{\Delta\rho}{\rho_2} g\left(\frac{\partial \zeta_2}{\partial x}\cos\beta - \sin\beta\right) \tag{III.64}$$

Introducing Coulomb friction III.62 into this equation, yields

$$\frac{\partial u_2}{\partial t} = -\frac{\Delta\rho}{\rho_2} g\cos\beta\left(\frac{\partial \zeta_2}{\partial x} - \tan\beta + \tan\delta\frac{\vec{u}}{|\vec{u}|}\right) \tag{III.65}$$

Here the Coulomb friction was inserted as τ_b/ζ_2. If the deformable slide is moving along the bottom where $\delta = \beta$ the acceleration does not vanish as for the rigid body slide since it changes due to the slide thickness variability in the space,

$$\frac{\partial u_2}{\partial t} = -\frac{\Delta\rho}{\rho_2} g\cos\beta\frac{\partial \zeta_2}{\partial x} \tag{III.65a}$$

11. Numerical simulation of tsunami generated by an underwater landslide in a channel.

We start by computing a tsunami generated by an underwater landslide in a simple geometry of a channel. The two-layered fluid dynamics as described by eqs III.36 - III.39 is considered. The landslide motion is dissipated by the two stresses: basal stress along the lower surface of the landslide and upper surface stress between the water and the landslide. The horizontal friction is neglected. This set of equation is solved for the landslide on the inclined bottom as depicted in FigIII.18 with x axis directed along the channel. A simple bathymetry of an inclined bottom is given as

$$H_1 = h_l + h_b x \qquad \text{and} \qquad h_b = \frac{h_r - h_l}{L} \tag{III.66}$$

Here: h_l is the depth at the left end, h_r is the depth at the right end of the channel, and L is the length of the channel. The ratio $(h_r - h_l)/L$ defines the bottom slope. An initial landslide's shape is parabolic, given by an equation

$$\zeta_2 = \zeta_{2,c}\Big[1 - \frac{(x - x_c)^2}{L_s^2}\Big] \tag{III.67}$$

Here: ζ_2 is the second layer thickness , $\zeta_{2,c}$ is the maximum thickness which is located at the distance $x = x_c$, and L_s is the length of the slide. In numerical calculations the

length of the channel L =2500 m and the uniform slope with inclinations of 1%, 10% and 20% is considered. The depth at the left end of the channel is in all experiments equal to 100 m and at the right end of the channel the depth has been changed from 125 m to 600 m. The slide length is L_s =100 m and the initial maximum slide thickness $\zeta_{2,c}$ =25 m. In numerical simulation, the space step hx = 1 m, the time step $T = 1 \times 10^{-3}$ s. The following parameters are used: ρ_1 = 1 g cm^{-3}, ρ_2 = 1.4 g cm^{-3}, the bottom friction coefficient r = 0.003 and the inter-layer friction is r_1 = 0.0015. All computations in this section are done with the program: landslide2layer1d.f90. The data file is :block_2layer1d. Depth and the parabolic landslide are given in Subroutine: beach2. At the initial moment the parabolic landslide is positioned on the sloping bottom and the ensuing sliding process will change the shape of the landslide and the velocity distribution. The domain of the heavier fluid is denoted by cell number cell2(j)=1, the lack of the heavy fluid is indicated by cell2(j)=0, therefore the boundary between the lighter and heavier fluid is between cell2=1 and cell2=0. (j denotes the space index). Let's assume the boundary is located between j and j+1, thus cell2(j)=1 and cell2(j+1)=0. The distance traveled by the landslide into the lighter fluid domain during one time step is $L_t = Tv_2$ (assume $v_2 > 0$). If the velocity direction holds during the consecutive time steps, the distances are summed up during each time step until the total distance is larger than the space step of numerical computation hx at this moment the boundary (the landslide) is moved one step forward so that cell2(j+1)=1 and cell2(j+2)=0.

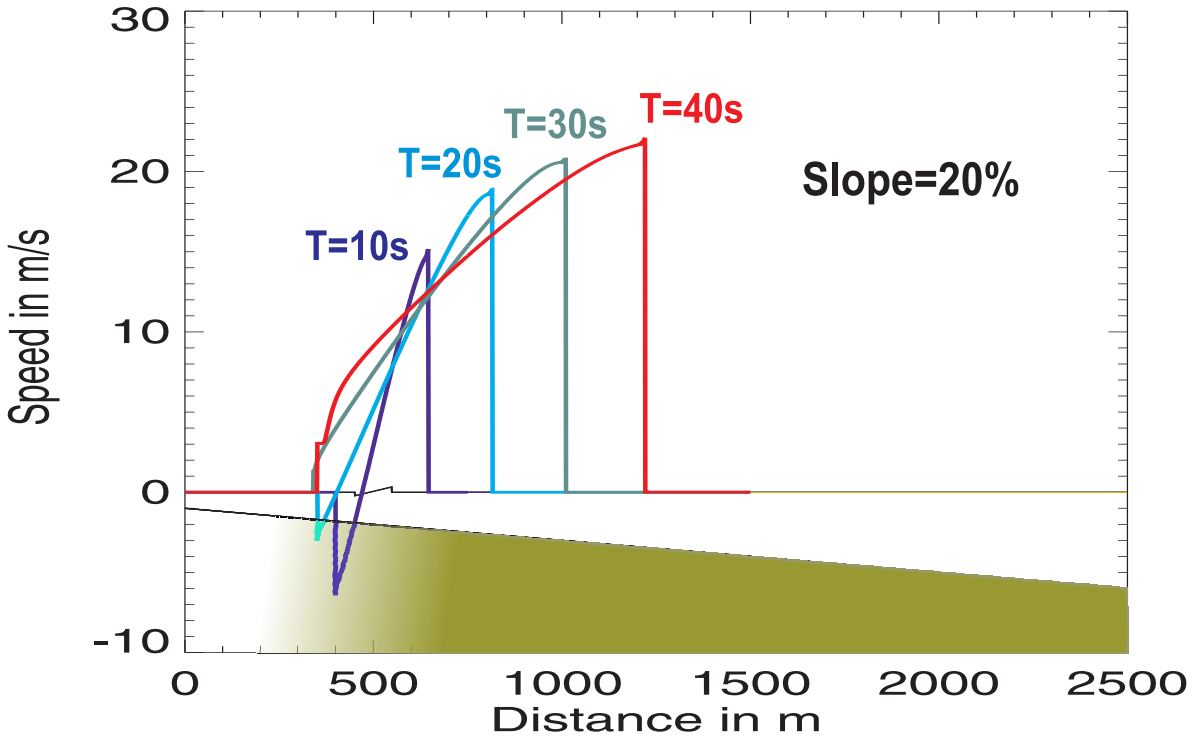

Figure III.21 A time-history of the slide velocity on the inclined bottom plane. The bottom slope is 20%. The shaded domain denotes the scaled bathymetry.

The typical slide velocity is given in FigIII.21 for the 20% bottom slope.

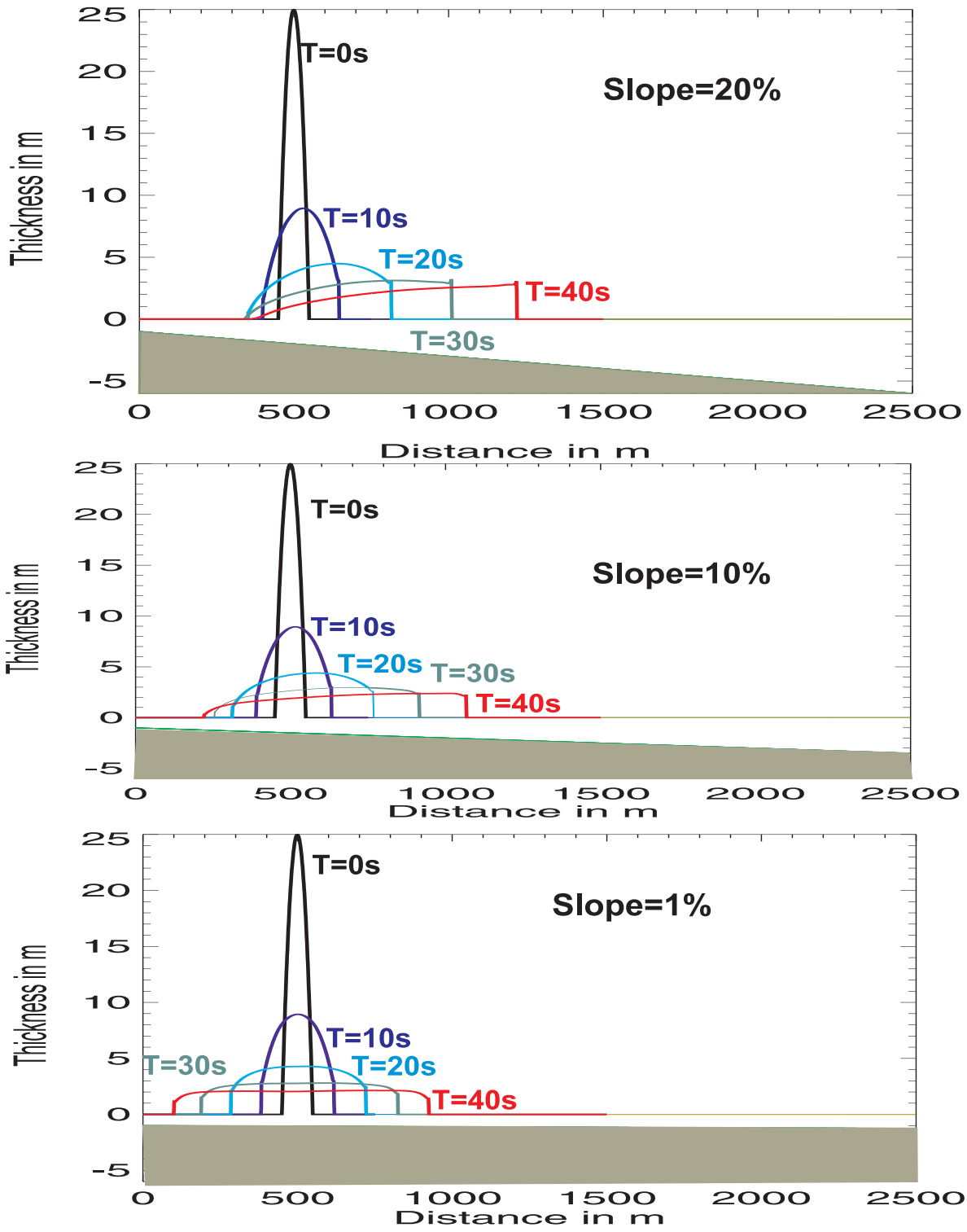

Figure III.22 A time-history of the parabolic slide on the inclined bottom plane. The bottom slope changes from 20%, to 1%. The shaded domain denotes the scaled bathymetry.

While the initial motion at the time $T = 10$ s and 20 s is taking place with the negative (upslope) and the positive (downslope) velocity, the accelerating motion sets in the entire slide body the positive (downslope) velocity ($T = 30$ s). In contrast to a rigid-body slide, which moves as an entity with a single speed, different parts of a viscous slide move with different speeds, causing the slide to spread.

The time-history of the slide movement is given in FigIII.22. As the bottom slope diminishes from 20% in the upper panel to 1% in the lower panel, the same initial parabolic slide is traveling the different distance down and upslope during the same time span. The average downslope velocity is 18.25m/s (upper panel), 14.4 m/s (middle panel) and 10.5 m/s (lower panel). The slide is moving upslope as well with the average velocity of 3.75m/s (upper panel), 7.5 m/s (middle panel) and 10 m/s (lower panel). The maximum sliding velocity of approximately 22 m/s occurs at the largest slope of 20%. The successive positions of the landslide surface and time history of the velocity distributions given in FigIII. 21 and 22 show that the downslope front is characterized by the strong change of velocity and amplitude over a few spatial cells. Although all numerical stability conditions are satisfied the strong changes of the level or velocity often cause numerical instabilities which express themselves as the short period oscillations. To remove these instabilities either an additional artificial viscosity is introduced (Jiang and LeBlond, 1993) or time/space filters are used (Kowalik and Murty, 1993). The evolution of the forced and the free surface waves in time together with the landslide successive positions describes FigIII.23. The coupling of the landslide to the free surface can be better understood if the shape of a simple landslide generated tsunami is recalled as plotted in FigIII.14. The basic components of the free surface motion are: the forced wave which propagates with the slide velocity and is "glued" to the landslide position, and the free waves propagating into the positive and negative directions as $\pm\sqrt{gH}$. In FigIII.23 all the basic elements of the free surface wave are explained at the time t=10 s. The positive free wave (2), as can be seen for the successive time positions, is moving much faster than the negative free wave (1) since the latter propagates upslope into the region of the smaller depth and the former is traveling downslope into the deeper water. The forced wave is structured with the tree elements: the oscillatory signal (3) above the main body of the slide, whose the wave length is growing in time as the slide length is increasing, and two intermittent signals (3a, 3b) caused by the front and back lobes of the slide. As the landslide time history depicts a diminishing the back lobe thickness (t=20 s) and the smooth change from the slide to the bathymetry is taking place, the forced signal due to the back lobe of the landslide disappears. On the other hand the front lobe of the landslide persists and the free surface signature associated with this lobe is present at all time steps. The rapid change of the amplitude and period of the free surface signal caused by the front and back of the moving landslide result in the numerical instabilities as such oscillations require the very fine temporal and spatial resolutions.

The longer time history of this landslide brings into scope the major problem related to the viscous fluid: the spreading of the landslide is continuous and it never stops. Thus one of the main objectives of the landslide dynamics i.e., calculation of the runout distance cannot be achieved.

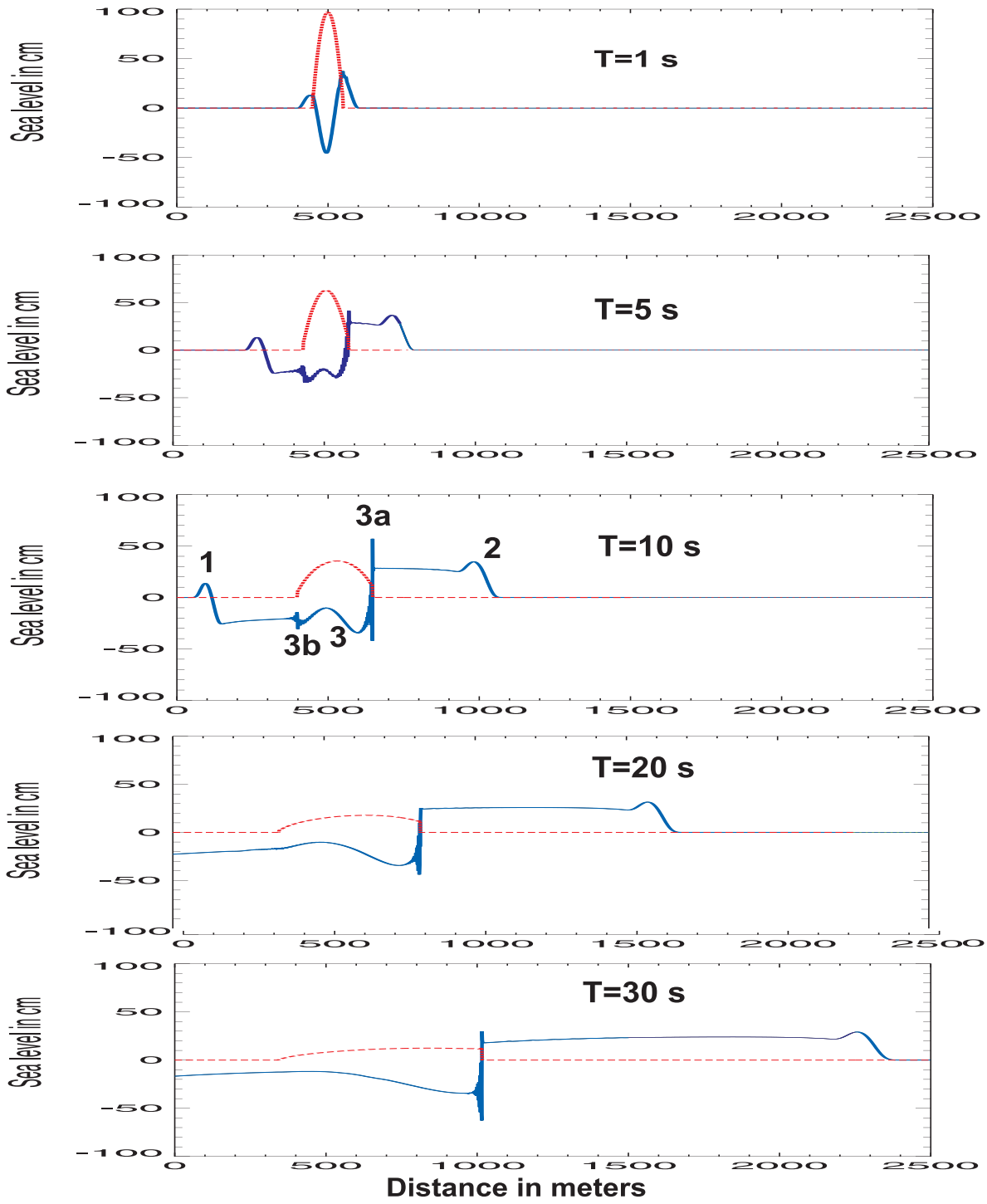

Figure III.23 A free surface response to a moving submarine slide. Slide thickness (red color) scaled to the figure. Sea level (blue). At the time t=10 s; 1. negative free wave, 2. positive free wave, 3. forced wave above the landslide, 3a. forced wave caused by the front of the landslide, 3b. forced wave at the back of the landslide.

12. Simple analytical solutions for an underwater landslide in a channel.

To study the landslide in an isolation from the upper layer of fluid let's consider the set of equations III.42 and III.43a in a channel

$$\frac{\partial \zeta_{2,L}}{\partial t} = -\frac{\partial}{\partial x_L}(\zeta_{2,L} u_{2,L}) \tag{III.68}$$

and

$$\frac{\partial u_{2,L}}{\partial t} + u_{2,L}\frac{\partial u_{2,L}}{\partial x_L} = -\frac{\Delta\rho}{\rho_2} g(\frac{\partial \zeta_{2,L}}{\partial x_L}\cos\beta - \sin\beta_x) + FR_x \tag{III.69}$$

Simplifying physics by neglecting external forces, dissipation and nonlinear terms we arrive at the system of equation

$$\frac{\partial \zeta_2}{\partial t} = -\zeta_2 \frac{\partial u_2}{\partial x} \tag{III.68a}$$

$$\frac{\partial u_2}{\partial t} = -\frac{\Delta\rho}{\rho_2} g \frac{\partial \zeta_2}{\partial x}\cos\beta \tag{III.69a}$$

which defines the free wave propagation in this media. (Here index L has been also neglected). Introducing the free wave solution in the form $(u_2, \zeta_2) = (u_0, \zeta_0)\Phi(x - ct)$ into these equations gives rise to a simple set

$$\zeta_2 u_0 - c\zeta_0 = 0, \tag{III.70a}$$

$$-cu_0 + \frac{\Delta\rho}{\rho_2} g\cos\beta\zeta_0 = 0 \tag{III.70b}$$

whose solution defines the well known dispersion relation as $c = \pm\sqrt{(g\zeta_2\frac{\Delta\rho}{\rho_2}\cos\beta)}$.

The frictionless landslide motion is a function of the landslide thickness ζ_2, the inclination angle β and the density difference between the upper and lower fluids. The celerity is further simplified if the upper fluid is the air

$$c = \pm\sqrt{(g\zeta_2\cos\beta)} \tag{III.71}$$

To account for the nonlinear terms the methods given for the dam-break problem (ChII, Sec.15) can be used. The full equation deduced from the method of characteristics describes the speed of the signal in the lower layer as (cf., Mangeney et al., 2000),

$$\frac{dx}{dt} = u \pm \sqrt{(g\zeta_2\frac{\Delta\rho}{\rho_2}\cos\beta)} \tag{III.72}$$

13. Numerical simulation of tsunami generated by an underwater landslide in a two-dimensional water body.

Above computations were based on numerical formulas for the 1-D channel as developed and tested in Ch.II. We now approach solution of the full set of equations in the 2-D space.

The vertically integrated equations in the upper layer are: equation of continuity (eq.III.36),

$$\frac{\partial(\zeta_1-\zeta_2)}{\partial t}=-\frac{\partial}{\partial x}(D_1u_1)-\frac{\partial}{\partial y}(D_1v_1) \tag{III.73}$$

equation of motion along the x direction (eq.III.38a)

$$\frac{\partial u_1}{\partial t}+u_1\frac{\partial u_1}{\partial x}+v_1\frac{\partial u_1}{\partial y}=$$

$$-g\frac{\partial\zeta_1}{\partial x}+\frac{1}{\rho_1D_1}[\tau_{s,x}-r_1u'\sqrt{(}u'^2+v'^2)] \tag{III.74a}$$

and along the y direction (eq.III.38b)

$$\frac{\partial v_1}{\partial t}+u_1\frac{\partial v_1}{\partial x}+v_1\frac{\partial v_1}{\partial y}=$$

$$-g\frac{\partial\zeta_1}{\partial y}+\frac{1}{\rho_1D_1}[\tau_{s,y}-r_1v'\sqrt{(}u'^2+v'^2)] \tag{III.74b}$$

Here $D_1=H_1+\zeta_1-\zeta_2$ is the total depth for the upper layer. In the lower layer the continuity equation is expressed as,

$$\frac{\partial\zeta_2}{\partial t}=-\frac{\partial}{\partial x}(D_2u_2)-\frac{\partial}{\partial y}(D_2v_2) \tag{III.75}$$

Here $D_2=\zeta_2$ does not refer to the internal surface oscillations as in Ch.I but it denotes the total depth of the second layer. The equations of motion in the lower layer are (eqs.III.47a and III.47b):

$$\frac{\partial u_2}{\partial t}+u_2\frac{\partial u_2}{\partial x}+v_2\frac{\partial u_2}{\partial y}=-\frac{\rho_1}{\rho_2}g\frac{\partial\zeta_1}{\partial x}-\frac{\Delta\rho}{\rho_2}g(\frac{\partial\zeta_2}{\partial x}-\frac{\partial H_1}{\partial x})+FR_x \tag{III.76a}$$

$$\frac{\partial v_2}{\partial t}+u_2\frac{\partial v_2}{\partial x}+v_2\frac{\partial v_2}{\partial y}=-\frac{\rho_1}{\rho_2}g\frac{\partial\zeta_1}{\partial y}-\frac{\Delta\rho}{\rho_2}g(\frac{\partial\zeta_2}{\partial y}-\frac{\partial H_1}{\partial y})+FR_y \tag{III.76b}$$

Frictional terms are expressed by the interlayer and basal stresses

$$FR_x=\frac{1}{\rho_2D_2}[r_1u'\sqrt{(}u'^2+v'^2)-ru_2\sqrt{(}u_2^2+v_2^2)]$$

$$FR_y=\frac{1}{\rho_2D_2}[r_1v'\sqrt{(}u'^2+v'^2)-rv_2\sqrt{(}u_2^2+v_2^2)]$$

The rectangular system of coordinates due to its simplicity is useful in developing equations and understanding the physics of tsunami. The tsunami generation and propagation takes

place on the spherical earth and therefore we recast above equations in the spherical system of coordinates introduced in Ch.I. We shall use the vertically integrated equation of motion and continuity (I.52)–(I.60) from Ch.I. For the upper layer fluid

$$\frac{Du_1}{Dt} - \frac{u_1 v_1 \sin\phi}{R\cos\phi} = -\frac{g}{R\cos\phi}\frac{\partial\zeta_1}{\partial\lambda} - \frac{1}{\rho_1 D_1} r_1 u' \sqrt{(u'^2 + v'^2)} \tag{III.77a}$$

$$\frac{Dv_1}{Dt} + \frac{u_1 u_1 \sin\phi}{R\cos\phi} = -\frac{g}{R}\frac{\partial\zeta_1}{\partial\phi} - \frac{1}{\rho_1 D_1} r_1 v' \sqrt{(u'^2 + v'^2)} \tag{III.77b}$$

$$\frac{\partial(\zeta_1 - \zeta_2)}{\partial t} + \frac{1}{R\cos\phi}\frac{\partial(D_1 u_1)}{\partial\lambda} + \frac{1}{R\cos\phi}\frac{\partial}{\partial\phi}(D_1 v_1 \cos\phi) = 0 \tag{III.78}$$

Here

$$\frac{D}{Dt} = \frac{\partial}{\partial t} + \frac{u_1}{R\cos\phi}\frac{\partial}{\partial\lambda} + \frac{v_1}{R}\frac{\partial}{\partial\phi} \tag{III.79}$$

The system of equation for the lower layer reads

$$\frac{Du_2}{Dt} - \frac{u_2 v_2 \sin\phi}{R\cos\phi} = -\frac{\rho_1}{\rho_2}\frac{g}{R\cos\phi}\frac{\partial\zeta_1}{\partial\lambda} - \frac{\Delta\rho}{\rho_2}\frac{g}{R\cos\phi}\left(\frac{\partial\zeta_2}{\partial\lambda} - \frac{\partial H_1}{\partial\lambda}\right)$$
$$+\frac{1}{\rho_2 D_2}[r_1 u' \sqrt{(u'^2 + v'^2)} - r u_2 \sqrt{(u_2^2 + v_2^2)}] \tag{III.80a}$$

$$\frac{Dv_2}{Dt} + \frac{u_2 u_2 \sin\phi}{R\cos\phi} = -\frac{\rho_1}{\rho_2}\frac{g}{R}\frac{\partial\zeta_1}{\partial\phi} - \frac{\Delta\rho}{\rho_2}\frac{g}{R}\left(\frac{\partial\zeta_2}{\partial\phi} - \frac{\partial H_1}{\partial\phi}\right)$$
$$+\frac{1}{\rho_2 D_2}[r_1 v' \sqrt{(u'^2 + v'^2)} - r v_2 \sqrt{(u_2^2 + v_2^2)}] \tag{III.80b}$$

$$\frac{\partial\zeta_2}{\partial t} + \frac{1}{R\cos\phi}\frac{\partial(D_2 u_2)}{\partial\lambda} + \frac{1}{R\cos\phi}\frac{\partial}{\partial\phi}(D_2 v_2 \cos\phi) = 0 \tag{III.81}$$

Although spherical and rectangular coordinates are closely related it is useful to notice that due to Earth's sphericity the new nonlinear terms appeared in equations of motion.

To render the above partial differential equations into the difference equations the continuous space domain is subdivided into space steps. Along the East-West (E-W) direction the space step of the numerical integration is $R\cos\phi d\lambda$, as the angle of latitude ϕ changes the space step changes as well. The constant portion of the step $Rd\lambda$ is named HX and the full step is $HX_1 = HX\cos\phi$. Along the North-South (N-S) the space step is always constant $Rd\phi = HY$. The index of numerical integration along the E-W is taken as j. Thus the distance (L) along E-W direction on the numerical lattice is calculated as $L = jHX\cos\phi$, here $j = 1, 2, 3, \ldots$. Along the N-S the index k is used, and the distance is expressed as $L = kHY$. The time stepping requires a similar approach. Introducing the time step T and index m, the time span t can be expressed as $t = mT$, where $m = 1, 2, 3, \ldots$.

Numerical form of the equations written in the spherical coordinates differs only slightly from equations given above for the rectangular system.

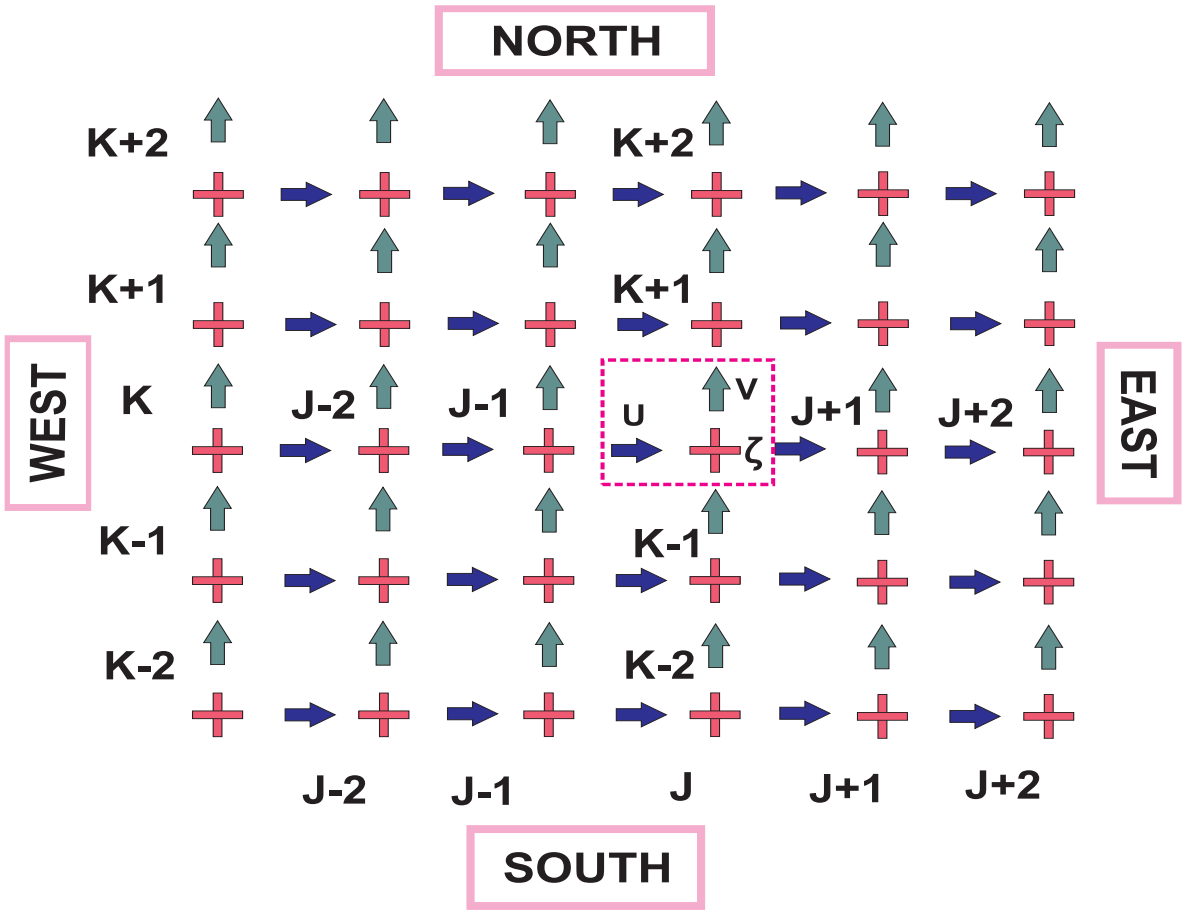

Figure III.24. Space staggered triplets with u (east-west component of velocity), v (north-south component of velocity) and ζ (sea level) located at the different positions but organized under the same spatial indexes j and k.

The rendering of the above partial differential equations into numerical forms is based on the formulas developed in Ch.II Sec.4. The following notation will be used to express variables in the discrete space-time domain.

$$\zeta_1(\lambda,\phi,t) = \zeta_1(jHX_1, kHy, mT) = \zeta^m_{1,j,k} \tag{III.82}$$

For the space and time derivative the Taylor series is used, but since ours is staggered grid the derivatives in the point u, v and ζ require some explanations. We start by rendering the acceleration in eq.III.77a into numerical form using grid from FigIII. 24 and 25.

$$\frac{\partial u_1}{\partial t} \simeq \frac{u^{m+1}_{1,j,k} - u^m_{1,j,k}}{T} \tag{III.83}$$

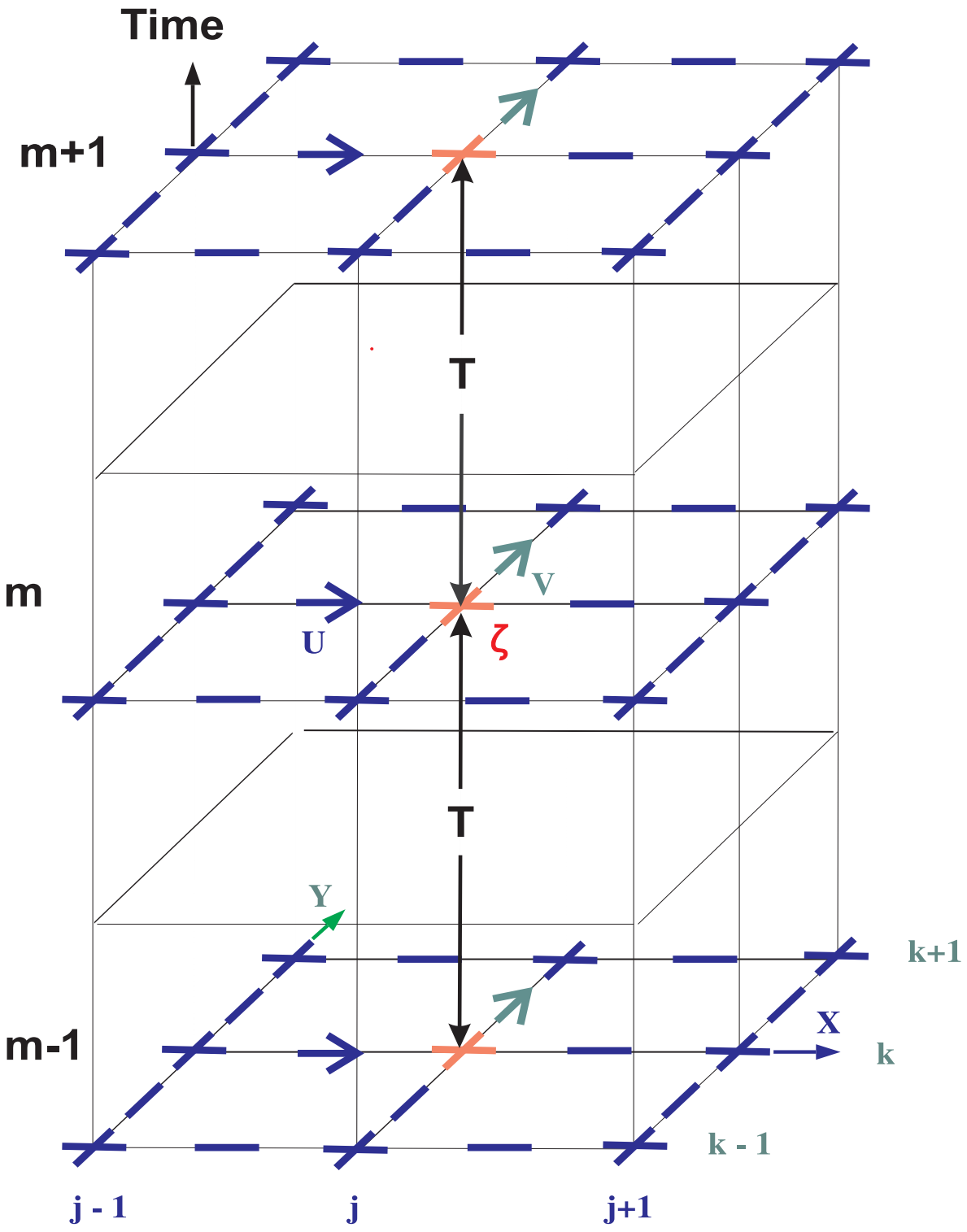

Figure III.25. Three-dimensional grid distribution for integration in time and space. Stepping in time is done with time step T while time index is changing from m to m + 1.

Advective terms for the u_1 velocity component (eqs.III.77a and III.79)

$$\frac{u_1}{R\cos\phi}\frac{\partial u_1}{\partial\lambda}+\frac{v_1}{R}\frac{\partial u_1}{\partial\phi}$$

are rendered into numerical form using the upstream/downstream approach. For the first expression when $u^m_{1,j,k}$ is positive, $u_{1,p}=0.5(u^m_{1,j,k}+|u^m_{1,j,k}|)$, the backward derivative is used

$$\frac{u_1}{R\cos\phi}\frac{\partial u_1}{\partial\lambda}\simeq u_{1,p}\frac{u^m_{1,j,k}-u^m_{1,j-1,k}}{HX_1} \tag{III.84a}$$

and if $u^m_{1,j,k}$ is negative, $u_{1,n}=0.5(u^m_{1,j,k}-|u^m_{1,j,k}|)$, the forward derivative is applied

$$\frac{u_1}{R\cos\phi}\frac{\partial u_1}{\partial\lambda}\simeq u_{1,n}\frac{u^m_{1,j+1,k}-u^m_{1,j,k}}{HX_1} \tag{III.84b}$$

The upstream/down stream derivatives assure strong numerical stability for the nonlinear advective terms (Kowalik and Murty, 1993). The numerical form for the derivative along the N-S direction in the advective equation is constructed again on the upstream/down stream approach, but now it depends on the sign of v velocity. The sign of the v component is tested in the u grid-point of the staggered lattice. The v velocity in the u grid-point is calculated as an average of the four v points which surround the u grid-point.

$$VAU=0.25*(v^m_{1,j,k}+v^m_{1,j-1,k}+v^m_{1,j-1,k-1}+v^m_{1,j,k-1}) \tag{III.85}$$

When VAU is positive $VAUP=0.5(VAU+|VAU|)$, the derivative reads

$$\frac{v_1}{R}\frac{\partial u_1}{\partial\phi}\simeq VAUP\frac{u^m_{1,j,k}-u^m_{1,j,k-1}}{HY} \tag{III.86a}$$

and when the VAU is negative $VAUN=0.5(VAU-|VAU|)$, the forward derivative is used

$$\frac{v_1}{R}\frac{\partial u_1}{\partial\phi}\simeq VAUN\frac{u^m_{1,j,k+1}-u^m_{1,j,k}}{HY} \tag{III.86b}$$

It is of interest to notice that in the staggered lattice the sea level is located on the both sides of u grid-point, therefore, the pressure gradient due to the sea level change in III.77a is

$$\frac{1}{R\cos\phi}\frac{\partial\zeta_1}{\partial\lambda}\simeq\frac{\zeta^m_{1,j,k}-\zeta^m_{1,j-1,k}}{HX_1} \tag{III.87}$$

Taking into account the above partial formulas the full numerical form for the equation of motion along the E-W direction reads

$$\frac{u^{m+1}_{1,j,k}-u^m_{1,j,k}}{T}+u_{1,p}\frac{u^m_{1,j,k}-u^m_{1,j-1,k}}{HX_1}+u_{1,n}\frac{u^m_{1,j+1,k}-u^m_{1,j,k}}{HX_1}+VAUP\frac{u^m_{1,j,k}-u^m_{1,j,k-1}}{HY}$$

$$+VAUN\frac{u^m_{1,j,k+1}-u^m_{1,j,k}}{HY}-\frac{u_{1,j,k}VAU\sin\phi}{R\cos\phi}$$

$$=-g\frac{\zeta^m_{1,j,k}-\zeta^m_{1,j-1,k}}{HX_1}-\frac{r_1u'\sqrt{(u'^2+v'^2)}}{\rho_1 0.5(D_{1,j,k}+D_{1,j-1,k})} \tag{III.88}$$

The total depth is defined in the sea level points, hence in the u and v grid points it is averaged from the two neighboring ζ points. The part of the total depth due to the sea level and variable landslide thickness is updated at each time step of numerical integration. The variables u' and v' denote the difference of the velocity (in the upper and lower layers) and are approximated the same way as the velocity components.

The numerical algorithm for the equation of motion (eq.III.77b) along the N-S direction is constructed in the similar way, but now the main point is $v_{j,k}$ located a half-space grid to the North from the $\zeta_{j,k}$ sea level point (see FigIII.24).

$$\frac{v^{m+1}_{1,j,k}-v^m_{1,j,k}}{T}+UAVP\frac{v^m_{1,j,k}-v^m_{1,j-1,k}}{HX_1}+UAVN\frac{v^m_{1,j+1,k}-v^m_{1,j,k}}{HX_1}+v_{1,p}\frac{v^m_{1,j,k}-v^m_{1,j,k-1}}{HY}$$

$$+v_{1,n}\frac{v^m_{1,j,k+1}-v^m_{1,j,k}}{HY}+\frac{UAV\times UAV\sin\phi}{R\cos\phi}=-g\frac{\zeta^m_{1,j,k+1}-\zeta^m_{1,j,k}}{HY}-\frac{r_1v'\sqrt{(u'^2+v'^2)}}{\rho_1 0.5(D_{1,j,k}+D_{1,j,k+1})} \tag{III.89}$$

Here: UAV average u velocity in the v grid-point, $UAV=0.25(u_{1,j,k}+u_{1,j+1,k}+u_{1,j+1,k+1}+u_{1,j,k+1})$; $UAVP=0.5(UAV+|UAV|)$; $UAVN=0.5(UAV-|UAV|)$, $v_{1,p}=0.5(v^m_{1,j,k}+|v^m_{1,j,k}|)$; $v_{1,n}=0.5(v^m_{1,j,k}-|v^m_{1,j,k}|)$.

Finally, the numerical code of the continuity equation is constructed

$$\zeta^{m+1}_{1,j,k}=\zeta^m_{1,j,k}-\frac{T}{HX_1}(flux_{x,j+1,k}-flux_{x,j,k})$$

$$-\frac{T}{cos\phi^\zeta_k HY}(flux_{y,j,k}-flux_{y,j,k-1})+\zeta^{m+1}_{2,j,k}-\zeta^m_{2,j,k} \tag{III.90}$$

In this numerical approach the upwind/downwind flux code proposed by Mader (1973, 2004) is used. This lower order of approximation is essential for the large scale computations as it displays strong numerical stability (see eq. II.102 and II.103).

The flux along the E-W direction is

$$flux_{x,j,k}=u^{m+1}_p(\zeta^m_{1,j-1,k}-\zeta^m_{2,j-1,k})+u^{m+1}_n(\zeta^m_{1,j,k}-\zeta_{2,j,k})+u^{m+1}_{j,k}\frac{(H_{1,j,k}+H_{1,j-1,k})}{2} \tag{III.90a}$$

$$u^{m+1}_p=0.5*(u^{m+1}_{j,k}+|u^{m+1}_{j,k}|)\quad\text{and}\quad u^{m+1}_n=0.5*(u^{m+1}_{j,k}-|u^{m+1}_{j,k}|) \tag{III.90b}$$

The flux $flux_{x,j,k}$ as defined above is the water volume transported in the upper layer whose the total depth is $D_1=\zeta_1-\zeta_2+H_1$. The transport velocity $u^{m+1}_{j,k}$ is taken at the

new $m+1$ time step, as it is already available from the equation of motion and because such approach assures stability of the system of equations.

The flux along the N-S direction at the $v_{j,k}$ point reads,

$$flux_{y,j,k} = \cos\phi_k^v \Big[v_{1,p}^{m+1}(\zeta_{1,j,k}^m - \zeta_{2,j,k}^m) + v_{1,n}^{m+1}(\zeta_{1,j,k+1}^m - \zeta_{2,j,k+1}) + v_{1,j,k}^{m+1} \frac{(H_{1,j,k} + H_{1,j,k+1})}{2} \Big] \tag{90c}$$

$$v_{1,p}^{m+1} = 0.5 * (v_{1,j,k}^{m+1} + |v_{1,j,k}^{m+1}|) \quad \text{and} \quad v_{1,n}^{m+1} = 0.5 * (v_{1,j,k}^{m+1} - |v_{1,j,k}^{m+1}|) \tag{90d}$$

The salient points related to the choice of the spatial and temporal time steps to assure the stability of the numerical integration can be gleaned from Ch.II or from Kowalik and Murty (1993). One simple way of checking stability is to consider the different speeds of the signal propagating in a physical system and to choose the largest speed. Examples to consider in the tsunami/landslide system are landslide velocity u_2 or v_2 and the long wave celerity in the upper layer $c_1 = \sqrt{gH_1}$. The first step in checking stability is to calculate a distance traveled by the signal during one time step (T). For example if the largest speed is achieved by the long wave celerity in the upper layer $c_1 = \sqrt{gH_1}$, the distance traveled is $l_d = c_1 T$. If the distance l_d is smaller than the shortest grid distance (HX_1 or HY) the numerical code should be stable and converge, otherwise the numerical scheme is unstable. The construction of the numerical scheme for the lower layer system of equations will follow the above approach.

14. Simulation of tsunami generated by an underwater landslide in a two-dimensional water body: numerical example.

We start by computing tsunami generated by an underwater landslide in a rectangular water body. The two-layered fluid dynamics as described by eqs III.77a - III.81 is considered.

This set of equations is solved for the landslide on the inclined bottom as shown in FigIII.26. A linear depth is changing only along the x direction and is constant along the y direction

$$H_1 = h_l + h_b x \qquad \text{and} \qquad h_b = \frac{h_r - h_l}{L_x} \tag{III.91}$$

Here: h_l is the depth at the $x = 0$ and $0 \le y \le 2000$ m, h_r is the depth at the $x = 2500$ m and $0 \le y \le 2000$ m, and $L_x = 2000$ m is the length of the water body along the x direction. The ratio $(h_r - h_l)/L_x$ defines the bottom slope along the x direction (it is approximately equal 17%). The slope along the y direction is zero. An initial landslide's shape is taken as paraboloid, given by an equation

$$\zeta_2 = \zeta_{2,c}\Big[1 - \frac{(x - x_c)^2}{L_{s,x}^2} - \frac{(y - y_c)^2}{L_{s,y}^2}\Big] \tag{III.92}$$

Here: ζ_2 denotes the second layer thickness , $\zeta_{2,c}$ is the maximum thickness which is located at the distance $x = x_c, y = y_c$, and $L_{s,x}$, $L_{s,y}$ is the length of the slide along the x and y respectively.

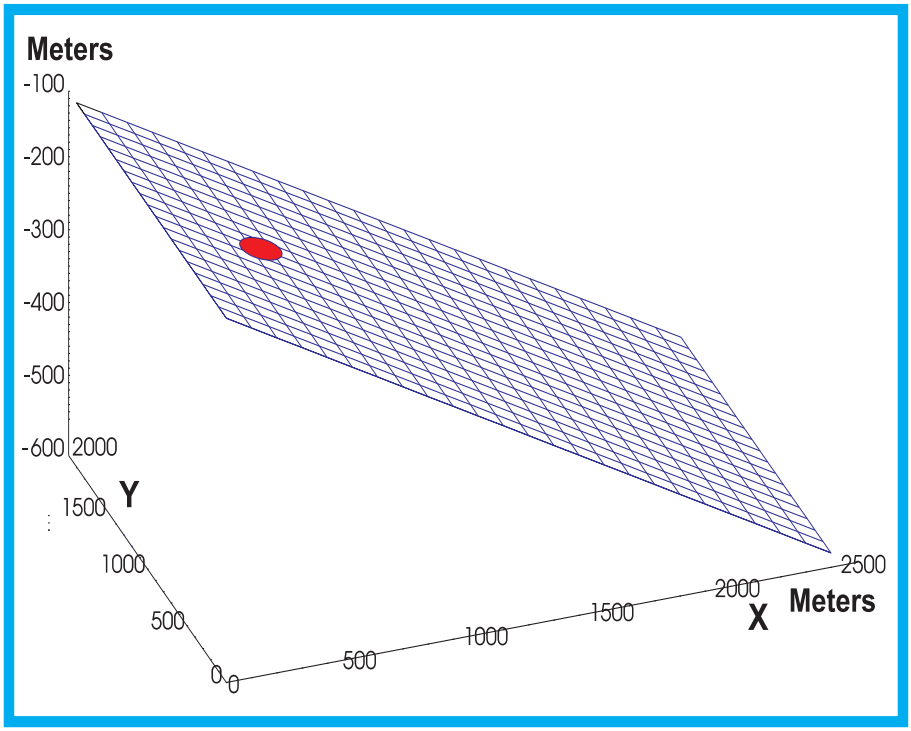

Figure III. 26 Inclined bottom of the rectangular water body. Paraboloid shape landslide is given by the red color.

The slide length is $L_{s,x} = L_{s,y}$ =100 m and the initial maximum slide thickness $\zeta_{2,c}$ =25 m. In the numerical simulation, the space step $HX_1 = R\cos\phi d\lambda = HY = Rd\phi = 1$ m, the time step $T = 1 \times 10^{-3}$ s, $R = 6370$ km, $\phi = 45°$, $\rho_1 = 1$ g cm^{-3}, $\rho_2 = 1.4$ g cm^{-3}, the bottom friction coefficient $r = 0.003$ and the inter-layer friction is $r_1 = 0.0015$. All computations in this section are done with the program: landslide2layer2d.f90. The data file is :block_2layer2d. Depth and the initial paraboloid shape of landslide are defined in Subroutine: BEACH2. At the initial moment the paraboloid landslide is positioned on the sloping bottom and the ensuing sliding process will change the shape of the landslide and the velocity distribution. The domain of the heavier fluid is denoted by cell number cell2(j,k)=1, the lack of the heavy fluid is indicated by cell2(j,k)=0, therefore the boundary between the lighter and heavier fluid is between cell2=1 and cell2=0. FigIII.27 describes a free surface response to the moving slide at the time of 1s from onset of motion. The basic components of the free surface previously noted in the 1D channel are also present in this figure: the forced wave which propagates with the slide velocity and is "glued" to the landslide position, and the free waves propagating into the positive and negative directions as $\pm\sqrt{gH}$ along the both x and y directions. The asymmetry in the free surface pattern is due to the predominant downslope slide motion.

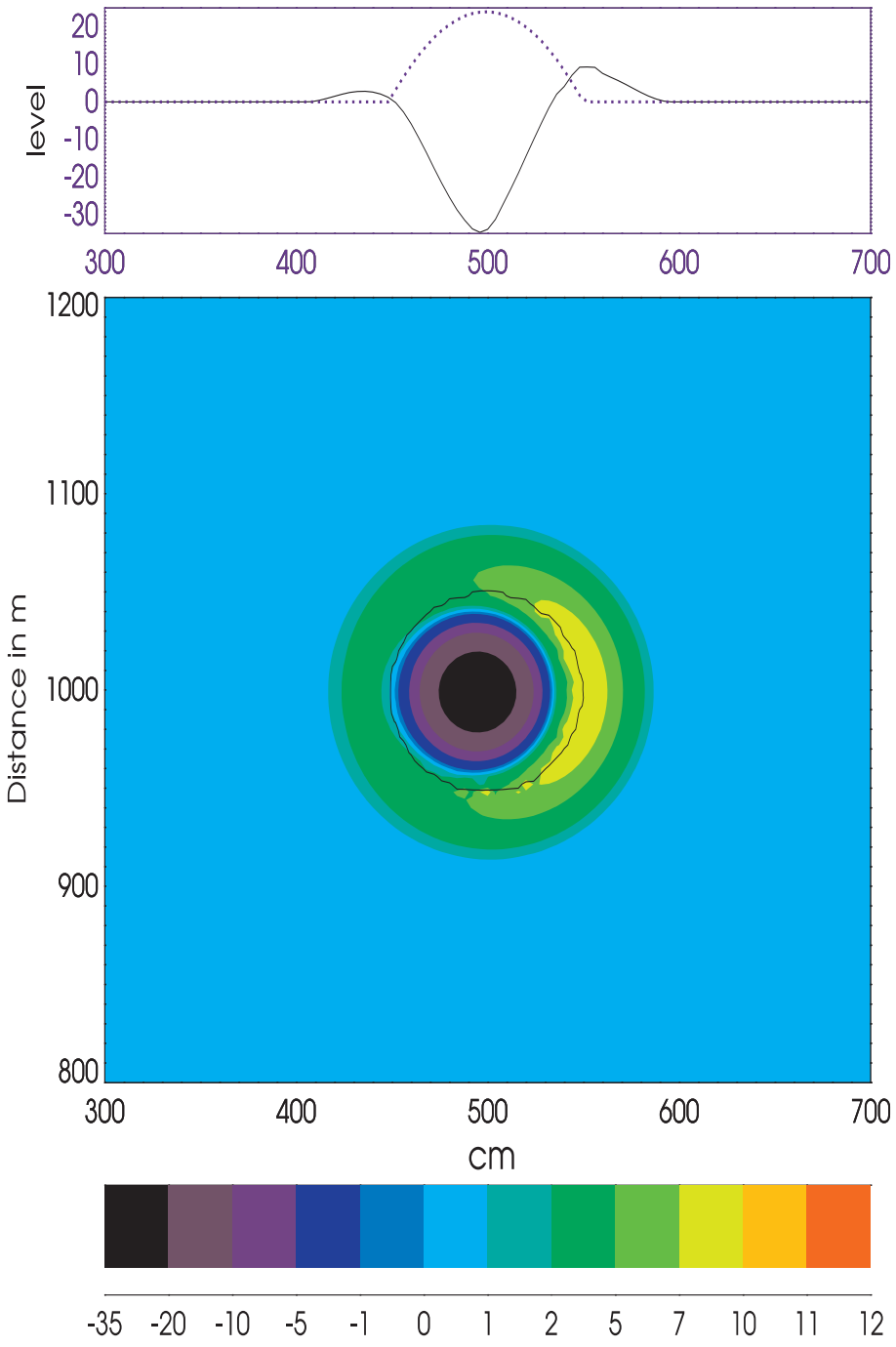

Figure III. 27 A free surface response to a moving submarine slide, 1s from the onset of motion. Upper panel describes cross-section along the x axis: Slide thickness (blue color, doted line) numbers in meters, sea level (continuous line, black color) numbers in centimeters. Lower panel: Free surface, landslide location depicts black line.

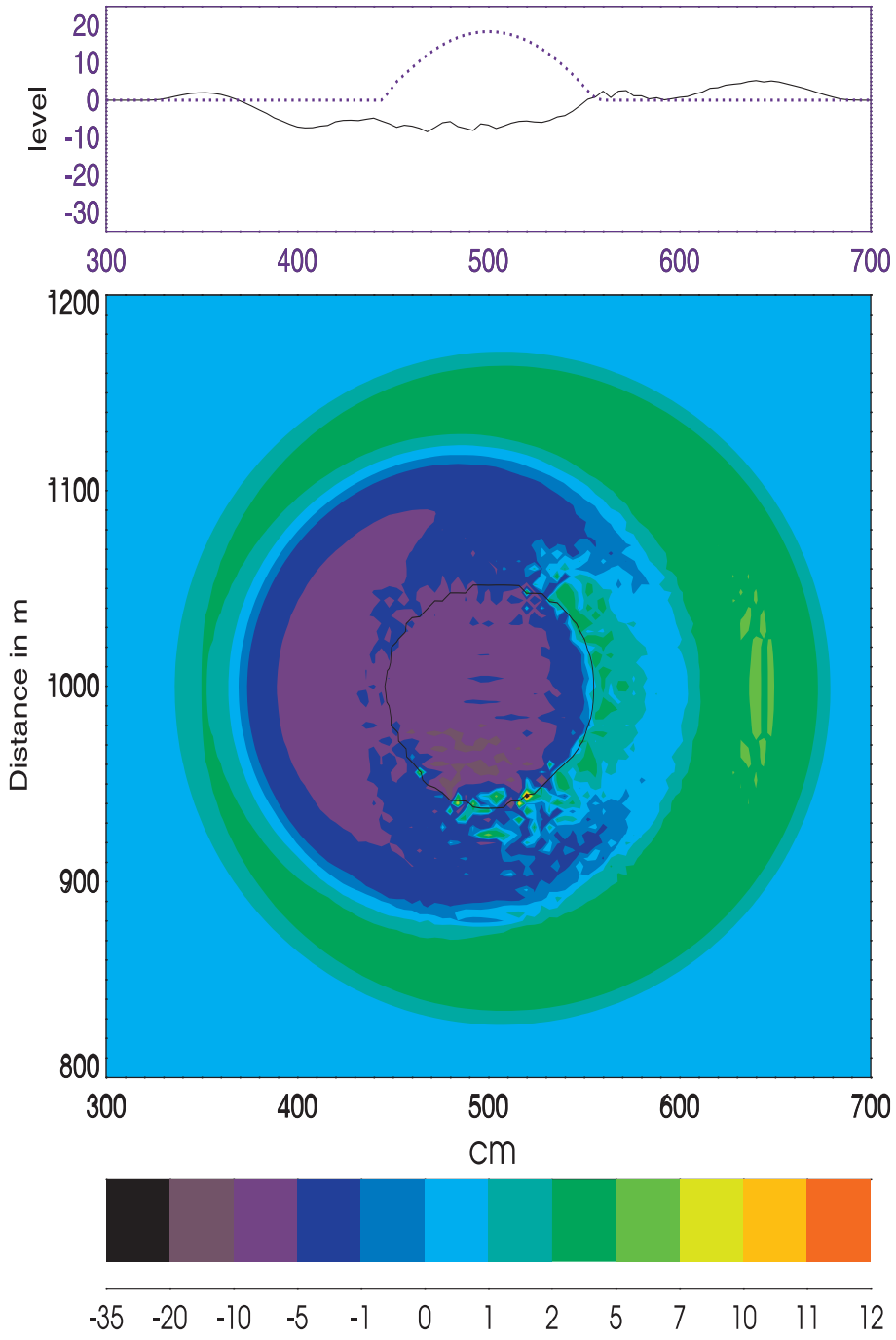

Figure III. 28 A free surface response to a moving submarine slide, 3s from the onset of motion. Upper panel describes cross-section along the x axis: Slide thickness (blue color, doted line) numbers in meters, sea level (continuous line, black color) numbers in centimeters. Lower panel: Free surface, landslide location depicts black line.

Changes in the wave trains generated by the landslide can be assessed by energy fluxes as they serve often to describe the energy transfer from the source to various locations (Tinti and Bortolucci, 2000b). Since the energy flux is a vector it describes not only changes in

the wave field but also directions which are responsible for higher or lower energy fluxes and especially it is useful in delineating the regions of the wave amplification. The flux describes the energy through a unit width surface extended from the ocean surface to the bottom (cf., eq.I.44). The components of the vector along latitude and longitude are

$$\mathbf{E_{h1}} = \{\rho g H u_1 \zeta_1, \rho g H v_1 \zeta_1\} \qquad \text{(I.45; III.93)}$$

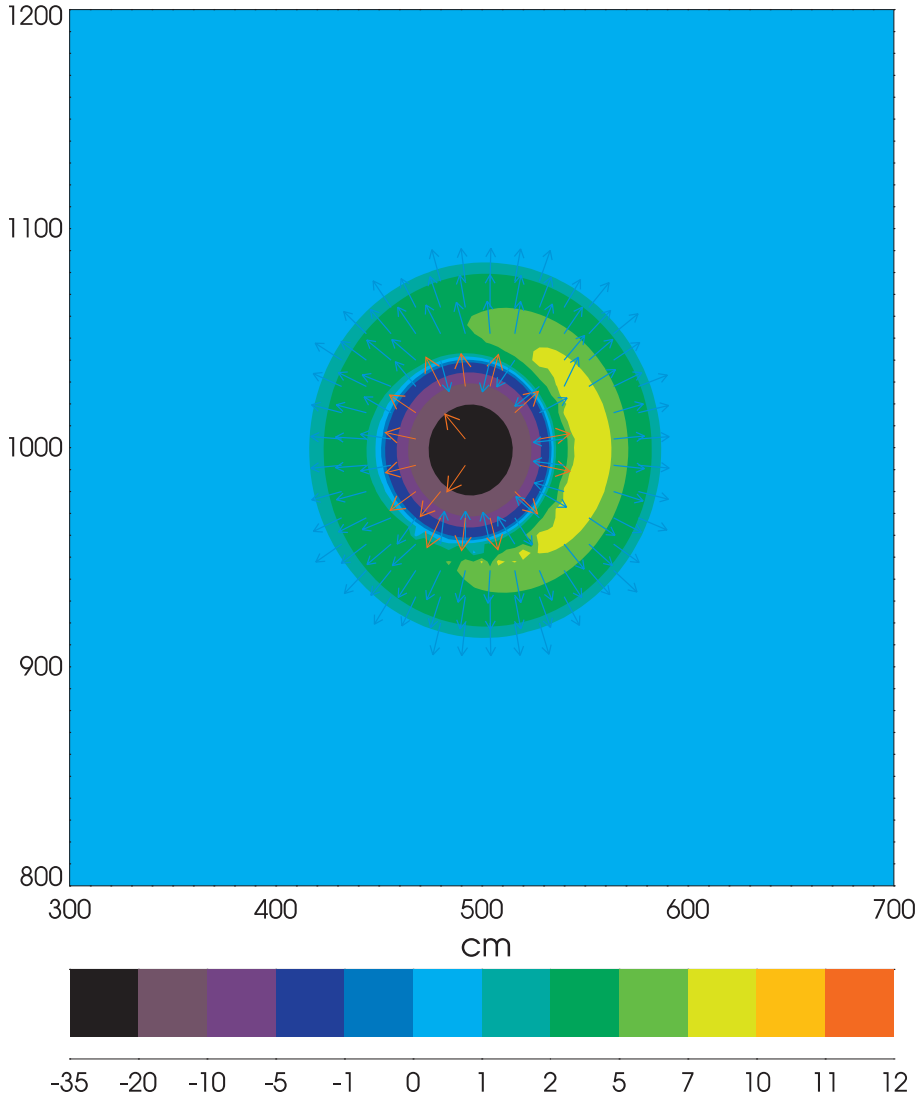

Figure III. 29 Energy flux (arrows) related to the free surface oscillations. Blue arrows are below and red arrows above the 3 10^{-3} watts. Color describe free surface at 1 s from the motion onset by the landslide.

In FigIII.29 the energy flux vectors are plotted for two ranges: below 3 10^{-3} watts (blue color) and above this limit (red color). As one is expecting the center of the plot (the landslide) is the source of energy, but the wave propagating outward, especially frontal maximum radiates some energy back towards the center. This can be one of the reasons of the slower energy dissipation around the circular tsunami source.

15. Numerical simulation of the landslide generated tsunami in a channel: subaerial landslide.

In Sec. 9 of this chapter a deformable slide of density ρ_2 has been considered and its geometry is outlined in FigIII.18 and FigIII.19. We investigate now a landslide which is initially located in the air and subsequently slides into the water as described in FigIII.30. As we pointed out before, the solid block experiments showed the difference between subaerial and subaqueous landslide on the wave generation. While the solid block sliding in the water converted between 3 and 7% of the kinetic block energy into wave energy; in subaerial block sliding impacts the energy conversions was up to 50%. Numerical models showed as well that the underwater landslides are ineffective at tsunami generation (LeBlond and Jones, 1995). Therefore, we turn our attention to the landslides generated in the subaerial domain. To investigate the landslide time-history and the water waves generated by the landslide impact a few approaches are possible. One approach is to track the landslide in the air neglecting the upper layer motion and susequently when the lanslide enters the water the two-layer model is applied. The local system of coordinate from Sec.9.2 of this chapter is used and the lanslide under consideration is a fluidized granular material. Dissipation in granular materials is given by the Coulomb-type friction law (eq.III.62) and therefore with this bottom friction the runout distance can be controlled. The runout distance is limited by setting the lanslide velocity to zero when the Coulomb bottom stress exceeds the forces due to gravitational pull and pressure forces due to the gradient of the sea level and the landslide surface.

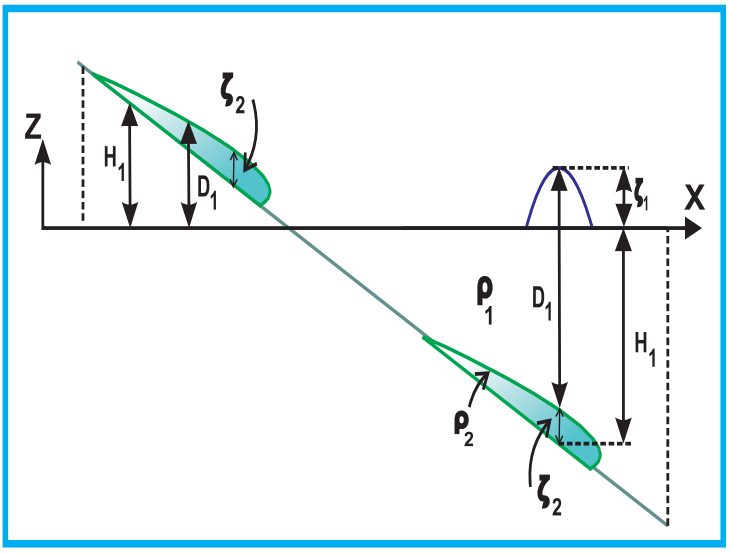

Figure III.30 A subaerial slide on the inclined bottom plane

The landslide motion describes the granular material in the lower layer along the x direction (based on eq.III.43a)

$$\frac{\partial u_{2,L}}{\partial t} + u_{2,L}\frac{\partial u_{2,L}}{\partial x_L} = -\frac{\rho_1}{\rho_2} g \frac{\partial \zeta_1}{\partial x_L} - \frac{\Delta\rho}{\rho_2} g \left(\frac{\partial \zeta_{2,L}}{\partial x_L}\cos\beta - \sin\beta\right) + FR_x \qquad \text{(III.94)}$$

$$FR_x = -\frac{\Delta\rho}{\rho_2} g \cos\beta \tan\delta \frac{u_{2,L}}{|u_{2,L}|}$$

To simplify the notation all terms related to 2D motion in eq.III.43a are neglected.

The downslope forces in eq.III.94, caused by the gravitational pool are multiplied by the density difference. This difference will change from the air to the water and it is only important while landslide is moving under the water. The frictional forces also are changing strongly from the air to the water. To simplify numerical experiments only the bottom stress is considered; the stress between water and upper surface of the landslide is neglected. The bottom stress for the granular material is taken as the Coulomb stress, therefore the lost of gravitational energy is defined by the friction angle δ.

$$\frac{\partial u_{2,L}}{\partial t} + u_{2,L}\frac{\partial u_{2,L}}{\partial x_L} = -\frac{\rho_1}{\rho_2} g \frac{\partial \zeta_1}{\partial x_L} - \frac{\Delta\rho}{\rho_2} g \frac{\partial \zeta_{2,L}}{\partial x_L} \cos\beta + \frac{\Delta\rho}{\rho_2} g \cos\beta (\tan\beta - \tan\delta \frac{u_{2,L}}{|u_{2,L}|}) \tag{III.94a}$$

The actual values of the friction angle are not well recognized, Heinrich at al., (2001) suggested that only low friction angles ($< 15^\circ$) describe the real landslides.

The equation of continuity for the slide in the local coordinates formally does not differ from the rectangular coordinates

$$\frac{\partial \zeta_{2,L}}{\partial t} = -\frac{\partial}{\partial x_L}(\zeta_{2,L} u_{2,L}) \tag{III.42, III.95}$$

although the local thickness shown in FigIII.19 differs from the regular thickness depicted in FigIII.30. As the regular thickness occurs in the upper layer continuity equation, it is usefull to calculate the regular thickness for the lower layer. For this a simple formula is applied $\zeta_2 = \zeta_{2,L} \cos\beta$.

The landslide thickness is a positive number both in the air and in the water. H_1 is the depth measured from $z = 0$ upward in the air to the land relief and downward in the water to the bottom profile. The H_1 is taken as positive in the water and negative in the air. The bottom and land profiles will vary in time due to the moving landslide. This variability will be tracked in time through the total depth in the water $D_1 = H_1 + \zeta_1 - \zeta_2$, and the land relief in the air $H_1 - \zeta_2$.

The landslide generated water waves are described by the set of equations related to the upper layer in the two-layer fluid. Starting with eq.III.38a, the equation of motion is simplified as

$$\frac{\partial u_1}{\partial t} + u_1 \frac{\partial u_1}{\partial x} = -g\frac{\partial \zeta_1}{\partial x} - \frac{1}{\rho_1 D_1} r_1 u' |u'| \tag{III.96}$$

Here $u' = u_1 - u_2 = u_1 - u_{2,L} \cos\beta$

The vertically integrated equation of continuity in the water (eq.III.36) includes bottom changes produced by the slide thickness ζ_2, for one dimensional flow it reads

$$\frac{\partial(\zeta_1 - \zeta_2)}{\partial t} = -\frac{\partial}{\partial x}(D_1 u_1) \tag{III.97}$$

Here $D_1 = H_1 + \zeta_1 - \zeta_2 = H_1 + \zeta_1 - \zeta_{2,L} \cos\beta$ is the total water depth.

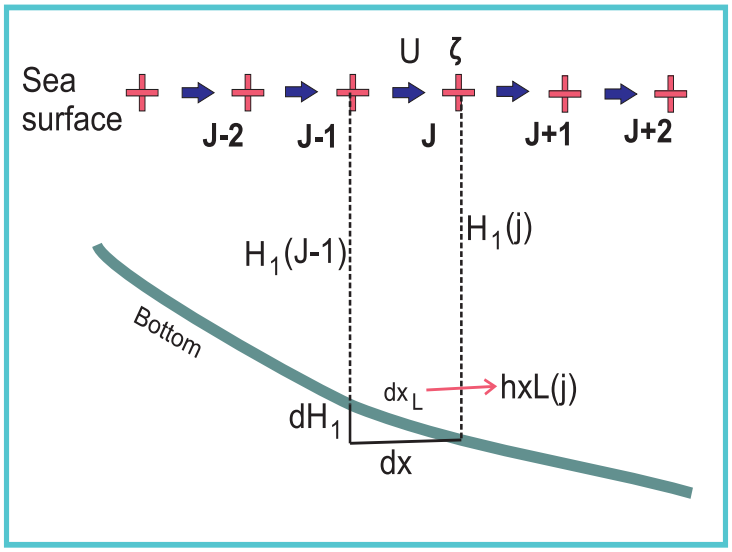

Figure III.31 A numerical grid for the inclined bottom plane

The above system of equation is rendered into numerical form by assuming space step in the upper layer to be constant and equal hx (in FigIII.31 it is denoted as dx). As the lower layer system of coordinates is directed along the bottom to every grid step in the upper layer is related variable grid step along the bottom dx_L. This grid step in the numerical calculation is named hxL(j). The distance along the bottom from the $j-1$ to the j grid point is

$$dx_L = hxL(j) = \sqrt{dx^2 + dH_1^2} = \sqrt{hx^2 + [H_1(j) - H_1(j-1)]^2}$$

As constant time step T and space step hx is applied for the upper fluid we apply the same constant time step for the lower fluid. Using FigIII.31 the lower fluid equation of motion (eqIII.94a) will be cast into a numerical form. Starting with the time derivative of the velocity

$$\frac{\partial u_{2,L}}{\partial t} \simeq \frac{u_{2,L,j}^{m+1} - u_{2,L,j}^{m}}{T}$$

To construct upstream/downstream numerical formulation the nonlinear acceleration term is split into two parts. For the first expression when $u_{2,L,j}^m$ is positive, $u_{2,p,j} = 0.5(u_{2,L,j}^m + |u_{2,L,j}^m|)$, the backward derivative assures numerical stability

$$u_{2,L}\frac{\partial u_{2,L}}{\partial x_L} \simeq u_{2,p,j}\frac{u_{2,L,j}^m - u_{2,L,j-1}^m}{0.5[hxL(j) + hxL(j-1)]}$$

If $u_{2,L,j}^m$ is negative, $u_{2,n,j} = 0.5(u_{2,L,j}^m - |u_{2,L,j}^m|)$, the forward derivative is used

$$u_{2,L}\frac{\partial u_{2,L}}{\partial x_L} \simeq u_{2,n,j}\frac{u_{2,L,j+1}^m - u_{2,L,j}^m}{0.5[hxL(j) + hxL(j+1)]}$$

For the sea level and the slide thicknes the spatial derivative in the u point according to FigIII.31 reads,

$$\frac{\partial \zeta_1}{\partial x_L} \simeq \frac{\zeta^m_{1,j} - \zeta^m_{1,j-1}}{hxL(j)}$$

$$\frac{\partial \zeta_{2,L}}{\partial x_L} \simeq \frac{\zeta^m_{2,L,j} - \zeta^m_{2,L,j-1}}{hxL(j)}$$

The variable $\cos\beta$ and $\tan\beta$ in eqIII.94a are defined in every grid point by combination of dx, dx_L and dH_1. Numerical code for the lower layer continuity equation (III.95) is constructed in the ζ_2 grid point based on the fluxes at the $j+1$ and j velocity points

$$\frac{\partial \zeta_{2,L}}{\partial t} \simeq \frac{\zeta^{m+1}_{2,L,j} - \zeta^m_{2,L,j}}{T}$$

$$\frac{\partial}{\partial x_L}(\zeta_{2,L} u_{2,L}) \simeq \frac{\left[u^{m+1}_{2,p,j+1}\zeta^m_{2,L,j} + u^{m+1}_{2,n,j+1}\zeta^m_{2,L,j+1}\right] - \left[u^{m+1}_{2,p,j}\zeta^m_{2,L,j-1} + u^{m+1}_{2,n,j}\zeta^m_{2,L,j}\right]}{0.5[hxL(j) + hxL(j+1)]}$$

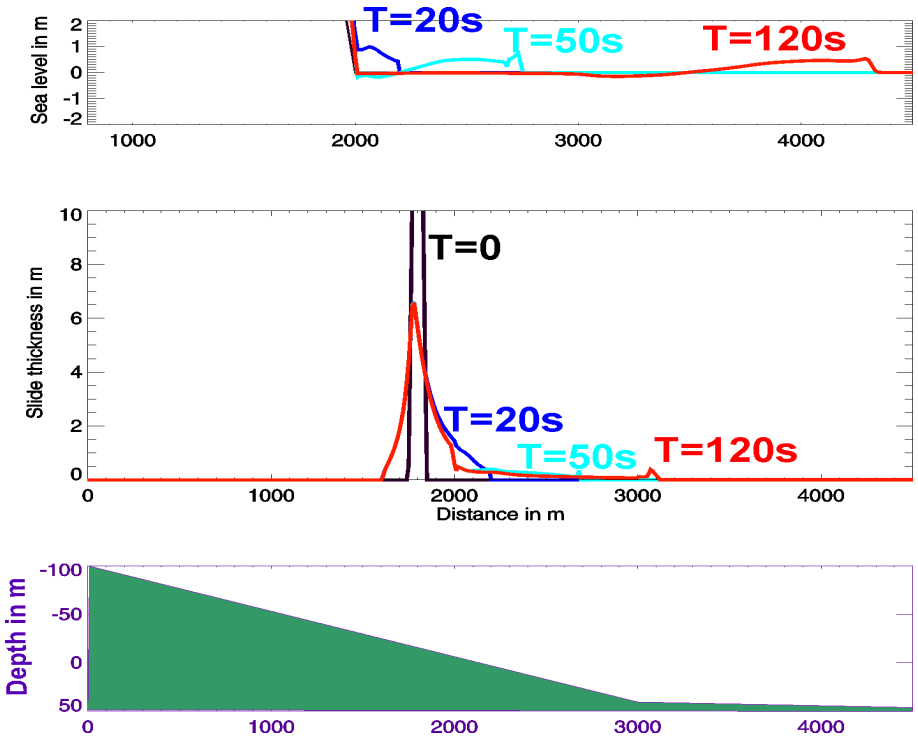

Figure III.32 A subaerial slide on the inclined bottom plane. Upper panel: the time history of the free surface. Middle panel: the time history of the landslide. Lower pannel: the depth distribution.

The set of equation is solved for the landslide on the inclined bottom as shown in FigIII.32. A linear depth is changing from -100 m on the land to about 50 m in the water. The water starts at the 2000 m from the beggining of the channel. At 3000m distance the

bottom inclination is diminished. The parabolic shape landslide is located in the air. It's maximum thickness is 25m and is initially located at the distance 200 m from the shoreline. The middle panel in FigIII.32 shows the time history of the landslide (the initial maximum is cut to better resolve small values in the water). After the landslide enters the water the portion of the landslide remaining in the air does not change the shape. Only that part of the slide which is in the water undergoes further transformation. The time history of the free surface starts approximately at time t=20 s from the onset of the landslide motion. The positive displacement of the free surface is dominating the initial phase of the motion as the lanslide due to the continuity equation pushes up the water.

References:

Aida, I. (1969). Numerical experiments for tsunamis caused by moving deformations of the sea bottom. Bull. Earthquake Res. inst. 47, 849-862.

Aki, K. and P. G. Richards (1980), Quantitative Seismology Theory and Methods Volume 2, W.H. Freeman and Co., 557 pp.

Ataie-Ashtiani, B and A, Nik-Khah (2008), Impulsive waves caused by subaerial landslides. Environ. Fluid Mech., 8:263–280

Blewitt, G., C. Kreemer, W. Hammond, H.-P. Plag, S. Stein, and E. Okal (2006), Rapid determination of earthquake magnitude using GPS for tsunami warning systems, Geophys. Res. Lett., L11309, doi:10.1029/2006GL026145.

Bryant, E. (2008), Tsunami, the Underrated Hazard. Springer, Praxis, 330 pp.

Bugge, T., Belderson, R.H., and Kenyon, N.H. (1988). The Storegga slide. Philosophical Trans. Roy. Soc. Lon. Series A, Meth. And Phys. Sci., 325(1586), 357–388.

Coulter, H.W. & Migliaccio, R.P., (1966). Effects of the earthquake of March 27, 1964, at Valdez, Alaska. United States Geological Survey Professional Paper 542-C, p. C1 - C36.

Elverhøi, A, D. Issler, F. V. De Blasio, T. Ilstad, C. B. Harbitz, and P. Gauer (2005), Emerging insights into the dynamics of submarine debris flows. Natural Hazards and Earth System Sciences, 5, 633-648.

Fernandez-Nieto, E. D., F. Bouchut, D. Bresch, M.J. Castro Diaz, and A. Mangeney (2008). A new Savage-Hutter type model for submarine avalanches and generated tsunami. Journal of Computational Physics 227, 7720–7754.

Fine, I.V., A.B. Rabinovich, Kulikov, E. A., Thomson, R. E., and Bornhold, B. D. (1998), Numerical Modelling of Landslide-Generated Tsunamis with Application to the Skagway Harbor Tsunami of November 3, 1994. In Proceedings, International Conference on Tsunamis (Paris, 1998) pp. 211223

Fine, I.V., A.B. Rabinovich, B.D. Bornhold, R.E. Thomson and E.A. Kulikov. (2005). The Grand Banks landslide-generated tsunami of November 18, 1929: preliminary analysis and numerical modeling. Marine Geology, Vol. 215, Nos. 1&2, pp. 45-57.

Fritz, H.M., Hager, W.H., Minor, H.-E. (2001). Lituya Bay case: rockslide impact and

wave run-up. Science of Tsunami Hazards 19(1):3-22.

Fritz HM, Hager WH, Minor HE (2004) Near field characteristics of landslide generated impulse waves. J Waterw Port Coast Ocean Eng 130(6):287302.

Fujima K., K. Masamura and C. Goto (2002), Theoretical examinations on long-wave damping by sea bottom friction, Coastal Engineering Journal, Vol. 44, No. 3, 217-245.

Fryer G.J., P. Watts, and L.F. Pratson (2004), Source of the Great Tsunami of 1 April 1946: a Landslide in the Upper Aleutian Forearc. MarineGeology 203, 201-218.

Gower, J. (2007), The 26 December 2004 tsunami measured by satellite altimetry, International Journal of Remote Sensing, Vol. 28, Nos. 1314, 28972913

Harbitz, C. B. (1992). Model simulations of tsunami generated by the Storega Slides. Marine Geology, 105, 1-21.

Heezen, B. C., and Ewing, C. (1952). Turbidity currents and submarine slumps, and the 1929 Grand Banks earthquake. Am. J. Sci., 250:849-873.

Heinrich, Ph., A. Piatanesi, and H. Hébert (2001) Numerical modelling of tsunami generation and propagation from submarine slumps: the 1998 Papua New Guinea event. Geoph. J. Int., 145, 97-111.

Hirata, K., K. Satake, Y. Tanioka, T. Kuragano, Y. Hasegawa, Y. Hayashi, and N. Hamada (2006) The Indian Ocean Tsunami: Tsunami Source Model From Satellite Altimetry. Earth, Planets and Space , 58, 195–201.

HRV - Harvard CMT Catalog (2005). Harvard Seismology: Centroid-Moment Tensor Project, posted at http://www.seismology.harvard.edu/CMTsearch.html.

Ishii, M., P. M. Shearer, H. Houston and J. E. Vidale (2005), Extent, diuration and speed of the 2004 Sumatra– Andaman earthquake imaged by Hi–Net array, Nature, 933-936.

Imamura, F., and M. M. A. Imteaz (1995). Long waves in two-layers: governing equations and numerical model, J. Sci. Tsunami Hazards, 13, 2–24.

Imamura F, and E. C. Gica (1996). Numerical model for wave generation due to subaqueous landslide along a coast A case of the 1992 Flores tsunami, Indonesia. J Sci Tsunami Hazards 14(1), 13–28.

Iwasaki, S.I. (2005). Posting of Thailand tide gage data to Tsunami Bulletin Board, also posted at http://www.navy.mi.th/hydro/tsunami.htm.

Jiang, L., LeBlond, P.H. (1992). The coupling of a submarine slide and the surface waves which it generates. J. Geophys. Res. 97(C8), 12,731–12,744.

Jiang L. and P. H. LeBlond (1993) Numerical modeling of an underwater Bingham plastic mudslide and the waves which it generates. J. of Geoph. Res., 98, C6, 10303–12280.

Ji, C. (2004). Preliminary Result of the 04/12/26 (Mw 9.0), off West Coast of Northern Sumatra Earthquake, posted at
http://www.gps.caltech.edu/%7Ejichen/Earthquake/2004/aceh/aceh.html.

Kajiura, K. (1963). The leading wave of tsunami. Bull. Earthquake Res. Inst. 41, 535-571.

Kamphuis, J. W., and R. J. Bowering (1970), Impulse waves generated by landslides, Proc. Coastal Eng. Conf., 11th, 575- 588.

Kanamori, H.,(1985), A numerical experiment on seismic tsunami warning network for Alaska and the Aleutians: Proc. Intern. Tsunami Symposium, August 6-9, 1985, British Columbia, Canada.

Keating H. B., C. F. Waythomas and A. G. Dawson (editors) (2000) *Landslides and Tsunamis*, Birkhäuser Verlag, 1313 pp

Koshimura, S., T. Oie, H. Yanagisawa, and F. Imamura (2009). Developing fragility functions for tsunami damage estimation using numerical model and post-tsunami data from Banda Aceh, Indonesia, Coastal Engineering Journal, JSCE, Vol.51, No.3, pp.243-273.

Kowalik, Z. (1997). Landslide-generated tsunami in Skagway, Alaska. Science of Tsunami Hazards, 15(2), 89–106.

Kowalik, Z., and T. S. Murty (1993), Numerical modeling of ocean dynamics, World Scientific Publ., 481 pp.

Kowalik Z., W. Knight, T. Logan, and P. Whitmore, 2005. Numerical Modeling of the Global Tsunami: Indonesian Tsunami of 26 December 2004. Science of Tsunami Hazards, Vol. 23, No. 1, 40- 56.

Lander, J. F. and P. A. Lockridge (1989) *United States Tsubanis 1690-1988*. National Geoph. Data Center, Boulder, Co., 265 pp.

Lay, T., H. Kanamori, C. J. Ammon, M. Nettles, S. N. Ward, R. C. Aster, S. L. Beck, S. L. Bilek, M. R. Brudzinsky, R. Butler, H. R. Deshon, G. Ekstrom, K. Satake, S. Sipkin. (2005). The Great Sumatra-Andaman Earthquake of 26 December 2004. Science, v. 308, pp. 1127-1139.

Lay, T. and H. Kanamori (2011). Insights from the great 2011 Japan earthquake. Phys. Today 64(12), 33 (2011); doi: 10.1063/PT.3.1361.

LeBlond, P. H., and A. T. Jones (1995) Underwater lanslides ineffective at tsunami generation, Science of Tsunami Hazards, 13 (1), 25-27.

Lee, H.J., and Edwards, B.D. (1986). Regional method to assess offshore slope stability. J. Geotech. Eng., 112:489-509.

Lobkovsky,L. I., R. Kh. Mazova, I. A. Garagash, L. Yu. Kataeva, and I. Nardin (2006), To analysis of source mechanism of the 26 December 2004 Indian Ocean tsunami. Russian Journal of Earth Sciences, Vol. 8, ES5001, doi:10.2205/2006ES000208.

Lobkovsky,L. I., R. Kh. Mazova, I. A. Garagash, and L. Yu. Kataeva (2005), Numerical simulation of the 7 February 1963 tsunami in the Bay of Corinth, Greece. Russian Journal of Earth Sciences, Vol. 8, ES5003, doi:10.2205/2006ES000210

Lopez A.M. and E.A. Okal (2006), A Seismological Reassessment of the Source of the 1946 Aleutian Tsunami Earthquake. Geophysical Journal International 165, 835-849.

Mader C. L. (1973). Numerical simulation of tsunamis. *Rept. HIG-73-3*, Hawaii Institute of Geophysics, Univ. of Hawaii.

Mader C. L. (1999). Modeling the 1958 Lituya Bay Tsunami, Science of Tsunami Hazards, Volume 17, Number 1, 57-67.

Mader C. L. (2004). *Numerical Modeling of Water Waves*, CRC Press, 274 pp.

Mangeney A., P. Heinrich, and R. Roche (2000), Analytical solution for testing debris avalanche numerical models. In Lanslide and Tsunamis, eds. Keating B. H., C. F. Waythomas, and A. G. Dawson. Birkhauser, 1081-1096.

Marchuk An. G. (2008), Numerical modeling of the resonance tsunami generation by the submarine landslide. *Bull. Nov. Comp. Center. Math. Mod. in Geoph.*, 12, 45-54.

Marchuk An. G., L. B. Chubarov, and Iu. I. Shokin (1983). *Numerical Modeling of Tsunami Waves*, Nauka Press, Siberian Branch, Novosibirsk. Available in English as LA-TR-85-40 and from Leo Kanner Associates, Redwood City, Ca.

Mei, C. C. amd K-F. Liu (1987). A Bingham- plastic model for a muddy seabed under long waves. J. Geoph. Res., 92, C13, 14,581-14,594.

Merrifield, M.A., Y.L. Firing, G. Brundrit, R. Farre, B. Kilonsky, W. Knight, L. Kong, C. Magori, P. Manurung, W. Mitchell, F. Shillington, E.M.S. Wijeratne, J. Jardin, S. Nakahara, F.-Y. Porter, and N. Turesky (2005). Tide Gauge Observations of the Indian Ocean Tsunami, December 26, 2004, Geophys.Res. Lett., 32, L09603, doi:10.1029/2005GL022610.

Miller, D.J. (1960). Giant waves in Lituya Bay, Alaska. Geological Survey Professional Paper 354 C. U.S. Government Printing Office, Washington D.C.

Mohrig, D., Whipple, K. X., Hondzo, M., Ellis, C., and Parker, G.(1998), Hydroplaning of subaqueous debris flows, GSA Bull., 110, 387–394.

Murty, T. S. (1977). *Seismic Sea Waves Tsunamis*, Dept. Of Fisheries and Environment Fisheries and Marine Service, Bull. 198, Ottawa, 337 pp.

NEIC - U.S. National Earthquake Information Center (2004). Magnitude 9.0 off the West Coast of Northern Sumatra, Sunday, December 26, 2004 at 00:58:53 UTC Preliminary Earthquake Report, posted at http://neic.usgs.gov/neis/bulletin/neic_slav_ts.html

NIO - India National Institute of Oceanography (2005). 26 December 2004 Tsunami, posted at http://www.nio.org/jsp/tsunami.jsp.

Nisbet, E. G. and Piper, D.J.W. (1998). Giant submarine landslides. Nature, 392.

Noda, E.,(1970) Water waves generated by landslides, J. Waterw. Harbors Coastal Eng. Div. Am. Soc. Civ. Eng., 96, 835-855.

Okada, Y. (1985). Surface deformation due to shear and tensile faults in a half-space, Bulletin of the Seismological Society of America, v. 75, 1135-1154.

Okada, Y. (1992). Internal deformation due to shear and tensile faults in a half-space, Bulletin of the Seismological Society of America, v. 82, No. 2, 1018-1040.

Okal, E. A. (1993). Predicting large tsunamis. Nature, 361:686-687.

Pelayo, A. M. and D. A. Wien (1992) Tsunami Earthquakes: Slow Thrust-Faulting Events in the Accretionary Wedge. J. Geoph. 97, NO. B11, PP. 15,321-15,337, doi:10.1029/92JB01305.

Pelinovsky, E.N. (1996) Hydrodynamics of tsunami waves. Institute of Applied Physics, Nizhny Novgorod, 273 pp.

Pelinovsky, E.N. (2003) Analytical models of tsunami generation by submarine slides. In: Submarine Landslides and Tsunamis , A. C. Yaliner, E. Pelinovsky, E. Okal, C. E. Synolakis (eds.), Kluwer Academic Publishers. pp 111-128.

Pelinovsky, E. and Poplavsky, A. (1996). Simplified model of tsunami generation by submarine landslides. Phys. Chem. of the Earth 21,13-17.

Piatanesi, A. and S. Lorito (2007), Rupture Process of the 2004 SumatraAndaman Earthquake from Tsunami Waveform Inversion, Bulletin of the Seismological Society of America, v. 97, no. 1A, S223-S231.

Plafker, G., Kachadoorian, R., Eckel, E.B. and Mayo, L.R. (1969). Effects of the earthquake of March 27, 1964 on various communities. US Geo. Surv. Prof. Paper 542-G, US Geological Survey, Washington, DC.

Rothwell, R.G., Thomson, J. and Kahler, G. (1998). Low-sea-level emplacement of a very large Late Pleistocene 'megaturbidite' in the western Mediterranean Sea Nature 392, 377-380.

Shapiro, N. M., S. K. Singh, and J. Pachero (1998), A fast and simple diagnostic method for identifying tsunamigenic earthquakes, Geph. Res. Letters, 25, 20, 3911-3914.

Shigihara Y., D. Goto, F. Imamura, Y. Kitamura,T. Matsubara, K. Takaoka and K. Ban (2006). Hydraulic and numerical study on the generation of a subaqueous landslide-induced tsunami along the coast, Natural Hazards, 39,159–177, DOI 10.1007/s11069-006-0021-y.

SOI - Survey of India (2005). Preliminary report of tsunami observations, posted at http://www.surveyofindia.gov.in/tsunami4.htm.

Stein, S. and Okal E. (2005). Ultra-long period seismic moment of the great December 26, 2004 Sumatra earthquake and implications for the slip process, posted at http://www.earth.northwestern.edu/people/seth/research/sumatra2.html.

Stein, S. and Wysession M. (2003), An Introduction to Seismology, Earthquakes, and Earth Structure. Blackwell Publishing, 498pp.

Tanioka, Y. and T. Seno (2001), Detailed analysis of tsunami waveforms generated by the1946 Aleutian tsunami earthquake, Natural Hazards and Earth SystemSciences, 1, 171175.

Tinti, S., and Bortolucci, E. (2000a) Analytical investigation of tsunamis generated by submarine slides, Annali di Geofisica, 43, 519–536.

Tinti, S., and Bortolucci, E. (2000b). Energy of water waves induced by submarine landslides. Pure appl. Geophys., Vol. 157, pp. 281-318.

Titov, V., A. B. Rabinovich, H. O. Mofjeld, R. E. Thomson and F. I.Gonzales (2005), The Global Reach of the 26 December 2004 Sumatra Tsunami, Science, 309, 20452048.

Tobita, M., H. Suito, T. Imakiire, M. Kato, S. Fujiwara, and M. Murakami (2006), Outline of vertical displacement of the 2004 and 2005 Sumatra earthquakes revealed by satellite radar imagery, Earth, Planets and Space , 58, e1-e4.

USGS Energy and Broadband Solution,posted at
http://neic.usgs.gov/neis/eq_depot/2004/eq_041226/neic_slav_e.html

Ward, S.N. and Day, S.J. (2003). Ritter Island Volcano - Lateral collapse and tsunami of 1888. Geophysical Journal International, 154, 891 - 902.

Watts, P. (1998). Wavemaker curves for tsunamis generated by underwater landslides. J. Waterway, Port, Coastal, and Ocean Engrg., ASCE, 124(3), 127-137.

Watts, P. (2000). Tsunami features of solid block underwater landslides. J. Waterway, Port, Coastal, and Ocean Engrg., ASCE, 126(3), 144-152.

Watts, P., Imamura, F., Grilli, S. (2000). Comparing model simulations of three benchmark tsunami generation cases. Science of Tsunami Hazards 18(2), 107-123.

Wiegel, R.L. (1955). Laboratory studies of gravity waves generated by the movement of a submerged body. Trans. Am. Geophys. Union 36(5):759-774.

Yagi, Y. (2005). Preliminary Results of Rupture Process for 2004 Off Coast of Northern Summatra Giant Earthqauke (ver. 1), posted at
http://iisee.kenken.go.jp/staff/yagi/eq/Sumatra2004/Sumatra2004.html.

CHAPTER IV

INVESTIGATION INTO TSUNAMI PROPAGATION BY VERTICALLY INTEGRATED EQUATIONS.

1. Introduction

Our aim is to present numerical tools for investigation tsunami propagation in the World Ocean based on the experience gained through modeling the Indian Ocean Tsunami (IOT) of December 2004 and of the Kuril Island Tsunami (KIT) of November 2006. As a tool the numerical computations aid in tsunami prediction and warning. The main parameter in the warning process is the tsunami travel times to various coastal locations. Even this seemingly simple parameter is quite difficult to define for the long distances propagation as strong tsunami signals generated along ridges and scattered by seamount travel much slower than the direct signal (often) of low energy arriving from the primary source. The second important purpose of tsunami prediction is estimation of the wave amplitudes at critical locations. Many years of observations suggested that the energy arriving from the tsunami sources is a function of the directional properties of such sources. A series of numerical experiments carried out more than 20 yr back (Zielinski and Saxena, 1984; Kowalik and Murty, 1987) delineated directional properties of the various tsunami sources. To study radiational pattern of a source a maximum tsunami amplitude in a given location was considered. From the space distribution of this parameter the direction of the main lobe of tsunami energy was inferred. For example, for the tsunami source located in the Shumagin Seismic Gap (Aleutian Islands) the main lobe of energy is directed towards the south and southeast which did explain the large tsunami occurred at the Hawaiian Islands.

Van Dorn (1984) and Candella et al.(2008) deduced from the coastal observations that the tsunami energy has an exponential decay in time. The experience gained from IOT and KIT indicated a more complicated pattern of signal amplification and decay because the sea levels recorded in the wake of these tsunamis showed strong tsunami signal enhancement of the later arriving secondary waves. Using these tsunami events we demonstrated that sudden changes caused by higher energy pulses in the intermittent tsunami wave trains can be assessed by energy fluxes. Therefore, to delineate the regions of tsunami wave amplification and travel time we proposed to use energy flux. A series of numerical experiments related to KIT defined in explicit way the bathymetric features which scatter tsunami signal towards ports, like Crescent City. Identification of the distant bathymetric features was achievable since the energy flux vector delineated the energy pathways that coupled distant bathymetric features to ports located thousands of kilometers apart. Calculations of the energy flux vector involves simple formulas based on two components of velocity and sea level. The maximum of the energy flux (which has no directional properties) can be evaluated from the sea level amplitude, hence both observed and computed

sea level can be used for this purpose (Koshimura at al.,2008).

Numerical computations of global tsunami events resulted in construction of a global tsunami model (GTM) based on the shallow water equations, as discussed in Kowalik et al. (2005, 2007). GTM covers entire globe with resolution of 1 arc min (200 millions grid points) and parallel version of code has been implemented at Alaska Region Supercomputing Center. To propagate tsunamis to the various coastal locations, along with the global model we shall use interactive grids, such as a combination of coarse and fine grids. The rationale behind using multiple grids is to reduce the total computational effort by placing a coarse grid in the deep ocean (and offshore) region and couple this with the finer grid in the shallow coastal areas. At the same time, increasing spatial resolution from the open ocean toward coastal regions provides greater accuracy in the numerical solution. The ocean–wide model will propagate the tsunami from the source to the shelf region (500m depth). From this depth, a fine resolution grid model will propagate the tsunami signals into bays, inlets and ports. In the final stage, the signal will be resolved by a superfine runup model with grid resolution of 10–50m. Already in 1991 Kowalik and Whitmore tested the multigrid approach by computing tsunami at Adak, Alaska. This geographical area has a complex bathymetry with multiple entrances connecting local bays to the open ocean. The method was tested with two tsunamis generated by the 1952 Kamchatka and 1986 Andreanof Islands earthquakes and recorded at Adak.

Although in the present book the numerical models for the tsunami are those developed by author and his students, these models are intimately connected to the studies of the entire tsunami and oceanography communities. The roots of numerical methods used in the tsunami hydrodynamics are numerical methods developed to study storm surges and tides in the 10 yr span between 1960–1970. The earliest application to tsunami was undertaken by R.O. Reid and his students to investigate island response to tsunami, viz., Vastano and Reid, 1967. The numerical model developed for the Northern Pacific by Hwang and Divoky, 1970, was verified by hindcasting the wave behavior following the Alaskan earthquake of 1964. The subsequent development by Hwang et al., 1972 allowed comparison with field measurements as well as provided explanations of the large tsunami at Crescent City, California. These earlier applications proved the usefulness of numerical solutions for tsunami warning, prediction and understanding tsunami physics. Applications of computer codes to tsunami and experience gained resulted in larger publications which consistently treated the tsunami generation, propagation and runup as one phenomenon. In the Soviet Union such book was coauthored by Marchuk, Chubarov and Shokin, 1983 and was translated at Los Alamos into English. In the USA the codes developed at Los Alamos and tested for various scenarios by Ch. Mader were summarized in the book titled Numerical Modeling of Water Waves, 1988. Although Japanese investigations initiated by Goto and Shuto (1981) were not compiled in the larger volume, they evolved into tsunami computation programs TUNAMI published as IOC manual by Imamura et al., 1997. These books and programs based on numerical schemes for the shallow water equations solved main stages of tsunami generation and propagation. Difficult problems were for the first time fully investigated, including tsunami generation by the moving bottom, proper resolution of tsunami wave while propagating from the open ocean towards the shore by developing interconnected latices of different spacial and temporal steps, and

constructing the numerical schemes for the runup where strong nonlinear effects dominate the tsunami physics.

2. Basic equations and tools

To study large scale tsunami propagation the equations of motion and continuity will be formulated in the spherical polar coordinates. λ, ϕ and R, are defined as longitude, latitude and distance from the Earth's center. If the origin of the system is located on the ocean surface, it is more suitable to introduce a vertical coordinate $z = R - R_0$. Here R_0 is the radius of Earth and is equal 6370 km.

Because Earth is not exactly spherical, the equations given below will better describe the large scale motion relative to the geopotential and not to the spherical surfaces. For further discussion of this problem see Gill (1982).

The vertically averaged equations of motion and continuity in the spherical system are (see ChI., Sec. 4)

$$\frac{\partial u}{\partial t} + \frac{u}{R_\circ \cos\phi}\frac{\partial u}{\partial \lambda} + \frac{v}{R_\circ}\frac{\partial u}{\partial \phi} - (2\Omega + \frac{u}{R_\circ \cos\phi})v \sin\phi = -\frac{g}{R_\circ \cos\phi}\frac{\partial \zeta}{\partial \lambda} - \frac{\tau^b_\lambda}{\rho_o D} \tag{IV.1}$$

$$\frac{\partial v}{\partial t} + \frac{u}{R_\circ \cos\phi}\frac{\partial v}{\partial \lambda} + \frac{v}{R_\circ}\frac{\partial v}{\partial \phi} + (2\Omega + \frac{u}{R_\circ \cos\phi})u \sin\phi = -\frac{g}{R_\circ}\frac{\partial \zeta}{\partial \phi} - \frac{\tau^b_\phi}{\rho_o D} \tag{IV.2}$$

$$\frac{\partial \zeta}{\partial t} - \frac{\partial \eta}{\partial t} + \frac{1}{R_\circ \cos\phi}\frac{\partial uD}{\partial \lambda} + \frac{1}{R_\circ \cos\phi}\frac{\partial}{\partial \phi}(Dv\cos\phi) = 0 \tag{IV.3}$$

In the above equations, u is the velocity in the λ (E-W) direction, v denotes the velocity in the ϕ (N-S) direction, and ζ is the sea level, η is the bottom displacement, t is the time, g is the Earth's gravity acceleration (g=981 cm s^{-2}), ρ is the water density, and D is the total depth $D = H + \zeta - \eta$. The Coriolis parameter will be taken as $f = 2\Omega \sin\phi$. It is a function of the Earth's angular velocity $\Omega = 7.29\times10^{-5} s^{-1}$ and the latitude ϕ. The components of the bottom friction force are nonlinear functions of velocity:

$$\tau^b_\lambda = ru\sqrt{(u^2+v^2)} \qquad \text{and} \qquad \tau^b_\phi = rv\sqrt{(u^2+v^2)}$$

To simplify the bottom friction terms in eqs. (1) and (2) the following notation is introduced:

$$\frac{\tau^b_\lambda}{\rho_o D} = \frac{ru\sqrt{(u^2+v^2)}}{\rho_o D} = R_x u \tag{IV.4a}$$

$$\frac{\tau^b_\phi}{\rho_o D} = \frac{rv\sqrt{(u^2+v^2)}}{\rho_o D} = R_y v \tag{IV.4b}$$

The dimensionless bottom friction coefficient r is taken as 3.3×10^{-3}.

In order to identify important steps in the construction of a global numerical code we shall jot down basic numerical formulas for the spherical coordinate system. The computation will be done in a space staggered grid (C grid) given in FigIV.1. The u velocity grid points denoted as horizontal bars are offset from the v velocity grid points (vertical bars). Sea level grid points are denoted by crosses. The grid size (space step) along the E-W direction is $h_\lambda = R_\circ \cos\phi \Delta\lambda$. Index $j = 1, \ldots$ stands for the space stepping along the parallels of latitude, thus the distance along the parallels is expressed as jh_λ. As the parallels of latitudes become very small circles near the poles, this geographical region needs to be either excluded from consideration or introduced into computation through a different map projection. In this study, we exclude the poles from the computational domain. The space step along the N-S direction is $h_\phi = R_\circ \Delta\phi$. Index k stands for the space stepping along the meridians of longitude. Locations of the grid points on the sphere are given by their j and k coordinates. The u, v and ζ points are organized into triplets as shown by the yellow triangles in FigIV.1. The depth is defined at the sea level points. To resolve some terms in the equations of motion the v velocity is needed at the u locations and vice versa. For this reason the blue and red circles are introduced to explain how the averaged values are constructed. The four values given by blue circles, when averaged will define the averaged v velocity at the u point location. This point location is given by $u_{j,k}$. The averaged v velocity at this location is $\bar{v}^u = 0.25(v_{j,k-1} + v_{j,k} + v_{j-1,k} + v_{j-1,k-1})$. In a similar way the average u velocity (four reddish circles) at the $v_{j,k}$ point is $\bar{u}^v = 0.25(u_{j+1,k} + u_{j+1,k+1} + u_{j,k+1} + u_{j,k})$.

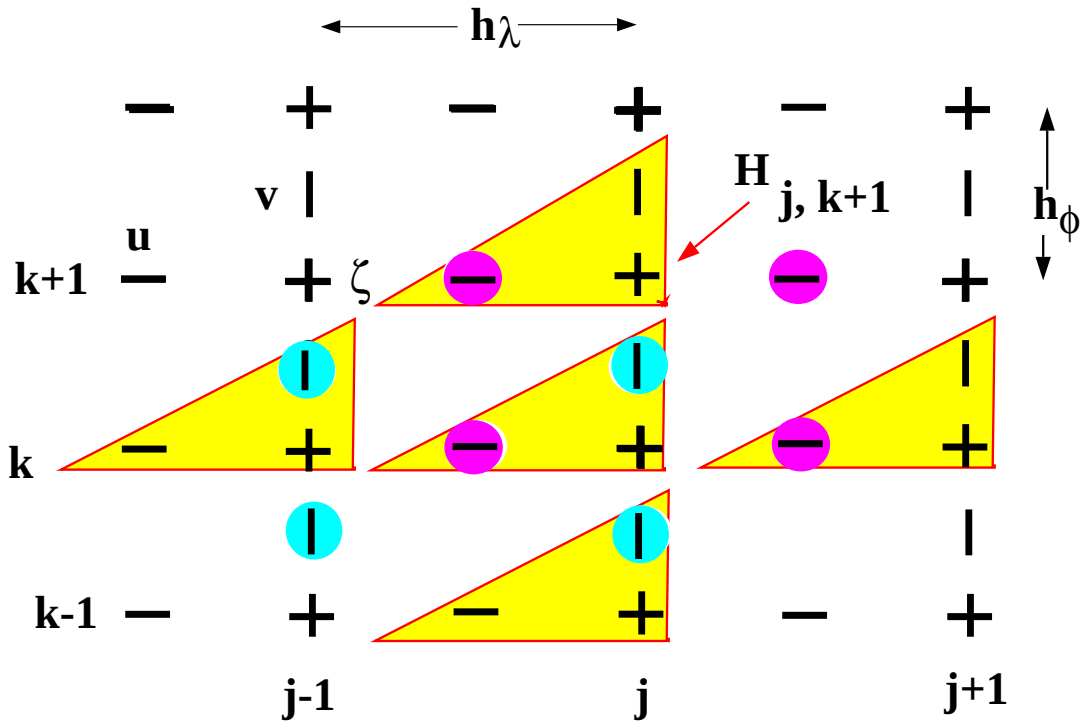

Figure IV.1 Spatial grid distribution in the spherical system of coordinates.

The solution of equations(IV.1-IV.3) is usually advanced in time by the two-time-level numerical scheme (Kowalik and Murty, 1993a; Imamura, 1996). For the spatial derivatives the second order of approximation is constructed.

$$u_{j,k}^{m+1} = u_{j,k}^{m} - \frac{gT}{h_\lambda}(\zeta_{j,k}^{m} - \zeta_{j-1,k}^{m}) + Tf\bar{v}^{u,m} + \frac{T\tan\phi_k^{\zeta}}{R_\circ}\bar{v}^{u,m}u_{j,k}^{m} - TR_{x,j,k}^{m}u_{j,k}^{m}$$
$$-\frac{u_p^m T}{h_\lambda}(u_{j,k}^{m} - u_{j-1,k}^{m}) - \frac{u_n^m T}{h_\lambda}(u_{j+1}^{m} - u_j^{m})$$
$$-\frac{T\bar{v}_p^{u,m}}{h_\phi}(u_{j,k}^{m} - u_{j,k-1}^{m}) - \frac{T\bar{v}_n^{u,m}}{h_\phi}(u_{j,k+1}^{m} - u_{j,k}^{m}) \qquad \text{(IV.5)}$$

$$v_{j,k}^{m+1} = v_{j,k}^{m} - \frac{gT}{h_\phi}(\zeta_{j,k+1}^{m} - \zeta_{j,k}^{m}) - Tf\bar{u}^{v,m+1} - \frac{T\tan\phi_k^{v}}{R_\circ}\bar{u}^{v,m}\bar{u}^{v,m+1} - TR_{y,j,k}^{m}v_{j,k}^{m}$$
$$-\frac{T\bar{u}_p^{v,m}}{h_\lambda}(v_{j,k}^{m} - v_{j-1,k}^{m}) - \frac{T\bar{u}_n^{v,m}}{h_\lambda}(v_{j+1,k}^{m} - v_{j,k}^{m})$$
$$-\frac{Tv_p^m}{h_\phi}(v_{j,k}^{m} - v_{j,k-1}^{m}) - \frac{Tv_n^m}{h_\phi}(v_{j,k+1}^{m} - v_{j,k}^{m}) \qquad \text{(IV.6)}$$

$$\zeta_{j,k}^{m+1} = \zeta_{j,k}^{m} - \frac{T}{h_\lambda}(flux_{\lambda,j+1,k} - flux_{\lambda,j,k})$$
$$-\frac{T}{cos\phi_k^{\zeta}h_\phi}(flux_{\phi,j,k} - flux_{\phi,j,k-1}) + \eta_{j,k}^{m+1} - \eta_{j,k}^{m} \qquad \text{(IV.7)}$$

In the numerical approach we aimed to construct a higher order of approximation in space as did Lynett et al., (2002). For this purpose we modified the upwind/downwind flux code proposed by Mader (2004). For the large scale computations the upwind/downwind scheme is essential as it displays strong stability (Imamura, 1996). We have improved the original code by an additional interpolation between the grid points and the resultant code given by eqs.IV.8 and IV.9 is close to the third order of approximation in space.

$$flux_{\lambda,j,k} = u_p^{m+1}(\zeta_{p,\lambda}^{m} - \eta_{j-1,k}^{m}) + u_n^{m+1}(\zeta_{n,\lambda}^{m} - \eta_{j,k}) + u_{j,k}^{m+1}\frac{(H_{j,k} + H_{j-1,k})}{2} \qquad \text{(IV.8a)}$$

$$\zeta_{p,\lambda}^{m} = (0.5 + u_p^{m+1}\frac{T}{h_\lambda})\zeta_{j-1,k}^{m} + (0.5 - u_p^{m+1}\frac{T}{h_\lambda})\zeta_{j,k}^{m} \qquad \text{(IV.8b)}$$

$$\zeta_{n,\lambda}^{m} = (0.5 + u_n^{m+1}\frac{T}{h_\lambda})\zeta_{j-1,k}^{m} + (0.5 - u_n^{m+1}\frac{T}{h_\lambda})\zeta_{j,k}^{m} \qquad \text{(IV.8c)}$$

$$u_p^{m+1} = 0.5 * (u_{j,k}^{m+1} + |u_{j,k}^{m+1}|) \quad \text{and} \quad u_n^{m+1} = 0.5 * (u_{j,k}^{m+1} - |u_{j,k}^{m+1}|) \qquad \text{(IV.8d)}$$

$$flux_{\phi,j,k} = \cos\phi_k^v \left[v_p^{m+1}(\zeta_{p,\phi}^m - \eta_{j,k}^m) + v_n^{m+1}(\zeta_{n,\phi}^m - \eta_{j,k+1}) + v_{j,k}^{m+1} \frac{(H_{j,k} + H_{j,k+1})}{2} \right] \quad \text{(IV.9a)}$$

$$\zeta_{p,\phi}^m = (0.5 + v_p^{m+1} \frac{T}{h_\phi})\zeta_{j,k}^m + (0.5 - v_p^{m+1} \frac{T}{h_\phi})\zeta_{j,k+1}^m \quad \text{(IV.9b)}$$

$$\zeta_{n,\phi}^m = (0.5 + v_n^{m+1} \frac{T}{h_\phi})\zeta_{j,k}^m + (0.5 - v_n^{m+1} \frac{T}{h_\phi})\zeta_{j,k+1}^m \quad \text{(IV.9c)}$$

$$v_p^{m+1} = 0.5 * (v_{j,k}^{m+1} + |v_{j,k}^{m+1}|) \quad \text{and} \quad v_n^{m+1} = 0.5 * (v_{j,k}^{m+1} - |v_{j,k}^{m+1}|) \quad \text{(IV.9d)}$$

In the above code the index m stands for the time stepping and the time step is T.

3. Domain, boundary conditions and numerical grid

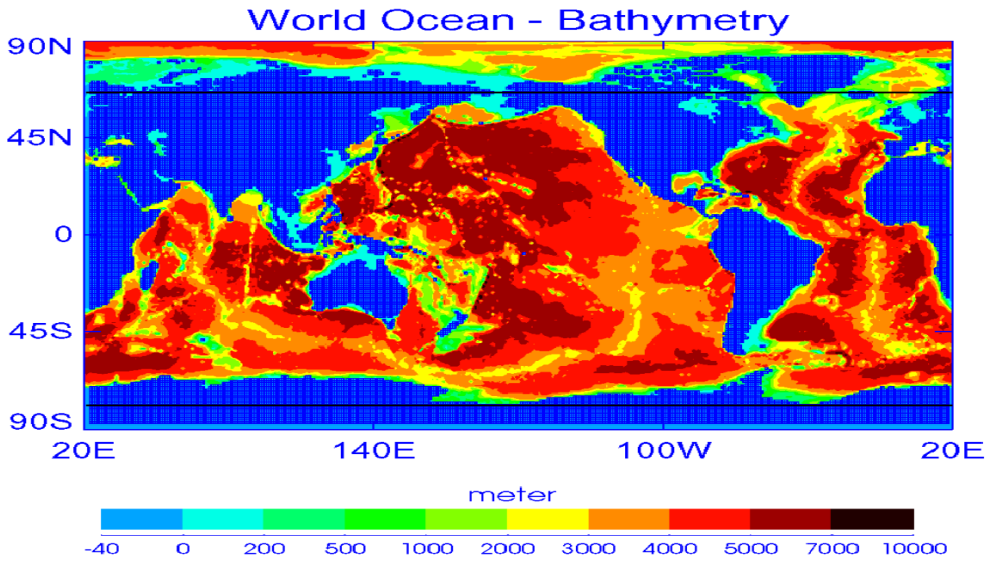

Figure IV.2. Ocean bathymetry. Computational domain extends from 80°S to 69°N.

The integration domain is shown in Fig.IV.2. It extends from 80°S to 69°N. The boundaries include both wet and dry points. Along the coastal (dry points) the normal velocity is set to zero. At the wet boundary points (along 69°N) the radiation condition, established by Reid and Bodine (1968) is used. The entire globe is cut along 20°E longitude, requiring a cyclic boundary condition for sea level and the E-W velocity on this meridian.

It appears at the first glance that the above boundary conditions are sufficient to derive a solution. Introductory numerical experiments showed that even with the relatively large space step of 1' the new dry and wet points may be generated due to runup or run-down. Therefore instead of defining the normal velocity at the shoreline, a numerical scheme for the wetting and drying was introduced.

The total depth $(H + \zeta - \eta)$ is usually taken as the parameter to be tested for the the presence of the wet or dry points (Flather and Heaps, 1975; Immamura, 1996 and Kowalik and Murty, 1993b). The wet and dry points are identified by setting the average (undisturbed) ocean depth as positive (wet points) and elevations (dry points) as the negative values. The total depth in the dry grid points is taken as zero $D = H + \zeta = 0$. A simple runup condition is used. The following steps are taken when the dry point $(j_{wet}+1)$ is located to the right of the wet point j_{wet}.

$IF(\zeta^m(j_{wet}) > -H(j_{wet}+1))$ THEN $u^m_{j_{wet}+1} = u^m_{j_{wet}}$. If wetting is possible (as indicated by the above condition) the velocity from the wet point is extrapolated to the right (dry point), but sea level is calculated through the equation of continuity. The runup algorithm used in the global tsunami model is based on the numerical schemes constructed in ChII, Sec.13 and elucidated in FigII.29.

The spatial grid step of numerical computation is $1'$, ($R_0\Delta\phi$=1.852km) and it changes along the circle of longitude as $R_0\Delta\phi\cos\phi$. Numerical stability requires that this step be greater than distance which wave travels in one time step i.e., $T\sqrt{gH}$. The deepest point in the World Ocean (h$\simeq$11000m) is located close to 11°N, therefore the time step of numerical integration is less than 7.9 s. This step was diminished to 2 s as the runup scheme requires smaller time stepping. The total number of the grid points was close to 2×10^8, therefore the simple time stepping solution, even on a supercomputer may take several weeks. The entire domain was split along the meridians into 40 subdomains to apply 40 processors. With this parallelization, 50hrs of tsunami propagation was reproduced in 9hrs of computer run time.

A small spatial step is important as the short-period waves can be obliterated during large distances of propagation when using large spatial steps. Taking the average depth of the World Ocean as 4000 m, a wave of 10 minute period has a wavelength close to 120 km. Such wave length is discretized by the $1'$ grid into about 64 mesh lengths. This case is close to the problem considered in Ch.II, Sec.6 of monochromatic wave propagating in the channel. The amplitude of a sinusoidal wave propagating over distance 6000 km practically is the same as the amplitude of the initial wave. The wave traveling over the 10000 km distance will diminish only about 2%, and some shorter dispersive waves will be generated as well as can be gleaned from FigII.9.

4. Tsunami in the Indian Ocean

The generation mechanism for the Indian Ocean tsunami is the static sea floor uplift caused by abrupt slip at the India/Burma plate interface. Permanent, vertical sea floor displacement was computed in ChIII., Sec.4 using the static dislocation formulae from Okada (1985).

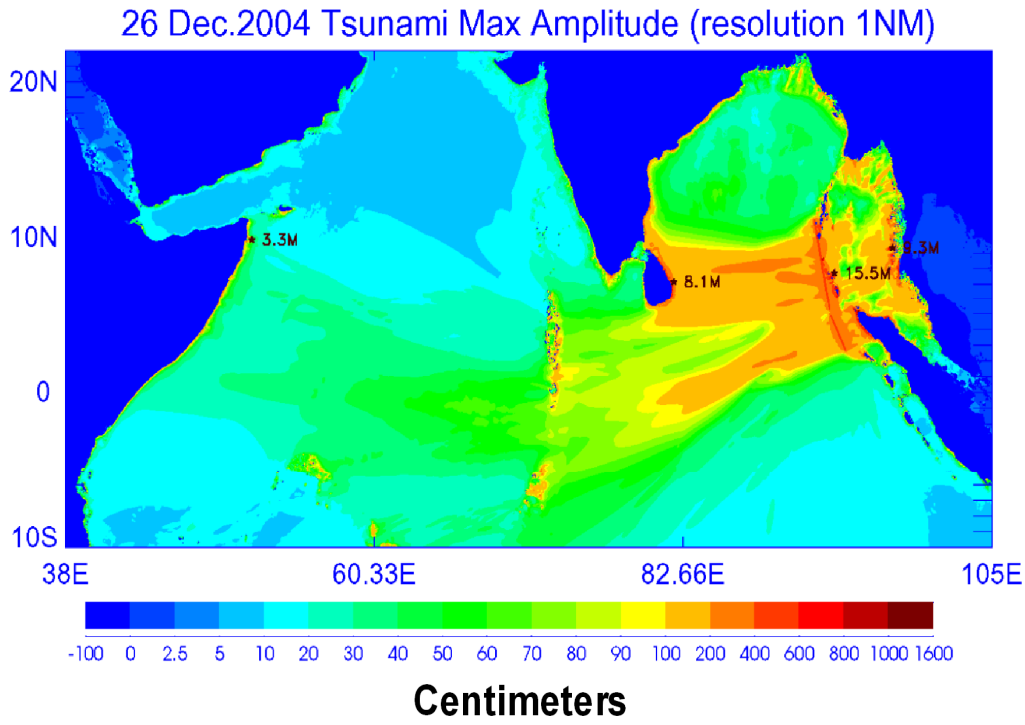

Figure IV.3. Maximum amplitude in the Indian Ocean.

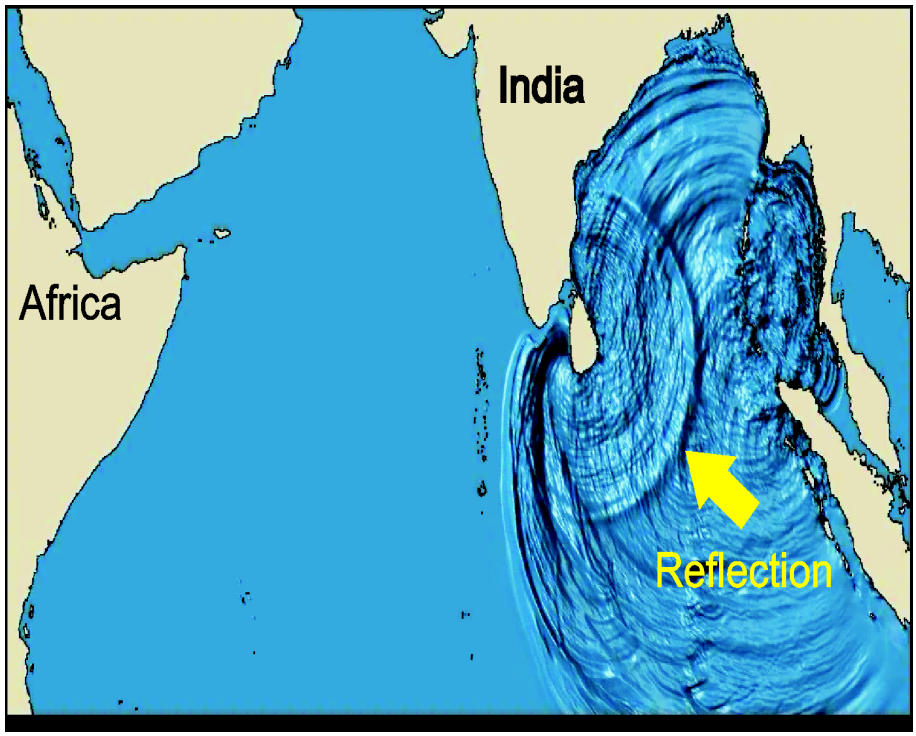

Figure IV.4 Distribution of the tsunami wave height in the Indian Ocean at 2 h 50 min from the tsunami onset. The wave reflected from the India and Sri Lanka propagates back to the source region.

Model computations with this source were made for the 50 hrs of propagation so that the tsunami signal could travel over the entire World Ocean. During this computation the maximum tsunami amplitude in every grid point was recorded. The plot of maximum amplitude in the proximity of the generation domain is given in Figure IV.3

The strongly directional signal generated by the elongated source dominates the Indian Ocean domain. The main energy lobe is directed towards Sri Lanka and the secondary lobe points towards South Africa, sending a strong signal into the Atlantic Ocean. The maximum amplitude is 15.5m in proximity to the fault, 9.3 m at the shore of Thailand, 8.1 m at Sri Lanka, and 3.3 m at the coast of East Africa.

This figure also depicts the amplitude enhancement in the shallow water and especially in proximity to peninsulas and islands due to energy concentration through the refraction process. The large domain of the Arabian Sea is located in the shadow of the main energy beam. Both computation and observation demonstrate significant increase of the tsunami amplitude up to 1.5 m at the coast of Oman at tide gauge in Salalah.

The IOT of 26 December 2004 was quite different from the large scale tsunamis of the Pacific and Atlantic Oceans. Post tsunami analysis suggests that boundary reflections significantly influenced tsunami heights in the Indian Ocean (Murty et. al, 2006). Reflections from land, focusing and trapping of tsunami energy by the long island chains, and amplification and reorganization of the tsunami signal in the straits between continents all played an essential role in the IOT propagation (Kowalik et al., 2005a; Titov et. al., 2005. FigIV.5 depicts multiple reflections from the Indian Peninsula and Sri Lanka as a reverse wave traveled back towards Indonesia. The initial reflection occurred about two hours after the earthquake onset. We will demonstrate later that this reflection sends more energy southward than the initial wave generated by the earthquake.

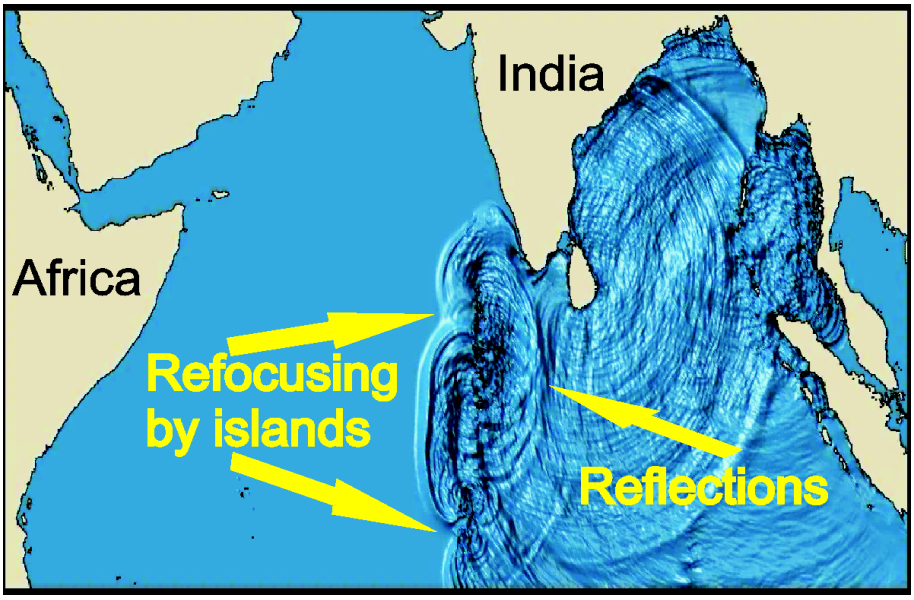

Figure IV.5 Distribution of the tsunami wave heights in the Indian Ocean at hour 4 from the tsunami onset. Along with the reflection shown in FigIV.4, the reflection from the Maldives also sends energy eastward.

The tsunami interaction with the semi-transparent Maldives islands was different from that with the India and Sri Lanka coasts (FigIV.5). While propagating towards Africa, the tsunami impinged on the Maldives Island chain. Only a portion of the incoming tsunami energy crossed this chain. Some energy was trapped around the islands and the rest was reflected backwards. As FigIV.5 depicts, the forward signal is changed through refocusing. An island (or a few islands) splits the tsunami into two parts. These two parts coalesce behind the island, often generating local amplification of the tsunami (see wave front south-west of the Maldives). The trapped signal around the islands tends to interact with the local bathymetry generating quite large amplitudes which are slowly dissipated through bottom friction and radiation into the open ocean.

The role of multiple reflections in the sea level variations during IOT is well depicted by the sea level recorded on the Cocos Island (FigIV.6). Even though Cocos Island (12 7'S 96 53'E) is not within the field of view of the figures (southern most latitude in FigIV.5. is 10S), it is close enough to draw valid conclusions on the arrival time of reflected waves.

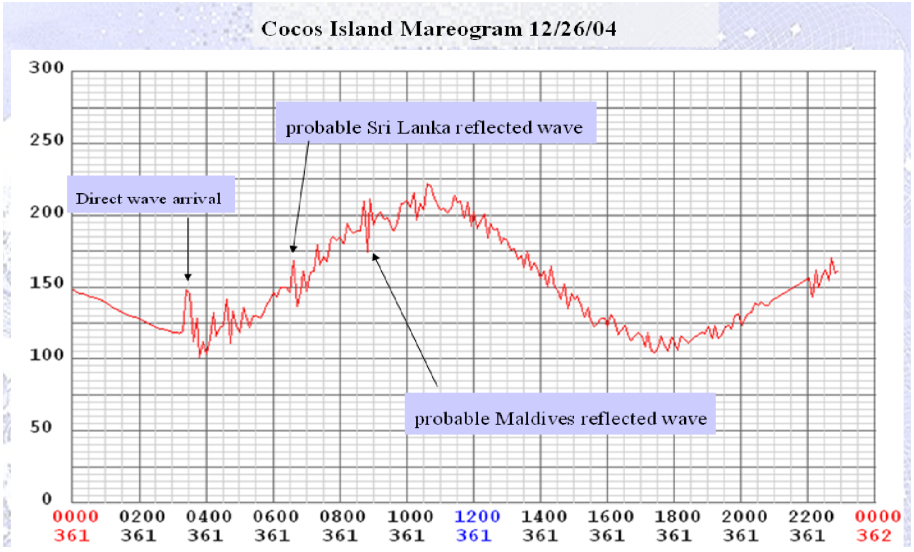

Figure IV.6 Sea level recorded at Cocos Island on December 26, 2004.

There is very good correspondence between predicted reflections from Sri Lanka and the Maldives and features recorded in the mareogram. The reflected wave from Sri Lanka arrived about 3 h after direct wave and the Maldives reflected wave arrived close to 5 h after the direct wave.

5. Global distribution of maximum amplitude

The global maximum amplitude distribution (FigIV.7) shows that the IOT encompassed all over the World Ocean. Although the source directed most of the wave energy towards South Africa, a strong signal was also directed towards the Antarctica. It is obvious that the ocean bathymetry affected the tsunami propagation. For example, tsunamis tended to propagate toward Antarctica along the oceanic ridges, and subsequently con-

tinued to transfer higher energy along the South Pacific ridge toward South and Central America. This mode of propagation resulted in the tsunami amplitude increase up to 65 cm along the Pacific coast of South America. A similar mode of energy transfer is observed in the Atlantic, where the Mid-Atlantic Ridge channelled this tsunami to produce 30 cm wave amplitude as far north as Nova Scotia. An especially large energy flux was ducted from the South Atlantic Ridge towards Brazil and Argentina. The filaments of energy trapped along the South Pacific Ridges are most spectacular as they ducted tsunami energy for many thousands of kilometers. A simple explanation of the energy trapping using the continuity equation leads us to conclude that the amplitude should increase over the ridges due to the relatively shallower depth there. At the same time the role of bottom friction over the 3 km deep ridge is negligible and, therefore, the tsunami can travel long distance without much energy losses. The trapping of this energy is probably related to the long waves trapped along the ridge (Mei, 1989; Koshimura et al., 2001). The cross-ridge trapping length, which is responsible for energy concentration, is approximately defined by the tsunami wavelength. As the Indonesian tsunami carried a wide spectrum of waves with periods from 20 to 50 min, the wavelength for the mid-ocean travel is in the range of 100 km to 600 km. A simple explanatory model for the long wave trapping may be based on different speed of the tsunami wave over and off ridge. As the wave over ridge is slower and wave off ridge is faster, the joint tsunami wave front is curved in such a way that the energy is fluxed towards the ridge. The above explanation neglects the influence of the Coriolis force on tsunami propagation. Tsunamis are typically computed without Coriolis force because their periods are much smaller than the inertial period. As propagation proceeds over long distances the compounding effect of Coriolis force may sum up and increase. In FigIV.8 the residual maximum amplitude is given as difference between two computed distribution, with and without Coriolis force. The difference given in FigIV.8 shows locations where Coriolis force dominates. The amplitudes are not very large and according to expectation the influence is increasing towards the south since the Coriolis term increase poleward from equator. Consistent change is observed along the South Pacific Oceanic Ridges (see also trapping in the South Atlantic). Those are regions of enhanced tsunami heights and wave currents as well and therefore the stronger action of the Coriolis force is present. Residuals due to Coriolis force are close to 1 cm and since the total amplitude along this ridge according to FigIV.7 is approximately 4cm, we may conclude that Coriolis force plays a certain role in the energy trapping along the oceanic ridges . A simple model for energy trapping due to the Coriolis force is a Kelvin wave propagating along the depth discontinuity (Longuet-Higgins, 1969). The across-discontinuity trapping distance is defined by the Rossby radius of deformation (Gill, 1982). This distance is a function of depth and latitude and for the depth from 1 km to 4 km and for latitude of 40° to 60° the Rossby radius ranges from 1000 km to 2000 km. As this length is much larger than the tsunami wavelength we can conclude that Coriolis force is less effective in the concentrating tsunami energy along the oceanic ridges, unless the longer period tsunami waves are generated.

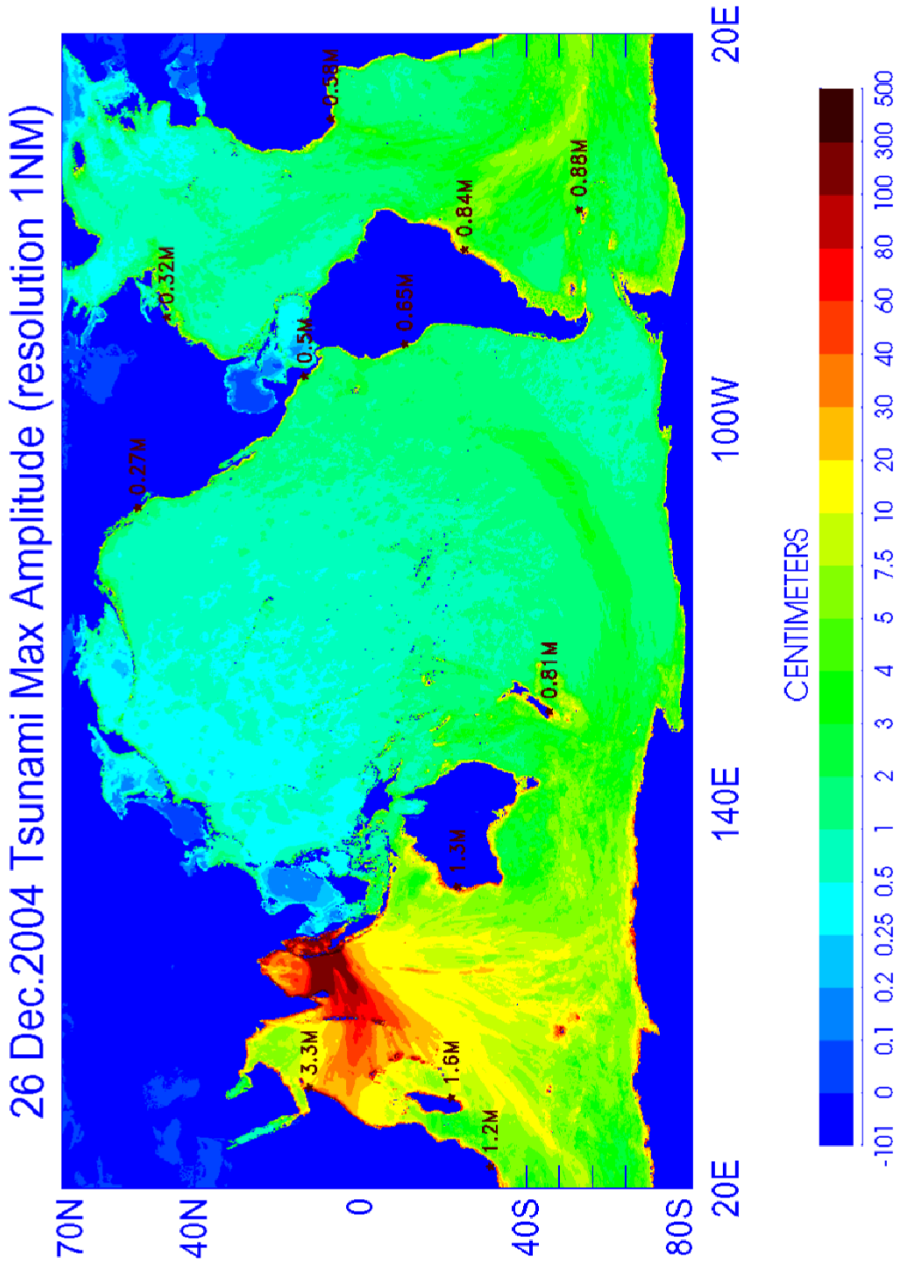

Figure IV.7. Maximum amplitude in World Ocean.

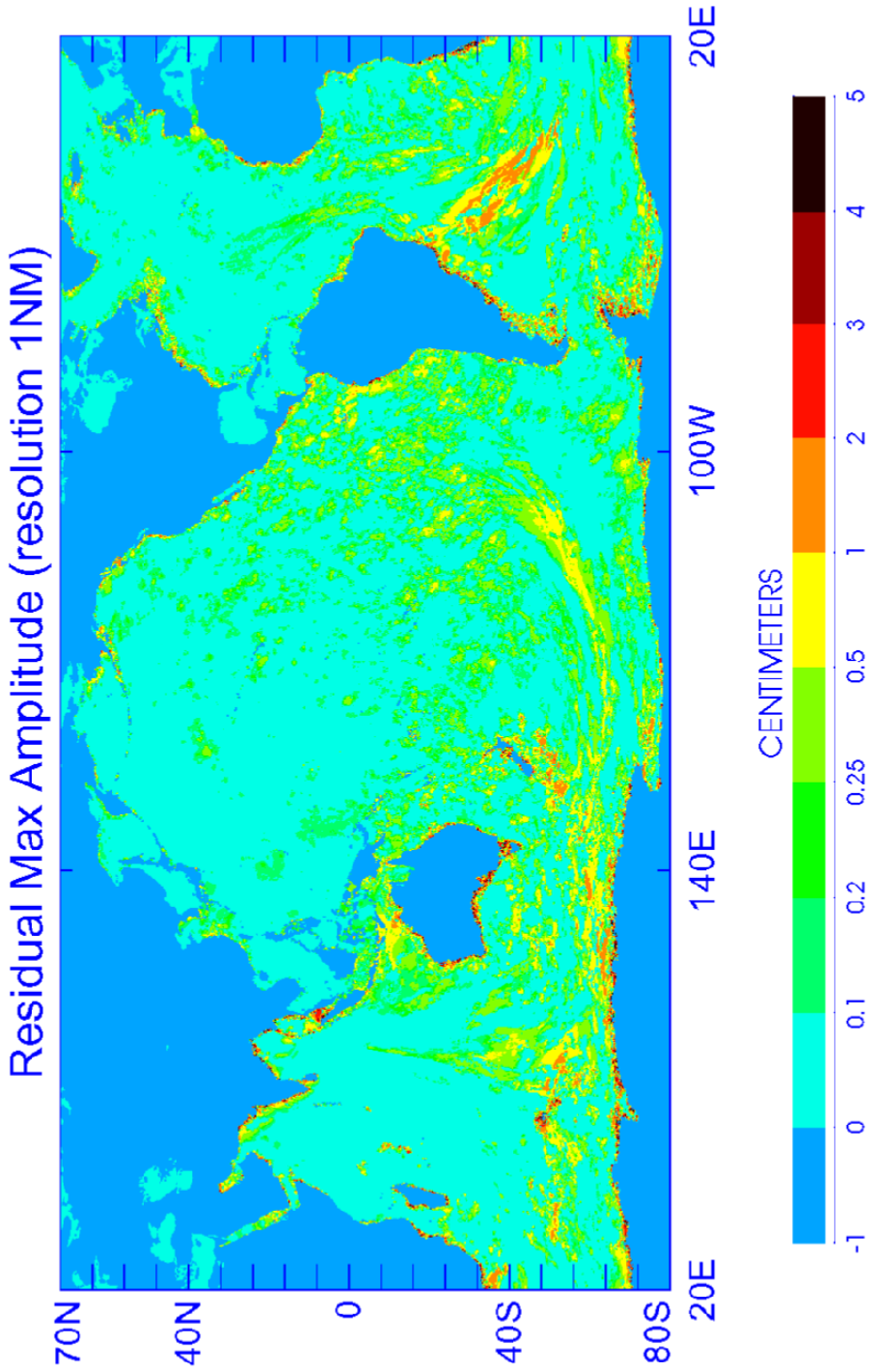

Figure IV.8. Residual maximum amplitude in World Ocean.

To demonstrate the pattern of the energy trapped over the various bathymetric features we introduce the energy flux (see ChI, Sec.7).

In the rectangular system of coordinates, with the x coordinate along E-W direction and y along N-S direction, the u component of velocity along x direction can be combined with the sea level (ζ) to define E-W component of the energy flux vector (Kowalik and Murty, 1993a):

$$E_x = \rho g H u \zeta \tag{IV.10}$$

Similarly, the N-S component of the energy flux vector is defined (with v, the velocity component along the y direction):

$$E_y = \rho g H v \zeta \tag{IV.11}$$

In the above: ρ is the sea water density, g=9.81m s^{-2} is the Earth's gravity acceleration and H is the ocean depth. The energy flux vector for the progressive wave is always propagating into the same direction as the sea level and velocity and its direction is perpendicular to the wave front. To preserve direction of the energy flux in the progressive wave the velocity and sea level elevation remain in phase (Nekrasov, 1992; Henry and Foreman, 2001). Energy flux units are expressed as Joule/(s cm) so this is an energy flux per unit width and per unit time. To derive the total energy flux the above expressions should be multiplied by the length of a crossection and integrated over the time period.

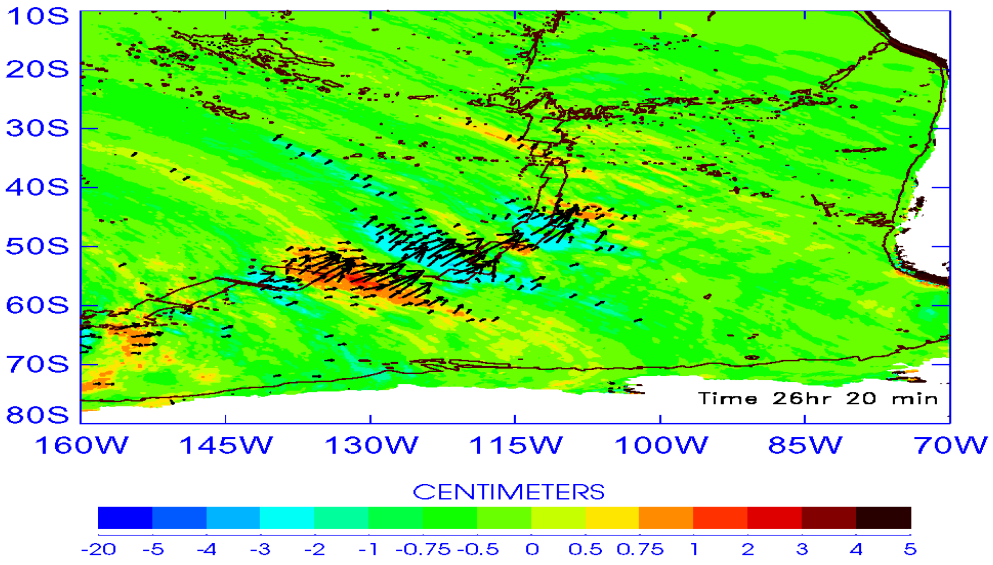

Figure IV.9. Energy flux vectors over the South Pacific Ridge at time 26 h 20 min. Colors denote the sea level. Dark-brown lines denote the ridge depth - 3000 m depth contour.

In FigIV.9 the energy flux vectors are shown in the south-western part of the Pacific Ocean. The larger tsunami amplitudes are located above the oceanic ridge and the energy flux is directed along the ridge. This small group of higher amplitude waves does not belong to the first tsunami signal arriving in this region. Its average wavelength is about 1350 km, as the depth of the ridge is close to 3 km the wave period was about 2 h. This is a somewhat long period for a free tsunami wave, but the longer wavelength as it is closer to the Rossby radius of deformation, suggested possible influence of the Coriolis force. The wave pattern also shows that the waves over ridges are slower than the off-ridge waves, suggesting trapping due to refraction and focusing of off-ridge energy towards the ridge. Nonetheless, we cannot exclude the possibility of a resonance interaction of the tsunami wave and the ridge bathymetry since Snodgrass et al., 1962 demonstrated the presence of discrete spectra in waves trapped over depth discontinuities. Mei, 1989 showed that over a stepped bottom ridge the discrete spectra exist as well. If an incident wave can excite these trapped modes, an amplification of the tsunami signal due to resonance will follow.

The IOT in the global ocean displays many interesting features. One of them observed through the animation technique is tsunami transformation when it travels through the narrows between oceans. The passage between Antarctica and Australia/New Zealand plays a noticeable role in tsunami amplification. As the passage is wide on the Indian Ocean side and constrained on the Pacific side, the eastward moving signal is amplified and also reorganized into periodic wave-like structures. A similar reorganization of a quasi-turbulent signal into oscillatory wave pattern can be observed in the passage between South America and Africa for the tsunami propagating from the Southern into the Northern Atlantic (FigIV.10).

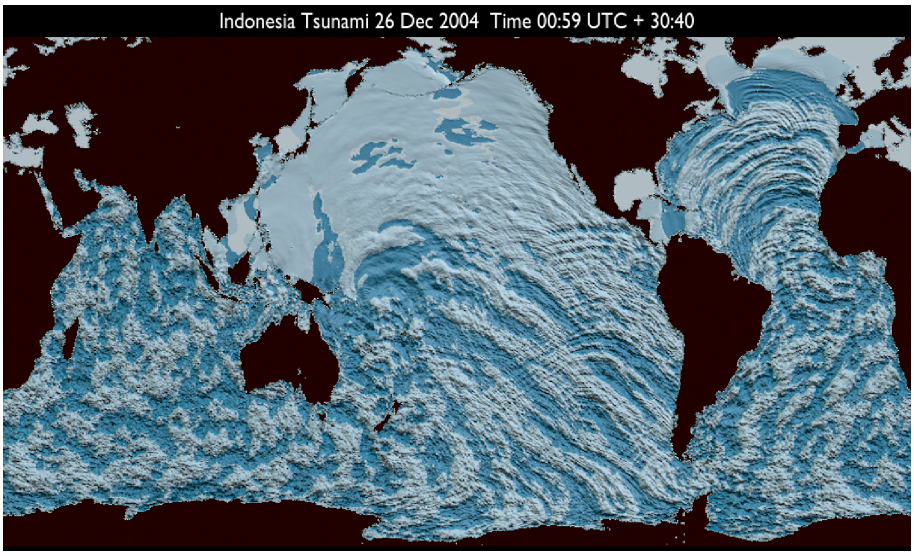

Figure IV.10. Sea level pattern generated by the IOT of 26 Dec. 2004 at 30 h 40 min from the onset. Tsunami signals in the Northern Atlantic and Southern Pacific have been reorganized into coherent waves after passing through the narrows between Africa and South America, and Australia and Antarctica.

6. Time dependent propagation

Although the maximum amplitude defines tsunami distribution in the World Ocean, it does not reveal the temporal development of tsunamis. To improve understanding of the large scale temporal processes we used the temporal change of the tsunami energy fluxes passing through various cross-sections. The first cross-section considered is in the Indian Ocean, from 80 E to 105 E along 10 S (see FigIV.3). The southward directed energy flux shown in FigIV.11 is responsible for the tsunami signal propagating into the Pacific. The first maximum in this figure has been associated with the direct wave passing through the latitude 10 S at 2 h after the initial source motion. The next, even bigger energy influx arrived 2 h later, and is caused by the reflection from Sri Lanka and the east coast of India. The reflection from the Maldives Islands generates a signal which passed the cross-section at about 6.5 h from the initial disturbance. This cross-section is located quite close to the Bay of Bengal and therefore a large portion of the Maldives-reflected signal omitted this route. Since the Bay of Bengal acted as a parabolic mirror, it sended many reflected signals of smaller amplitude southward. The conclusion from the above experiment is that the reflected signal may send more energy south than the direct signal.

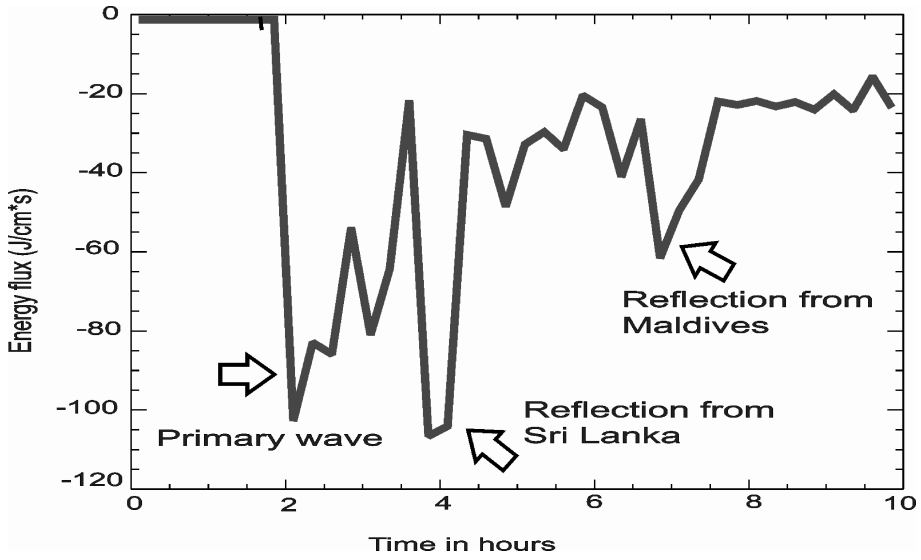

Figure IV.11. Southward directed energy flux through the E-W cross-section located in the Indian Ocean along 10 S from 80 E to 105 E.

To understand better the global energy flux into the Atlantic and Pacific Oceans we notice from FigIV.7 that the leakage of energy into the Atlantic Ocean (between Africa and Antarctic) showed a unidirectional pattern since the energy was pumped into this domain through the directional properties of the source function. From the above experiment we can infer that the energy was redirected into Pacific.

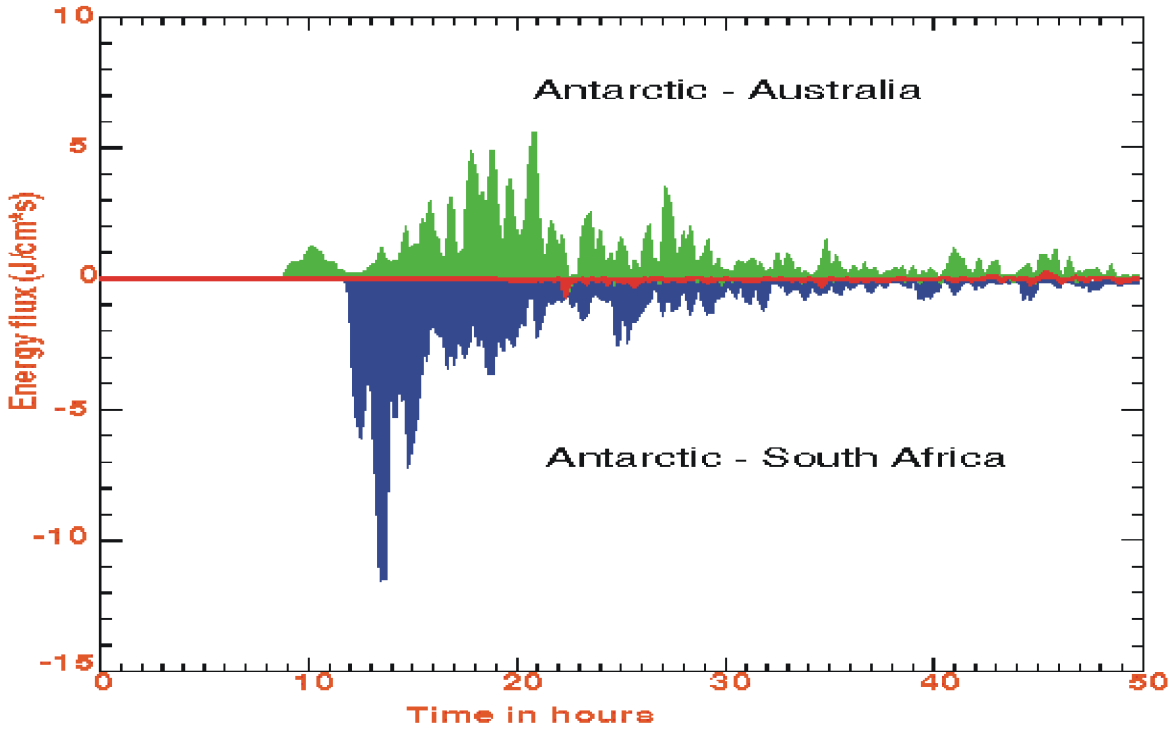

Figure IV.12. Energy flux through the cross-sections located between Antarctic and major continents. Along 20E from Antarctic to South Africa (AS), blue color, along 140E, from Antarctic to Australia (AA), green color, along 70W from South America to Antarctic, red color (after Kowalik et al., 2005b).

To investigate the mechanisms for redirection and quantity of energy entered the Southern Pacific Ocean an energy flux is considered (Kowalik et al., 2005b, 2007a) through the three cross-sections located between Antarctica and the major continents. The cross-section (blue color in FigIV.12) along the longitude 20°E from Antarctica to South Africa (AS) shows the time variation of the energy flux between Indian and Atlantic Oceans (eastward is the positive direction). This flux remains negative for the entire period of 50 h, thus confirming that the inflow is directed into the Atlantic Ocean. On the other hand, the energy flow through a cross-section along 140°E (green color) from Antarctic to Australia (AA) is at all times positive (from the Indian to Pacific Oceans). The flux through the cross-section located between South America and Antarctica at 70W (red color), reveals a small inflow from the Atlantic into the Pacific. FigIV.12 clearly demonstrates that the magnitude and the time variability of energy fluxes through cross-sections AA and AS are quite different in character. The flux passing AS has a large value and the maximum energy inflow to the Atlantic is located close to the initial wave front, even though the first arriving signal is not related to the maximum energy. The energy flow into the Atlantic is a result of the source orientation. The energy flow through AA demonstrates that tsunami arrives to this cross-section about 10 h from the onset of the earthquake; it initially has small amplitude which slowly increases in time from 18 to 21 h to achieve a few maxima.

Analysis made by Kowalik et al., (2005b, 2007b) demonstrated that the maxima from 18 to 21 h in FigIV.12 were related to the energy flux arriving by the various routes from the Indian Ocean. The arrival time of these signals depends on the depth and on the traveled distance. Signals which travel from the generation area to the section AA through the deep ocean travel faster, in about 10 h, but transfer less energy. The large inflow of energy shown in FigIV.12, is related to the reflected signals off the Seychelles, Maldives and Africa, and to a slow wave which traveled along ridges and was originated through reflections in the Bay of Bengal. To compare the total energy flux entering Pacific and Atlantic Oceans over the first 50 h of process, the energy fluxes given in FigIV.12 have been integrated in time. The total energy leakage into the Pacific Ocean is approximately 75% of the total leakage to the Atlantic Ocean. This large value is quite remarkable considering that the source directs energy into Atlantic Ocean and the energy is re-routed into Pacific by reflections. As pointed out by Murty et al., (2006), the Indian Ocean resembles an elliptical shape which has a tendency to multiple reflections and focusing. FigIV.12 is closely related to the time-history of the tsunami energy in the Indian Ocean. Van Dorn (1984) and Candella et al.(2008) deduced from the coastal observations that the tsunami energy has an exponential decay in time. The energy leakage to the Atlantic and Pacific (FigIV.12) shows a similar pattern in time. After an initial build up the energy started to decay in time, but the decay pattern is dominated by the strong energy pulses, due to multiple reflections and energy trapping along the ridges, islands and seamounts.

7. Travel time

Tsunami travel time from the source region to the given location is important parameter in the tsunami prediction and warning. The Indonesian tsunami arrival times have been determined for many locations (Merrifield et al, 2005; Rabinovich, 2005; http://www-sci.pac.dfo-mpo.gc.ca/osap/projects/tsunami/tsunamiasiax_e.htm; http://ilikai.soest.hawaii.edu/uhslc/iotd/; http://www.nio.org/jsp/tsunami.jsp). This set of data presents a possibility for the ocean-wide comparison of the data and the model. Our first numerical experiment delineates the tsunami arrival time at every grid points for a signal of 0.1cm amplitude. The computed tsunami travel time chart depicted in FigIV.13 shows that even at such small limiting amplitudes the tsunami signal arriving at Alaska and North America did not pass through the Indonesian Straits but rather around the Australia and New Zealand.

The next numerical experiment computes isolines of arrival time for the tsunami signal of 0.5cm amplitude (FigIV.14). In the vast regions of Northern and Central Pacific this figure does not show a consistent arrival time. We may conclude that the main premise used to construct these figures, namely that the first train of tsunami waves is associated with the significant wave, does not hold true. We were able to construct isolines of arrival time in the regions of larger amplitudes, i.e. in the Indian Ocean, in the South Pacific (especially along the South Pacific Ridge) and in the South Atlantic. By checking results of computations (given in FigIV.7) at the coastal locations we found that a tsunami of 0.5 cm amplitude arrived at every location in the Pacific Ocean. This wave did not arrive at western North America by refracting around New Zealand; it traveled closer to South America via energy ducts located over South Pacific ridges. The travel time for these

larger energy waves is much longer compared to the travel time depicted in FigIV.13 for the signal of 0.1cm amplitude. In Table 2 the observed arrival time is compared with the computed arrival time of 0.1cm and 5cm tsunami amplitude. The observations define travel times uniquely when amplitude of the signal is above the noise level. The mixed signal of meteorological and tsunami origin is difficult to differentiate. We took, somewhat arbitrarily, the amplitude of 5 cm as a signal strong enough to be seen above the meteorological noise. As can be seen from FigIV.12 in many locations, and as close to the source as New Zealand, the first waves to arrive were quite small and they slowly increased in amplitude. For example, the observed arrival time at Jackson Bay, NZ was 18 h18 min, while according to the travel time computed by the first perturbation of 0.1cm at this location, the arrival time for the first wave was 12 h 30 min. The stations located in the Northern Pacific showed the largest differences between the calculated and observed travel time. This is caused either by small tsunami signal-to-noise ratio, or by multiple paths between the source and gauge locations. As amplified tsunami along ridges and scattered wave by seamounts travel much slower than the direct signal from the primary source, the interaction between wave fronts generated by primary and secondary sources leads to difficulties in prediction of arrival time for the tsunami with the largest amplitude.

Table 1. Observed and calculated travel time.

Station location	Travel time observed	Travel time for 0.1cm amplitude	Travel time for 5cm amplitude
Chennai, (80°.17E, 13°.04N	2h36min	2h18min	2h20min
Male, (73°.52E, 4°.18N	3h25min	3h12min	3h18min
Hanimadhoo, (73°.17E, 6°.77N)	3h41min	3h24min	3h30min
Diego Garcia, (72°.40E, 7°.28S)	3h55min	3h40min	3h40min
Hillarys, (115°.73E, 31°.82S)	6h41min	6h24min	6h36min
Salalah, (54°.00E, 16°.93N)	7h17min	7h6min	7h6min
Pt. La Rue, (55°.53E, 4°.57S)	7h25min	7h24min	7h24min
Lamu, (40°.90E, 2°.27S)	9h9min	8h30min	8h30min
Zanzibar, (39°.18E, 6°.15S)	9h49min	10h24min	10h36min
Portland, (141°.60E, 38°.33S)	10h39min	9h48min	10h18min
Richard's Bay, (32°.08E, 28°.80S)	11h13min	11h00min	11h12min
Port Elizabeth, (25°.63E, 33°.97S)	12h28min	12h00min	12h6min
Jackson Bay, (168°.62E, 43°.98S)	18h18min	12h30min	19h30min
Arraial de Cabo, (42°.02W, 22°.97S)	21h56min	20h54min	21h30min
Arica, (70°.21W, 18°.22S)	26h36min	26h6min	29h20min
Char. Amalie,(64°.55W, 18°.20N)	28h42min	27h45min	33h30min
San Diego, (117°.12W, 32°.45N)	31h25min	29h0min	35h30min
Halifax, (63°.59W, 44°.66N)	31h30min	30h6min	32h6min
Atl.City,(74°.25W, 39°.21N)	31h48min	30h45min	33h30min
Toffino, (125°.55W, 49°.09N)	32h1min	29h0min	38h30min
Adak, (176°.65W, 51°.87N)	35h	27h	40h

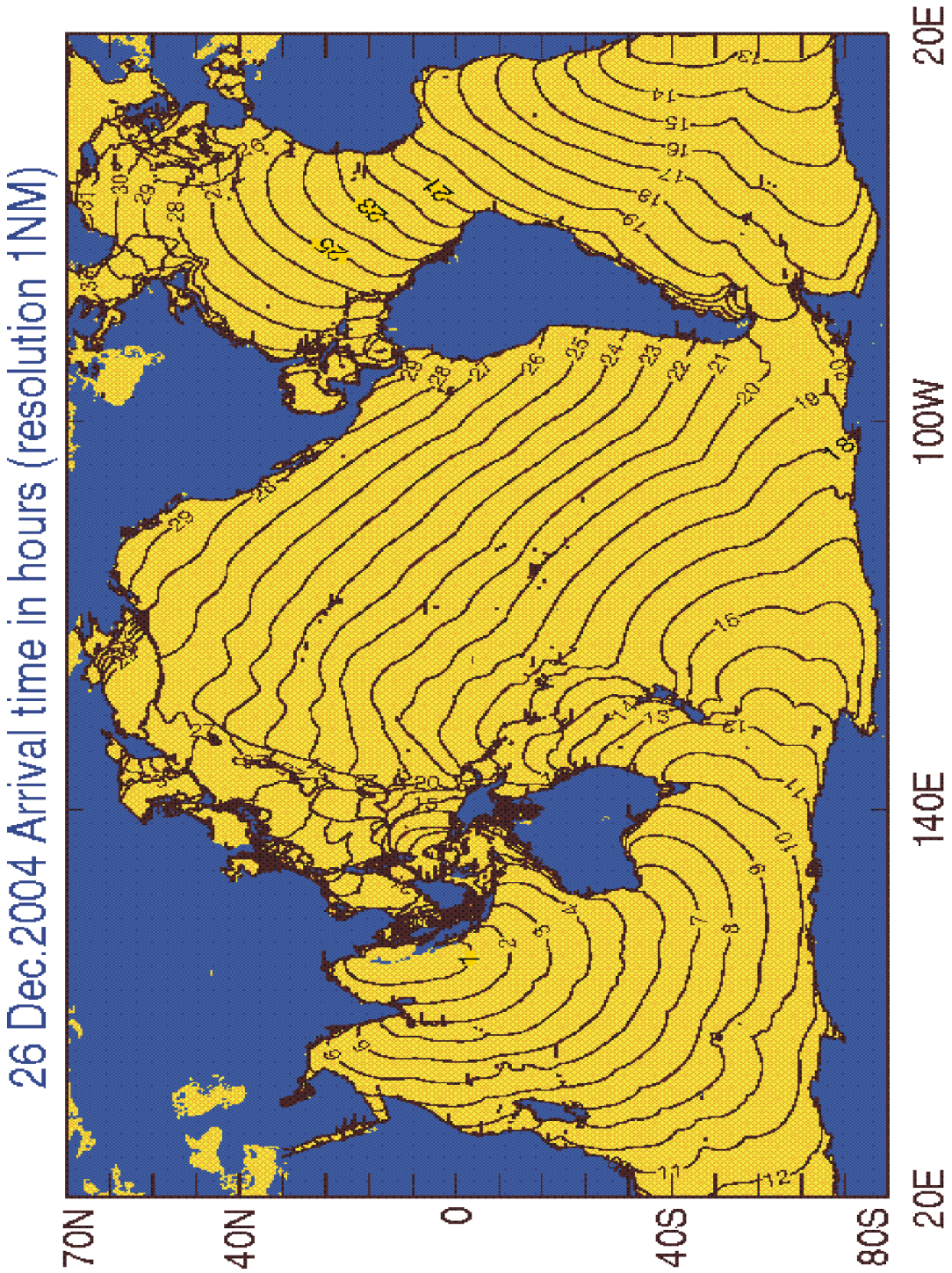

Figure IV.13. Travel time (in hours) for the tsunami of 0.1cm amplitude.

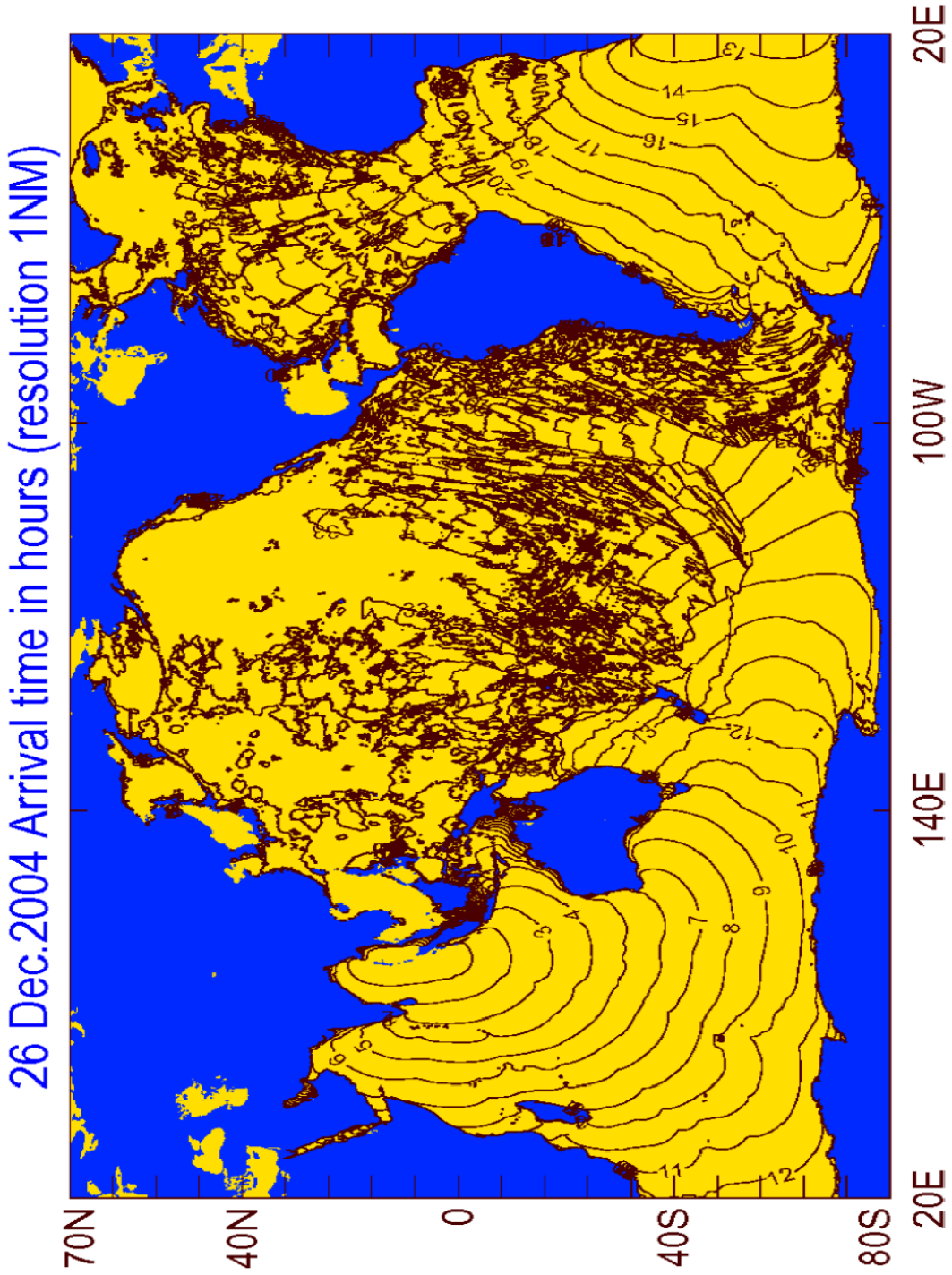

Figure IV.14. Travel time (in hours) for the tsunami of 0.5cm amplitude.

8. Observations versus computations

Although the $1'$ computational mesh resolves many coastal and bathymetric features, nonetheless it is too large to resolve the local dynamics such as runup. In FigIV.15, the sea level at four stations have been chosen from the Indian Ocean area and compared with observations described by Merrifield et al. (2005). The stations are located on Maldives Island (Male), on the Seychelles Islands (Pt LaRue), on the African coast of Kenya (Lamu) and on the Arabian Peninsula coast of Oman (Salalah). The model reproduces quite well the maximum amplitude and the temporal behavior of the tsunami, indicating that with higher resolution bathymetry an even better comparison can be achieved. The fine resolution bathymetry around Maldives Island is very important for the distant propagation towards Seychelles, or Oman, as the signal observed at these locations depends on tsunami reflection, trapping and refocusing in the Maldives Island chain as can be gleaned from FigIV.5.

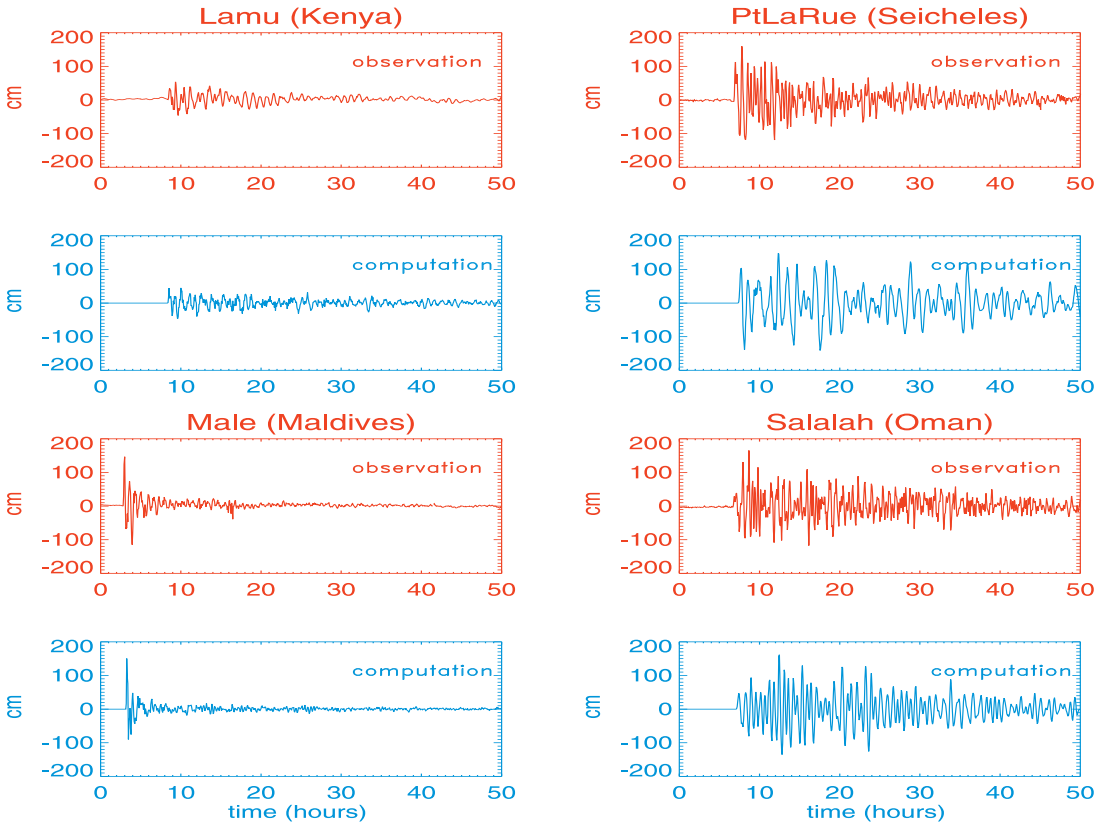

Figure IV.15 Sea level observations and computations from the four stations in the Indian Ocean.

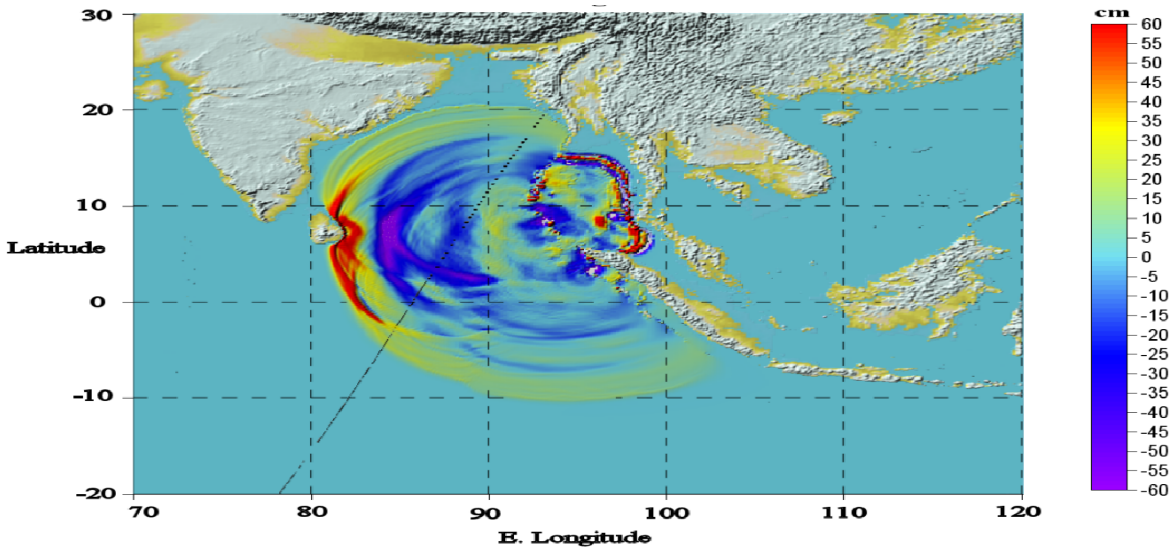

Figure IV.16. Ground track of Jason-I and computed tsunami amplitude at 2:55 UT on Dec. 26, 2004 in the Indian Ocean.

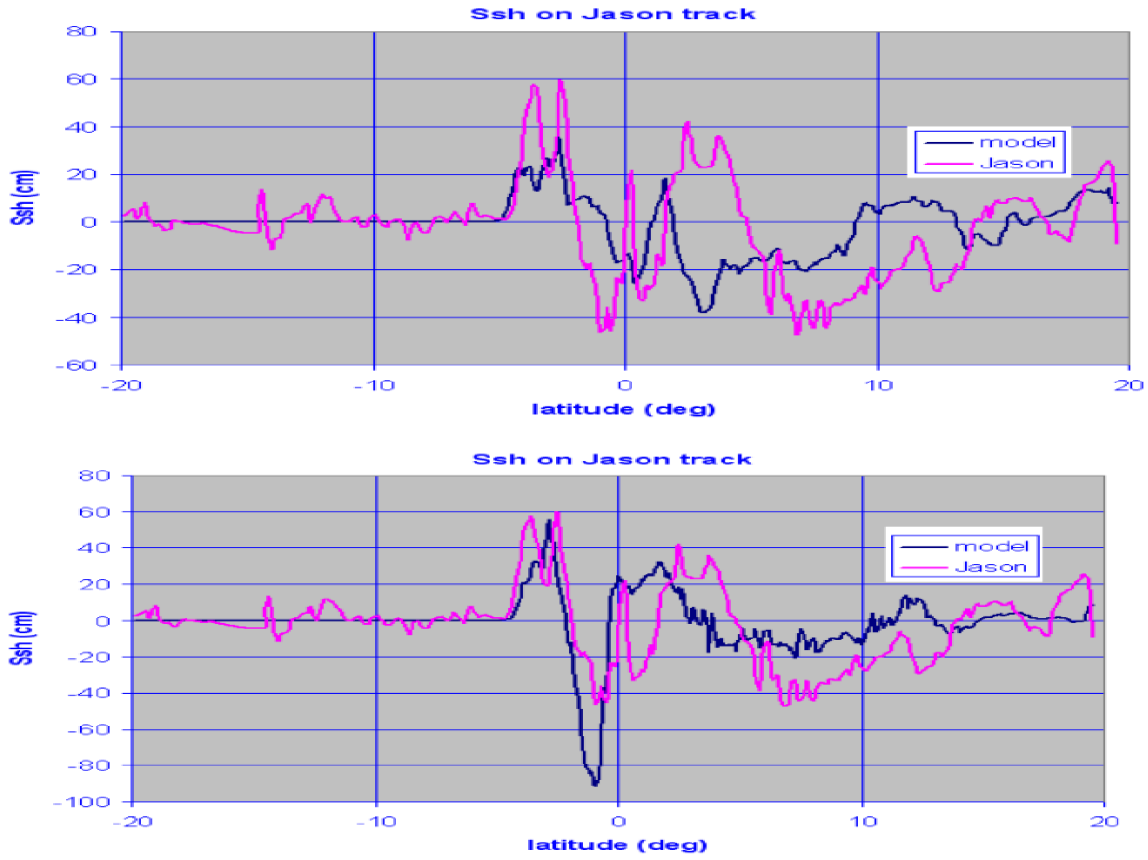

Figure IV.17. Computed and observed tsunami amplitude along the Jason-I track. Upper panel: source function given in FigIII.9. Lower panel: source function orientation and width adjusted.

As luck would have it, the Jason-I altimetry satellite traversed the Indian Ocean about 2 hours after the event origin time. It crossed the equator on a NNE path at 02:55 UTC on 12-26-2004 (FigIV.16). The non-validated altimetry data was downloaded from the JPL Physical Oceanography website at ftp: //podaac.jpl.nasa.gov/pub/sea_surface_height/jason/j1nrtssha/data/. Altitude is sampled approximately once per second and is corrected for tides. In order to remove any background, the raw data from the tsunami pass was corrected by subtracting out an average of 4 non-tsunami passes. Jason-I repeats its track about once every ten days, so four repeat paths were averaged to generate the background. The corrected signal, was then smoothed by removing fluctuations with wavelengths shorter than 20km. The smoothed signal with background removed was compared against the model data. Note that Jason-I was above the tsunami for about ten minutes. During this time the tsunami was in motion, so the comparison is made to dynamic model predictions and not against a static snapshot. The model wave heights at the moment of equatorial crossing of Jason-I are shown in FigIV.16. Jason-I crosses the leading edge wave at a point on the wave front where the amplitude is rapidly increasing towards the NW. The comparison between data and model is therefore sensitive to small variations in source details. The final comparison is shown in FigIV.17 (upper panel). The leading edge wave location is predicted accurately by the model, even if the amplitude is not. The modeled leading wave with the amplitude similar to the recorded by satellite was in the satellite footprint 15 min earlier (see, FigIV.16). A closer amplitude/period match was obtained by rotating the source strike counterclockwise slightly, and by reducing the fault width from 200km to 125km. The comparison, given in FigIV.17 (lower panel) shows that the model as driven by the adjusted source function reproduces more accurately the leading wave recorded by Jason-I.

9. Construction of the Fortran program for tsunami propagation

The fortran program titled Neowave is based on the numerical set of equations described in Sec. 2 of this chapter. The solution starts from the North Pacific domain whose bathymetry with resolution of 2 nautical mile (2' arc minutes) is given in FigIV.18. Although, the tsunami signal from the source in the Kurile Islands propagates to the entire Pacific, we choose to consider the region in proximity to Crescent City as at this location the tsunami signal was strongly amplified. Hence, in this region the multiple grids are used by placing a coarse grid in the deep ocean (and offshore) region and couple this with the finer-grid in the shallow coastal areas. The grid-size is diminished from the 2' to 24" (arc seconds) in FigIV.19 and in the latter domain a subdomain with 3" (arc seconds) is placed (FigIV.20). The finest resolution of 1" (close to 30 m) is achieved in FigIV.21 to describe the bathymetry and land elevation in proximity to the Crescent City port, as we intend to resolve here the runup and rundown processes.

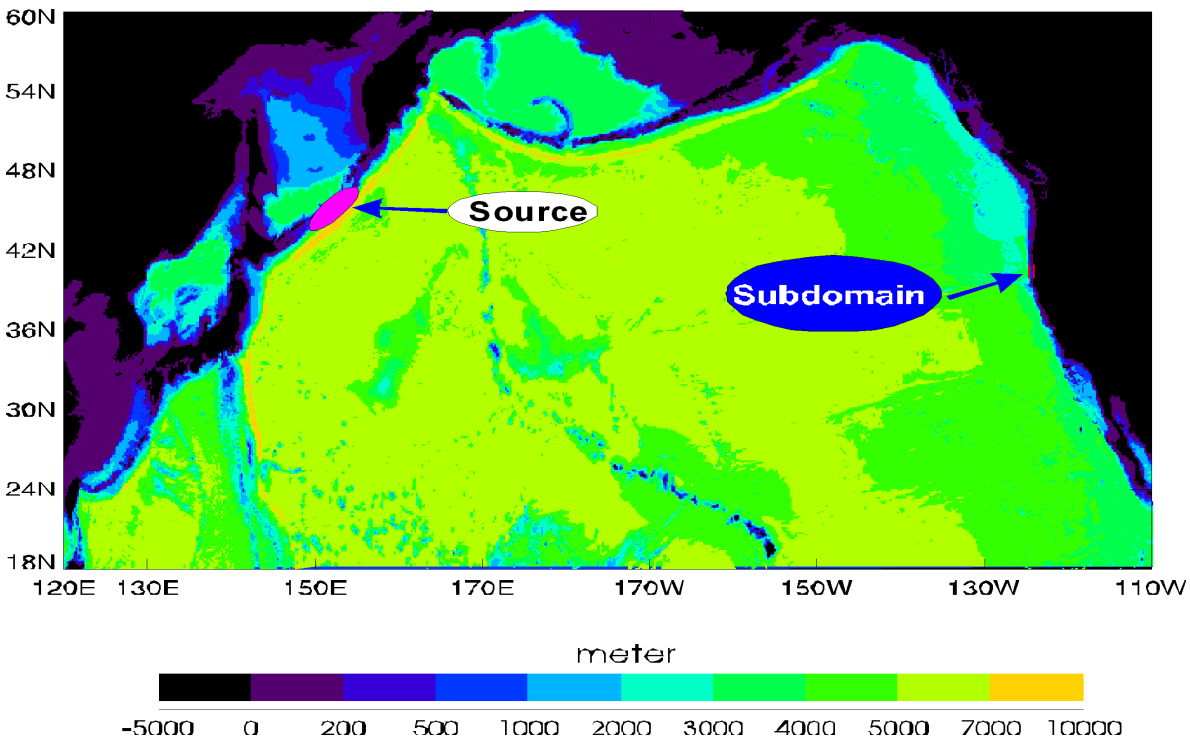

Figure IV.18.Bathymetry of the North Pacific. Resolution 2' arc minutes.

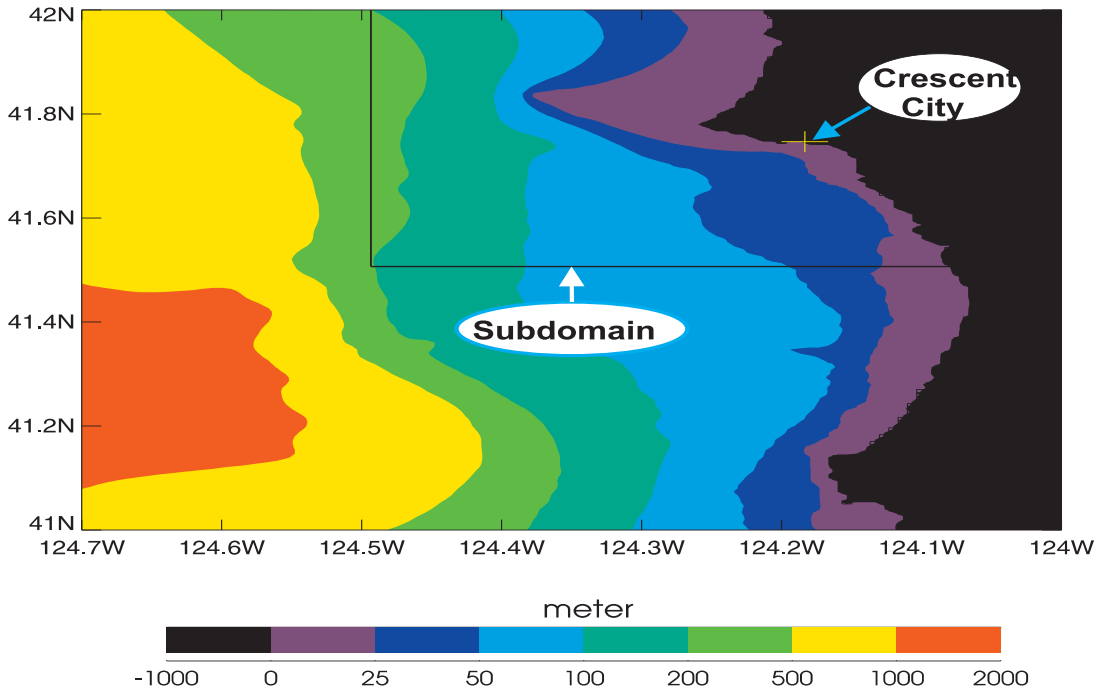

Figure IV.19. Bathymetry of the shelf in proximity to the Crescent City. Resolution 24" arc seconds.

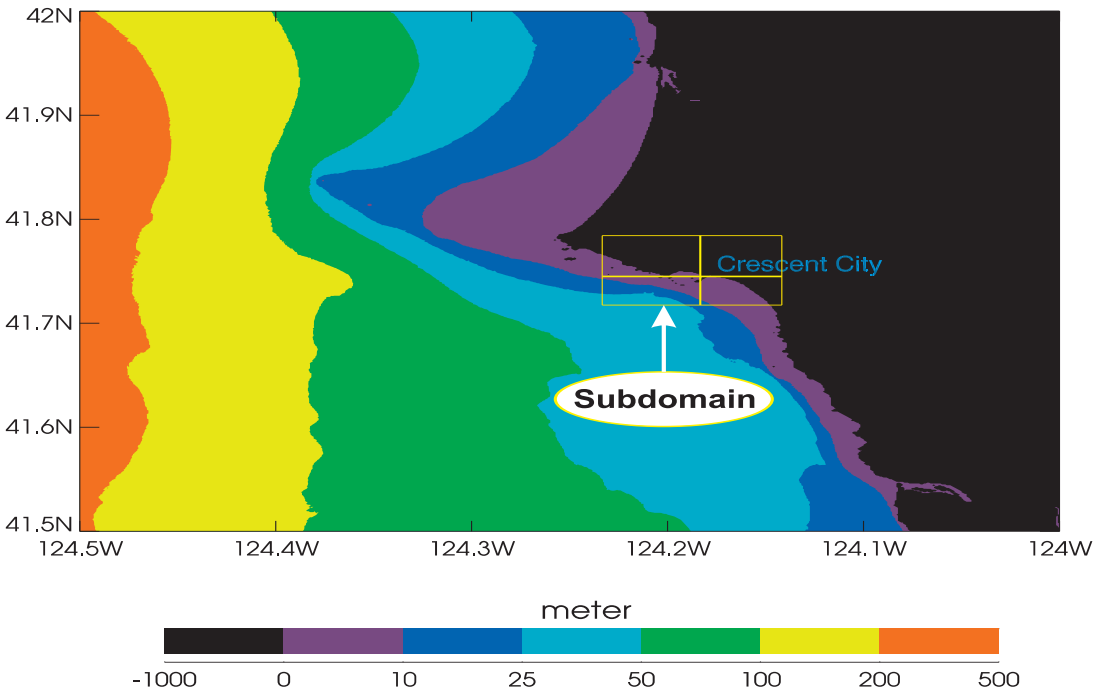

Figure IV.20. Bathymetry in proximity to the Crescent City. Resolution 3" arc seconds.

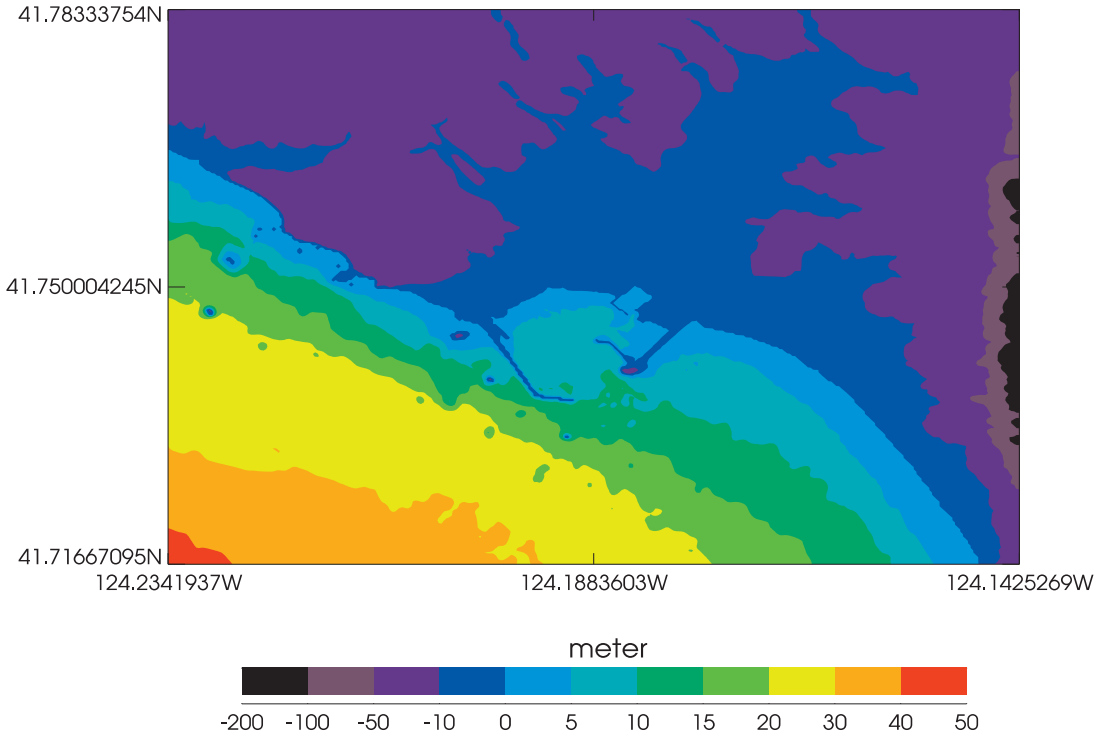

Figure IV.21. Bathymetry and elevation in proximity to the Crescent City Port. Resolution 1" arc seconds.

As the bathymetry in the above domains and interconnections of different domains is important and quite difficult task to simplify this organizational step we used an excell program Domain Setup North Pacific.xls. The main Fortran program Neowave4Gc.f90 is calling basic parameters and subroutines to perform computations. The principal part of the program where all parameters and variables are defined is named all_input_kurile and it is called into the program by command: INCLUDE "all_input_kurile". Every dependent variable of the problem, i.e., u velocity along the E-W (x) direction, v velocity along the N-S (y) direction, and the sea level z is defined in each point of the numerical grid by index j, along x and k along y direction, respectively. The numerical computations in time proceed at the two time levels, therefore the variables already computed (old) are named uo, vo, zo and the variables which are going to be computed (new) are named un, vn, zn. To distinguish these variable among the different domains, the variables belonging to the first domain acquire additional number 1, the variable in the second domain have number 2 and so on. Thus, e.g., velocity along x direction in the first domain is written as $uo1$ (old value) and $un1$ (new value).

The computational domains are defined as rectangulars in the all_input_kurile by the indeces along the x direction and y directions. The starting index is js and the ending index is je for the x (for the first domain they are $js1, je1$) and for the y direction the indeces are ks and ke (and again for the first domain the notation is $ks1, ke1$). As rectangular domains include both wet (ocean) and dry (land) grid points to discriminate among the wet and dry cells the *cell* number is introduced. For the wet grid points $cell(j,k) = 1$ but for the dry points $cell(j,k) = 0$. The dry and wet points are defined by the total depth $D = h(j,k) + \zeta(j,k) - \eta(j,k)$ (see, Sec.2 of this chapter). The approach to using the cell number is explained in the detail at Sec. 13 Ch.II for the runup computation.

The major set of data to be prepared before computation is bathymetry in the four considered domains. It is expressed by the variable $H(j,k)$ and respectively for the first domain it is named $H1(j,k)$. The subroutine INPUT_BATHYMETRY specifies bathymetry for the four domains. In this computation the bathymetry files are: ale2min.dat, crescent24sec.dat, crescent3sec.dat, cresport1s.dat.

The source of the tsunami wave is the bottom displacement due to earthquake. The vertical sea floor displacement is computed in the subroutine SURFACE_OKADA_REC_1 using the static dislocation formulae from Okada (1985). Input to this subroutine defines fault geometry and is given in the file fault_2006_USGS.txt The following parametrs are listed:

Trise = 0.0d0 !Trise(s) :rise time
D0 = 5.2d2 !D0(cm) :dislocation(slip)
lonR = 153.50d0 !x0(deg E) :reference point
latR = 47.00d0 !y0(deg N) :reference point
dR = 13.00d5 !d (cm) :focal depth
L = 240.00d5 !L (cm) :fault length
W = 80.00d5 !W (cm) :fault width
strike = 215.00d0 !phi (deg):strike angle
dip = 15.00d0 !delta (deg):dip angle
rake = 92.00d0 !lambda(deg):rake angle

Although the subroutine SURFACE_OKADA_REC_1 together with Okada (1985) paper is self explanatory it is useful to remember that the program okada.f90 given in Ch.III, Sec.4, is actually copy of the above subroutine.

The time stepping for computing the variables at the new time step is done through the time loop

TIMELOOP: DO m=mINI, mFIN !TIME LOOP

Here m is time index, and the computation runs from mINI to mFIN. The first command in this time loop is calling subroutines OPEN_BC_LR and OPEN_BC_BT which define the radiation open boundary condition along the open (water) boundaries in the North Pacific domain. These open boundary conditions were constructed in Ch.II, Sec.3. The dry and wet points in the first domain are defined through the following computational loops (the same algorithm is used in all domains by changing index 1 to 2 in the second domain, 1 to 3 in the third domain and so on).

```
DO k=ks1,ke1
DO j=js1,je1
Hb1(j,k) = H1(j,k) -eto1(j,k)
D1(j,k) = zo1(j,k) +Hb1(j,k)
IF( D1(j,k) .LT. EPSILON ) THEN
zo1(j,k) = -H1(j,k) +eto1(j,k)
CELL1(j,k) = 0.
ELSE
!ELSE IF ( D1(j,k) .GE. EPSILON ) THEN
CELL1(j,k) = 1.
END IF
END DO
END DO
```

The total depth denoted D1 is a sum of the mean sea level depth H1 the sea level change zo1 and the the bottom displacement eto1 (eto denotes old value). EPSILON is a small positive number given in all_input_kurile. After the total depth is checked to every grid point is ascribed cell number; cell1(j,k)=1 for the wet grid points and cell1(j,k)=0 for the dry grid points. The variable Hb1 is the sum of the mean sea level depth H1 and the deformable part of the bottom eto1. The positive vertical bottom displacement (eto1 positive) diminishes Hb1 and negative increases Hb1.

Two subroutines RUNUP and WET_DRY_UV_BC introduce runup algorithm discussed previously in Ch.II, Sec. 13.

Subroutine Dlim_Du_Dv_CAL limits the total depth in the grid point where u and v velocities are computed. This limitation is related to the bottom friction term. As in the very shallow water the total depth is close to zero (or even can be negative) the bottom friction term (see eq. IV.4a and 4b) may bring an unrealistic large value.

The main subroutines to compute the new value of velocity and sea level are: XMOMENT_1ST, YMOMENT_1ST and CONT.

Computations in the finer-resolution domains are patterned on the first domain codes. Such computation is organized through the DOUBLE_COUPLE subroutines. The second domains is called from the main program by command CALL DOUBLE_COUPLE_D12

from this subroutine the call to connect second domain and perform calculation in the third domain follows as CALL DOUBLE_COUPLE_D23. Finally from the latter subroutine the last call to connect domains 3 and 4 and to do computations in the domain number four closes the entire cycle. We have coupled two computational domains by inputing the velocity and sea level from the coarser-grid to the finer-grid along the boundary where the finer-grid is attached to the coarser grid. Since in the finer-grid the space and time steps of numerical integration differ from the coarser-grid domain to pass variables to the finer-grid domain the linear interpolation of the data is used. In this computational procedure we first solve u, v and ζ in the first domain and afterwards the first domains values which overlap the boundary of the second domain are interpolated and used to begin computation in the second domain. A potential problem is that the higher frequency waves generated within the second domain but not resolved by the boundary condition given from the first (coarser-grid) domain may be trapped in the finer domain and trigger a numerical instability. To avoid trapping of the signal in the finer-grid domains a special radiation condition is used. It is defined in the subroutine DC_BOUND_RADIATION. This radiation condition is constructed in ChII, Sec 3. Considering only one (x) direction and defining the the sea level ζ_b and velocity u_b as given from the coarser-grid, the sea level in the finer-grid can be defined by the radiation condition as,

$$\zeta = \zeta_b + (u_b - u)\sqrt{H/g} \qquad \text{(II.38; IV.12)}$$

Thus if the calculated velocity in the finer-grid u is equal to u_b the sea level is equal to prescribed boundary value ζ_b. Otherwise the difference $(u_b - u)$ will be radiated out of the computational domain.

10. Kurile Islands Tsunami of November 2006

On November 15, 2006 at 11:14:16 (UTC) an earthquake with moment magnitude 8.3 (http://earthquake.usgs.gov/ eqcenter/recenteqsww/Quakes/usvcam.php) generated a tsunami near the Kuril Islands. Tsunamis propagated over the entire Pacific Ocean. The resulting sea level disturbance was recorded by DART buoys located in the open ocean and by many coastal tide gauges. Buoy data showed that the duration of tsunami signal while propagating away from the source was steadily increasing (with distance from source) and that often the first group of tsunami waves did not include the highest waves. Along the Japanese coast, the highest tsunami waves arrived just minutes after the initial tsunami waves arrival (largest amplitude 40 cm occurred at Hanasaki). The initial wave at Kahului (Maui) of 50 cm amplitude was followed 2 hours later by a wave of 76 cm amplitude. This pattern can be observed in many locations along the Pacific coast. The small initial tsunami of about 20 cm was barely noticed at Crescent City (CC). The highest wave of about 88 cm amplitude was recorded 2–3 hours later. No other west coast tidal stations recorded such a high wave. The physics of tsunami propagation and amplification during this event was analyzed and described in two papers by Kowalik et al., 2008 and Horrillo et al., 2008.

Large tsunamis which propagate globally can be amplified in locations remote from the source zone. The Chile (1960) and Alaska (1964) earthquakes generated tsunamis which produced unusually high waves in many distant locations. The 1960 tsunami, well

recorded along the US West Coast, produced amplitudes often in excess of 1 m with the largest wave height of 1.7 m measured at CC (Lander and Lockridge, 1989). The tsunami from the Alaska Good Friday earthquake (1964) generated wave amplitudes in excess of 1 m along the US West Coast. Again CC suffered the greatest damage due to a high wave exceeding 4 m amplitude (Wiegel, 1965). Using the Kuril tsunami example we intend to investigate the behavior of the transoceanic tsunami and the special conditions which cause tsunami enhancement at CC. Our investigation is aimed to demonstrate that the tsunami amplification at CC is caused by both the redirection of tsunami energy over long distances of propagation and by amplification due to the local bathymetry. The effects of amplifications of the distant tsunami were studied by Hebert et al., 2001 by examining tsunami inundations observed on the Marquesas Islands. One case study considered by Hebert et al., 2001 was the 1994 Kuril tsunami. It clearly demonstrated the importance of long volcanic ridges and fracture zones in directing tsunami signal towards the distant locations and it bears strong resemblance to the November 15, 2006 tsunami. Studies of topographic transformations of tsunami signal in the open ocean due to ridges were summarized by Mei et al., 2005. Usually, incident energy flux on a ridge is split into reflected, transmitted and trapped fluxes. The scattering of tsunami energy by bottom topography in such an approach is a function of depth of water over topographic features. In order to better understand this process (Mofjeld et al., 2000) introduced a tsunami scattering index which is expressed by the ratio of the transmitted wave amplitude to that of the incident wave.

Amplification of the tsunami signal at CC during the events of 1960 and 1964 was investigated by assuming distant or local enhancement (Hwang et al., 1972). Mader and Bernard, 1993 and Bernard et al., 1994 modeled the Aleutian Island (Unimak Island) tsunami of April 1946 and the March 1964 tsunami generated in the Gulf of Alaska, concluding that directionality of the tsunami source was the primary cause of the tsunami enhancement. On the other hand the amplification was frequently studied assuming that either local (harbor) geometry or shelf and coastal geometry has natural periods in the tsunami range of periods (Roberts and Kauper, 1964; Keulegan et al., 1969). The interaction of the tsunami wave with the shelf geometry often results in the trapping and amplification of the tsunami energy. Gonzalez et al., 1995 suggested that the high amplitude tsunami waves generated by the 25 April 1992 Cape Mendocino earthquake at CC were induced by the coastal trapped edge wave. An analytical solution of tsunamis obliquely incident on a continental slope derived by Koshimura et al., 1999 confirmed existence of the amplification of the edge waves and possibility of a resonance in the period range of tsunamis. New observations of tsunamis at the coast of Japan by Yanuma and Tsuji, 1998 indicated that the shelf trapped edge wave strongly interacted with the fundamental mode of a nearby harbor.

11. Source function and distribution of maximum amplitude

The generation mechanism for the Kuril Islands tsunami model is the static sea floor uplift caused by abrupt slip at the plate interface. Actual sea floor uplift has a complicated structure composed of many blocks motion (Lobkovsky et al., 2006) but often it is considered as one continuous block (Okada, 1985). Permanent, vertical sea floor displace-

ment is computed using the static dislocation formulae from Okada, 1985. Inputs to these formulae are parameters defining the fault plane geometry: depth (13 km), strike (215°), dip (15°), slip (92°), length (240 km), and width (80 km) as well as seismic moment (Mo = 3.5 $\times 10^{-28}$ dyne cm) and rigidity (4.2 $\times 10^{11}$dyne cm^{-2}). The bottom displacement used in computation is given in a rectangular region 45°N-49°N and 152°E-156°E; see FigIV.22.

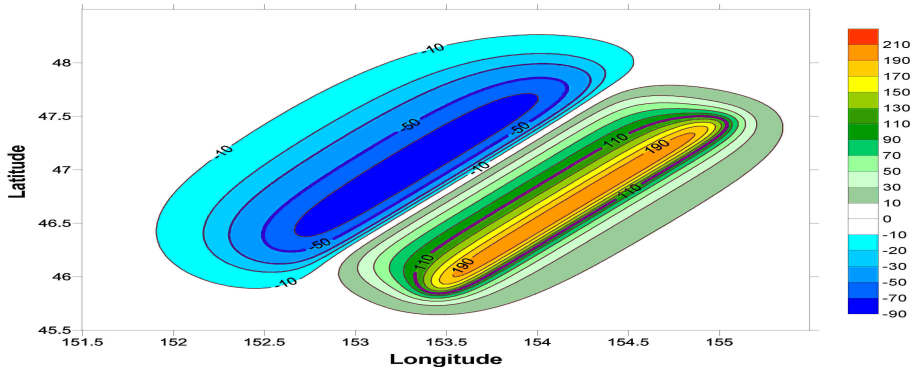

Figure IV.22. Source function (bottom deformation in centimeters) for the tsunami of 15 November 2006.

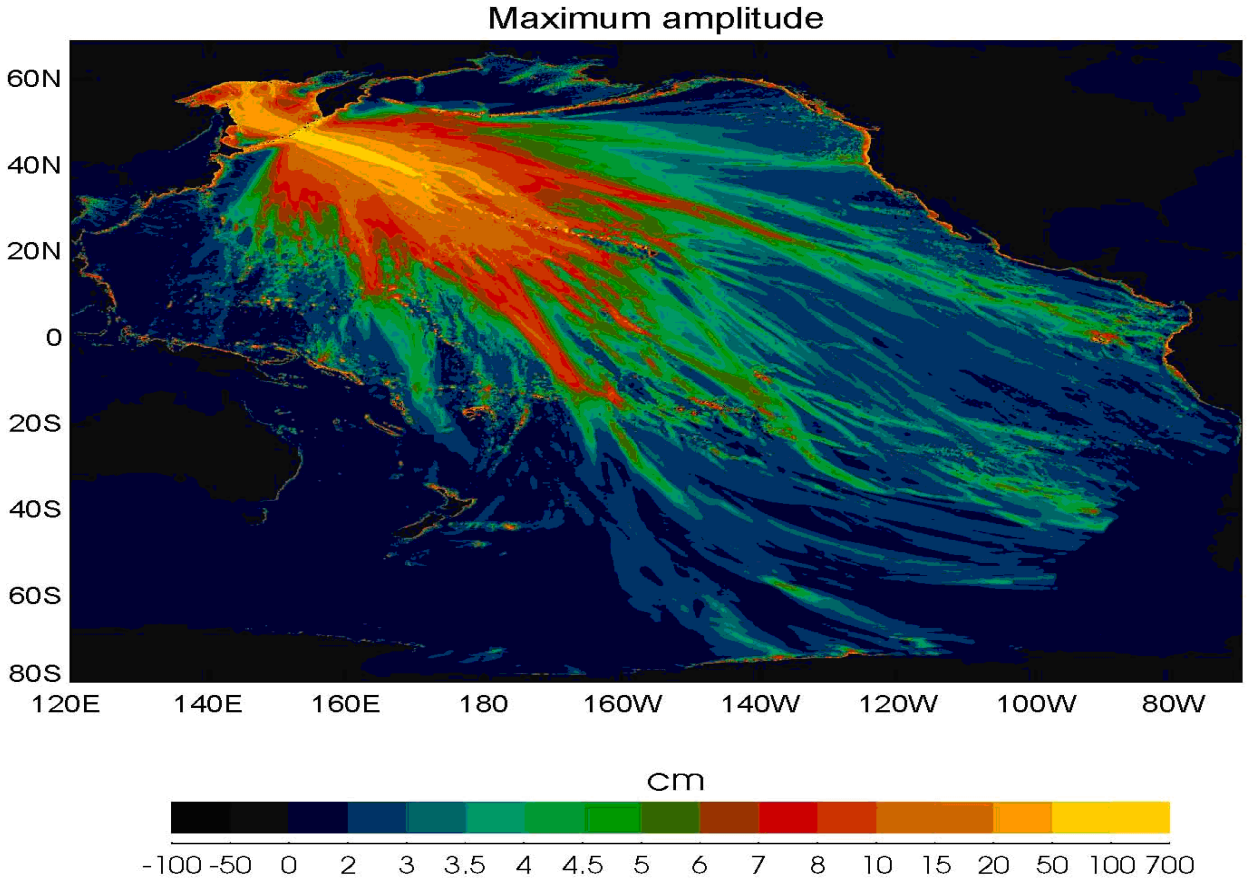

Figure IV.23. Maximum modeled tsunami amplitude in the Pacific.

Model computations using this tsunami source were made in the domain depicted in FigIV.18 (see also FigIV.24) for the grid resolution of 1 arc minute. The 20 hours of propagation were computed, allowing the tsunami signal to cross the entire Pacific Ocean. During computation the maximum tsunami amplitude in every grid point was recorded. The plot of the maximum amplitude in the Pacific Ocean is shown in FigIV.23. The maximum amplitude distribution in FigIV.23 shows that the tsunami traveled over the entire Pacific. The elongated tsunami source (FigIV.22) directed the main lobe of wave energy toward the southern hemisphere, but strong amplitude maxima are also observed along the shores of the North Pacific. Some of the tsunami energy propagated in a finger-like pattern, a product of wave refraction and focusing around islands/seamounts/passages chain systems. Closer examinations show that the oceanic ridges and seamounts tend to refocus tsunami energy. Our interest is in energy concentration along the Mendocino Escarpment which is directed toward Crescent City. FigIV.23 also depicts the amplitude enhancement in shallow water region along the coasts and especially around the islands. Even islands located far from the source such as the Galapagos or Marquesas show quite strong tsunami amplification due to coastal energy trapping.

12. Important stages in the Kuril Islands Tsunami development

Although tsunami spreads over the entire Pacific, the main signal was confined to the northern hemisphere. In this domain we intend to investigate tsunami development and especially tsunami amplification in the vicinity of Crescent City (CC). The tsunami onset was registered on 15 November 2006 at 11:14:16(UTC). The starting time in all our computations (t = 0) is the tsunami onset time. The model results will be compared with data recorded by DART buoys. In FigIV.24 the bathymetry used in our computation (based on work by British Oceanographic Data Centre, 2003) and some locations of DART buoys are given. Bathymetric features important in reorganizing and focusing tsunami signal toward CC are also shown in this figure.

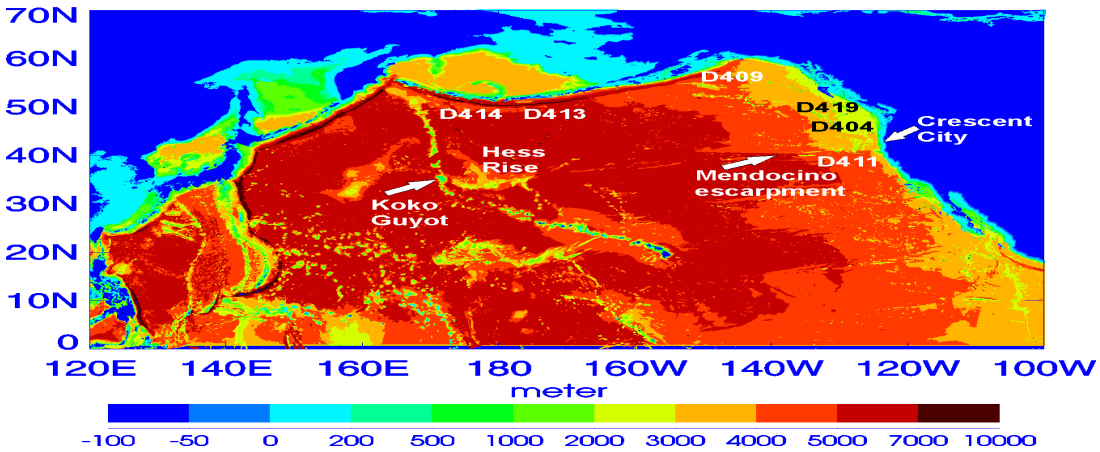

Figure IV.24. One-minute resolution bathymetry based on the GEBCO Atlas (British Oceanographic Data Centre, 2003). Shown are DART buoys locations.

The consecutive stages of tsunami propagation in the open ocean are shown in FigIV.25.

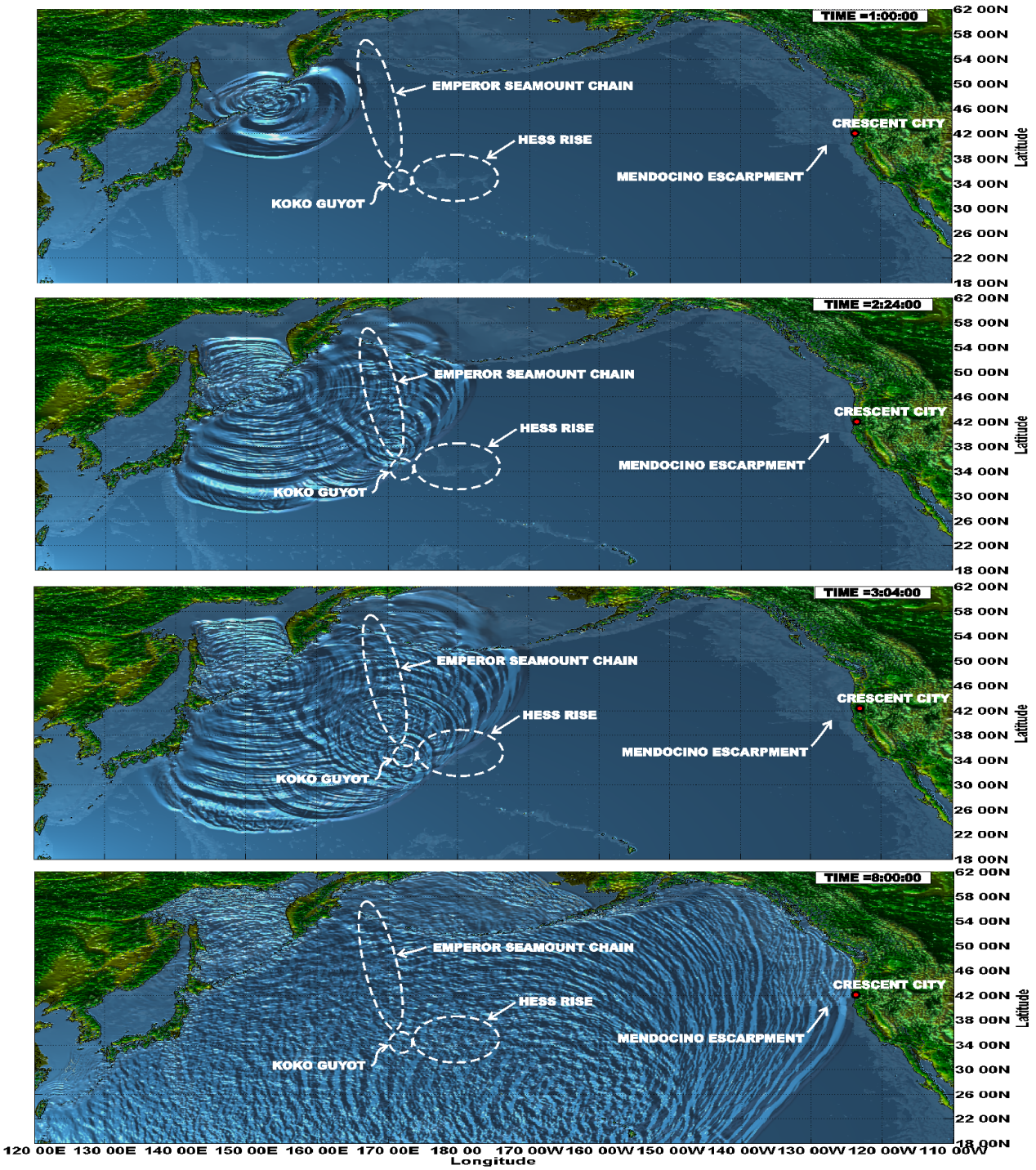

Figure IV.25. Snapshots of Kuril tsunami development in the northern Pacific. Large bathymetric features, like Koko Guyot and Hess Rise, scatter tsunami in directions different from the incident direction. Time is given from the tsunami onset.

The signal as generated by the source from the FigIV.22 is traveling as a positive wave toward the southeast Pacific and as a negative wave into Okhotsk Sea (Fig.IV25, top plot). While interacting with the Emperor Seamount Chain and with the exceptionally large Koko Guyot (Davies et al., 1972) tsunami is scattered into new directions and by interference generates a new set of waves (FigIV.25, second plot). Further tsunami energy is trapped and dispersed by the Hess Rise (FigIV.25, third plot). A complicated packet of waves arrives at CC, with the first arrival preserving the properties of the initial wave generated in the Kuril Islands trench, and a second, larger wave group arriving about 2 hours later. Differences in the wave front direction show that the two waves travel different routes. While the first wave group arrives from the northwest via the great circle route and deep Aleutian trench, the second wave group arrives from the west. This latter wave is directed toward CC by secondary sources.

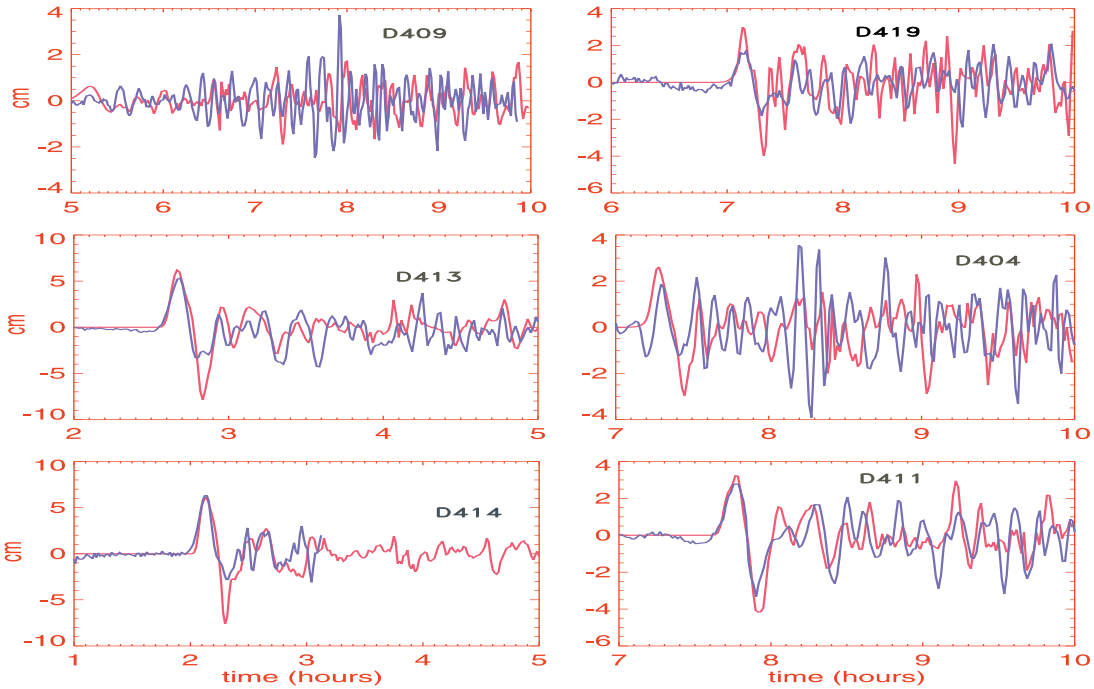

Figure IV.26. Sea level during Kuril Tsunami of 15 November 2006. Blue denotes recorded by DART buoys; red denotes model computation. Time is given from the tsunami onset.

The comparison of the tsunami signal recorded by DART buoys and calculated by the model are given in FigIV.26. The overall amplitude recorded at DART buoy locations is of the order of a few centimeters. These are typical tsunami amplitudes for buoys anchored in deep oceanic basins far from the source zone and off the main energy lobe. The computation simulates relatively well the first cycle of wave motion and the amplitude modulation in time in all buoys. Computations for the DART buoy closest to CC (D411, located at 127°W, 39.34°N) turned out to be in satisfactory agreement with recorded sea level.

To investigate tsunami signal enhancement by the Mendocino Escarpment (i.e., step-like bathymetry change) three time series numerical results are shown in FigIV.27.

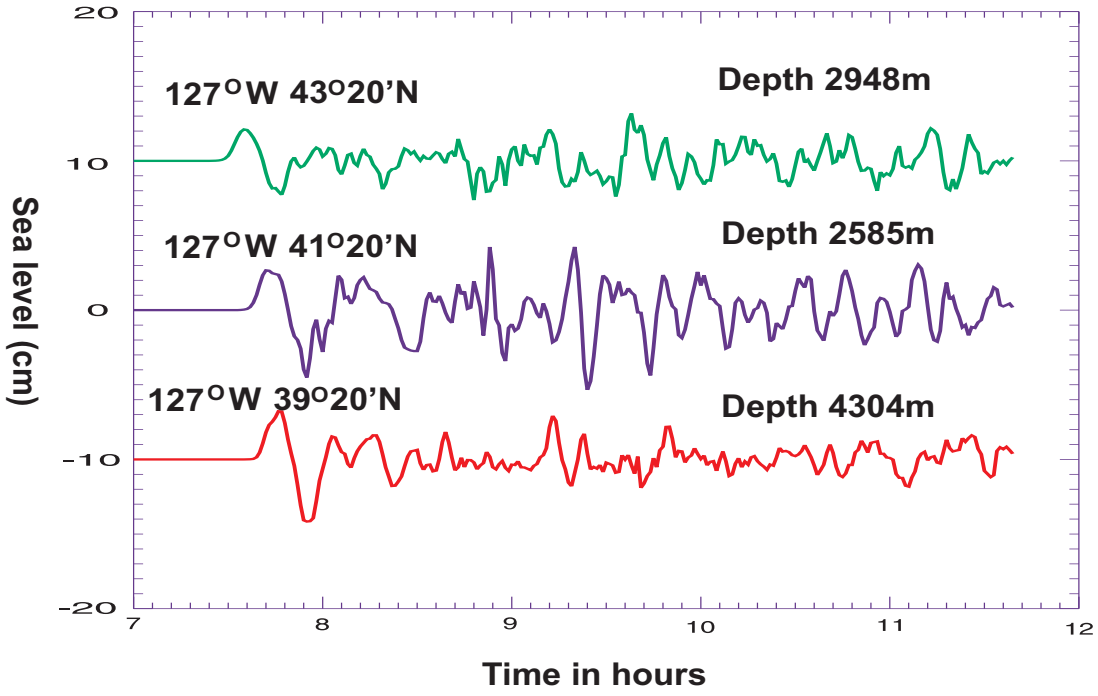

Figure IV.27. Computed time series of the tsunami waves in the proximity of Crescent City. The middle numerical gauge is located north of the Mendocino Escarpment facing Crescent City. Time is given from the tsunami onset.

The numerical gauges are located along 127°W longitude at 43°20'N, 41°20'N and 39°20'N, respectively. The deeper numerical gauge is situated south of the Mendocino Escarpment at a depth of 4304 m. The other two are situated north of the Mendocino Escarpment (on the step). One is facing CC (middle gauge) at a depth of 2585 m and the other just north at a depth of 2948 m. The first wave arrivals are quite similar at all numerical gauges and they show an increasing time delay going from north to south. Thus we can conclude that the first tsunami signal arrives from the north or northwest. The largest amplitude in the second packet of waves arrives about 2 hours after the initial tsunami, and peaks at about 2.7 cm at the northern numerical gauge, 4.7 cm at the middle gauge, and 2 cm at the southern gauge.

13. Why tsunami is amplified along the Mendocino Escarpment: energy flux approach

Observations of the Kuril Islands tsunami in Crescent City (CC) showed that the initial wave of 15-25 cm amplitude was followed about 2 hours later by a wave of 60-80 cm amplitude. Inspection of the DART buoy D411 (127°W, 39.34°N, in FigIV.26) which is closest to CC, show that the sea level variations two hours after the initial wave are only slightly amplified when compared to the initial wave. It follows from FigIV.27 that the amplification shown in FigIV.23 takes place in the very narrow range of latitudes. To study the energy from the distant tsunami sources it is natural to introduce the energy flux vector (Kowalik et al., 2007b, Kowalik, 2008). In the rectangular system of coordinates, with the x coordinate along E-W direction and y along N-S direction, the u component

of velocity along x direction can be combined with the sea level (ζ) to define the E-W component of the energy flux vector (see Ch.I, Sec. 7)

$$E_x = \rho u D\left[(u^2 + v^2)/2 + g\zeta\right] \tag{IV.13a}$$

Similarly, the N-S component of the energy flux vector is defined (with v, the velocity component along the y direction)

$$E_y = \rho v D\left[(u^2 + v^2)/2 + g\zeta\right] \tag{IV.13b}$$

To investigate the pattern of energy trapping over the Mendocino Escarpment as shown in FigIV.23, the energy flux is used in two simple experiments. Three waves of 16 minutes period each and 10 cm amplitude are sent toward the west coast of North America from the open boundary located at 150°W (FigIV.28a, left). In FigIV.28a, right the wave pattern 160 min later is shown.

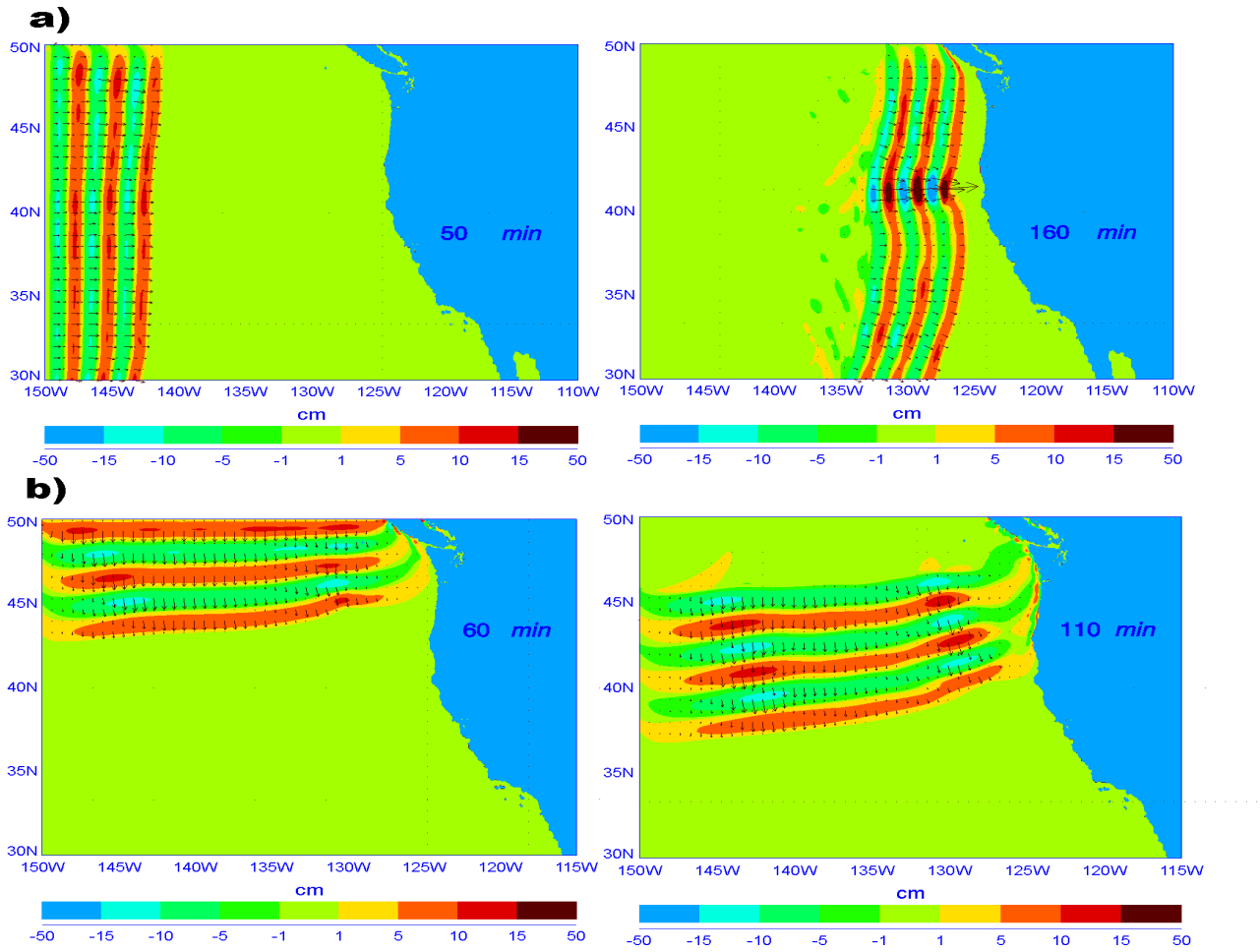

Figure IV.28. a) Three waves of 10 cm amplitude and 16-min period traveling parallel to the Mendocino Escarpment. (b) Three waves of 10 cm amplitude and 25-min period traveling from the north toward Mendocino Escarpment. Amplitude is given by colors. Vectors denote energy flux.

These figures demonstrate strong local amplification of the energy flux and the wave amplitude during wave propagation toward CC. The central latitude for the amplified wave is 41°N-42°N, while the Mendocino Escarpment is located close to 40°N. Thus the center of amplification is located in the narrow range of 1-2 degrees of latitude just north from the escarpment. This result is confirmed by FigIV.27 where tsunami traveling along 41°20'N shows the strongest amplification for the later arriving wave group. Experiments with various wave periods resulted in the same pattern of high amplification within a narrow latitude band just north of the Mendocino Escarpment. Obviously the energy flux pattern depicted in FigIV.28a is related to the depth difference along the N-S direction when crossing the escarpment. The wave south of the escarpment travels faster than the wave on the northern side of escarpment. This difference in the phase speed causes wave refraction (Wiegel, 1965; Mei et al., 2005) resulting in steady energy amplification and focusing toward CC. The type of amplification shown in FigIV.28 is related to the second wave group in the KIT which as we are going to demonstrate arrives from the west. The initial wave as seen from FigIV.25 arrives from the northwest and does not travel along the Mendocino Escarpment for any great distance.

In the second experiment three waves of 25-min period each and 10 cm amplitude are sent from the northern boundary toward the Mendocino Escarpment (FigIV.28b, left). The wave pattern 110 min later is shown in FigIV.28b, right. Tsunami waves cross the escarpment without amplification. The direction of wave propagation seems to play the major role in tsunami enhancement along the Mendocino Escarpment.

In the above computations according to FigIV.27 we have applied shorter period (16 min) for the wave arriving from the west and longer period for the wave arriving from the north (25 min). Numerical experiments with wave periods from 10 min to 60 min confirmed that the above patterns of wave propagation are independent of the wave period.

From FigIV.28, one can also appreciate an important property of the energy flux. While the sea level can change sign, the energy flux of the progressive wave is always aligned with the direction of wave front propagation. Thus the noisy behavior of the sea level is replaced by the steadier behavior of the energy flux. This property is important in our search for the energy incoming toward CC. To investigate energy flux traveling toward CC during the Kuril tsunami we consider a 5° box enclosing CC for deducing the energy flowing into and out of the box. The box around CC is constructed as follows. The west boundary is located at 129°W, the north boundary at 44.5°N, the south boundary at 39.5°N and the east boundary is on land. The time dependent energy flux is averaged over the length of each boundary. The results given in FigIV.29 show two distinct pulses of energy crossing the western face of the box toward CC. Within the second pulse, two maxima occur separated by 20 min time interval. Energy appears to have a period of about 6-15 min. The periodicity of the energy flux of the progressive waves is different from the sea level oscillation, as its period of propagation is 2 times shorter than that of the sea level or velocity (Henry and Foreman, 2001). It is interesting to see that there is very little reflected energy coming back across the faces of the box. This must mean that most of the incident energy is dissipated by the near shore bottom friction. Nearly the entire energy flux enters the box through the western wall. Although the first wave group propagates from the northwest (see FigIV.25), the front of these waves becomes nearly

parallel to the shore owing to refraction (see FigIV.25 and 28b).

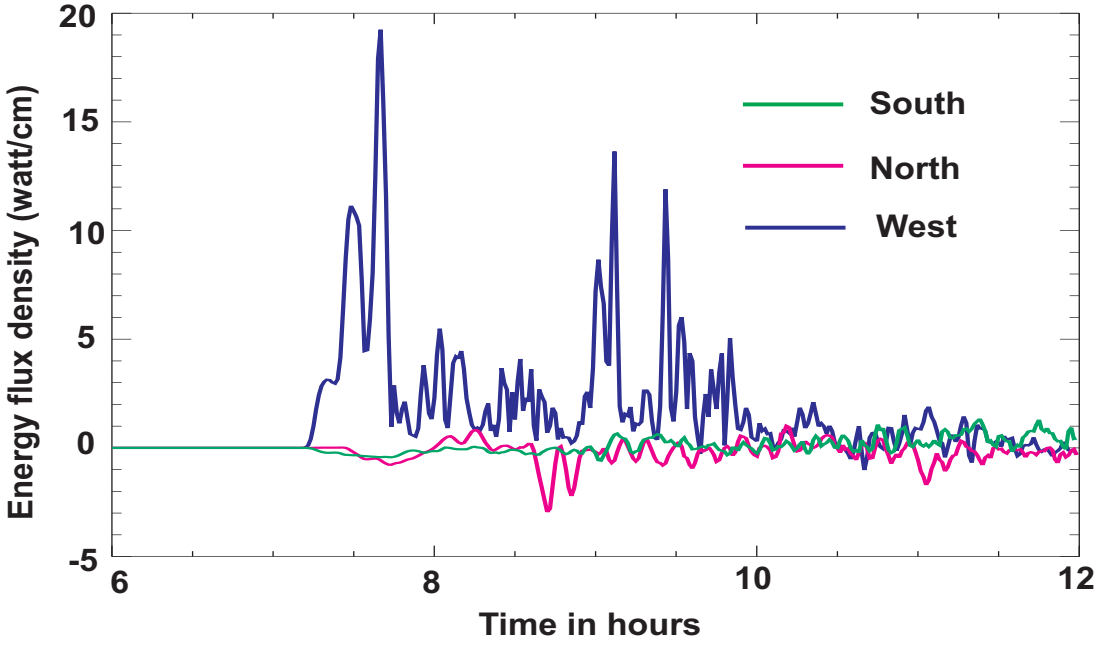

Figure IV.29. Energy flux through the western (blue), northern (red), and southern (green) walls of a 5° box around Crescent City.

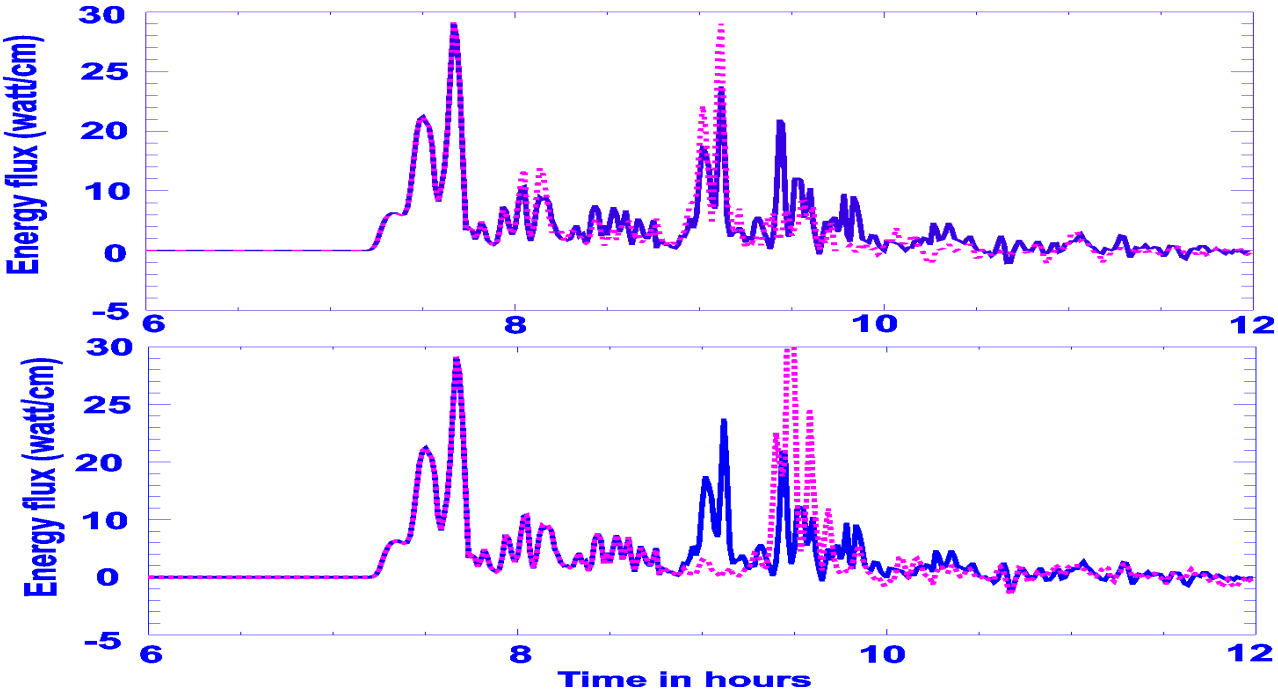

Figure IV.30. Energy flux through the western wall of a 5° box around Crescent City. Blue line shows the result due to regular bathymetry. Red line denotes distribution (top) when Hess Rise is removed from bathymetry and (bottom) when Koko Guyot is removed from bathymetry.

Energy flux through faces of the box around CC can be easily applied to pinpoint the source of the second wave packet. First we simply remove from the bathymetry the Hess Rise (see FigIV.24) by setting it to the depth of 5000 m. Next, the Koko Guyot is removed in the same manner. In FigIV.30 the energy flux crossing the western wall is plotted; in FigIV.30 (top) the Hess Rise is removed but the Koko Guyot stays unchanged and in FigIV.30 (bottom) the Koko Guyot has been removed while the Hess Rise remains unchanged. For comparison the energy flux across the western face from FigIV.29 is also given. The absence of Koko Guyot resulted in a restructuring of the energy flux through the western face of the box in such a way that the first maximum in the second wave group practically disappeared (FigIV.30, bottom). The second maximum in this later wave group, as FigIV.30 (top) shows, is related to the Hess Rise. The absence of the Hess Rise leads to energy amplification from the Koko Guyot as the Hess Rise did not scatter any longer the energy send by Koko Guyot toward CC. We can also conclude from FigIV.30 that the first group of waves to arrive at CC must travel a route unobstructed by either Koko Guyot or the Hess Rise. The immense influence of the Koko Guyot on tsunami signal scattering is due to its size and strong contrast between shallow and deep waters. It rises from the depth of 4750 m to within 250 m of the ocean surface (Davies et al., 1972). To further identify Koko Guyot as an important bathymetric feature, we plot in FigIV.31 the energy flux vectors immediately following passage of the main energy lobe past Koko. Note the new wave front radiating from this secondary source. The Hess Rise is an elongated plateau, located to the east from Koko Guyot, with a few smaller subdomains which generally parallel the Mendocino Escarpment (British Oceanographic Data Centre, 2003). Although it rises from the deep ocean plain to just 1500 m below the surface, it extends 1000 km in the E-W direction. The Hess Rise ridge like structure tends to enhance tsunami scattered from Koko Guyot and directs it toward Mendocino Escarpment; see FigIV.31. This vector plot depicts both direction and magnitude of the energy flux. Along with the vector representation to further identify important stages in the Kurile Islands Tsunami development the time history of energy flux contours is considered (Kowalik, 2008). The contours are given by the magnitude $E = \sqrt{(E_x^2 + E_y^2)}$. Here the energy flux components are defined by eq.(IV.13 a,b). The latter approach is very useful for identification of the bathymetric features which generate the high amplitude secondary signals. The contour plots serve well to delineate the time delay between initial tsunami wave and secondary signals. To identify the Koko Guyot as an important bathymetric feature, we plot in FigIV.32, upper panel, the energy flux contours immediately following passage of the main energy lobe past Koko. Note that only the second front is centered on the Koko Guyot, the first front has been generated by the Emperor Seamount Chain and it is not centered on Koko Guyot. The tsunami front in the Northern Pacific shows two closely spaced maxima. Notice that these maxima are related to the initial waves positive and negative amplitudes. The two maxima can be easily tracked up to the arrival at Crescent City.

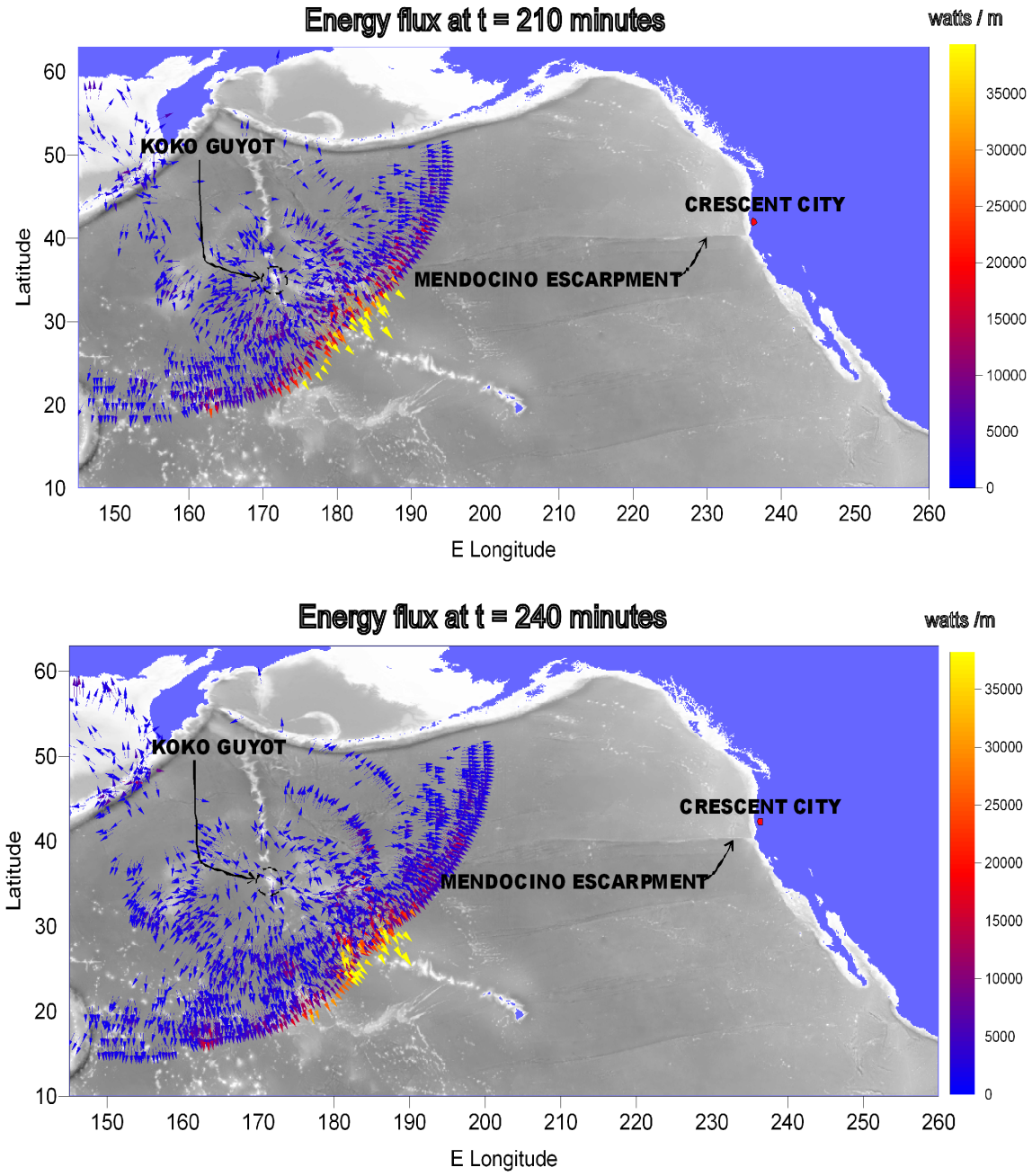

Figure IV.31. Energy flux vectors (top) 3.5 hours and (bottom) 4 hours after tsunami onset. Note radially expanding wave front centered on Koko Guyot.

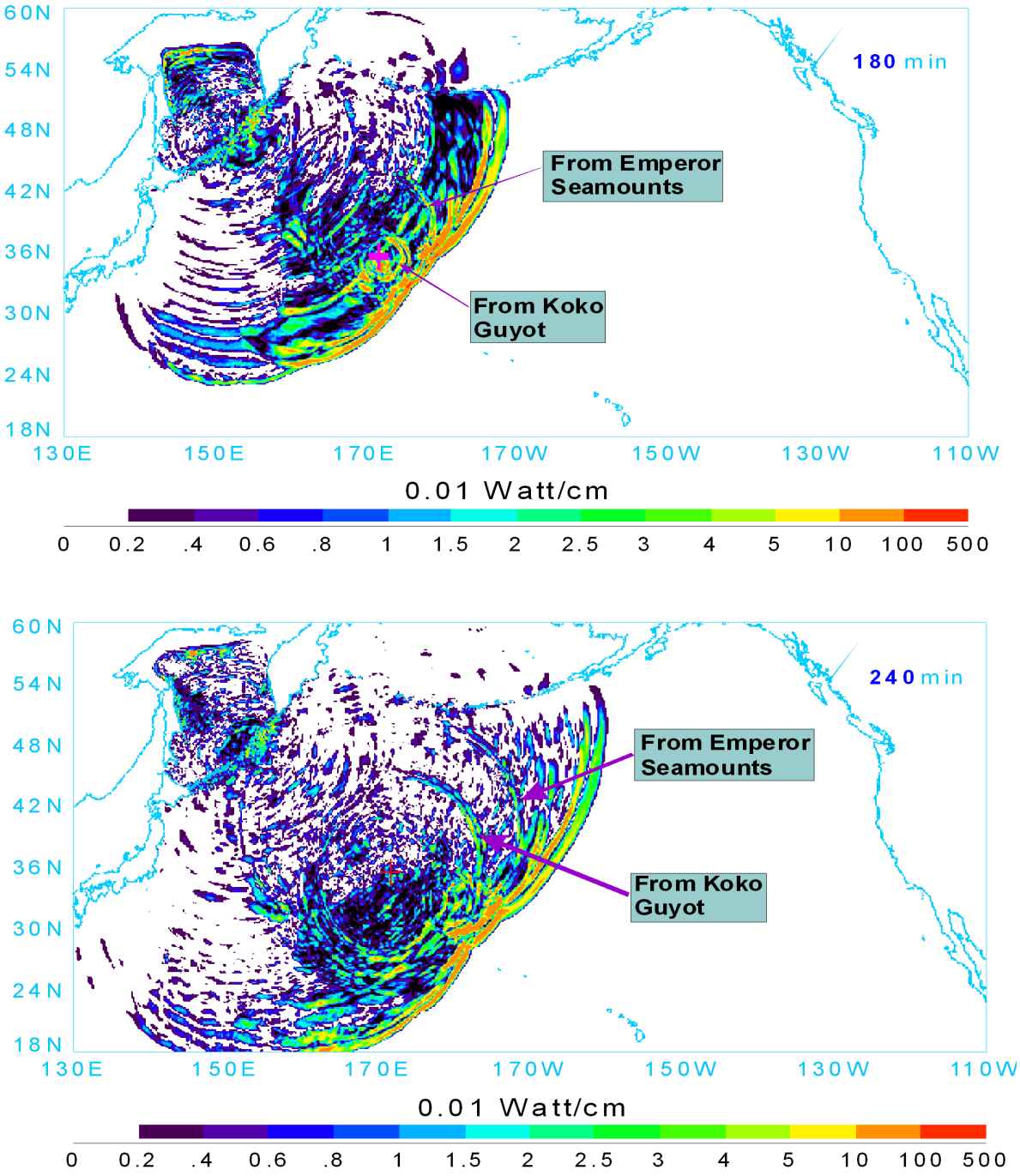

Figure IV.32. Energy flux contours, 180 min (upper panel) and 240 min (lower panel) after the tsunami onset. Two signals of higher energy have been identified as scattered from the Emperor Seamounts and the Koko Guyot. Note that only the second stronger front is centered on the Koko Guyot. Red plus marker points to location of the Koko Guyot seamount.

14. Influence of the spatial resolution on tsunami computations

The latter experiments show that the strength of the second group of waves arriving at Crescent City (CC) depend strongly on bottom topography. Therefore it is important to investigate whether the numerical bottom bathymetry changes resulting from different spatial resolutions will change the predicted tsunami amplitude and phase. The influence of the magnitude of the spatial step used in the numerical model is investigated by computing the Kuril Islands tsunami generated by the same source function but with two different space steps, namely 1 and 2 arcminutes.

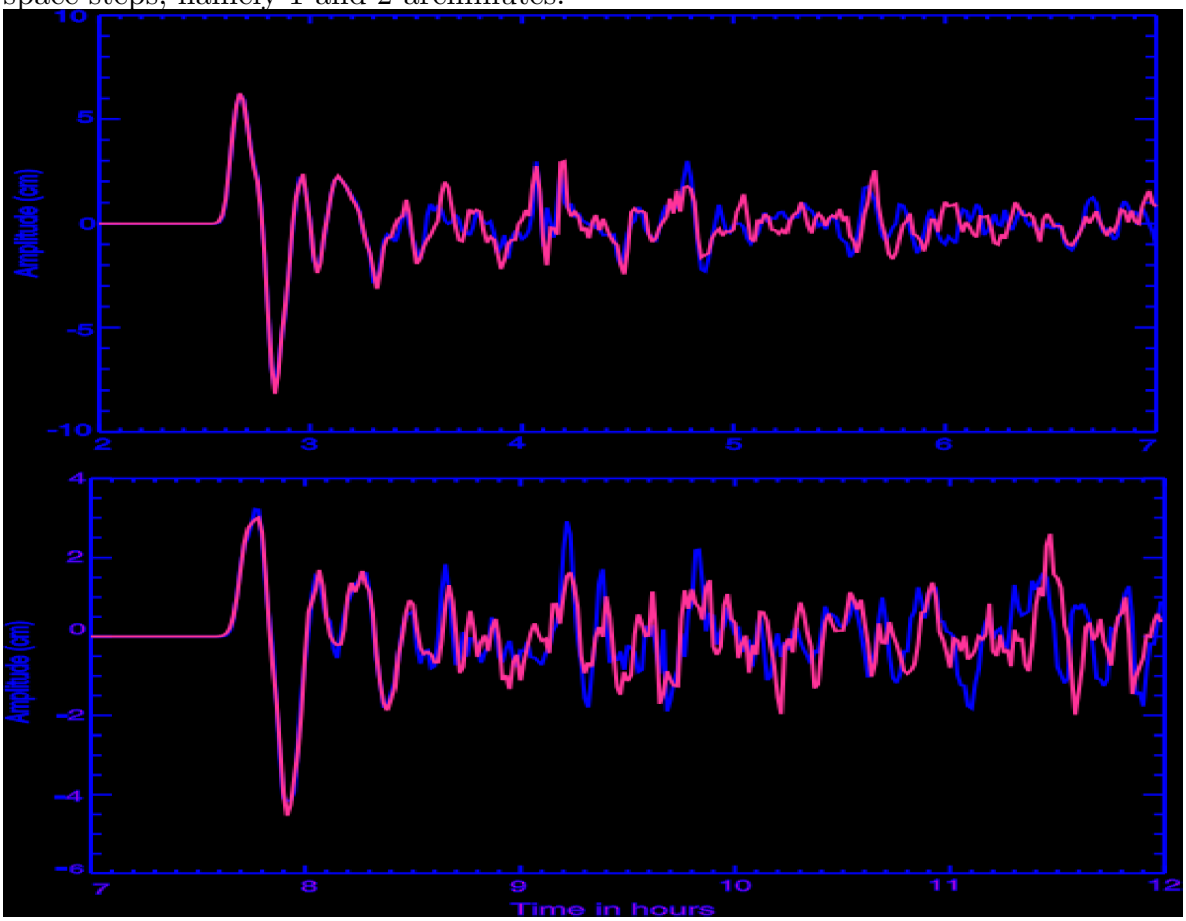

Figure IV.33. Sea level computed at two DART buoy locations. Blue denotes 1 arcminute spatial resolution; red denotes 2 arcminutes spatial resolution.

The comparison is made for the two DART buoy locations: D413 and D411; see FigIV.24. We can glean from FigIV.33 that the initial signals at D413 (close to the source) and at D411 (far from the source) are unchanged when computed with either spatial resolution. Later waves, however, show phase and amplitude differences for the two space steps. Waves which follow the initial signal show differences in amplitude and phase for the computations with the different space step. These secondary waves are generated by various bathymetric features through scattering and refocusing of the initial signal and as we have observed often can be much stronger than the initial signal. Obviously the differences in signal between the various bathymetric features depends strongly on the depth contrast between shallower and deeper domains surrounding bathymetric features

(Mei et al., 2005; Mofjeld et al., 2000). It is important, therefore to consider the influence of spatial resolution on the calculated results. Presently the open ocean bathymetry is resolved with 1 arcminute spatial step. Finer resolution is available in some coastal regions and the 1 arcminute bathymetry in many locations (especially close to Aleutian Islands) is smoothed owing the lack of measurements. Two time series in FigIV.33 derived with the different spatial resolution have shown that the later arriving group of waves which is generated by tsunami/bathymetry interaction depends on the spatial resolution of the bathymetry. These differences cannot be explained by numerical dispersion since neither of these spatial resolutions introduce significant dispersion. Therefore further improvement to tsunami calculations will require finer resolution of the major bathymetric features.

Our investigations are based on the long wave approach. Unique measurements of currents and sea level taken by Bricker et al., 2007 in the wake of Kuril Islands tsunami 2006 delineate periodical motion with periods less than 10 min thus pointing toward short dispersive waves. Examination of tsunami signals (FigIV.29) scattered from the bathymetric features also shows stronger influence of shorter wave periods when compared with the primary tsunami signal generated by source. This may be the direct result of the long wave interaction with bathymetry leading towards generation of the shorter dispersive wave such as edge waves. Similar conclusion follows from Horrillo et al., 2006 numerical experiments on interaction of dispersive and nondispersive wave trains with bathymetry; the dispersive wave trains tend to generate shorter wave periods. Therefore, the role of the small scale bathymetry in the tsunami scattering through the dispersive waves is even more important.

15. Discussions

It is important to recognize that the failure to predict the arrival time of the maximum tsunami in the wake of Kuril Islands Tsunami is due to lack of the proper tools being used by Tsunami Warning Centers. To investigate tsunami wave amplification and time delay we use energy flux. This tool when tested against IOT of 2004 and KIT of 2006 shows that strong secondary signals are generated by scattering, reflection and refocusing of the primary tsunami wave. Tsunami scattering by seamounts and trapping along ridges and escarpments needs further investigations to understand how signal is changed during the tsunami/bathymetry interactions. We cannot solely relay on experiments like those done for the Koko Guyot in FigIV.29 and IV.30. Although the bathymetric features responsible for the tsunami scattering have been identified but we did not arrive to the complete understanding of the generation, scattering and trapping by Koko Guyot. One of the important results from FigIV.29 and IV.30 is that the scattering from Koko Guyot has extended the duration of Kuril Islands tsunami and scattered signal showed directional modulation which resulted in stronger tsunami in the distant locations.

Importance of seamounts and islands in tsunami trapping and scattering was recognized early in tsunami research by Van Dorn, 1970 when he analyzed the sea level change caused by 1957 tsunami recorded at Wake Island. Tsunami of 1964 recorded at Macquarie Island showed a maximum energy at 6 min period which Longuet-Higgins, 1967 explained as trapped long wave by the local bathymetry. A number of theoretical investigations of isolated island/seamount, ridge response to the incoming tsunami signal, see Murty 1977,

Mei, 1989 and Mofjeld et al., 2000 for summary, leads to conclusion that trapped motion can significantly modify the sea level and currents in the island/seamount proximity. Spectra examinations of the sea level oscillations recorded during tsunami events (Loomis, 1966; Van Dorn, 1984; Rabinovich, 1997, Munger and Cheung, 2008, Horrillo et al., 2008) reveal standing waves and strong resonance amplification related to the local bathymetry and to the frequency window of the arriving tsunami waves.

Directional and temporal properties of tsunami signal in proximity to the bathymetric features depend on the superposition of two waves; a primary wave arriving from the tsunami source and a secondary wave generated by the bathymetry. One can straightforwardly assume that such superposition (cf. Lautenbacher, 1970, Fujima et al., 1995; Liu et al., 1995) generates larger amplitudes at the islands perimeter by refraction process, however there is no straightforward approach to deduce temporal changes in the wave trapped around the island/seamount. The question is how the trapped energy decay in time? Often decay is relatively short in time when caused by the nonlinear frictional dissipation. However, sometimes such waves have been observed to last for a long time pointing towards the existence of resonant trapped and partially leaky modes of oscillations (Yanuma, and Tsuji, 1998; Nirupama et al. 2006) and interaction between oscillations trapped at the coast and the continental slope (Nekrasov, 1970; Horrillo et al., 2008). The main parameter which defines resonant trapping or simple reflection of the tsunami wave is the fine resolution bathymetry. The search for the resonance periods which are responsible for the tsunami energy trapping is often based on an assumption of stationary oscillations in the primary wave arriving from the source. The short and variable in time tsunami train impinging on a bathymetric feature does not develop the full resonance response (Munk et al., 1956; Horrillo et al., 2008). Examination of tsunami signals (Kowalik et al., 2008) scattered from the bathymetric features also shows stronger influence of shorter wave periods when compared with the primary tsunami signal arriving from a source. As Mofjeld et al., 2000 have noticed these short period waves also contribute to the random appearance of tsunami time series when waves reflected from various bathymetric features interact with each other.

An intermittent behavior of the tsunami train seems to be the crux of all problems related to response calculation of tsunami impinging on seamounts and ocean ridges: shorter and longer tsunami trains result in different enhancement and trapping (Munk et al., 1956; Horrillo et al., 2008). In the above applications to the Indian Ocean Tsunami of 2004 and Kuril Islands Tsunami of 2006 we have demonstrated that sudden changes caused by higher energy pulses in the intermittent tsunami wave trains can be assessed by energy fluxes. These experiments defined in explicit way the bathymetric features which scatter tsunami signal towards ports, like Crescent City. Identification of the distant bathymetric features was achievable since the energy flux delineated the energy pathways that coupled bathymetric features (like Koko Guyot) to ports located thousands of kilometers apart.

References

Bernard, E., C. Mader, G. Curtis, and K. Satake (1994), Tsunami inundation model study of Eureka and Crescent City, California. *NOAA Tech. Memo. ERL PMEL-103*, 81 pp., NOAA, Silver Spring, Md.

Bricker, J. D., S. Munger, J. R. Wells, G. Pawlak, and K. F. Cheung (2007), ADCP observations of edge waves off Oahu in the wake of the November 2006 Kuril Islands tsunami. *Geophys. Res. Lett.*, 34, L23617, doi:10.1029/2007GL032015.

British Oceanographic Data Centre (2003), *GEBCO Digital Atlas [CD-ROM]*, Disk 1, Liverpool, U.K.

Candella, R. N., A. B. Rabinovich and R. E. Thomson (2008), The 2004 Sumatra tsunami as recorded on the Atlantic coast of South America.*Adv. Geosci.*, 14, 117128.

Davies, T. A., P. Wilde, and D. A. Clague (1972), Koko Seamount: A major guyot at the southern end of the Emperor Seamounts. *Mar. Geol.*, 13, 311 321.

Flather, R.A. and Heaps, N.S. (1975), Tidal computations for Morecambe Bay. *Geophys. J. Royal Astr. Soc.*, **42**, 489-517.

Fujima, K., Y. Dede, Goto, C. Hayashi, K., Shigemura, T. (1995), Characteristics of long waves trapped by conical island. *Coastal Engineering Journal*, 38(2), 111-132

Gill A. E. (1982), *Atmosphere-Ocean Dynamics*. Academic Press, 662 pp.

Goto, C. and N. Shuto (1981), Numerical simulation of tsunami propagations and run-up. *Tsunami-Their Science and Engineering*, ed., Iida, K. and T. Iwasaki, 439-451.

Gonzalez, F. I., K. Satake, E. F. Boss, and H. O. Mofjeld (1995), Edge wave and non-trapped modes of the 25 April 1992 Cape Mendocino tsunami, *Pure Appl. Geophys.*, 144(3/4), 409 426.

Goring D. (2005), Sumatra Tsunami at New Zealand Ports and Harbours, http://www.mulgor.co.nz/SumatraTsunami/index.htm.

Hebert, H., P. Heinrich, F. Schindele, and A. Piatanesi (2001), Far-field simulation of tsunami propagation in the Pacific Ocean: Impact on the Marquesas Island (French Polynesia), *J. Geophys. Res.*, 106(C5), 9161 9177.

Henry, R. F. and M. G. G. Foreman (2001), A representation of tidal currents based on energy flux. *Marine Geodesy*, 2493, 139-152.

HRV - Harvard CMT Catalog (2005), Harvard Seismology: Centroid-Moment Tensor Project, posted at http://www.seismology.harvard.edu/CMTsearch.html.

Horrillo, J., Z. Kowalik, and Y. Shigihara (2006), Wave dispersion study in the Indian Ocean-Tsunami of December 26, 2004. *Marine Geodesy*, 29, 149- 166.

Horrillo, J., W. Knight, and Z. Kowalik (2008), Kuril Islands tsunami of November 2006: 2. Impact at Crescent City by local enhancement, *J. Geophys. Res.*, 113, C01021,

doi:10.1029/2007JC004404.

Hwang, L–S., and D. J. Divoky (1970), Tsunami generation. *J. Geoph. Res.*, 75, 6802–6817.

Hwang, L–S., H. L. Butler and D. J. Divoky (1972), Tsunami model: Generation and open-sea characteristics. *Bulletin of the Seismological Society of America*, v. 62, no. 6, 1579-1596

Imamura F. (1996), Review of tsunami simulation with a finite difference method. In *Long-Wave Runup Models*, H.Yeh, P. Liu and C. Synolakis, Eds, World Scientific, 25–42.

Imamura, F., C. Goto, Y. Ogawa and N. Shuto (1997), *IUGG/IOC Time Project, Numerical Method of Tsunami Simulation with the Leap–Frog Scheme.* IOC, Manuals and Guides, 35, 126pp.

Iwasaki, S.I. (2005), Posting of Thailand tide gage data to Tsunami Bulletin Board, also posted at http://www.navy.mi.th/hydro/tsunami.htm.

Ji, C. (2004). Preliminary Result of the 04/12/26 (Mw 9.0), OFF W COAST of Northern Sumatra Earthquake, posted at

Keulegan, G. H., J. Harrison, and M. J. Mathews (1969), Theoretics in design of the proposed Crescent City harbor tsunami model, *Tech. Rep. H-69-9*, 124 pp., Waterw. Exp. Stn., U.S. Army Corps of Eng., Vicksburg, Miss.
http://www.gps.caltech.edu/%7Ejichen/Earthquake/2004/aceh/aceh.html.

Koshimura, S., Y. Hayashi, K. Munemoto and F. Imamura. 2008. Effect of the Emperor seamounts on trans-oceanic propagation of the 2006 Kuril Island earthquake tsunami. *Geoph. Res. Letters*, v. 35, L02611, doi:10.1029/2007GL032129.

Koshimura, S., F. Imamura, and N. Shuto (2001), Characteristics of Tsunamis Propagating over Oceanic Ridges. *Natural Hazards*, 24(3), 213229.

Koshimura, S., F. Imamura, and N. Shuto (1999), Propagation of obliquely incident tsunami on a slope Part I: Amplification of tsunamis on a continental slope. *Coastal Eng. J.*, 41(2), 151 164.

Kowalik, Z. (2003), Basic Relations Between Tsunami Calculation and Their Physics - II. *Science of Tsunami Hazards*, v. 21, No. 3, 154-173

Kowalik, Z. 2008. Energy flux as a tool in locating tsunami secondary sources, *Science of Tsunami Hazards*, Vol. 27, No. 3, 1-27.

Kowalik, Z., J. Horrillo, W. Knight, and T. Logan (2008), Kuril Islands tsunami of November 2006: 1. Impact at Crescent City by distant scattering, J. Geophys. Res., 113, C01020, doi:10.1029/2007JC004402.

Kowalik, Z., Knight, W. Logan, T. and P. Whitmore (2007a), The tsunami of 26 December 2004: Numerical Modeling and energy considerations-II. In: Tsunami and Its Hazard in Pacific and Indian Oceans,Eds: Satake,K., Okal, E. A., Borrero, J. C.,*Pure and Applied Geophysics (PAGEOPH)*,vol. 164, No. 2/3,379-393.

Kowalik Z., W. Knight, T. Logan, and P. Whitmore (2007b), Numerical Modeling of the Indian Ocean Tsunami. In: *The Indian Ocean Tsunami*. Co-editors: T. Murty, U. Aswathanarayana and N. Nirupama. Taylor and Francis, London, pp. 97-122.

Kowalik Z., W. Knight, T. Logan, and P. Whitmore (2005a), Numerical Modeling of the Global Tsunami: Indonesian Tsunami of 26 December 2004. *Science of Tsunami Hazards*, Vol. 23, No. 1, 40- 56.

Kowalik, Z., Knight, W. Logan, T. and P. Whitmore (2005b), The tsunami of 26 December 2004: Numerical Modeling and energy considerations. *Proceedings of the International Tsunami Symposium*, Eds.: G.A. Papadopoulos and K. Satake, Chania, Greece, 27-29 June, 2005, 140-150.

Kowalik, Z. and Murty, T.S. (1993a), *Numerical Modeling of Ocean Dynamics*. World Scientific, 481 pp.

Kowalik, Z. and Murty, T.S. (1993b), Numerical simulation of two-dimensional tsunami runup. *Marine Geodesy*, 16, 87–100.

Kowalik, Z. and P. M. Whitmore (1991), An investigation of two tsunamis recorded at Adak, Alaska. *Science of Tsunami Hazards*, 9(2):67-83.

Kowalik, Z. and T. Murty (1987), Influence of size, shape and orientation of the earthquake source area in the Shumagin Seismic gap on the resulting tsunami. *J. Phys. Oceanogr.* 17(7):1057-1062.

Lander, J. F., and P. A. Lockridge (1989), *United States tsunamis 1690 1988*, http://www.ngdc.noaa.gov/seg/hazard/tsu.shtml, Natl. Geophys. Data Cent., Boulder, Colo.

Lautenbacher, C. C. (1970), Gravity wave refraction by islands. *J. Fluid Mech.* 41, 655-672.

Liu PLF, Cho YS, Briggs MJ, Kanoglu U, Synolakis CE. (1995), Runup of solitary wave on a circular island. *Journal of Fluid Mechanics*. 302:259-285.

Lobkovsky, L. I., B. V. Baranov, R. K. Mazova, and L. Y. Kataeva (2006), Implications of the seismic source dynamics for the characteristics of a possible tsunami in a model problem of the seismic gap in the Central Kurile region. *Russ. J. Earth Sci.*, 8, ES5002, doi:10.2205/2006ES000209.

Longuet-Higgins, M.S. (1967), On the Trapping of Wave Energy Round Islands. *Jour. Fluid Mech.*, Vol. 29, Part 4, pp 781-821.

Longuet-Higgins, M. S. (1969), On the transport of mass by time-varying ocean currents. *Deep-Sea Res.*, 16, 431–447.

Loomis, H. G. (1966), Spectral analysis of tsunami records from stations in the Hawaiian Islands. *Bull. Seismol. Soc. Am.*, 56, 697 713.

Lynett, P. J.,T.-R. Wu and P.L.-F.Liu (2002), Modeling wave run-up with depth–integrated equations, *Coast. Engrg.*, 46(2), 89-107.

Mader, C. L. (1988), *Numerical Modeling of Water Waves*. Univ. of California Press, Brkeley, Calif..

Mader, C. L. (2004), *Numerical Modeling of Water Waves*. CRC Press, 274 pp.

Mader, C. L., and E. N. Bernard (1993), Modeling tsunami flooding of Crescent City, paper presented at *16th IUGG/IOC International Tsunami Symposium, Int. Union of Geod. and Geophys.*, Wakayama, Japan.

Marchuk, A. G., L. B. Chubarov and Iu. I. Shokin (1983), *Numerical Modeling of Tsunami Waves*, Izd. Nauka, Novosibirsk. (Los Alamos, 1985), 282 pp.

Mei, C. C. (1989), *The Applied Dynamics of Ocean Surface Waves*. World Scientific, 740 pp.

Mei, C. C., M. Stiassnie, and D. K.-P. Yue (2005), *Theory and Applications of Ocean Surface Waves. Part 1: Linear Aspects*, Adv. Ser. Ocean Eng., vol. 23, 506 pp., World Sci., Hackensack, N. J.

Merrifield, M.A., Y.L. Firing, G. Brundrit, R. Farre, B. Kilonsky, W. Knight, L. Kong, C. Magori, P. Manurung, W. Mitchell, F. Shillington, E.M.S. Wijeratne, J. Jardin, S. Nakahara, F.-Y. Porter, and N. Turesky (2005), Tide Gauge Observations of the Indian Ocean Tsunami, December 26, 2004, manuscript submitted to *Geophysical Research Letters* Jan., 2005.

Mofjeld, H. O., V. V. Titov, F. I. Gonzalez, and J. C. Newman (2000), Analytic theory of tsunami wave scattering in the open ocean with application to the North Pacific, *NOAA Tech. Memo. OAR PMEL 116*, 38 pp., NOAA, Silver Spring, Md.

Munger S. and K. F. Cheung (2008), Resonance in Hawaii waters from the 2006 Kuril Islands Tsunami. *Geophysical Research Letters*, 35, L07605, doi:10.1029/2007 GL032843

Munk, W., F. Snodgrass, and G. Carrier (1956), Edge waves on the continental shelf. *Science*, 123(3187), 127 132.

Murty, T.S. (1977), *Seismic Sea Waves - Tsunamis*. Bulletin 198, Fisheries Research Board of Canada, Dept. of Fisheries, Ottawa, Canada, 337 pp.

Murty, T., Rao, A.D, Nirupama, N., and Nistor, I. (2006), Tsunami warning systems for the hyperbolic (Pacific), parabolic (Atlantic) and elliptic (Indian) oceans, *J. of Ind. Geophysical Union*, Vol. 10, No. 2, 69-78.

Nekrasov, A. V. (1970), Transformation of tsunamis on the continental shelf. In: *Tsunamis in the Pacific Ocean*, W.M. Adams, ed, East–West Center Press, Honolulu, 337-350.

Nekrasov, A. V. (1992), On tidal energy horizontal circulation. *The Journal of the Korean Society of Coastal and Ocean Engineers*, 4(3), 168–177.

NIO - India National Institute of Oceanography (2005), 26 December 2004 Tsunami, posted at http://www.nio.org/jsp/tsunami.jsp.

NEIC - U.S. National Earthquake Information Center (2004), Magnitude 9.0 OFF THE

WEST COAST OF NORTHERN SUMATRA Sunday, December 26, 2004 at 00:58:53 UTC Preliminary Earthquake Report, posted at
http://neic.usgs.gov/neis/bulletin/neic_slav_ts.html

Nirupama, N., T.S. Murty, I. Nistor and A.D. Rao (2006), Persistent high water levels around Andaman & Nicobar Islands following the 26 December 2004 Tsunami. *Science of Tsunami Hazards*, Vol. 24, No. 3, 183-193.

Okada, Y. (1985), Surface deformation due to shear and tensile faults in a half-space. *Bulletin of the Seismological Society of America*, 75, 1135-1154.

Rabinovich, A. B. (1997), Spectral analysis of tsunami waves: Separation of source and topography effects. *J. Geophys. Res.*, 102, 12,663 12,676.

Rabinovich, A.B. (2005), Web compilation of tsunami amplitudes and arrival times. http://www-sci.pac.dfo-mpo.gc.ca/osap/projects/tsunami/tsunamiasia_e.htm.

Reid, R.O. and R.O. Bodine (1968), Numerical model for storm surges in Galveston Bay. *J. Waterway Harbour Div.*, 94(WWI), 33–57.

Roberts, J. A., and E. K. Kauper (1964), The effects of wind and precipitation on the modification of South Beach, Crescent City, California, Including an appendix on the focusing of tsunami energy at Crescent City, prepared by C.-W. Chien, final report, 98 pp., Environ. Sci. Div., Dep. of the Army, Washington, D. C.

Snodgrass, F.E., Munk, W.H. and Miller, G. R. (1962), Californias continental borderland. Part I. Background spectra. *J. Mar. Research*, v. 20, pp. 330.

SOI - Survey of India (2005), Preliminary report of tsunami observations, posted at http://www.surveyofindia.gov.in/tsunami4.htm.

Stein, S. and Okal E. (2005), Ultra-long period seismic moment of the great December 26, 2004 Sumatra earthquake and implications for the slip process, posted at http://www.earth.northwestern.edu/people/seth/research/sumatra2.html.

Titov, V., Rabinovich, A. B., Mofjeldt, H. O., Thomson, R. E., and Gonzales, F. I. (2005), The global reach of the 26 December, 2004 Sumatra tsunami, Science 309, 20452048.

Van Dorn W. G. (1970), Tsunami Response at Wake Island: a Model Study. 1970. *J. of Mar. Res.*, v.28, no.3, 336-344.

Van Dorn, W.G. (1984), Some Tsunami Characteristics Deducible from Tide Records. *J. Phys. Oceanography*, Vol. 14, No. 2, 353-363

Vastano, A. C. and R. O. Reid 1967. Tsunami response for islands: verification of a numerical procedure, *J. Mar. Res.*, 25(2), 129–139.

Wiegel, R. L. (1965), Protection of Crescent City California from tsunami waves, report, 112 pp., Redev. Agency of the City of Crescent City, Calif., Crescent City.

Yagi, Y. (2005), Preliminary Results of Rupture Process for 2004 off coast of Northern Sumatra Giant Earthqauke (ver. 1), posted at

http://iisee.kenken.go.jp/staff/yagi/eq/Sumatra2004/Sumatra2004.html.

Yanuma, T., and Y. Tsuji (1998), Observation of edge waves trapped on the continental shelf in the vicinity of Makurazaki Harbor, Kyushu, Japan. *J. Oceanogr.*, 54, 9 18.

Zielinski, A. and N. K. Saxena (1984). Modeling of tsunami directivity. Science of Tsunami Hazards, 2, 2, 113-118.